

## Durham E-Theses

---

### *Development of a thermal sensor for probing small volumes*

ATHERTON, JOSEPH,JAMES

#### How to cite:

---

ATHERTON, JOSEPH,JAMES (2012) *Development of a thermal sensor for probing small volumes*, Durham theses, Durham University. Available at Durham E-Theses Online:  
<http://etheses.dur.ac.uk/3526/>

#### Use policy

---

The full-text may be used and/or reproduced, and given to third parties in any format or medium, without prior permission or charge, for personal research or study, educational, or not-for-profit purposes provided that:

- a full bibliographic reference is made to the original source
- a [link](#) is made to the metadata record in Durham E-Theses
- the full-text is not changed in any way

The full-text must not be sold in any format or medium without the formal permission of the copyright holders.

Please consult the [full Durham E-Theses policy](#) for further details.



# Development of a thermal sensor for probing small volumes

Joseph James Atherton

School of Engineering and Computing Sciences

Durham University

A thesis submitted for the degree of Doctor of Philosophy

14<sup>th</sup> May 2012

This thesis presents the design, fabrication and characterisation of a thermal micro-sensor capable of operating on small scale samples. It was initially characterised by measuring the thermal conductivity of 100  $\mu\text{l}$  liquid droplets and thin materials (sheets of paper) before being applied to the measurement of the water content of plant leaves. The device consists of a micro-heater and two thin-film thermocouples formed on a flexible polyimide substrate and used microfabrication techniques to precisely pattern the sensing elements.

The heater was used to induce a temperature gradient within a sample in contact with the device, which was recorded as a difference in temperature ( $\Delta T$ ) between the two thermocouples. Various experiments have demonstrated that  $\Delta T$  was dependent on the total thermal resistance (consisting of the bulk thermal conductivity and thermal contact resistance) of the sample under inspection. The device's sensitivity to bulk thermal conductivity was shown by recording the variation in  $\Delta T$  for 100  $\mu\text{l}$  droplets of glycerine/water mixtures. Different compositions of the mixture served as thermal conductivity standards. The measurement of mixtures of propanol/water further demonstrated that the device could be used to indirectly monitor the composition of small volume binary solutions by measurement of the thermal conductivity.

By monitoring the thermal conductivity of wetted paper, it was shown that the device was sensitive to the increase in the total thermal resistance as the paper dried out. Furthermore, theoretical and experimental drying times were in agreement and exhibited a similar dependence on the air temperature. This provided clear evidence of the device's ability to monitor thermal conductivity of small samples.

The final element of this work was the real-time monitoring of the water content of plant leaves. The device was clamped to an abscised leaf which was allowed to dry over a period of 6 hours. A

comparison between the weight of the leaf and  $\Delta T$  measurements showed a linear dependence. It was found that the changes in thermal properties were dominated by the water content of the leaf. The device was subsequently shown to be sensitive to changes in the water content of the leaves of plants subjected to water stress conditions, demonstrating its ability to monitor the real-time water content in-situ.

## *Acknowledgements*

---

I would like to thank Dr. Dagou Zeze, for his help guiding me through this work as my supervisor.

I am grateful to everyone who has helped out throughout this project: the members of the cleanroom for their advice and friendship, the proof readers (Sarah, Grant, Gordon and Dad) for their attention to detail and particularly Dr. Mark Rosamond for the innumerable times he has helped me while working on this project, acting as a teacher, mentor and friend.

Finally, I would like to thank my family and Katie for their support and love.

## ***Declaration***

---

The work contained in this thesis has not been submitted elsewhere for any other degree or qualification and unless referenced otherwise is the author's own work.

The copyright of this thesis rests with the author. No quotation from it should be published without prior written consent and information derived from it should be acknowledged.

## *Table of Contents*

---

1. Introduction.....	1
1.1. Research Question .....	1
1.2. Project aims.....	3
1.3. Structure of this thesis.....	4
1.4. Need for plant water status monitoring.....	6
1.5. Current technologies .....	9
1.5.1. Leaf tissue based methods.....	9
1.5.1.1. Pressure probe technique .....	9
1.5.1.2. Pressure chamber .....	10
1.5.1.3. Psychrometer.....	11
1.5.1.4. Patch clamp pressure probe.....	11
1.5.1.5. Leaf thickness sensor .....	12
1.5.2. Remote methods.....	12
1.5.2.1. Infrared techniques.....	12
1.5.2.2. Terahertz techniques .....	13
1.5.2.3. Satellite imaging .....	13
1.5.3. Other methods .....	13
1.5.3.1. Visual methods.....	13
1.5.3.2. Sap flow monitors .....	13
1.5.3.3. Trunk diameter measurements .....	14
1.5.3.4. Xylem cavitation .....	14

1.5.3.5.	Soil water content.....	14
1.6.	Thermal detection of water content .....	15
1.7.	References.....	16
2.	Principle of Operation.....	22
2.1.	Rationale for the device .....	22
2.1.1.	Why measure thermal conductivity?.....	23
2.1.2.	Small scale thermal sensors .....	24
2.1.3.	Methods for the measurement of thermal conductivity .....	25
2.1.3.1.	The guarded hot-plate method .....	27
2.1.3.2.	Line heat source method .....	27
2.1.3.3.	Single and dual probe methods .....	28
2.1.3.4.	Standards.....	28
2.1.4.	Devices in this project.....	29
2.1.5.	Thin-film thermocouples.....	30
2.1.6.	Thermocouple theory .....	33
2.1.7.	Effect of small scales on thermocouple operation .....	37
2.2.	Device designs .....	38
2.2.1.	Early designs.....	39
2.2.1.1.	Junction area .....	40
2.2.1.2.	Metal combinations.....	42
2.2.2.	SU-8 and polyimide devices .....	45
2.2.2.1.	Polymer substrates .....	45
2.2.2.2.	Design A .....	48

2.2.2.2.1.	SU-8 suspended membrane devices.....	50
2.2.2.2.2.	Polyimide based devices .....	54
2.2.2.3.	Design B.....	57
2.3.	Conclusions.....	60
2.4.	References.....	61
3.	Microfabrication .....	66
3.1.	Device fabrication.....	67
3.1.1.	Metallisation and patterning.....	70
3.1.2.	Lift-off trials.....	76
3.1.2.1.	Introduction.....	76
3.1.2.2.	Lift-off profile.....	76
3.1.2.3.	Single layer process .....	78
3.1.2.4.	Bi-layer process.....	81
3.1.2.5.	Development time .....	82
3.1.2.6.	Exposure time .....	83
3.1.3.	Metallisation effects.....	87
3.1.3.1.	Deposition method .....	87
3.1.3.2.	Thickness effect .....	89
3.1.3.3.	Metal choice.....	91
3.1.4.	SU-8 membrane devices .....	93
3.1.4.1.	SU-8 as a substrate.....	93
3.1.4.2.	Fabrication of SU-8 devices.....	95
3.1.5.	Polyimide devices .....	96

3.1.5.1.	Advantages of polyimide as a substrate .....	96
3.1.5.2.	Fabrication of polyimide devices .....	98
3.2.	Jigs for probing the device .....	102
3.2.1.	Probe station.....	103
3.2.2.	Gold sprung-probe jig .....	103
3.2.3.	Molex connector .....	105
3.3.	Control electronics .....	106
3.4.	Conclusions.....	108
3.5.	References.....	110
4.	Device Characterisation & Modelling .....	114
4.1.	Modelling.....	115
4.1.1.	Heat flow mechanisms .....	115
4.1.1.1.	Conduction.....	115
4.1.1.2.	Convection .....	116
4.1.1.3.	Radiation .....	117
4.1.2.	1-D model .....	117
4.1.3.	2-D model with axial symmetry.....	120
4.1.4.	Dimensional effects of the model .....	122
4.1.5.	Effect of the mesh quality .....	126
4.1.6.	Sample thermal conductivity .....	127
4.1.7.	Effect of the substrate .....	130
4.2.	Characterisation .....	132
4.2.1.	Characterisation requirements.....	132

4.2.2.	Temperature calibration .....	133
4.2.3.	Monitoring thermal properties of small samples .....	136
4.2.3.1.	Liquid samples .....	137
4.2.3.1.1.	Large volumes – 50 ml.....	137
4.2.3.1.2.	Small volumes – 100 $\mu$ l.....	140
4.2.3.2.	Monitoring the drying rate of wetted paper .....	144
4.3.	Conclusions.....	149
4.4.	References.....	151
5.	The Effect of Thermal Contact Resistance .....	153
5.1.	Thermal contact resistance theory.....	153
5.2.	Experimental determination of thermal contact resistance .....	160
5.3.	Material effects .....	163
5.4.	Effect of a TIM .....	165
5.5.	Conclusions.....	169
5.6.	References.....	170
6.	A Sensor for Leaf Water Content .....	172
6.1.	Plant water status theory .....	173
6.2.	Relating induced thermal gradient to water content .....	176
6.2.1.	Experimental measurements on an abscised leaf .....	177
6.2.2.	$\Delta T$ dependence on water content .....	180
6.2.3.	Dependence of $\Delta T$ on leaf water content .....	183
6.2.3.1.	Structural effects .....	183
6.2.3.2.	Effect of thermal contact resistance on leaf measurements .....	186

6.3.	Plant water status monitoring.....	191
6.3.1.	Aims .....	191
6.3.2.	Real-time detection of water stress in a plant .....	192
6.3.2.1.	A comparison between Pak Choi and Lettuce plants suffering water stress	198
6.4.	Potential applications .....	202
6.4.1.	Real-time irrigation feedback.....	202
6.4.2.	Fresh produce monitoring .....	205
6.4.3.	Detection of water variations across a leaf .....	205
6.5.	Conclusions.....	206
6.6.	References.....	207
7.	Conclusions and Further Work .....	210
7.1.	Conclusions.....	210
7.2.	Further work.....	213
8.	Publications.....	215
8.1.	Journal articles .....	215
8.2.	Conferences.....	215

## *List of Figures*

---

Figure 1.1 – Schematic diagram (not to scale) of the pressure probe technique for determining the water potential of individual plant cells.....	10
Figure 1.2 – Pressure chamber technique for determining the water potential of an abscised leaf	11
Figure 2.1 – Thermal conductivity based on the composition of glycerine/water mixtures at 20 °C which is seen to vary as a function of the composition. Values taken from [2] .....	24
Figure 2.2 – Examples of one-dimensional heat flow. a) an insulated cylinder; b) a sphere & c) heated, insulated plate.....	26
Figure 2.3 – The guarded hot plate method .....	27
Figure 2.4 – The line heat source method.....	28
Figure 2.5 – By monitoring the thermal gradient set up by a resistive heater, the thermal conductivity of the sample can be determined.....	30
Figure 2.6 – a) The net emf produced by two similar conductors is zero due to the law of homogenous circuits; b) an emf is produced when two dissimilar materials have a temperature difference across their junctions & c) stacking several pair of thermocouples increases the emf generated.....	37
Figure 2.7 – Early devices were fabricated on silicon and glass substrates for ease of fabrication, however the device took many seconds or minutes to achieve steady state conditions due to the thermal mass of the substrate. ....	40
Figure 2.8 – Schematic diagram of one examples of an early device which was used to investigate the effect of junction area. Red areas were patterned with Cr while black areas were Ni.....	41
Figure 2.9 –Output from four TFTCs plotted against the distance from the heater (to the midpoint of the sensing junction). Also shown are thermal camera measurements taken at six points. All values were normalised against the value at a distance of 325 µm from the heater, which represented the nearest TFTC junction .....	42

Figure 2.10 – Output response for several thermocouple metal combinations. Cr-Ni devices were seen to give the highest Seebeck coefficient, regardless of the order of deposition. Annealing the device at 350 °C was seen to increase the output response.....	44
Figure 2.11 – Comparison between polymer-based devices; a) A silicon based device; b) An SU-8 membrane device & c) A released polyimide device. Hatched areas represent the sensing area of the device .....	47
Figure 2.12 – Details of Design A: a) Detail of the sensing area (red tracks are Cr, black are Ni); b) View of the entire device, with the highlighted area shown in detail in a) & c); c) Dimensioned SEM image of the sensing area.....	49
Figure 2.13 – A comparison between the output of a TFTC before and after suspension. The TFTC was located 50 µm from the heater on a Design A device formed on a silicon substrate (pre-suspension) and then on an SU-8 membrane after this was released from the substrate (post-suspension).....	51
Figure 2.14 – SEM image showing the suspended SU-8 membrane. The sensing area of the device is suspended underneath the SU-8 membrane. ....	52
Figure 2.15 – SEM images showing the pitting and cracking observed in metal tracks suspended underneath the SU-8 membrane, viewed through a patterned hole in the SU-8 membrane .....	53
Figure 2.16 – A comparison of the sensitivity of devices formed on silicon, SU-8 and polyimide. The TFTC was located 50 µm from the heater on a Design A device. Inset shows the detail of the SU-8 and polyimide devices .....	55
Figure 2.17 – Photograph showing a Design A polyimide device.....	56
Figure 2.18 – Photograph showing a Design A polyimide device with electrical connections made using the gold sprung-probe jig .....	56
Figure 2.19 – Photographs showing a Design B device and the Molex connector used to make electrical connections.....	57
Figure 2.20 – Details of Design B: a) Detail of the sensing area (red tracks are Cr, black are Ni); b) View of the entire device, with the highlight area shown in detail in a) & c); c) Dimensioned SEM image of the sensing area.....	59

Figure 3.1 – A photograph showing a traditional thermocouple alongside a Design A TFTC device.....	69
Figure 3.2 – Fabrication stages required to form a device on a silicon substrate: A) Wafer cleaning; B) Oxidation of the wafer; C) Hexamethyldisiloxane Priming; D) Photolithography; E) RIE de-scum; F) Deposition of metal 1; G) Lift-off & H) Repeat C-G for metal 2.....	71
Figure 3.3 – A schematic representation of the silylation process. Adapted from [15].....	73
Figure 3.4 – Photoresist profiles for lift-off. A) shows the ideal profile while B) to F) show defective profiles.....	78
Figure 3.5 – SEM image of a line (with 90° bend) after processing using a single layer lift-off profile process.....	79
Figure 3.6 – An SEM showing a 500 nm layer of Ni (e-beam deposited over a line feature formed using the single-layer lift-off process) which caused curling of the photoresist.....	80
Figure 3.7 – The effect of development time on the overhang produced using the bi-layer lift-off technique. The trial was run using a mask with 7 μm dots and a 3 s exposure time .....	83
Figure 3.8 – The effect of exposure dose (time) on the overhang produced using a bi-layer. Each exposure was developed for 2.5 minutes .....	85
Figure 3.9 – An SEM image showing the lift-off profile obtained using the process outlined in Table 3.4 .....	86
Figure 3.10 – Microscope image showing overlapping layers of Ni (left) and Cr (right) with severe cracking in the Cr and overlapping region.....	89
Figure 3.11 – A typical calibration graph obtained for a Design A device formed on a polyimide substrate .....	91
Figure 3.12 – Measured Seebeck coefficients for various metal combinations. Label denotes deposition order, * denotes annealing after deposition.....	92
Figure 3.13 – SEM images showing the 10 μm thick SU8 layer with holes acting as an etch mask for the Xe F <sub>2</sub> silicon etch. The void created in the silicon is clearly visible beneath the holed region of SU8.....	94

Figure 3.14 – Fabrication stages required to form an SU-8 membrane device: A) Cleaning; B) Oxidation and metallisation; C) Spin SU-8; D) Expose; E) Develop; F) Etch SiO <sub>2</sub> ; G) & H) XeF <sub>2</sub> etch.....	94
Figure 3.15 – Fabrication stages required to form a device on a polyimide substrate: A) Clean wafer; B) Spin polyimide; C) Metallise and pattern; D) Encapsulate with polyimide; E) RIE etch to expose connections & F) Peel from substrate.....	98
Figure 3.16 – An SEM image showing the thickness of the polyimide after it has been spin coated with 3 layers and removed from the silicon carrier.....	99
Figure 3.17 – A Molex ribbon cable connector can be used to make electrical connections to Design B type devices. Note the Kapton which has been bonded to aid insertion into the Molex connector.....	102
Figure 3.18 – a) 3-D drawing of the sprung-probe testing jig; b) Schematic showing the details of the boom and the location of the sprung-probes & c) A photograph showing the sprung-probe test jig probing a device fabricated on a glass microscope slide .....	104
Figure 3.19 – Schematic diagram of the instrumentation amplifier.....	107
Figure 4.1 – Simplified one-dimensional, steady state analytical model of conduction, based upon Fourier’s law applied to a sphere with constant thermal conductivity.....	118
Figure 4.2 – Visualisation from 2-D numerical model (COMSOL) based on a PI device surrounded by water.....	120
Figure 4.3 – The ‘standard’ model. These geometries and boundary conditions were used to create a 2-D model with axial symmetry .....	122
Figure 4.4 – Boundary conditions used to investigate the effect of the model’s dimensions.....	124
Figure 4.5 – The radius of the model is seen to play a diminishing role as the volume of the model increases.....	125
Figure 4.6 – A comparison of two meshes shows that the coarse mesh is adequate as decreasing the mesh size has no effect on the output.....	126

Figure 4.7 – Validation of model by comparison with experimental results for a) water and b) IPA, based on a heater input power of 13.5 mW ( $\pm 5\%$ error bars added to the IPA graph).....	129
Figure 4.8 – Normalised results from models run using the spatial and thermal properties of the 4 different substrate types used during this work. The key shows the substrate type and its thickness .....	131
Figure 4.9 – Schematic diagram of the calibration set up.....	135
Figure 4.10 – Photograph of the wire-wound resistor clamped over the sensing area of the device for temperature calibration.....	135
Figure 4.11 – A typical calibration result for a device fabricated with 100 nm Cr and 200 nm Ni ( $V_{out}$ calculated prior to amplification with a gain of 10083) .....	136
Figure 4.12 – Transient response of $\Delta T$ for a device submerged in IPA with a heater input of 13.5 mW.....	138
Figure 4.13 – Steady state $\Delta T$ values observed for large volumes of three liquid samples: IPA, glycerine and water .....	139
Figure 4.14 – A photograph of the Design A device used for experimentation on 100 $\mu$ l droplets of liquid. The tubing was attached to the device to contain the liquid over the sensing area of the device.....	141
Figure 4.15 – Experimental steady state $\Delta T$ values as a function of water composition for 100 $\mu$ l droplets of glycerine / water and IPA / water mixtures .....	142
Figure 4.16 – Experimental $\Delta T$ values plotted against nominal thermal conductivity values for water [14], glycerine and water mixtures [18] and pure glycerine [18] and IPA [19] with a linear best fit line and $\pm 10\%$ error bars (based on the $\Delta T$ value for pure water) .....	143
Figure 4.17 – Time dependent response of $\Delta T$ measurements taken on wetted paper allowed to dry at 30 $^{\circ}$ C.....	145
Figure 4.18 – Drying time for wetted paper at ambient temperatures from 20 $^{\circ}$ C to 50 $^{\circ}$ C (293 K to 323 K).....	146

Figure 4.19 – Vapour pressure calculated from the Goff-Gratch equation and the exponential approximation over the range 295 – 325 K (20 – 50 °C).....	148
Figure 5.1 – a) A diagram showing 1-D heat flow through an isotropic cylinder with insulated edges and one end heated; b) the resulting temperature profile.....	154
Figure 5.2 – a) A diagram showing 1-D heat flow through two identical cylinders with TCR; b) the resulting stepped temperature profile.....	155
Figure 5.3 – The two mechanisms which act to reduce the effective contact area ( $A_r$ ) and cause thermal contact resistance: non-conforming faces and surface roughness .....	155
Figure 5.4 – Heat flow mechanisms across the TCR gap created by surface roughness .....	156
Figure 5.5 – Electrical equivalent models for: a) bare solid-solid interface; b) a solid TIM & c) a liquid TIM.....	159
Figure 5.6 – Schematic diagram and photograph of the experimental setup used to investigate the effect of a compressive force on the TCR.....	161
Figure 5.7 – Loading and unloading curves for a quartz sample .....	161
Figure 5.8 – $\Delta T$ loading curves for quartz, nickel and acrylic (2 curves are presented for each material).....	163
Figure 5.9 – Photographs showing the water droplet deforming as the device is lowered into the sample by the stepper.....	166
Figure 5.10 – $\Delta T$ loading curves for quartz, nickel and acrylic with and without a TIM (each curve is an adjacent average fit of 2 data sets based on 10 points).....	167
Figure 5.11 – $\Delta T$ measurements taken with a contact pressure of 4 kPa with and without a TIM, plotted against nominal values of thermal conductivity taken from Table 5.1 .....	168
Figure 6.1 – A colourised SEM image showing a stoma on the underside of a leaf. A dotted line has been drawn to highlight the guard cells, which form the stoma .....	175
Figure 6.2 – Photograph showing the device clipped onto an abscised Pak Choi leaf to monitor its water content as it dries.....	179
Figure 6.3 – Time dependence of RWC and $\Delta T$ for an abscised Pak Choi leaf, allowed to dry under ambient conditions for a period of 6 hours .....	180

Figure 6.4 – $\Delta T$ measurements increase linearly with the relative water content (RWC) of the leaf. Error bars represent the maximum variation observed across three repeated experiments using different leaves.....	181
Figure 6.5 – Time dependence of measured RWC taken on three abscised Pak Choi leaves over a period of 4 hours .....	182
Figure 6.6 – a) Diagram of the microstructure of paper; b) SEM of paper used in Section 4.2.3.2; c) $\Delta T$ as a function of time for paper as it dries (taken from Figure 4.17); d) Diagram of the microstructure of a leaf; e) SEM of a Pak Choi leaf & f) $\Delta T$ as a function of time for a leaf as it dries (taken from Figure 6.3) .....	185
Figure 6.7 – Two loading and unloading curves for an abscised Pak Choi leaf. Solid lines indicate the curve was recorded immediately after abscission and the dotted lines indicate the curve was recorded 4 hours after abscission .....	186
Figure 6.8 – Loading curves for a freshly abscised leaf (black) and a 4 hour old leaf (red) using water as a TIM. Unloading curves are not shown for clarity and a 5 point averaged curve is fitted to the data.....	188
Figure 6.9 – Loading curves for abscised leaves with and without a TIM. Black lines indicate the freshly abscised leaves and red lines indicate loading curves for leaves 4 hours after abscission. Dotted lines indicate that water was used as a TIM and solid lines were recorded without a TIM .....	189
Figure 6.10 – A diagram showing the experimental setup for plant water status monitoring .....	193
Figure 6.11 – Time dependence of $\Delta T$ for a device attached to a Pak Choi plant suffering water stress conditions. Blue vertical lines show when the plant was watered .....	194
Figure 6.12 – Relative humidity measurements within the dry-box superimposed over the $\Delta T$ measurements shown in Figure 6.11. Blue vertical lines show when the plant was watered .....	196
Figure 6.13 – Ambient temperature measurements within the dry-box superimposed over the $\Delta T$ measurements shown in Figure 6.11. Blue vertical lines show when the plant was watered .....	196
Figure 6.14 – Ambient relative humidity values recorded within the dry-box plotted against the $\Delta T$ values obtained on a Pak Choi plant (taken from Figure 6.12).....	197

Figure 6.15 – Ambient temperature values recorded within the dry-box plotted against the $\Delta T$ values obtained on a Pak Choi plant (taken from Figure 6.13).....	197
Figure 6.16 – Time dependence of $\Delta T$ for a device attached to a Lettuce plant suffering water stress conitions. Blue vertical lines show when the plant was watered .....	198
Figure 6.17 – SEM images of a) Lettuce & b) Pak Choi .....	200
Figure 6.18 – Schematic diagram showing how the leaf-sensors could fit into an intelligent irrigation system.....	204

## *List of Tables*

---

Table 2.1 – Examples of some common thermocouple combinations and their operating range. Taken from [21] .....	31
Table 2.2 – A comparison of the sensitivity for 3 substrates used in this work.....	60
Table 3.1 – Process parameters used for de-scum plasma etch .....	74
Table 3.2 – Process parameters used for sputter deposition .....	75
Table 3.3 – Process parameters used for creating a Single-Layer lift-off profile .....	81
Table 3.4 – Process parameters used for bi-layer lift-off.....	86
Table 3.5 - Process parameters used to improve the adhesion of metal to the polyimide substrate. .....	100
Table 3.6 – Process parameters used for the polyimide etch (~2.5 $\mu\text{m}$ ) .....	101
Table 4.1 – Parameters used to calculate the Rayleigh number for a heater on the lower surface of a volume of water and IPA .....	117
Table 4.2 – A comparison of the 1-D model results with experimental values taken from Figure 4.13 .....	119
Table 4.3 - Thermal properties used to generate the model results shown in Figure 4.7.....	128
Table 4.4 – Thermal conductivity and thickness values used for the substrate within the model	130
Table 5.1 – Thermal and surface properties of the materials used in the experiment.....	164

### **1.1. Research Question**

Thermal conductivity is an important material property as it is a key parameter for heat flow in materials. Much research is ongoing into heat transfer at micro- and nanometre scales, where traditional macroscopic theories cannot necessarily be used to accurately predict physical systems [1]. Microfabrication technology is essential to create devices which can be used to study heat flow at such scales. A seminal work in this area was the creation of the scanning thermal microscope by Williams and Wickramasinghe in 1986 [2], which sparked much further research into the flow of heat at small scales.

Experimental determination of the thermal properties of materials is extremely important because of the difficulty in estimating the values of the thermal conductivity from a knowledge of the constituent parts [3]. While the properties of pure bulk materials are well known, this is not the case for many heterogeneous materials such as food [4] or fluids containing nano-particles [5]. When the materials under investigation assume dimensions at the micro-scale or below the issue becomes even more complex as the mechanisms underpinning the flow of heat are likely to be influenced by phenomena which are not apparent at larger scales. Examples include ballistic transport in carbon nanotubes [6] or the formation of a water meniscus around scanning thermal

microscope probes [7]. As such, theoretical studies alone cannot predict how physical systems will react.

The study of heat flow in biological systems is the focus of much experimental work as biological materials are frequently heterogeneous and knowledge of their thermal conductivity is of great interest. At larger scales, heat sources during medical procedures can damage tissue [8]. However, heat transfer is also being used to gain a better insight into the operation of biological systems at much smaller scales. For example, microcalorimetry has been used for monitoring biochemical thermodynamics [9], while scanning thermal microscopy has been used to make thermal conductivity measurements on proteoliposomes [10] and MEMS sensors have been applied to monitoring metabolic processes [11].

The measurement of the thermal properties of biological samples is coupled with a number of difficulties. Firstly, any sensor operating on a biological sample must be biocompatible so as not to interfere with the system being scrutinised. Secondly, biological systems are easily damaged by excessive heating or cooling. Thirdly, biological samples are frequently of limited size, hence the ability to measure small sample volumes is highly desirable. Finally, biological systems often operate in chemically aggressive environments, so any device must be able to operate without degradation. All these factors must be taken into account when designing and operating sensors to probe the thermal properties of a biological sample. The intention of this work is to create a device which can fulfil these criteria.

Microfabricated devices are ideally suited for measuring such samples as they can overcome many of the issues outlined above. However, they suffer from one particular drawback: they are generally delicate and producing devices which are capable of operating for long periods of time in 'real-world' environments can be very challenging. Devices which can bridge the divide and operate beyond the laboratory offer exciting opportunities. For example, many microfluidic flow sensors have been demonstrated (e.g. [12]) however the production of a robust and biocompatible

device has opened up the opportunity for a non-invasive implanted drug delivery system which can be located within the mouth in order to deliver drugs as and when required [13].

## **1.2. Project aims**

The aim of this work was to create a device which utilises the benefits of microfabrication to produce a thermal sensor capable of operation on biological samples. Throughout the work, the overarching theme was to ensure that the device would be suitable for operation in ‘real-world’ settings. The particular application of the device is the real-time monitoring of the water content of plant leaves. This application is well suited to a microfabricated thermal sensor, as changes in the water content of a leaf will affect its thermal properties [14]. To allow thermal measurements to be taken on a single leaf a sensor capable of operating on small scale samples is required as the thickness of a leaf is  $\sim 100\ \mu\text{m}$ . For the device to be utilised as a real-time monitor of leaf water content, it must be robust enough to be mounted in-situ on a plant. Finally, there is a real desire for plant based sensing of water content, because such methods could improve significantly the performance of irrigation systems by providing real-time, quantitative information about plant water status [15]. The following section outlines the structure of this thesis, while the remainder of this chapter discusses the desire for a leaf-mounted thermal sensor for the detection of water content.

### 1.3. Structure of this thesis

This work is intended to introduce a microfabricated thermal sensor as well as demonstrating how it can be applied to monitor the thermal properties of small volumes. As such, the focus of the work is primarily on the engineering of a device, with the focus on design, fabrication and characterisation. However, the end application (a leaf-mounted sensor) also informed the design decisions, resulting in a robust sensor. The following overview of each chapter gives the reader an outline of the content of each of the chapters in this thesis.

**Chapter 1: *Introduction*** – To introduce the rationale behind this work, the research question underpinning the work is posed before a literature review highlights the motivation for this work. The aim is to give a broad review of some of the relevant previous work in the area and highlight the gaps which this work aims to fill. The literature review focuses on the application of the work, while the following chapter discusses specific details relating to small scale thermal measurements.

**Chapter 2: *Principle of Operation*** – Once the rationale for the work has been introduced, principles underlying the operation of the devices and relevant thermal sensing devices are presented. This gives the reader an understanding of the way in which the devices measure thermal conductivity, particularly whilst operating on small scale samples. It begins with a discussion of the rationale behind the device and the desire for monitoring small scale samples. It concludes by introducing the designs, patterns and substrates used to create the devices.

**Chapter 3: *Fabrication*** – The devices were microfabricated, which required a significant amount of work to refine and improve the processes to achieve robust devices capable of operating on small scale samples. The metallisation processes are discussed initially, as they were common to all the devices created during this work. Subsequently, the modification of the substrates is discussed, as this element of the devices was seen to have a significant impact on device performance. Two substrates were used: SU-8 membranes and polyimide. The chapter concludes

by introducing the experimental systems used to make electrical connections to the devices and the control electronics required to condition the signals produced.

**Chapter 4:** *Device characterisation and modelling* – Characterisation followed once devices could be reliably fabricated. This was achieved by monitoring the thermal properties of liquid samples, demonstrating that the sensor was capable of measuring changes in bulk thermal conductivity. In order to demonstrate that the experimental results are consistent with heat transfer theory, a 2D numerical model is presented. The model shows that the results are consistent with theory and was used to investigate the effect of the various substrates available on the operation of the device. To highlight how the device could respond to changes in composition it was used to measure the drying rate of wetted paper. The experimental dependence of drying rate on air temperature was seen to be consistent with theory. This work has been reported in a peer reviewed journal [16].

**Chapter 5:** *Thermal contact resistance* – Heat flow between two solid materials is inhibited by thermal contact resistance caused by the surface roughness of the two mating surfaces. This has the potential to introduce inaccuracies to the measurements taken by the devices. This chapter introduces the pertinent theory which underpins thermal contact resistance and demonstrates experimentally that the contact resistance cannot be neglected, however, its effect can be mitigated by the application of water as a thermal interface material.

**Chapter 6:** *Monitoring the water content of plants* – This chapter demonstrates the application for the device: monitoring the water content of a leaf. Initial experiments prove that the device is sensitive to the water content of a leaf which has been abscised (removed) from a plant by comparing the sensor's output with the weight of the leaf. Once its operation was proven, the device was mounted on a leaf in-situ on a plant and shown to be sensitive to changes in water content related to water stress within the plant.

#### **1.4. Need for plant water status monitoring**

As the world's population increases, there is a need to increase food production yields, whilst improving the efficiency of use of scarce commodities, such as water [17]. In England and Wales, the volume of water used for irrigation of vegetables has increased by around 3 % per year and for soft fruits, 2.9 % per year between 1982 and 2005, with the demand placing growing pressure on summer supplies in southern England [18]. Even in a temperate location such as Great Britain, summer water resources are now overcommitted [19]. In many other regions the situation is worse, for example some Mediterranean regions are suffering desertification and severe water shortages [20].

Global agriculture accounts for 70 % of water withdrawals from rivers and aquifers [17] and hence solutions which can improve the efficiency of irrigation would be particularly effective at conserving water. In addition, plant growth is one of the most sensitive indicators of water stress [21]. Hence, technologies which prevent plants becoming water stressed, could also help to improve crop yields, offering an added incentive by boosting yields while reducing production costs.

While large scale projects (e.g. dam building or diverting watercourses) offer local solutions to water shortage, they do little to promote long term sustainability in the use of water [22]. As a response, irrigation decision systems have been developed with the aim of improving water use by applying irrigation in a more efficient manner [23]. Traditional set irrigation schemes consume considerably more water than alternative methods. For example, a comparison between a traditional set irrigation scheme, a scheme based on historic rainfall and a scheme based on soil water content measurements showed that the latter methods used only 31-36 % of the water applied in the traditional scheme [24].

The desire for improving yields and efficiency of agricultural production has lead to increasing use of technology including crop mapping, radio frequency identification (RFID), disease detection and monitoring crop water status [25] which is one application of the work reported

here. Such methods are referred to as precision agriculture which “*involves aspects of remote sensing, crop protection, field sampling, precision planting, precision tillage, precision fertilizer placement, precision irrigation, on-the-go yield monitoring and other emerging applications*” [23] and results in economic benefits as well as improved environmental stewardship [23].

Several methods for implementing irrigation decision systems exist with varying levels of complexity. The simplest systems use historical rainfall patterns to predict when irrigation will be required [24], however reliance on repeatable weather patterns mean that such systems will inevitably not optimise water use during periods with unusual weather patterns. The more complex irrigation decision systems operate by taking a series of environmental inputs such as rainfall levels, irrigation rate, soil type and evapotranspiration rate in order to generate a water balance which allows an estimation of the present and future soil moisture levels [26]. From this water balance, decisions can be made as to which crops require irrigation.

The complex nature of many of the input factors affects the reliability of the systems. For example, prediction of the spatial water availability across a farm is possible, but requires complex and time consuming methods to monitor the soil composition and its effect on soil water levels [27]. In addition, ongoing monitoring of soil moisture levels is required (e.g. time domain reflectometry [27] or thermal methods [28]) which are generally too expensive for growers to utilise in many locations across a farm [23].

In addition to the physical phenomena which affect the need for irrigation, large scale irrigation decision systems must balance priorities and optimise water use [29], however on a smaller scale, individual farms must also optimise water use when it becomes a production limiting factor in order to maximise farm profit [30]. Such decisions add to the complexity of the systems, but also offer increases in profitability and demand improvements in information quality.

Adoption of irrigation decision systems is still low, even in more developed areas of the world (e.g. ~18 % of large area farms surveyed in Washington State, U.S.A. [31]). This is primarily as many systems are developed without consideration of the knowledge and skill levels of farmers.

The systems require in depth knowledge of a number of important parameters to allow accurate predictions of water requirements and inaccuracies can be introduced by a number of factors. For example, a lack of availability of soil water parameters, real time data on the current status of the system and the complexity of the system to be modelled [32]. In response, simpler methods have been introduced such as visual aids based on pluviometer / evaporimeter buckets [32]. While these have a role to play, particularly in areas where expensive irrigation decision systems are unaffordable, they are impractical for large scale, industrial crop production.

Irrigation decision systems would benefit greatly from improvements in the quality and quantity of information available, particularly those allowing real-time feedback of water availability [23]. Current systems generally have inputs based on weather conditions and current or historical soil moisture levels. However, soil water content can only be indirectly linked to the availability of water to the crop and does not reflect the water availability at the root surface [33] [15]. Improvements in the technologies available for monitoring the real-time water status of a crop would allow an extra layer of information to be added into the decision systems, improving their accuracy. Plant-mounted sensors are required to provide this extra information. In addition, research has shown that some crops benefit from slight water deficits [34], so irrigation systems which induce a 'regulated deficit' can be beneficial. Plant-mounted sensing would act as an aid to allow a greater control over such systems providing accurate measurement and maintenance of plant water status [15].

Plant-mounted sensors have a number of practical difficulties which need to be overcome before such devices can be adopted on a more widespread basis. In particular, the devices need to be sensitive to plant water status, but also robust enough to operate in field-based settings. This is the niche in which the devices developed in this work are design to operate, offering a simple to use and robust system for plant-mounted detection of water status. The following section introduces some of the technologies currently available.

## **1.5. Current technologies**

To allow improvements in irrigation systems, plant-mounted sensors capable of detecting water stress are required [35]. Severe water stress can be seen when a plant begins to wilt, however, at this point the plant has already stopped growing and is nearing a point at which permanent damage will occur [36]. Leaf tissue or water potential measurements can be used to detect water stress within a plant [15] before visible wilting and damage occurs. A variety of techniques exist, ranging from traditional, laboratory based techniques to field-based techniques for continuous measurements. However, field-based techniques are not widely used as they tend to require expensive equipment which is difficult to operate [15]. Some of the current methods available for determining the water status of a plant are outlined below and can be broadly split into three categories: leaf tissue based sensors which detect the water content of the leaves of a plant, remote methods and other plant based methods, such as sap flow sensors.

### **1.5.1. Leaf tissue based methods**

Leaf tissue based methods have the advantage that they give a direct measurement of the water content of the leaves of a plant, which are the most sensitive areas to water stress. Leaf water potentials have been shown to be a good indicator for managing irrigation [37]. However, the practicalities of mounting sensors on a leaf have limited their use to date.

#### ***1.5.1.1. Pressure probe technique***

The pressure probe technique determines the water potential of individual cells within a leaf by inserting a needle into the cell and measuring the pressure exerted by the vacuole on the cell wall (see Figure 1.1). The pressure is measured by a capillary tube or pressure probe [38]. The pressure probe technique is necessarily invasive and does not lend itself to real-time monitoring in situ on a plant, however some microfabricated versions are beginning to overcome such issues [39]. Such sensors are also affected by ambient humidity levels and electrolyte potential within the tissue [39].

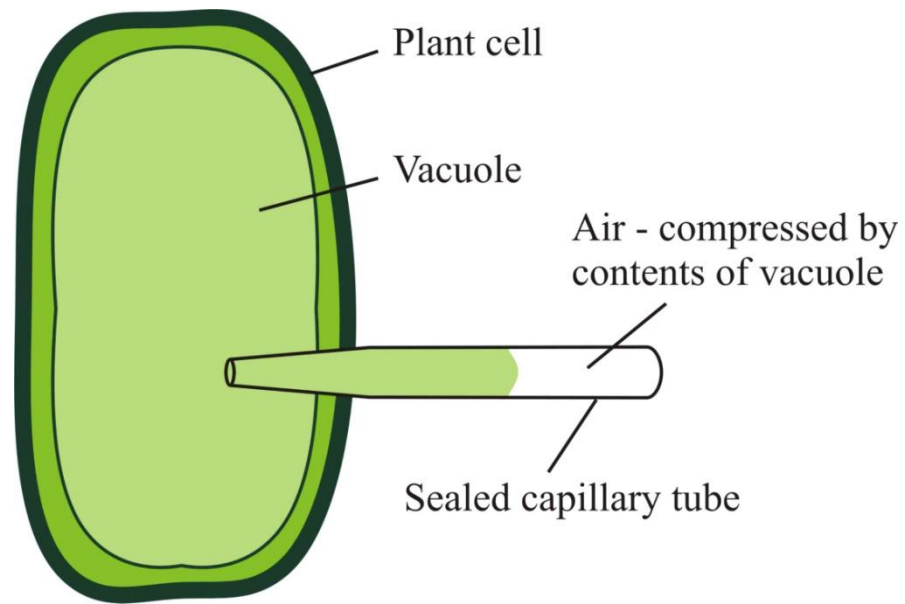


**Figure 1.1 – Schematic diagram (not to scale) of the pressure probe technique for determining the water potential of individual plant cells**

#### ***1.5.1.2. Pressure chamber***

The pressure chamber technique involves placing an abscised leaf within a sealed chamber, with only the stem of the leaf protruding through the chamber wall (see Figure 1.2). The pressure inside the chamber is increased until water is seen to be forced from the leaf and through the stem, giving a measure of the water potential within the leaf. This technique was developed at the beginning of the twentieth century and has been widely used (e.g. [40]) and offers an accurate and robust technique. However, it is not suitable for real-time monitoring and is necessarily destructive as the leaf must be abscised prior to measurement.

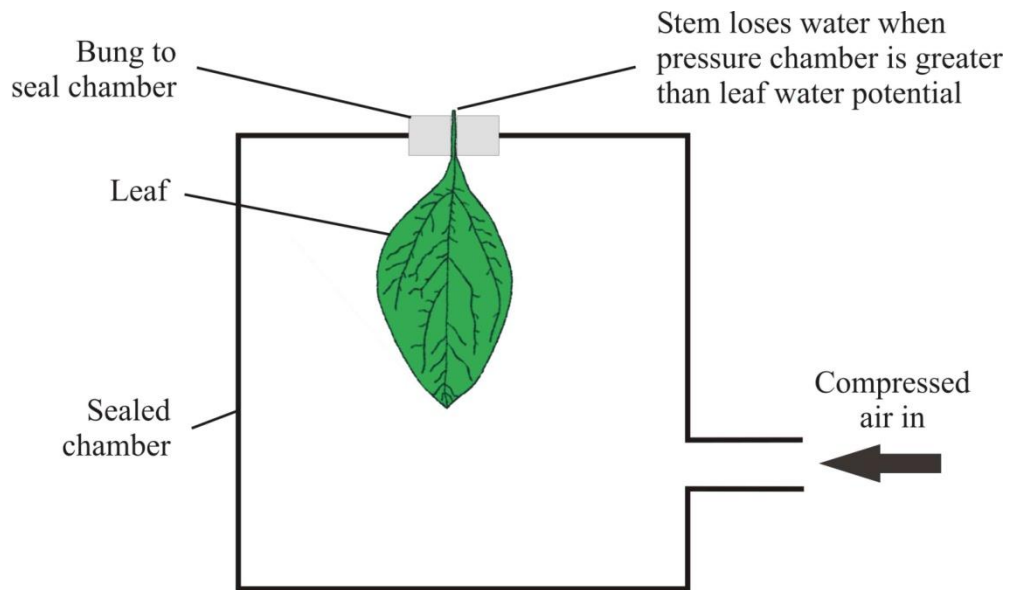


**Figure 1.2 – Pressure chamber technique for determining the water potential of an abscised leaf**

### **1.5.1.3. Psychrometer**

Psychrometers measure the water vapour pressure of a leaf placed within a pressure chamber [41] by using two temperature sensors – one dry and one wetted. Changes in the temperature difference between the two temperature sensors can be related to the water potential of the leaf. While this technique automates the detection process somewhat, it suffers the same limitations as the pressure chamber technique.

### **1.5.1.4. Patch clamp pressure probe**

A magnetically controlled patch clamp has been shown to be capable of non-invasively determining the water potential of a leaf [42]. The clamp applies a known pressure to the leaf and the resulting attenuation of the pressure signals is a function of the turgour pressure and structure of the leaf. Such a sensor relies on a miniturised silicon pressure sensor mounted within one arm of the clamp, demonstrating the potential of microfabricated devices for leaf-mounted sensing of plant water status. The ability to integrate micro-sensors into devices for leaf-mounted sensing opens up the possibility of real-time sensing under field conditions [43].

#### **1.5.1.5. Leaf thickness sensor**

Rapid changes in leaf thickness can be related to the water content of a leaf which has lead to leaf thickness sensors [44] [45]. However, these sensors tend to be delicate and their use is complicated as the measurements can be affected by leaf age, stress history and, in young leaves, by the effects of leaf growth [15]. Also lateral changes in dimension are much more pronounced than changes in leaf thickness [15].

#### **1.5.2.Remote methods**

The primary reason that leaf-mounted sensors are not widely used for field-based measurements is the difficulty in producing a device which is both sensitive and robust enough to operate on a leaf. Remote methods do not suffer the difficulties of mounting delicate sensors onto a plant. However, they generally require technical expertise to operate expensive equipment. This generally prevents their use for real-time and long term measurements. In addition, the nature of the measurements means that changes in the environmental conditions (e.g. humidity and sunlight levels) can influence the measurement technique.

##### **1.5.2.1. Infrared techniques**

The canopy temperature of a crop can be used as a measure of plant water status [46]. While such measurements could be achieved using plant mounted sensors, infrared techniques tend to be utilised (e.g. [35]). One potential issue with infrared techniques is the non-selective nature of the measurement, so any section of the IR image taken can influence the reading. If woody areas of the crop, posts, soil or sky etc... form part of the image, then the results can be skewed. This weakness can be overcome by utilising visual images taken simultaneously with the IR images. Machine vision software can then be used to discriminate between canopy areas of the image and erroneous areas [47]. A second issue which can affect IR techniques is changes in the atmospheric conditions. To overcome this, a well watered area of the crop can be used as a baseline measurement for the rest of the crop between the canopy and the sensor [25]. While such IR techniques show promise, however they are still a relatively expensive and complex technique when scaled up to allow automation for field-wide sensing [35].

#### **1.5.2.2. Terahertz techniques**

Terahertz frequency electromagnetic radiation is strongly absorbed by water, leading to a non-invasive technique for measuring water content [48]. While such techniques can be useful for laboratory measurements, they are not currently practical for field based measurements due to the complexity and expense of the equipment required.

#### **1.5.2.3. Satellite imaging**

Wide area effects of water deficit and other environmental factors, such as soil composition can be investigated using satellite imagery [25]. While satellite images can be used for determining the amount of water in the foliage of a crop, such a technique is more suited to studies covering large areas over long periods of time (e.g. several years) [49] than for the shorter timescales and smaller areas required for irrigation scheduling.

### **1.5.3. Other methods**

While the leaf tissue is the most sensitive part of a plant to water stress, other elements of the plant respond to water stress conditions and can be easier to measure. Detecting these responses can lead to methods for detecting water stress.

#### **1.5.3.1. Visual methods**

The most obvious indication that a plant is suffering water stress is visible wilting [36]. However, by the time a plant is wilting, it has generally been water stressed for a significant period and methods to detect wilting are complex and hard to automate.

#### **1.5.3.2. Sap flow monitors**

Water use for plants with relatively thick stems can be monitored by sap flow sensors. Knowledge of the evapotranspiration rate can be combined to estimate the current water status of the plant. In addition, sap flow rate is strongly dependent on stomatal closure which is a strong indicator of water stress [15]. Thermal methods are widely used for detecting sap flow rates (e.g. constant power warm thermistor setups [50]).

#### ***1.5.3.3. Trunk diameter measurements***

For plants with woody stems, changes in trunk diameter can be correlated with stem water potential [51]. To achieve this, a linear variable displacement transducer is placed around the stem of the plant to periodically measure changes in the diameter of the stem. The readings require caution in their interpretation, as many factors can affect the diameter, from changes in water status, thermal expansion and growth of the plant [51]. Such measurements can only be taken on relatively large plants with woody stems, smaller leafy plants cannot be measured in this way.

#### ***1.5.3.4. Xylem cavitation***

Water is transported from the roots of a plant to the leaves through the xylem and the column of water is under tension [52]. During periods of water stress, the leaves continue to pull water from the roots, increasing the tension on this column. This leads to the formation of water vapour bubbles within the xylem. The creation of these bubbles can be detected through acoustic methods [53]. While such methods give a good insight into the transport of water through the hydraulic architecture of the plant, and are sensitive indicators of the onset of water stress, cavitation events can occur after a water stressed plant has been watered and so these sensors do not provide feedback on when sufficient irrigation has been applied [15].

#### ***1.5.3.5. Soil water content***

Soil water content sensors are widely used to predict water deficit in crops (e.g. [33]). However, such methods can only give an indirect measure of the water available to the plant in the soil and do not indicate whether the water is taken up by the plant as changes in the soil water content can be influenced by evaporation, run-off and drainage [50]. While a number of different methods are available for monitoring soil water content, a majority rely on thermal methods such as the single or dual probe method [54] where the thermal gradient generated by a heated needle is related to the water content.

## 1.6. Thermal detection of water content

The previous section has identified some of the broad range of sensing methods which exist to monitor the water status of plants. While soil moisture and plant stem based sensors are widely used, there is a dearth of leaf-mounted sensors. This is likely to be due to the practical issues of operating on leaves which tend to make such devices unreliable [15]. The operation of a leaf-mounted sensor presents a number of challenges. Firstly, leaves offer a large surface area, but they are generally very thin. For examples, the leaves studied in the work were measured at  $\sim 100 \mu\text{m}$  thick. This requires sensors which are capable of detecting changes in relatively small samples. Microfabrication offers the potential for devices to be scaled to operate on such samples. However, such devices tend to be relatively fragile and so not suited to operation in field settings. This is the second challenge leaf-mounted sensor must overcome: the operating environment. The sensor must be robust enough to operate on a leaf for extended periods of time. Furthermore, if the leaf is to support the sensor then the sensor must be light-weight [55]. Finally, the sensors must be plant-compatible, so as not to damage or interfere with the leaf. Microfabricating the sensors ensures they can operate on small scale samples, while utilising a thermal sensor offers a non-invasive and robust technique.

As thermal conductivity is a strong indicator of changes to structure and composition of a material [56] it offers a sensitive an non-invasive technique for determining changes in the water content of a leaf. However, to achieve a thermal sensor capable of making such measurements, it must be suitable for operation on small scale samples. This has certain benefits and solutions which can achieve this would be useful in their own right. A multitude of small scale thermal sensors have been reported in literature. The following chapter introduces some of the pertinent methods and describes the rationale and theory behind the devices in this work, before describing the device designs created.

## 1.7. References

1. **Sobhan, C.B. and Peterson, G.P.** *Microscale and Nanoscale Heat Transfer*. Florida : CRC Press, 2008.
2. **Williams, C.C. and Wickramasinghe, H.K.** Scanning thermal profiler. *Applied Physics Letters*. 1986, Vol. 49, 23.
3. **Suleiman, B.M.** Effective thermal conduction in composite materials. *Appl. Phys. A*. 2010, pp. 223-228.
4. **Muramatsu, Y., Tagawa, A. and Kasai, T.** Thermal Conductivity of Several Liquid Foods. *Food Science and Technology Research*. 11, 2005, Vol. 3, pp. 288-298.
5. **Wongwises, W. and Duangthongsuk, S.** Measurement of temperature-dependent thermal conductivity and viscosity of TiO<sub>2</sub>-water nanofluids. *Experimental Thermal and Fluid Science*. 33, 2009, pp. 706-714.
6. **Brown, E., Hao, L., Gallop, J.C. and Macfarlane, J.C.** Ballistic thermal and electrical conductance measurements on individual multiwall carbon nanotubes. *Applied Physics Letters*. 2005, Vol. 87.
7. **Calleja, M., Tello, M. and Garcia, R.** Size determination of field-induced water menisci in noncontact atomic force microscopy. *Journal of Applied Physics*. 2002, Vol. 92, 9, pp. 5539-5542.
8. **Davidson, S.R.H. and James, D.F.** Measurement of thermal conductivity of bovine cortical bone. *Medical Engineering and Physics*. 2000, Vol. 22, pp. 741-747.
9. **Kwak, B.S., Kim, B.S., Cho, H.H., Park, J.S. and Jung, H.I.** Dual thermopile integrated microfluidic calorimeter for biochemical thermodynamics. *Microfluid Nanofluid*. 2008, 5, pp. 255-262.

10. **Haeberle, W., Pantea, M. and Hoerber, J.K.H.** Nanometer-scale heat-conductivity measurements on biological samples. *Ultramicroscopy*. 2006, Vol. 106, pp. 678–686 .
11. **Wang, L., Sipe, D.M., Xu, Y. and Lin, Q.** A MEMS Thermal Biosensor for Metabolic Monitoring Applications. *Journal of Microelectromechanical Systems*. 2008, Vol. 17, 2, pp. 318-327.
12. **Billat, S., Kliche, K., Gronmaier, R., Nommensen, P., Auber, J., Hedrich, F. and Zengerle, R.** Monolithic integration of micro-channel on disposable flow sensors for medical applications. *Sensors and Actuators A*. 2008, Vol. 145, pp. 66-74.
13. **Velten, T., Knoll, T., Haberer, W., Koch, T. and Scholz, O.** Biocompatible flow sensor with integrated solvent concentration measurement. *Sensors and Actuators A*. 2008, 145, pp. 257-262.
14. **Opoku, A., Tabil, L.G., Crerar, B and Shaw, M.D.** Thermal conductivity and thermal diffusivity of timothy hay. *Canadian Biosystems Engineering*. 2006, Vol. 48.
15. **Jones, H.G.** Irrigation scheduling: advantages and pitfalls of plant-based methods. *Journal of Experimental Botany*. 2004, Vol. 55, 407, pp. 2427-2436.
16. **Atherton, J.J, Rosamond, M.C. Johnstone, S. and Zeze, D.A.** Thermal characterisation of micro-litre volumes using a thin film thermocouple based sensor. *Sensors and Actuators A*. 2011, Vol. 166, pp. 34-39.
17. **HM Government.** *Foresight: The Future of Food and Farming*. London : The Government Office for Science, 2011.
18. **Knox, J.** Managing the Water Footprint of Irrigated Food Production in England and Wales. *Sustainable Water*. 2011, Vol. 31, pp. 78-92.
19. **Bakker, K.** Paying for water: water pricing and equity in England and Wales. *Transactions of the Institute of British Geographers*. 2001, Vol. 26, 2, pp. 143–164.

20. **Brauch, H.G.** Desertification – a new security challenge for the mediterranean? Policy agenda for recognising and coping with fatal outcomes of global environmental change and potentially violent societal consequences. *NATO Security through Science Series*. 2006, Vol. 3, pp. 11-85.
21. **Ortuno, M.F., Conejero, W., Moreno, F., Moriana, A., Intrigliolo, D.S., Biel, C. and Mellisho, C.D.** Could trunk diameter sensors be used in woody crops for irrigation scheduling? A review of current knowledge and future perspectives. *Agricultural Water Management*. 2010, 97, pp. 1-11.
22. **Palmer, M. A.** Beyond infrastructure. *Nature*. 2010, Vol. 467, pp. 534-535.
23. **Sadler, E.J., Evans, R.G., Stone, K.C. and Camp, C.R.** Opportunities for conservation with precision irrigation. *Journal of Soil and Water Conservation*. 2005, Vol. 60, 6, pp. 371-379.
24. **Migliaccio, K.W., Schaffer, B., Crane, J.H. and Davies, F.S.** Plant response to evapotranspiration and soil water sensor irrigation scheduling methods for papaya production in south Florida. *Agricultural Water Management*. 2010, 97, pp. 1452-1460.
25. **Lee, W.S., Alchanatis, V., Yang, C., Hirafuji, M., Moshou, D. and Li, C.** Sensing technologies for precision specialty crop production. *Computers and Electronics in Agriculture*. 2010, 74, pp. 2-33.
26. **Leib, B.G., Elliott, T.V. and Matthews, G.** WISE: a web-linked and producer oriented program for irrigation scheduling. *Computers and Electronics in Agriculture*. 2001, 33, pp. 1-6.
27. **Hedley, C. B. and Yule, I. J.** A method for spatial prediction of daily soil water status for precise irrigation scheduling. *Agricultural Water Management*. 2009, Vol. 96, pp. 1737-1745.
28. **Lu, S., Ju, Z., Ren, T. and Horton, R.** A general approach to estimate soil water content from thermal inertia. *Agricultural and Forest Meteorology*. 2009, Vol. 149, pp. 1693-1698.

29. **Alminana, M., Escudero, L.F., Landete, M., Monge, J.F., Rabasa, A. and Sanchez-Soriano, J.** WISCHE: A DSS for water irrigation scheduling. *Omega*. 2010, pp. 492-500.
30. **Brown, P.D., Cochrane, T.A. and Krom, T.D.** Optimal on-farm irrigation scheduling with a seasonal water limit using simulated annealing. *Agricultural Water Management*. 2010, 97, pp. 892-900.
31. **Leib, B.G., Hattendorf, M., Elliott, T. and Matthews, G.** Adoption and adaption of scientific irrigation scheduling: trends from Washington, USA as of 1998. *Agriculture Water Management*. 2002, 55, pp. 105-120.
32. **Torres, J.S.** A simple visual aid for sugarcane irrigation scheduling. *Agricultural Water Management*. 1998, 38, pp. 77-83.
33. **Thompson, R.B., Gallardo, M., Valdez, L.C. and Fernandez, M.D.** Using plant water status to define threshold values for irrigation management of vegetable crops using soil moisture sensors. *Agricultural Water Management*. 2007, 88, pp. 147-158.
34. **Chalmers, D.J., Mitchell, P.D. and Vanheek, L.** Control of peach tree growth and productivity by regulated water supply, tree density and summer pruning. *Journal of the American Society of Horticultural Science*. 1981, 106, pp. 307-312.
35. **Loveys, B. R., McCarthy, M., Jones, H. G., Theobald, J. C. and Skinner, A.** When to water? Assessment of plant-based measurements to indicate irrigation requirements. *Final contract report (CSP02/02) from CSIRO to the Australian Grape and Wine Research and Development Corporation*. 2005.
36. **Meyer, B.S., Anderson, D.B. and Bohning, R.H.** *Introduction to Plant Physiology*. New York : Van Nostrand, 1960.
37. **Peretz, J., Evans, R.G. and Proebsting, E.L.** Leaf water potentials for management of high frequency irrigation on apples. *Transactions of the ASABE*. 1984, Vol. 27, 2, pp. 437-442.

38. **Smith, J.A.C. and Griffiths, H., [ed.]**. *Water Deficits: Plant Responses from Cell to Community*. Oxford : BIOS Scientific, 1993.
39. **Iwashita, T., Katayanagi, H. and Miki, N.** Needle-type in situ water content sensor with polyethersulfone polymer membrane. *Sensors and Actuators B*. 2011, 154, pp. 41-45.
40. **Olufayo, A., Baldy, C. and Ruelle, P.** Sorghum yield, water use and canopy temperatures under different levels of irrigation. *Agricultural Water Management*. 1996, 30, pp. 77-90.
41. **Boyer, J.S. and Knipling, E.B.** Isopiestic technique for measuring leaf water potentials with a thermocouple psychrometer. *The National Academy of Sciences*. 1965, Vol. 54, 4, pp. 1044-1051.
42. **Zimmermann, D., Reuss, R., Westhoff, M., Geßner, P., Bauer, W., Bamberg, E., Bentrup, F.W. and Zimmermann, W.** A novel, non-invasive, online-monitoring, versatile and easy plant-based probe for measuring leaf water status. *Journal of Experimental Botany*. 2008, Vol. 59, 11, pp. 3157-3167.
43. **Westhoff, M., Reuss, R., Zimmermann, D., Netzer, Y., Gessner, A., Geßner, P., Zimmermann, G., Wegner, L.H., Bamberg, E., Schwartz, A. and Zimmermann, U.** A non-invasive probe for online-monitoring of turgor pressure changes under field conditions. *Plant Biology*. 2008, 11, pp. 701-712.
44. **Barvdo, B., Sharon, Y. and Selieman, R.** *Leaf thickness sensing device*. 6185833B1 U.S. Patent, Filed 13th February 2001.
45. **McBurney, T.** The Relationship Between Leaf Thickness and Plant Water Potential. *Journal of Experimental Botany*. 1992, Vol. 43, 248, pp. 327-335.
46. **Tanner, C.B.** Plant temperatures. *Agronomy Journal*. 1963, 55, pp. 210–211.

47. **Jiménez-Bello, M.A., Ballester, C., Castel, J.R. and Intrigliolo, D.S.** Development and validation of an automatic thermal imaging process for assessing plant water status. *Agricultural Water Management*. 2011, 98, pp. 1497-1504.
48. **Hadjiloucas, S., Karatzas, L. S. and Bowen, J. W.** Measurements of Leaf Water Content Using Terahertz Radiation. *IEEE Transactions on Microwave Theory and Techniques*. 1999, Vol. 47, 2, pp. 142-149.
49. **Yilmaz, M.T., Raymond Hunt Jr, E. and Jackson, T.J.** Remote sensing of vegetation water content from equivalent water thickness using satellite imagery. *Remote Sensing of Environment*. 2008, 112, pp. 2514-2522.
50. **Skinner, A. J. and Lambert, M.F.** A Log-Antilog Analog Control Circuit for Constant-Power Warm-Thermistor Sensors - Application to Plant Water Status Measurement. *IEEE Sensors Journal*. 2009, Vol. 9, 9, pp. 1049-1057.
51. **Livellara, N., Saavedra, F. and Salgado, E.** Plant based indicators for irrigation scheduling in young cherry trees. *Agricultural Water Management*. 2011, 98, pp. 6894-690.
52. **Steudle, E.** The cohesion-tension mechanism and the acquisition of water by plant roots. *Annual Review of Plant Physiology and Plant Molecular Biology*. 2001, 52, pp. 847-875.
53. **Milburn, J.A.** *Water flow in plants*. London : Longmans, 1979.
54. **Greswell, R.B., Riley, M. S., Alves, P.F. and Tellam, J.H.** A heat perturbation flow meter for application in soft sediments. *Journal of Hydrology*. 2009, Vol. 370, pp. 73-82.
55. **Gutschick, V.P., Barron, M.H., Waechte, D.A. and Wolf, M.A.** Portable monitor for solar radiation that accumulates irradiance histograms for 32 leaf-mounted sensors. *Agricultural and Forest Meteorology*. 1985, Vol. 33, 4, pp. 281-290.
56. **Gustavsson, M. and Gustafsson, S.E.** Thermal conductivity as an indicator of fat content in milk. *Thermochim. Acta*. 2006, 442, pp. 1-5.

This chapter begins with the rationale behind the devices created in this work, outlining why small scale thermal conductivity sensors are required. It outlines various experimental methods which can be used to measure thermal conductivity before some pertinent theory is introduced. The second half of this chapter is devoted to the designs of devices used during the project. Some of the early device designs are discussed before the final two iterations are described. To improve the thermal sensitivity, the sensors were patterned on polymer substrates (SU-8 and polyimide). A description of how these substrates were used is given along with the patterns used to form the active areas of the devices.

#### **2.1. Rationale for the device**

The aim of the project was to develop a sensor which was able to monitor the thermal properties of small scale samples, opening up new avenues of research and allowing new applications to be achieved. This sub-section introduces the rationale behind the devices, discussing the reasons for measuring thermal conductivity and outlining the methods currently available, as well as the difficulties and necessity for making small scale measurements. The principles underpinning the

operation and design of the devices are then discussed, with particular attention paid to thermocouple theory.

### **2.1.1. Why measure thermal conductivity?**

The thermal conductivity of a material is inextricably linked to its composition, meaning that measurements of thermal conductivity can be a sensitive indicator of changes to composition or structure of a material [1]. For example, the thermal conductivity of a mixture of glycerine and water varies from  $0.60 \text{ W m}^{-1} \text{ K}^{-1}$  for pure water to  $0.28 \text{ W m}^{-1} \text{ K}^{-1}$  for pure glycerine [2] (Figure 2.1). Therefore, thermal conductivity can be used as a measure of the composition of a material. A variety of other techniques could be utilised to make this measurement, such as measuring the density, viscosity or electrical conductivity. However, thermal conductivity is an intrinsic property of a material which can be easily probed by placing a thermal sensor in contact with the material. Other methods such as measuring electrical conductivity require direct electrical connections to be made, while measuring viscosity and density need expensive and/or bulky equipment, excluding their use on small samples.

Examples of other applications which utilise thermal properties to characterise materials include water content sensors for soil [3] [4], moisture measurement of building materials [5] or sensors for monitoring the fat content of milk [1]. By measuring the ability of heat to penetrate a material, these applications all study other material properties indirectly. As the difference between a thermal conductor (e.g. nickel) and insulator (e.g. acrylic) is  $\sim 10^3 \text{ W m}^{-1} \text{ K}^{-1}$  the difference between electrical conductors and insulators is  $\sim 10^{24} \text{ ohm cm}$ , it is clear that thermal probes will be able to operate on a wider range of materials, as insulating surfaces will have a smaller effect.

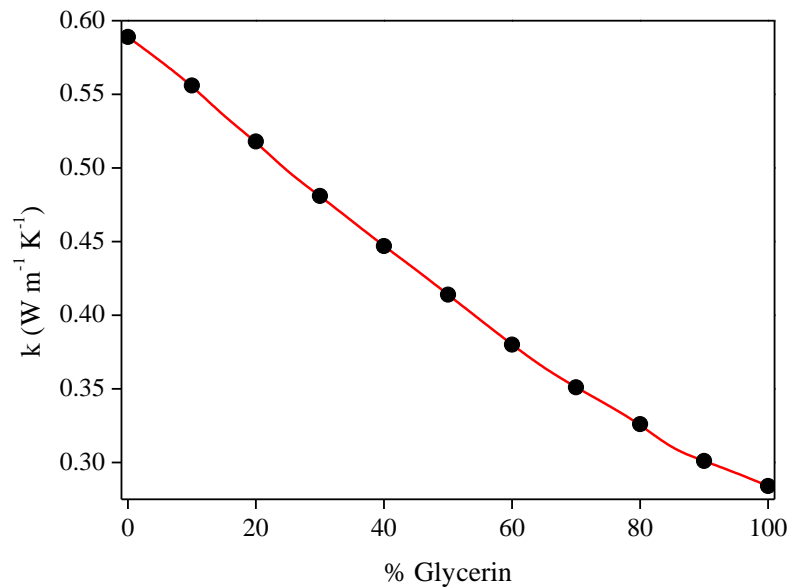


**Figure 2.1 – Thermal conductivity based on the composition of glycerine/water mixtures at 20 °C which is seen to vary as a function of the composition. Values taken from [2]**

However, having a knowledge of the thermal properties of a material itself can also be important. For example, the thermal conductivity of heat sink compounds must be known to allow an estimation of their performance, while thermal conductivity of building materials is becoming increasingly important as new buildings must meet stringent environmental standards [6] and a knowledge of the thermal conductivity of bone is essential to allow the flow of heat generated during surgery to be modelled [7]. While the thermal properties for many common materials are well documented (e.g. [8]), the thermal properties for nano-fluids [9] or heterogeneous mixtures (e.g. food [10]) are difficult to estimate even with a knowledge of the constituent parts [11]. In such cases, experimental measurement may be the only way of determining the thermal conductivity. This work aims to create a sensor which can fulfil this requirement, and take such measurements on small scale samples.

### **2.1.2.Small scale thermal sensors**

There are clear applications for sensors which can measure the thermal properties of a material. Reducing the scale of the sensor to the micro-scale introduces an element of novelty to the project, as it allows a range of samples to be probed which are too small for traditional probes to

monitor. Examples of such samples include thin sheets (e.g. paper or leaves) and droplets of liquid.

A range of applications for small scale thermal sensors have been reported. For example, Williams and Wickramasinghe [12] developed the scanning thermal microscope in 1986 and this is now a standard instrument for characterising samples with small dimensions [13]. Other examples of devices include those used on biological samples [14] or carbon nanotubes [15]. Many infrared sensors have been reported, for example Mattsson et al. [16] describe a device with pixels of 1.8 mm x 1.8 mm fabricated from thin-film thermocouples (TFTCs) with individual thermocouple junctions having line widths of 8  $\mu\text{m}$  and separations of 5  $\mu\text{m}$ . Micro- and nano-calorimeters have found many uses in drug discovery [17], monitoring the metabolism of single cell organisms [18] and studying biological processes [19]. Thermal sensors have also found applications as flow sensors [20].

The above only gives an indication of the wide range of applications and designs available to probe the thermal properties of small volumes. This work aims to create a sensor which is capable of determining the thermal conductivity of samples with characteristic dimensions of 10 – 100  $\mu\text{m}$  and find novel applications which utilise this ability.

### **2.1.3. Methods for the measurement of thermal conductivity**

A number of thermal properties of a sample can be measured, including its relative or absolute temperature, thermal conductivity, heat capacity or thermal diffusivity. In this work, a known heat input was applied to a sample which induced a temperature gradient within the sample which was recorded by small scale temperature sensors. A comparative method was used to relate the induced thermal gradient with the thermal conductivity of the sample.

Thermal conductivity defines a material's ability to conduct heat and it can be calculated using Fourier's law, which in three-dimensions is given by Equation 2.1 .

$$q'' = -k\left(i\frac{\partial T}{\partial x} + j\frac{\partial T}{\partial y} + k\frac{\partial T}{\partial z}\right) \quad 2.1$$

Where  $q''$  is the heat flux per unit area,  $k$  is the thermal conductivity of the material in question,  $i, j$  and  $k$  are unit vectors (in the  $x, y$  and  $z$  directions respectively) and  $T$  is temperature. The simplest form of this equation is that which represents steady state conditions and one-dimensional heat flow. In such a situation, the thermal conductivity can be calculated by Equation 2.2.

$$k = -qA\frac{dx}{dT} \quad 2.2$$

Where  $q$  is the heat flow rate and  $A$  is the area through which heat is flowing.

To use this equation, it is necessary to have a sufficiently simple geometry, which approximates a heat flow that varies in only one-dimension. For example a long cylinder or plate insulated along its edges or a sphere, as shown in Figure 2.2.

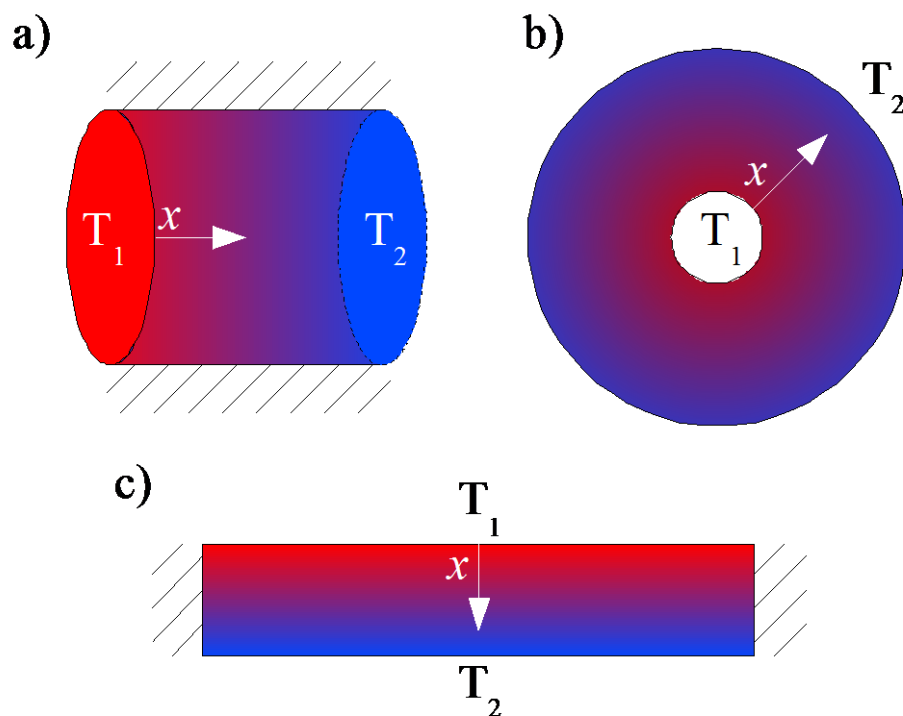


**Figure 2.2 – Examples of one-dimensional heat flow. a) an insulated cylinder; b) a sphere & c) heated, insulated plate**

Many variations of designs have been reported which utilise the simplification offered by inducing a one-dimensional heat flow. Variations arise based on the sample to be measured, the

accuracy of the measurement and the properties of the material under test. For example, finding an insulator with a significantly lower thermal conductivity than a polymer sample may preclude methods which rely on insulated edges. Some examples are given below.

### 2.1.3.1. *The guarded hot-plate method*

A heated plate is sandwiched between two identical samples and heat sinks (Figure 2.3). As the heat input  $q$ , area  $A$ , sample thickness  $\Delta x$  and temperature difference  $(T_1 - T_2)$  are known, Equation 2.3 can be used to calculate the thermal conductivity. This method is suitable for relatively large samples with high thermal conductivity, such as soil samples which have an ISO standard (ISO 8302). Various geometries and combinations of samples / calibrated materials have been demonstrated.

$$k = \frac{q \Delta x}{A (T_1 - T_2)} \quad 2.3$$

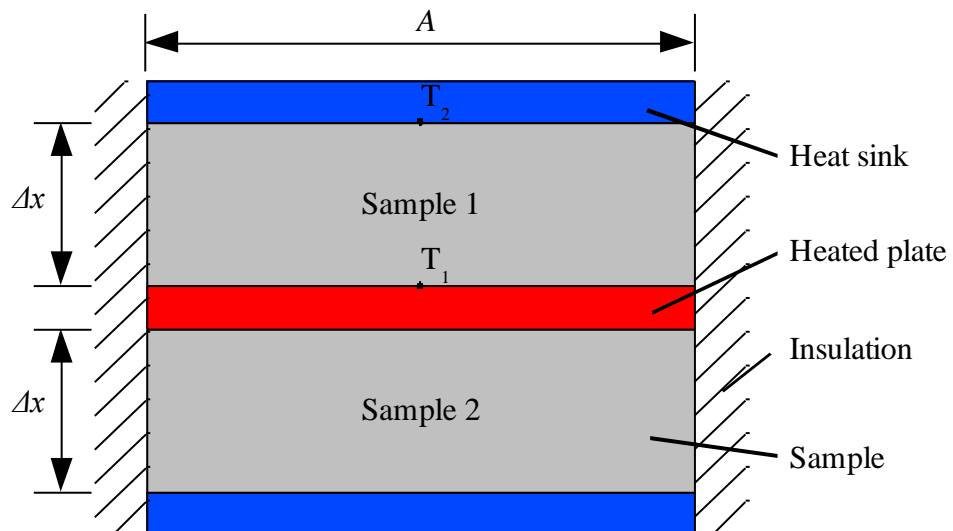


Figure 2.3 – The guarded hot plate method

### 2.1.3.2. *Line heat source method*

A heated line source (e.g. a long, thin wire) is embedded within a sample (Figure 2.4). The temperature increase at a known distance from the heat source is recorded (e.g. by a thermocouple also embedded within the sample) and this allows the thermal conductivity to be calculated using Equation 2.4.

$$k = \frac{q}{4\pi(T_1 - T_2)} \ln(t_1/t_2) \quad 2.4$$

Where  $T_1$  is the temperature at radius  $t_1$ , and  $T_2$  is the temperature at radius  $t_2$ .

As this method relies upon a heat source being embedded within the sample, its use is limited to those samples which can be formed around the heat source, for example liquids or soil.

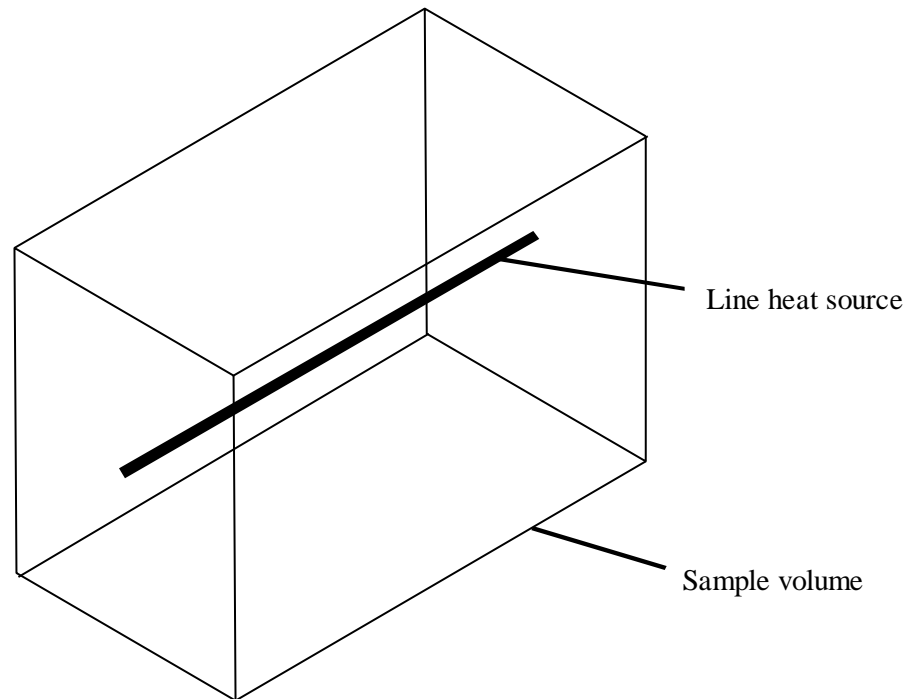


**Figure 2.4 – The line heat source method**

### **2.1.3.3. Single and dual probe methods**

These methods are similar to the line source heat method, however the line source is replaced by a heated needle, which is inserted into the sample. The temperature disturbance created is monitored either by a sensor within the needle (single probe method) [10] or at a set distance (dual probe method) [4].

### **2.1.3.4. Standards**

Thermal conductivity is such an important and often measured quality of a material that standards have been defined, such as: ASTM E1225–09 (Standard Test Method for Thermal Conductivity of Solids by Means of the Guarded-Comparative-Longitudinal Heat Flow Technique), ASTM C835–06 (Standard Test Method for Total Hemispherical Emittance of Surfaces up to

1400°C) or IEEE Std 982002 (IEEE Standard for the Preparation of Test Procedures for the Thermal Evaluation of Solid Electrical Insulating Materials). However, standards tend to be based on large samples and are primarily aimed at building materials or electrical materials. While the methods outlined above offer reliable measurements, the current devices do not necessarily scale down well for small scale samples.

#### **2.1.4.Devices in this project**

As the size of the sample under test reduces, traditional methods begin to fail. Not only do the assumptions required to justify methods become invalid, but the equipment used to probe the sample limits the operation. For example, the guarded hot plate method requires the measurement of the temperature at each face of the sample (with the hot plate and the heat sink). For very thin samples, the size of the heat sink and source becomes relatively large so the temperature difference observed across the sample may be small, leading to inaccuracies in measurement. For samples with small lateral dimensions, the area through which the heat flows reduces, so the heat lost through the insulation may not be negligible. The traditional methods must therefore be altered to account for the difficulties faced when measuring the thermal conductivity of small scale samples. In this work, 100  $\mu\text{l}$  droplets of liquid,  $\sim 100\ \mu\text{m}$  thick sheets of paper and leaves are tested. Thus, the sensor must be designed to operate on samples with critical dimensions at or below 100  $\mu\text{m}$ .

The devices presented here consist of a thin-film resistive heater and two micro-TFTCs (as temperature sensors) patterned on a polymer substrate (SU-8 and polyimide were both used). The resistive heater creates a thermal gradient which is recorded as a temperature difference ( $\Delta T$ ) between the two temperature sensors. This temperature difference is a function of the thermal conductivity of a sample in contact with the device, shown graphically in Figure 2.5. Calibrating the device on samples of known thermal conductivity allows a comparative method to be used on samples with an unknown thermal conductivity. Microfabricating the devices on thin polymer substrates ensures that they are capable of monitoring small volume samples as it allows the sensing junctions of the TFTCs to be made with line widths of 12  $\mu\text{m}$ , whilst also allowing the

sensing junctions to be precisely patterned at a known distance from the heater. Details of the device designs are given in Section 2.2.

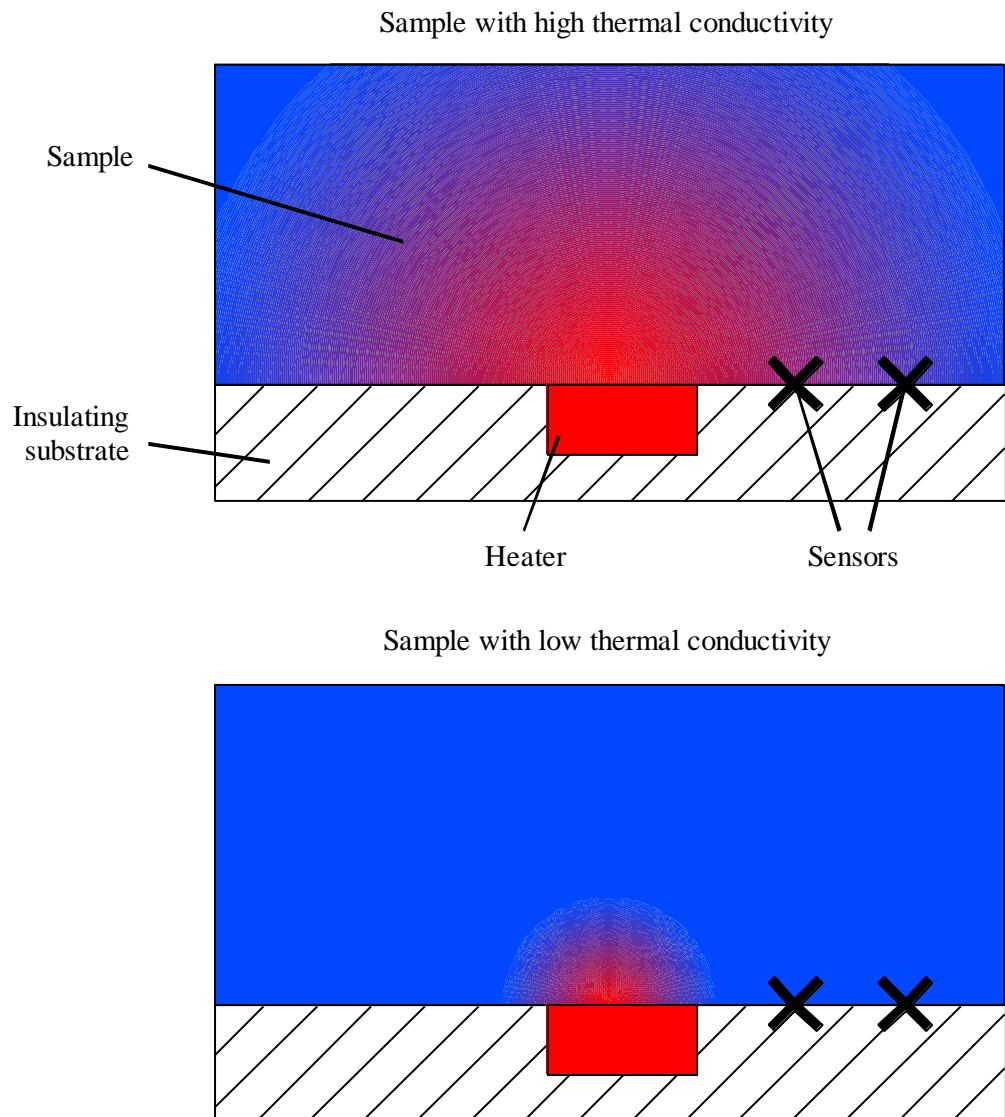


**Figure 2.5 – By monitoring the thermal gradient set up by a resistive heater, the thermal conductivity of the sample can be determined**

### **2.1.5. Thin-film thermocouples**

TFTCs were chosen as temperature sensors for this work. Thermocouples are formed from two dissimilar metal wires are joined at either end. One junction is held at a known temperature – this is the ‘cold’ or reference junction. An open circuit voltage is then produced which is a function of the temperature difference between the reference junction and the ‘hot’ or sensing junction and the combined Seebeck coefficient of the two metals. Traditionally, thermocouples were formed

from metal wires bonded together at the sensing junction and the reference junction. The reference junction was placed in an iced water bath to give a constant 0 °C reference point. However, the practicalities of maintaining an iced water bath mean that this is normally replaced by an electronic offset, based on a Wheatstone bridge and a thermistor.

Thermocouples are widely used as temperature sensors, as they are durable, robust and have a wide operating range. They are identified by their ‘type’ which is defined by the combination of metals which form the thermocouple. Examples of some common types are shown in Table 2.1.

**Table 2.1 – Examples of some common thermocouple combinations and their operating range. Taken from [21]**

<b>Type</b>	<b>Composition</b>	<b>Operating range (°C)</b>
K	Chromel / Alumel	0 – 1250
J	Iron / Constantan	0 – 750
B	Platinum 6% - Rhodium / Platinum 30% - Rhodium	800 – 1700
R	Platinum / Platinum 13% Rhodium	0 – 1450

To create TFTCs, the wires of a traditional thermocouple are replaced by thin-films (a few  $\mu\text{m}$ s or less) of metal or semiconductor. The reduction in the volume of the junction increases the speed of response of such thermocouples. TFTCs can also be patterned directly onto a surface being monitored, ensuring intimate contact. TFTCs offer a number of advantages as small scale thermal sensors. In particular, no size dependence is seen in devices until dimensions reach the order of  $\sim 10$  nm [22]. Devices in this work have line widths of  $> 12$   $\mu\text{m}$  and thicknesses of over 100 nm and so will have only limited performance degradation as a result of their small scale and achieve near bulk Seebeck coefficients. The law of homogenous materials ensures that a thermocouple is only sensitive to the temperature at its junctions, thus the TFTCs will only respond to temperature changes observed at their sensing junction. This is a useful property for a small scale thermal sensor as it means that tracks leading to the sensing junction will play no role in determining the output.

TFTCs are relatively easy to fabricate, simply requiring two layers of metals to be patterned so they overlap to form ‘hot’ and ‘cold’ junctions. However, commercial thermocouples are generally formed from specific alloys, which improves the output characteristics by increasing the

Seebeck coefficient and standard combinations are used, as specified in various standards (e.g. ASTM E230). However, pure metals offer simpler processing with the microfabrication techniques available. In these cases, the Seebeck coefficients must be determined experimentally.

The nature of a thermocouple requires care when designing the connections to the sensing element due to the law of intermediate temperatures: if a connection is made by a third metal which has a different composition to the two metals used to form the thermocouple, then a second thermocouple may be inadvertently created. To negate this, a cold junction was formed on every device and external connections were created in such a way as to produce no temperature difference between either connection, leading to no net voltage generation by the addition of the third metal. The formation of a cold junction on the device also ensured that all temperature measurements were made relative to the ambient conditions, allowing the device to account for small fluctuations in the ambient temperature. The cold junctions were created around 20 mm from the heater and sensing junctions and so would not see a temperature change caused by the device.

Resistive methods were the most attractive alternative to TFTCs. Platinum based resistance thermometers offer very high levels of accuracy [23] and are even simpler to fabricate than TFTCs, requiring only a single layer of patterned metal. However, resistive sensors offer some disadvantages over TFTCs. Firstly their output is highly size dependent and reducing the size of the resistive element degrades their performance. The area sensed by the device is also difficult to define, as the resistance of the leads and tracks on the device must be accounted for. Finally, operating a resistive sensor on a flexible substrate may introduce inaccuracies due to strains induced in the device as the substrate flexes. Many alternative methods exist, from very accurate but highly complex methods such as noise thermometry [24], non-contact methods such as infrared thermography [23] or Rayleigh scattering [25]. However, TFTCs were chosen for their simplicity, ease of fabrication on a flexible substrate and ability to operate over the required temperatures and dimensions.

### 2.1.6. Thermocouple theory

To demonstrate that TFTCs are unlikely to suffer from size dependence, it is necessary to introduce the theory underpinning their operation. Thermocouples operate on the thermoelectric effect which is based upon differences in the energy transfer of the charge carriers within a metal or semiconductor. Before the principle of operation of a thermocouple can be understood, it is necessary to look at the conduction of heat in an electrical conductor.

There are two modes of transport of energy within a solid: electron transport and lattice vibrations (phonons). Electron transport is brought about by the bulk movement of electrons within a solid whereas lattice vibrations transport energy by passing energy in the form of a vibration from one point to another without any overall movement of the carriers. Both forms of thermal energy transport will occur within a metallic conductor, whereas only lattice vibrations will occur in an electrical insulator. Thus a comparison of the thermal conductivity of electrical conductors and electrical insulators gives an indication that the bulk of the thermal conduction in an electrical conductor is by electron transport. The difference in electrical conductivity of conductors and insulators is around  $10^{24}$  while the difference in thermal conductivity is around  $10^3$  (Copper has a thermal conductivity of  $401 \text{ W m}^{-1} \text{ K}^{-1}$  at 300 K [8] while SU-8 has a thermal conductivity of  $0.3 \text{ W m}^{-1} \text{ K}^{-1}$  [26]). As the difference in thermal conductivity between a thermal insulator and a thermal conductor is due to the lack of electron transport in an insulator, it is clear that electron transport dominates in metallic materials.

To understand thermal conductivity in a metal due to electron transport, a simplified electron theory model can be used, which assumes that each electron within the metal is free to move and has an average energy. Equation 2.5 [27] relates the average electron energy to the temperature:

$$E_{AVG}(T) = \frac{3}{5} E_{FO} \left[ 1 + \frac{5\pi^2}{12} \left( \frac{k_B T}{E_{FO}} \right)^2 \right] \quad 2.5$$

Where  $E_{AVG}(T)$  is the average electron energy at temperature  $T$ ,  $E_{FO}$  is the Fermi energy at 0K and  $k_B$  is Boltzmann's constant. Thus, it is clear that the average energy of an electron within the metal will increase with the temperature.

However, if the metallic conductor has a thermal gradient across it such that the hot region is at  $T + \delta T$ , it follows that electrons in the hotter region have more energy than those in the cooler region, as given by Equation 2.6:

$$E_{AVG}(T + \delta T) = \frac{3}{5} E_{FO} \left[ 1 + \frac{5\pi^2}{12} \left( \frac{k_B(T + \delta T)}{E_{FO}} \right)^2 \right] \quad 2.6$$

As electrons in the hotter region have more energy, they will tend to diffuse into the colder region. This gives rise to a thermodynamic potential which acts in a similar way to an electric potential and results in a drift motion of the electrons due to a thermodynamic force. As electrons drift from the hot region to the cold region, an electric potential will build up, opposing this motion. In equilibrium, this electric potential will balance out the thermal potential and there will be no net electron flow. If the temperature difference between the hot region and cold region is  $\delta T$  and this sets up a potential  $\delta V$  then the energy required by one electron to diffuse from the hot region to the cold region is given by Equation 2.7:

$$-e\delta V = E_{AVG}(T + \delta T) - E_{AVG}(T) \quad 2.7$$

Where  $e$  is the charge on an electron.

Substituting Equations 2.5 and 2.6 into Equation 2.7 and expanding and neglecting  $\delta T^2$  terms, as they will be much smaller leads to Equation 2.8:

$$-e\delta V \approx \frac{\pi^2 k_B^2 T \delta T}{2E_{FO}} \quad 2.8$$

This can be re-written as:

$$\frac{\delta V}{\delta T} = \alpha = -\frac{\pi^2 k_B^2 T}{2eE_{FO}} \quad 2.9$$

Where  $\alpha$  is the Seebeck coefficient: a measure of the electromotive force (emf) produced for a given temperature difference.

The sign of the Seebeck coefficient is important, as intuitively it should be negative, implying that electrons diffuse from the hot end to the cold end. However, certain metals have a positive Seebeck coefficient (e.g. Chromium where  $\alpha_{Cr} = +21.8 \mu\text{V K}^{-1}$  [28]) implying that electrons diffuse from the cold end to the hot end. Equation 2.9 does not take this effect into account, implying that there is a gap in the theory.

It can be shown [27] that by including the energy dependence of the scattering processes, the Seebeck coefficient can be described by Equation 2.10 where  $C_{mat}$  is a numerical constant which is dependent on the temperature dependence of the mean free path length and scattering time of electrons within the material.  $C_{mat}$  can be positive or negative, depending on the metal in question, leading to some materials with positive Seebeck coefficient and some with negative.

$$\alpha = -\frac{\pi^2 k_B^2 T}{3eE_{F0}} C_{mat} \quad 2.10$$

In order to measure the emf produced and calculate a value for  $\alpha$ , a voltmeter must be attached to either end of the metal in order to create a circuit. However, if the metal used to make this connection is the same metal as that under test, then the net emf produced by the circuit would be zero. This concept is known as the law of homogenous circuits and exists due to Equation 2.11. It is shown diagrammatically in Figure 2.6 a).

$$\text{emf} = [\alpha_1(T_{hot} - T_{cold})] + [\alpha_1(T_{cold} - T_{hot})] = 0 \quad 2.11$$

Where  $\alpha_1$  is the Seebeck coefficient of the metal and  $T_{hot}$  &  $T_{cold}$  are the temperatures of the hot and cold junctions respectively.

To create a measurable emf, a second material with a different Seebeck coefficient must be used.

In this case, the resultant emf is given by Equation 2.12:

$$\text{emf} = [\alpha_1(T_{hot} - T_{cold})] + [\alpha_2(T_{cold} - T_{hot})] \quad 2.12$$

Re-writing this in a more useful form:

$$V_{out} = (\alpha_1 - \alpha_2)(T_{hot} - T_{cold}) \quad 2.13$$

or

$$V_{out} = \alpha_{1-2}(T_{hot} - T_{cold}) \quad 2.14$$

Where  $V_{out}$  is the emf measured and  $\alpha_{1-2}$  is the combined Seebeck coefficient of the metals.

Metals have relatively low  $\alpha$  values compared with semiconductors, for example:

- Chromium:  $\alpha = + 21.8 \mu\text{V K}^{-1}$  [28]
- n-PolySi:  $\alpha = + 520 \mu\text{V K}^{-1}$  [29]

By stacking several hot-cold junctions (see Figure 2.6 c)), the output performance can be improved as the combined Seebeck coefficient is the sum of the individual junction's Seebeck coefficients:

$$\alpha_{overall} = \sum_1^n \alpha_n \quad 2.15$$

Where  $n$  is the number of pairs of thermocouples.

Thus, for applications where sensitivity is important, many junctions can be created (e.g. [30]).

However, this comes at the expense of size, as increasing the number of junctions will increase the area sensed by the device.

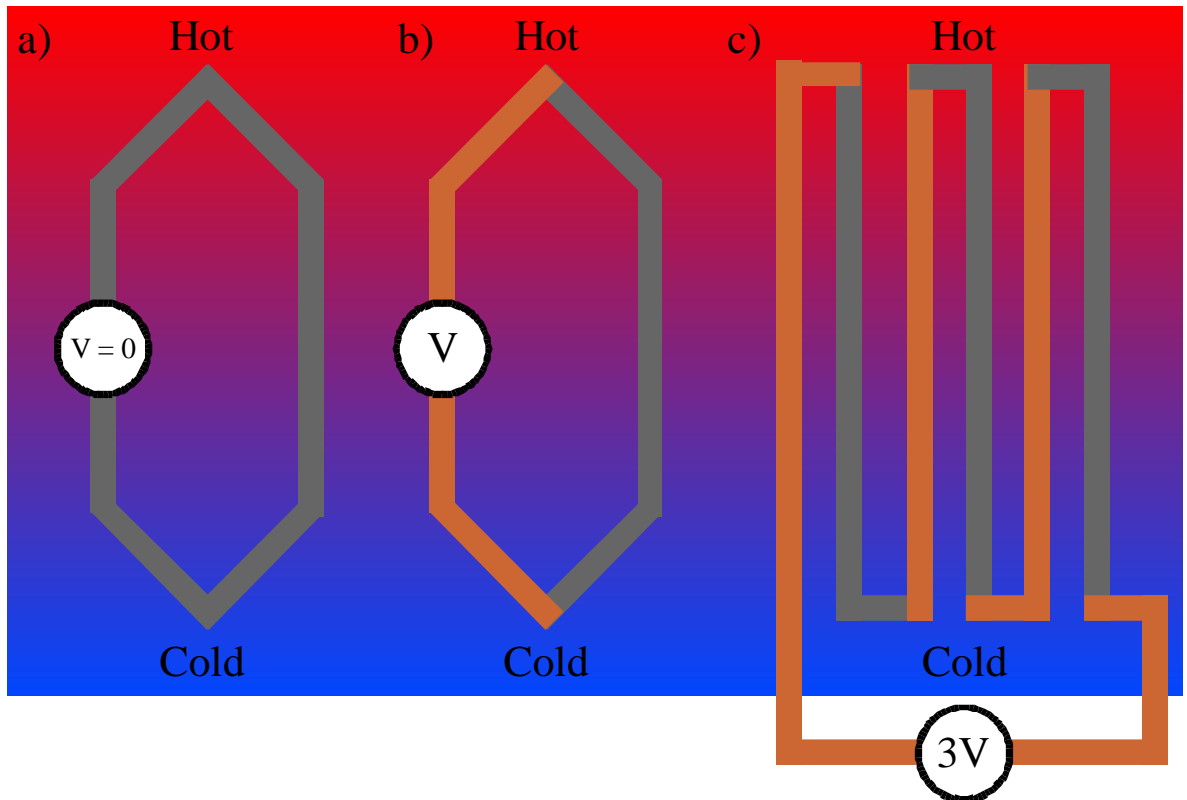


**Figure 2.6 – a) The net emf produced by two similar conductors is zero due to the law of homogenous circuits; b) an emf is produced when two dissimilar materials have a temperature difference across their junctions & c) stacking several pair of thermocouples increases the emf generated**

### **2.1.7. Effect of small scales on thermocouple operation**

An important consideration which arises from the theory outlined in Section 2.1.6 is that electron scattering times and mean free path lengths play an important role in the function of a thermocouple. For large thermocouples, it is valid to assume that edge effects will be negligible and electrons will follow the theory outlined above. However, as the dimensions of the metal shrink, surface effects become increasingly important and the assumptions made may not be valid. In fact very thin films can even have different Seebeck coefficients to those seen in bulk materials [31]. Thus, a thermocouple could be fabricated from platinum wire and a thin-film of platinum, despite the bulk Seebeck coefficient of both elements being identical.

For such small scale effects to be observed, the critical dimension must approach the mean free path length of the electrons [32]. In the thermocouples presented in this work, the only dimension that may satisfy this requirement is the thickness of the metal as this is of the order of 100 -

250 nm, whereas the lateral dimensions are 10 – 100  $\mu\text{m}$ . So it is expected that the thermocouples used in this work may experience some degradation in performance due to their thickness. However, experimental work shows that this degradation is minimal ( $> 10\%$ ) and has no effect once the thermocouples are calibrated. Experimental determination of the effect of the thin-film thickness is discussed further in Section 3.1.3.2.

Assuming the TFTCs are suitably thick and the lateral dimensions are much larger than the mean free path length of the charge carriers, Equations 2.10 and 2.14 hold. This means that the Seebeck coefficient will not be dependent on the lateral size of the thermocouple junction. Thus there is no loss in sensitivity as the lateral dimensions of the sensor are shrunk, as long as the junctions remain in the  $\mu\text{m}$  scale. This is a key advantage of micro-TFTC thermal sensors over other methods, such as resistive or thermistor based sensors. However, it should be noted that nano-TFTCs (i.e. sensors with lateral dimensions of  $<100\text{ nm}$ ) will begin to suffer from small scale effects.

## **2.2. Device designs**

Section 2.1 has introduced the theory and rationale behind the devices as well as justifying TFTCs as suitable temperature sensors. Theory indicates that TFTCs with lateral dimensions down to 1  $\mu\text{m}$  should demonstrate no size effects. The following sections outline specific details of the device designs used in this work. Three distinct types of devices were produced during this project: early prototyping devices, SU-8 based devices and polyimide devices.

The early devices were used to develop the microfabrication methods and trial device designs. It quickly became clear that the substrate was dominating the thermal response of the devices, so polymer substrates were developed to improve the sensitivity of the devices. Two methods were used to achieve this, the first used SU-8 to form a suspended membrane above a silicon substrate, which improved device performance but would be unsuitable as a robust sensor for mounting on a leaf. The second and final substrate used was polyimide. This offered improved sensitivity while also being flexible and robust. Two design patterns are discussed in detail below: Design A

patterns were used to pattern both SU-8 and polyimide substrates while Design B patterns were formed exclusively on polyimide substrates and used during plant testing.

### **2.2.1. Early designs**

During the development of the devices, a number of trials were undertaken, investigating how different parameters affected the device's performance. These early devices were tailored to allow ease of fabrication while testing various design parameters such as metal combinations, metal thickness, junction widths and separation distances between the heater and sensors. An example of one such device is shown in Figure 2.8. This device was used to assess the effects of reducing the junction area. It has four individually addressable sets of TFTCs, each with a sensing junction located around 100  $\mu\text{m}$  from a resistive heater and a reference junction located  $\sim 20$  mm from the heater. Further details of this experiment are given in Section 2.2.1.1.

Most of the early devices were fabricated on glass microscope slides or 2" oxidised silicon wafers, as these offered the simplest fabrication process. However, the performance of the devices was poor, as the substrate acted as a heat sink, causing slow device response and poor sensitivity. The thermal response of the system would therefore be dominated by the substrate and not the sample brought into contact with the device. A representative output for a device fabricated on an oxidised silicon wafer and glass microscope slide operating in air is shown in Figure 2.7. Both glass and silicon substrates show very poor sensitivity and response times of over 1 min. By comparison, the polyimide based devices reach thermal equilibrium within 0.2 seconds. This matter is discussed further in Section 4.1, where models are presented showing how the SU-8 and polyimide based devices are much more sensitive due to the reduction in thermal mass.

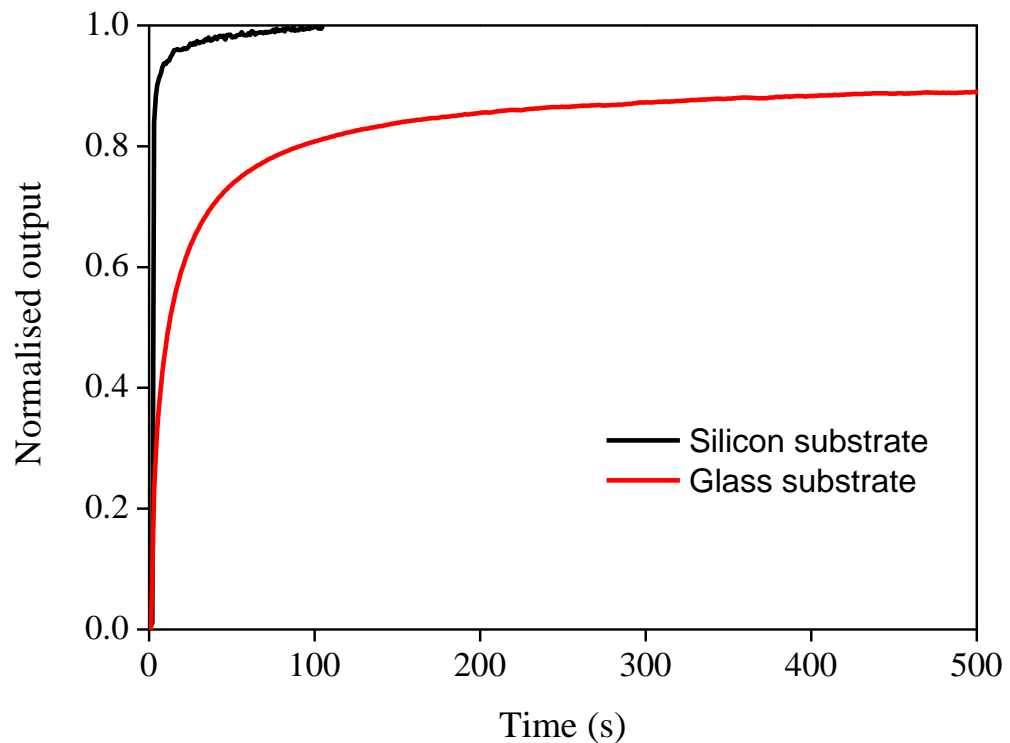


**Figure 2.7 – Early devices were fabricated on silicon and glass substrates for ease of fabrication, however the device took many seconds or minutes to achieve steady state conditions due to the thermal mass of the substrate.**

### **2.2.1.1. Junction area**

While thermoelectric theory suggests that only the choice of metal should influence the output characteristics of a TFTC, parasitic resistances created by narrow tracks could play a role. To investigate whether the TFTCs demonstrated small scale effects, a device was produced with four sensing junctions of increasing area. The smallest junction had dimensions of  $30 \times 30 \mu\text{m}$  and the largest  $1 \times 1 \text{ mm}$ . The TFTCs were formed from  $\sim 200 \text{ nm}$  thick Nickel (Ni) and  $\sim 100 \text{ nm}$  thick Chromium (Cr) on a glass microscope slide for ease of fabrication. A resistive heater was used as a heat source and  $150 \text{ mW}$  was applied using a current source/meter (Keithley, 2400). The temperature profile created was monitored by a thermal camera (ThermoVision A40M, FLIR). A thermal camera was required as the thermocouples were not calibrated but were large enough to be visible in the IR spectrum. To allow a comparison between the voltage output of the TFTCs and the thermal camera, all results were normalised, with the value observed at a distance of

325  $\mu\text{m}$  taken as the reference value. This corresponded to the distance between the edge of the heater and the centre of the smallest (and hence closest) TFTC. The results are shown in Figure 2.9.

The results demonstrate that the output of the TFTCs show the same pattern as that obtained by the thermal camera. This indicates that the larger junction shows a smaller output as the centre point of the junction lies further away from the heater, leading to a smaller temperature measurement. This indicates that there is no change in performance as the area of the TFTCs are shrunk from an area of 1 mm x 1 mm to 30  $\mu\text{m}$  x 30  $\mu\text{m}$ .

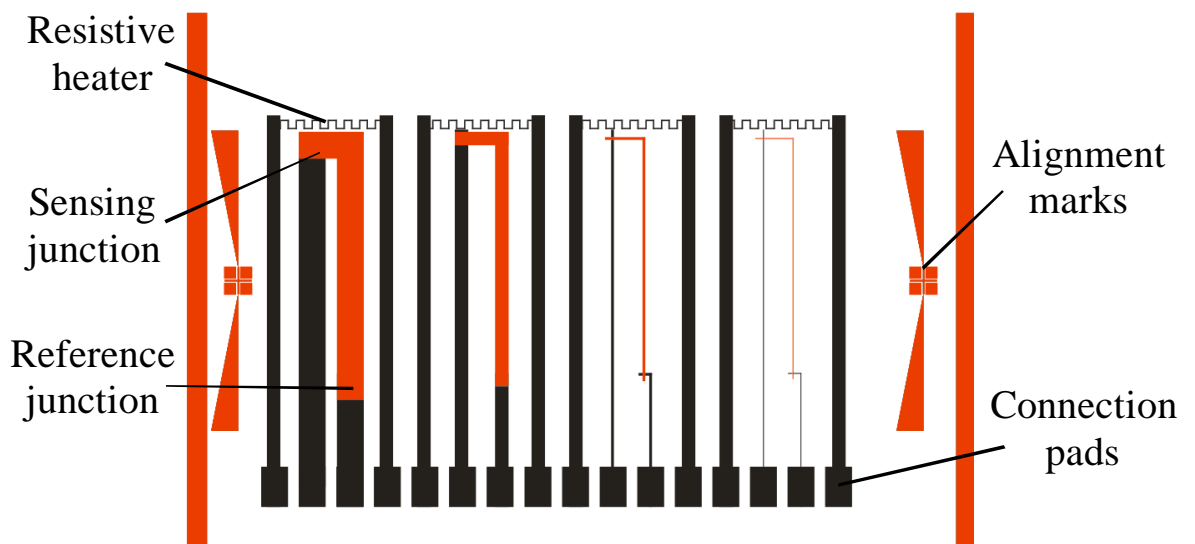
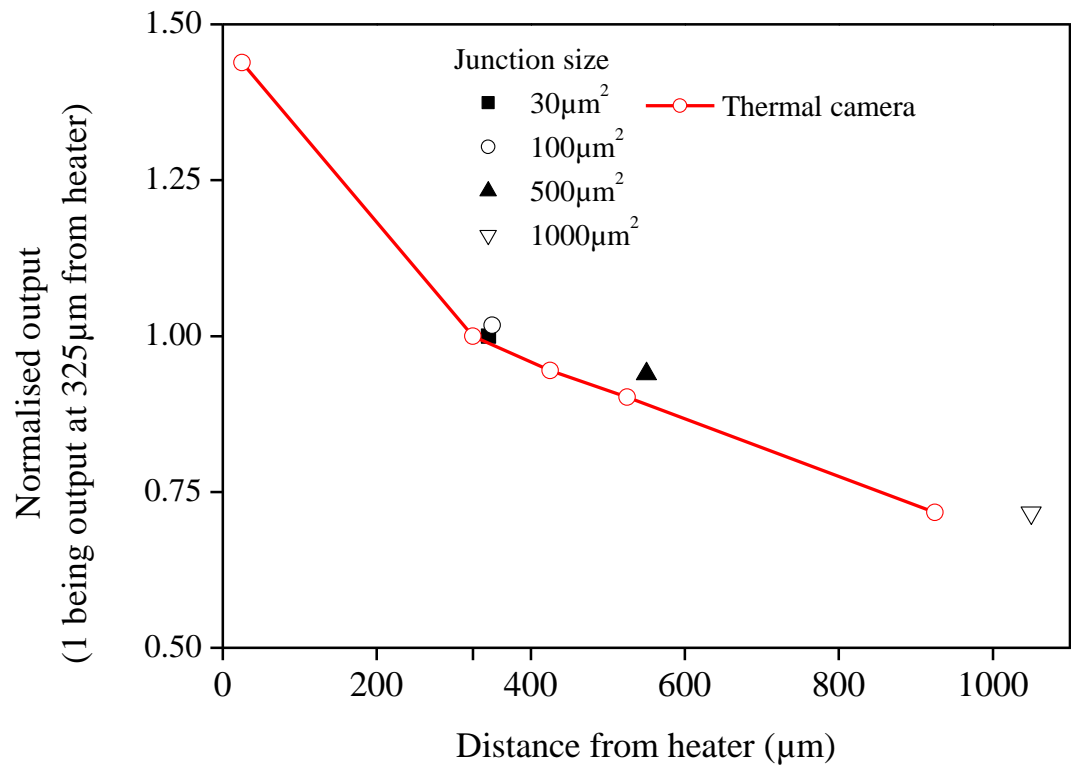


Figure 2.8 – Schematic diagram of one examples of an early device which was used to investigate the effect of junction area. Red areas were patterned with Cr while black areas were Ni



**Figure 2.9 –Output from four TFTCs plotted against the distance from the heater (to the midpoint of the sensing junction). Also shown are thermal camera measurements taken at six points. All values were normalised against the value at a distance of 325 µm from the heater, which represented the nearest TFTC junction**

### 2.2.1.2. Metal combinations

As the response of the device is strongly influenced by the Seebeck coefficient of the metal combinations, various combinations of metal pairs were formed on oxidised silicon wafers, to investigate which showed the best performance and to allow experimentation with deposition of different metals.

Throughout the project, pure metals were chosen for ease of fabrication. While alloys can offer higher Seebeck coefficients, the improvement makes the deposition methods much more complicated. The metals were generally deposited using either electron beam deposition or sputtering. Only sputtering can be used to reliably deposit an alloy. However, sputtering a combination of two or more metals could introduce an extra process variation as the pressure, temperature, electrical bias and other factors can affect the end composition of the metal and

hence material properties such as its intrinsic stress [33] or Seebeck coefficient. As the outputs of the devices were ultimately conditioned by an instrumentation amplifier, the small improvement in Seebeck coefficient is negated by the increase complexity required to fabricate TFTCs with a specific alloy composition.

As discussed in Section 2.1.6, metals have Seebeck coefficients around an order of magnitude lower than semiconductors. However, in order to achieve high Seebeck coefficients (e.g. 520  $\mu\text{V } ^\circ\text{C}^{-1}$  for n-PolySi [29]), a doped silicon substrate is required ( [29] or [34]). This process would not be compatible with an SU-8 or polyimide substrate, which is essential for operation on plant leaves. Sputtering and patterning doped silicon was attempted, however the resulting silicon formed an amorphous layer and had an extremely high electrical resistance, preventing its use as a thermocouple material. Thus, only pure metals were used to form devices for ease of fabrication and to allow a flexible polyimide substrate to be used.

Of the metals available (by electron beam deposition and sputtering) Ni and Cr offered the best combination of Seebeck coefficients:

$$\alpha_{\text{Ni}} = - 14.5 \mu\text{V } ^\circ\text{C}^{-1} [28]$$

$$\alpha_{\text{Cr}} = + 21.8 \mu\text{V } ^\circ\text{C}^{-1} [28]$$

Although Ni / Cr devices were expected to give the highest Seebeck coefficient, several other combinations were also tested to ensure that the Ni / Cr thermocouples were not adversely affected when operating as thin-films, for example titanium has a high affinity for oxygen and can form an oxide layer, which would impact on its performance. Platinum (Pt) and gold (Au) in particular offer advantages as they are extremely resistant to corrosion and may offer improved lifetimes.

TFTCs with line widths of 20  $\mu\text{m}$  were fabricated on an oxidised silicon wafer, a distance of 40  $\mu\text{m}$  from a resistive heater with dimensions of 600 x 140  $\mu\text{m}$ . A range of electrical powers from 10 mW to 60 mW were applied to the resistive heater and the output from the TFTC was

recorded. The collated results showing the output voltage as a ratio of the power input applied to the heater are shown in Figure 2.10.

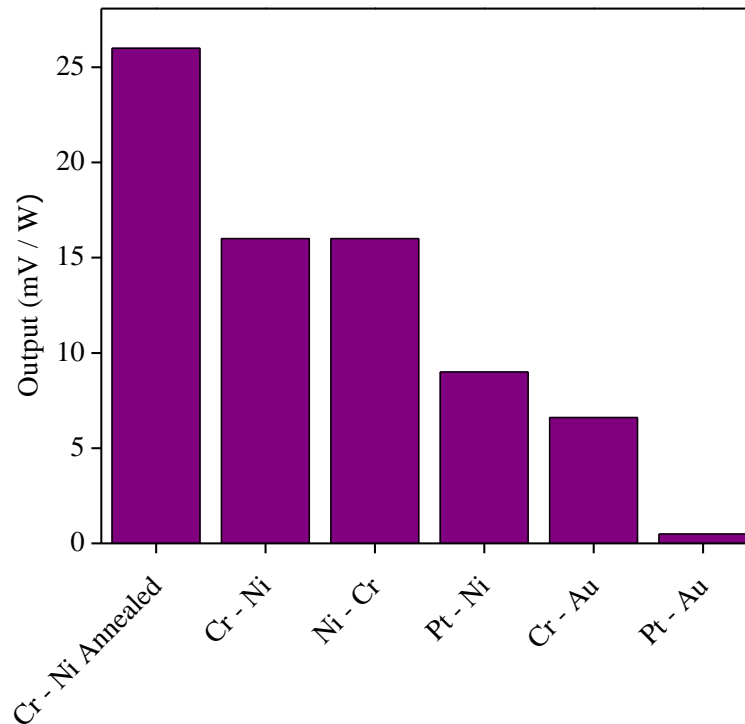


**Figure 2.10 – Output response for several thermocouple metal combinations. Cr-Ni devices were seen to give the highest Seebeck coefficient, regardless of the order of deposition. Annealing the device at 350 °C was seen to increase the output response**

As expected, Ni / Cr TFTCs produced the largest output response for the combinations tested. The order of deposition was seen to have no influence on the sensitivity of the device, with Cr / Ni devices demonstrating the same sensitivity as Ni / Cr devices. However, annealing the device at 400 °C for 30 minutes in a nitrogen atmosphere was seen to improve the response by 62 %. A similar increase is seen in the thermoelectric properties of bismuth-tellurium thin-films deposited by sputtering, which is due to an increase in the size of the grain structure [35]. While the devices used in this work are Ni / Cr thermocouples, it is suggested that a similar effect is being observed. While it is of interest to note this improvement in performance, it was beyond the scope of the project to investigate the mechanisms underpinning the effect. For polyimide based

devices, the encapsulation layer requires a curing bake at 350 °C. This stage also acted to anneal the metal layers, improving the sensitivity of the device to near bulk values.

### **2.2.2.SU-8 and polyimide devices**

The early devices discussed in Section 2.2.1 served a useful purpose for trialling different design criteria. However, they suffered from a number of flaws. Firstly, the sensing junctions were in direct contact with the substrate, which was thick and thermally conductive, so acted as a large heat sink. This meant that the devices offered poor sensitivity and slow response times. Secondly, the aim of the work was to improve the fabrication processes and test functionality of the devices, so little attention was paid to the connection mechanism, which meant each device could only be probed manually using a probe test station (described in Section 3.2.1). Thirdly, the metal tracks that formed the TFTCs and heaters were not insulated. This meant that if a sample was brought into contact with the device, it would cause noise, damage the thin-film layers and potentially electrically short tracks together.

#### **2.2.2.1. *Polymer substrates***

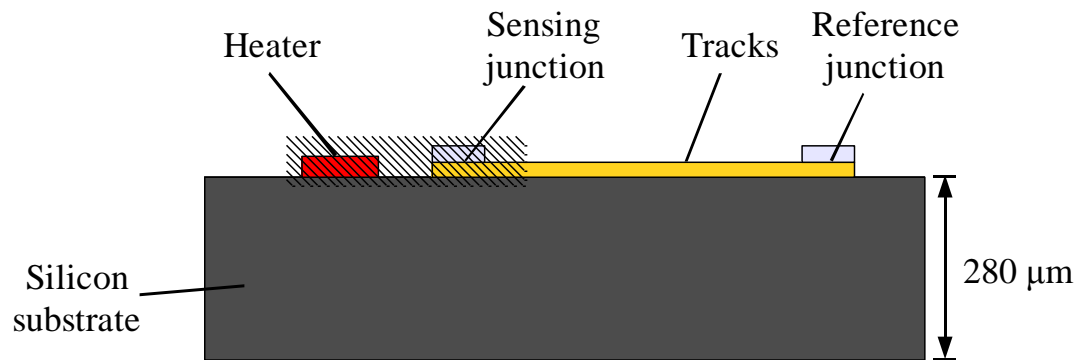
This and subsequent sections discuss polymer based substrates which were used to improve the operation of the sensors. Moving to these substrates offered two key advantages over silicon and glass. Firstly they have good material properties, acting as electrical and thermal insulators as well as encapsulants. Secondly, they can be spin coated to form thin layers 1 – 10s µm thick, offering a relatively easy fabrication route to forming structures with small thermal masses. Specific details of the polymers are given in the microfabrication chapter (Section 3.1).

SU-8 and polyimide devices were formed in slightly different ways. SU-8 devices were formed by patterning the metal layers on a 2” oxidised silicon wafer before a 10 µm thick layer of SU-8 was spun and patterned to act as a mask through which the silicon substrate could be etched. It also formed a structural component, as the TFTCs were suspended from the resulting membrane. This is in contrast to polyimide devices, where the metal layers were patterned on a ~10 µm thick polyimide substrate which was subsequently encapsulated and peeled from the silicon carrier

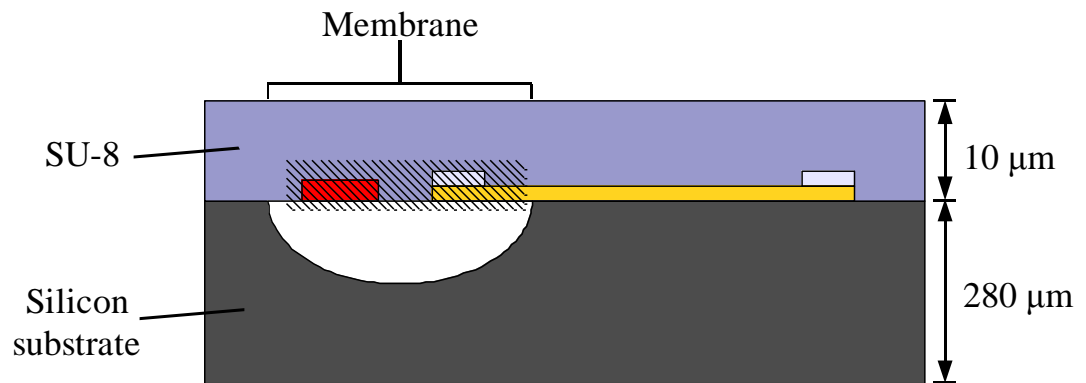
wafer entirely. Diagrams of the three substrates are shown in Figure 2.11 and detailed descriptions of the fabrication methods for each device is given in Chapter 3.

SU-8 devices offer a more complex fabrication route than those on silicon substrates or polyimide, as the devices must first be patterned on an oxidised silicon substrate prior to the addition of the SU-8 layer and subsequent suspension of the membrane. However, the devices could be better integrated with other microfabricated structures or devices formed on the silicon substrate. The polyimide devices by contrast remove the need for operation on a silicon wafer (although a silicon wafer is used to carry the substrate during fabrication). While this removes the ability of the device to be integrated with other structures on a silicon wafer, the fabrication route of such devices is much simpler and the resulting devices have a fully flexible polymer substrate. This ensures that they are robust and capable of operating on non-flat surfaces, such as plant leaves.

**a) Silicon device** – patterned with Design A



**b) SU-8 device** – patterned with Design A



**c) Polyimide device** – patterned with Designs A & B

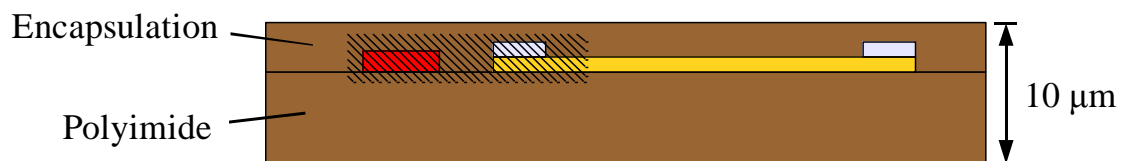


**Figure 2.11** – Comparison between polymer-based devices; a) A silicon based device; b) An SU-8 membrane device & c) A released polyimide device. Hatched areas represent the sensing area of the device

Two metallisation patterns are discussed in detail in the following sections. The first (Design A) was used to pattern both SU-8 and polyimide substrates, while the second (Design B) was only used to pattern polyimide substrates, as it utilised the flexible, thin substrate to make electrical connections using a commercially available Molex connector.

#### 2.2.2.2. *Design A*

Experience gained during the production of the early devices lead to the creation of Design A, which was the first successful device, capable of monitoring the thermal properties of a sample [36]. This design was used to pattern both SU-8 and polyimide substrates. The device consisted of two resistive heaters (500  $\mu\text{m}$  x 80  $\mu\text{m}$ ) each having three 20  $\mu\text{m}$  x 20  $\mu\text{m}$  TFTC sensing junctions located at increasing distances. The sensing junctions each had separations of 40  $\mu\text{m}$  between their midpoints, leading to temperature measurements at 50  $\mu\text{m}$ , 110  $\mu\text{m}$  and 170  $\mu\text{m}$  from the nearest edge of the heater. The reference junctions were located around 20 mm from the heaters and so experienced no heating. All TFTCs were Cr / Ni and the resistive heaters were Ni. While the thickness of the metals varied between batches, the Cr was generally deposited to a thickness of ~100 nm and the Ni ~200 nm. The design is shown in Figure 2.12.

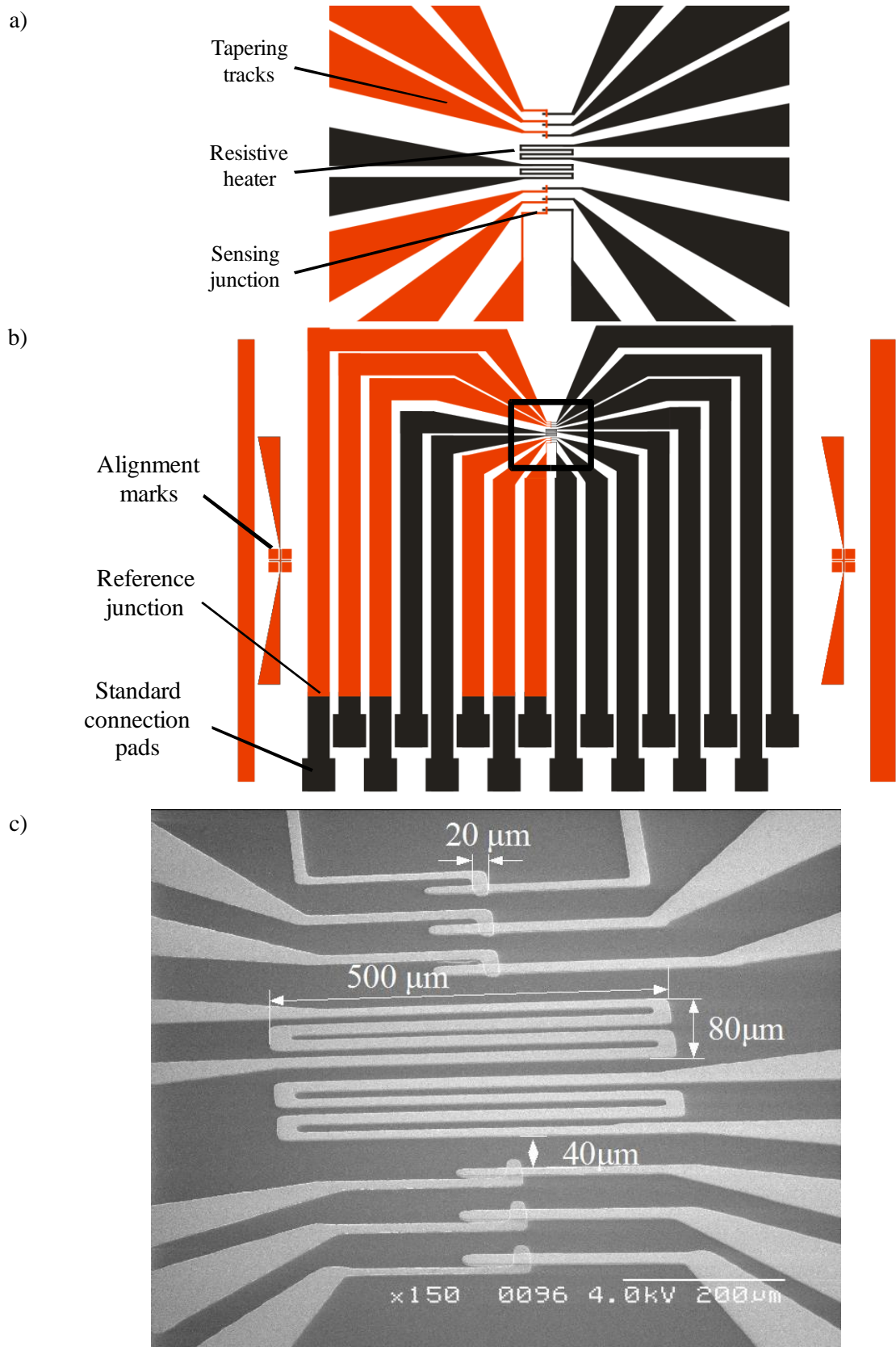


Figure 2.12 – Details of Design A: a) Detail of the sensing area (red tracks are Cr, black are Ni); b) View of the entire device, with the highlighted area shown in detail in a) & c); c) Dimensioned SEM image of the sensing area

There are several important design points to note: The tracks leading to the sensing area of the device were kept around 1 mm wide and only taper down to 20  $\mu\text{m}$  line widths close to the sensing area of the device. This ensures that the parasitic resistance of the tracks is as small as possible, helping to reduce the noise level. It also offers the advantage of improving the manufacturing yield, as pin-hole defects created during metal deposition had minimal effect on the wide tracks, but could destroy the thinner tracks.

Two sets of resistor/sensor arrays were created on each device. Each resistor had 3 sensing junctions patterned at increasing distances (heater-midpoint separations: 50  $\mu\text{m}$ , 110  $\mu\text{m}$  and 170  $\mu\text{m}$ ), to allow a variety of experiments to be run using a single set of masks. Building in a redundancy of 2 devices per substrate also improved the yield.

The final important design feature to note is the connection pads. These were 1.5 mm x 1.5 mm pads arranged in a staggered pattern with a spacing of 2.8 mm. A testing rig was created to allow simultaneous and reliable probing of all pads. This simplified the connection procedure and allowed multiple connections to be made to the device. Further details of the connection methods are given in Section 3.2. The following sections give details on both SU-8 and polyimide based devices patterned using Design A.

#### **2.2.2.2.1. SU-8 suspended membrane devices**

Design A devices were fabricated using both the SU-8 suspended membrane and polyimide substrates. While both methods offered a significant increase in sensitivity over glass and silicon based devices, the SU-8 method proved less reliable than the polyimide method and ultimately the advantages of polyimide as a substrate (material properties and flexibility) meant that SU-8 devices were not developed beyond a proof of principle.

However, SU-8 devices offered a significant improvement over earlier devices, as suspension on the membrane reduced the thermal mass of the sensing element. A comparison of the response of a Design A device before and after suspension is given in Figure 2.13. Prior to suspension, when the sensing area of the device was in contact with the silicon wafer, the device had a sensitivity of

0.35 mV W<sup>-1</sup>. After the SU-8 membrane was released and the device was suspended, it attained a sensitivity of 19.3 mV W<sup>-1</sup> which is 55 times higher than pre-suspension.

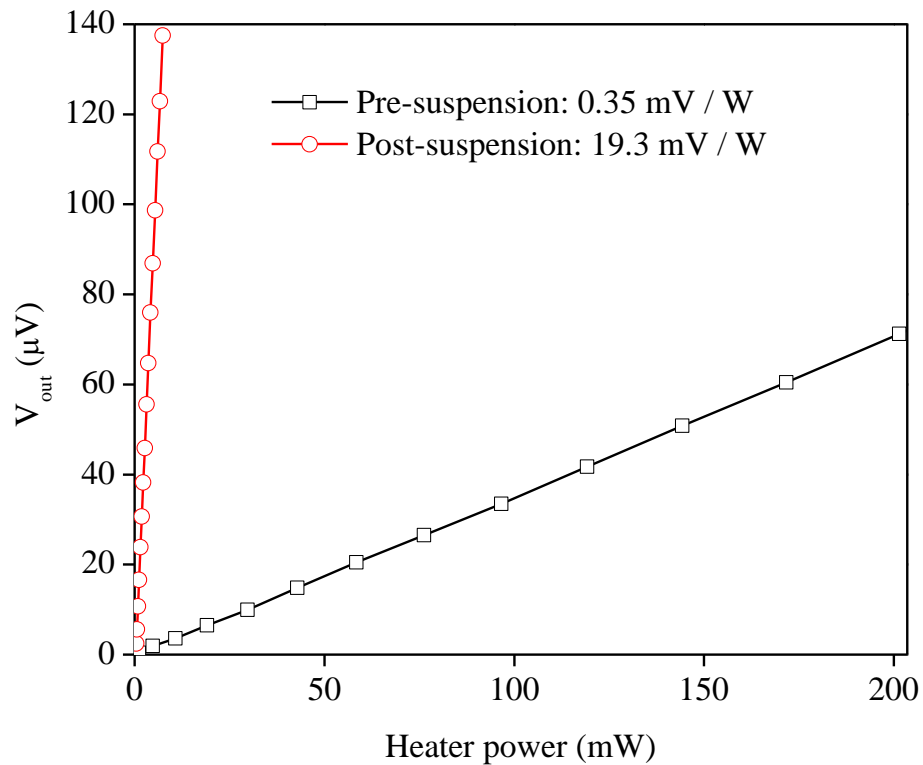


**Figure 2.13 – A comparison between the output of a TFTC before and after suspension. The TFTC was located 50 μm from the heater on a Design A device formed on a silicon substrate (pre-suspension) and then on an SU-8 membrane after this was released from the substrate (post-suspension)**

The improvement in sensitivity of the SU-8 devices after suspension was due to the reduction in thermal mass surrounding the sensing area of the device. Before suspension, the sensing junction and resistive heater were in intimate contact with the silicon substrate. This gave the sensor a large thermal mass, resulting in a low sensitivity (i.e. a lower thermoelectric emf was generated for a given heater input power). Suspending the sensing area of the device reduced the thermal mass surrounding the sensor, improving its sensitivity. An SEM image of a released membrane is shown in Figure 2.14.

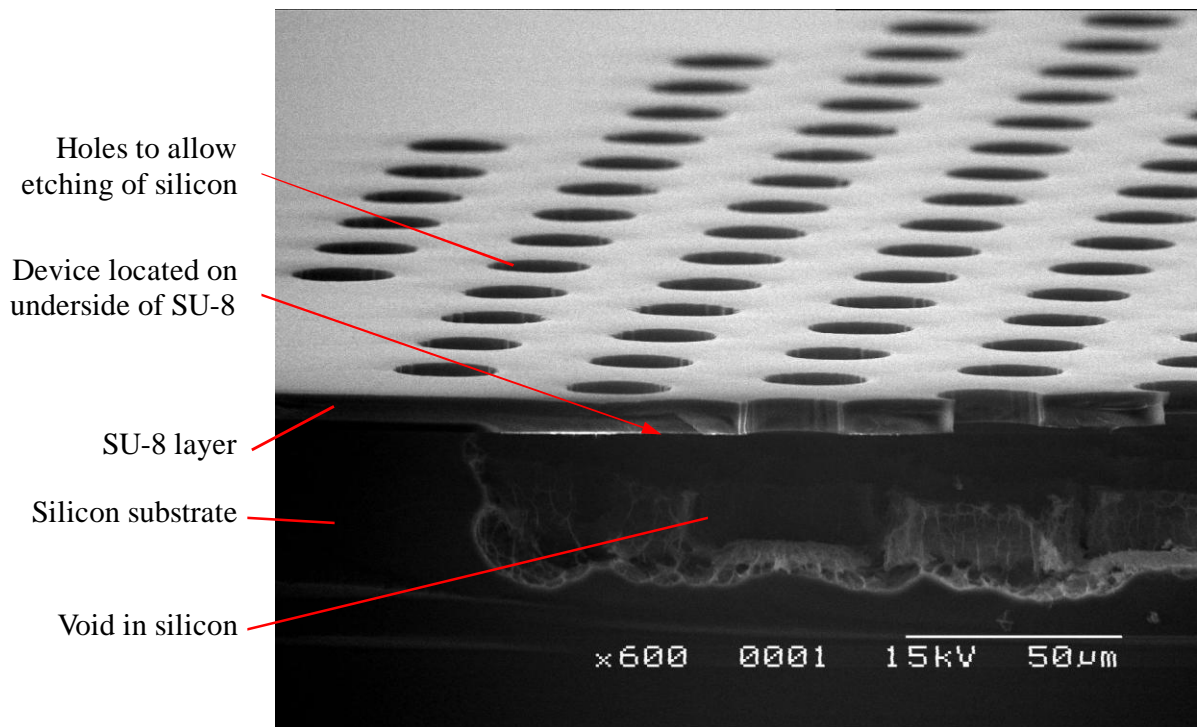


**Figure 2.14 – SEM image showing the suspended SU-8 membrane. The sensing area of the device is suspended underneath the SU-8 membrane.**

While devices suspended on an SU-8 membrane showed good sensitivity, they were found to be very fragile, with cracking observed in the metal tracks caused by excessive expansion within the membrane as it heated up. The tracks were also compromised if a second layer of SU-8 was spun over the membrane in an attempt to encapsulate the device. A third issue identified was that the etch (xenon difluoride) used to release the membrane was found to cause pitting on the surface of any Ni areas exposed to the gas. Figure 2.15 shows an SEM image of the pitting caused in a Ni track, observed through one of the SU-8 holes.

As the SU-8 devices were mounted on a silicon wafer (only the sensing area could be suspended), they were unsuitable as a plant-mounted sensor, so polyimide devices were developed to counter these issues. Despite these flaws, the SU-8 membrane devices offered a significant improvement in performance over silicon and glass substrates and despite its disadvantages when compared with polyimide, it could be developed further for applications which do not require a flexible substrate, or those which require integration with a silicon substrate.

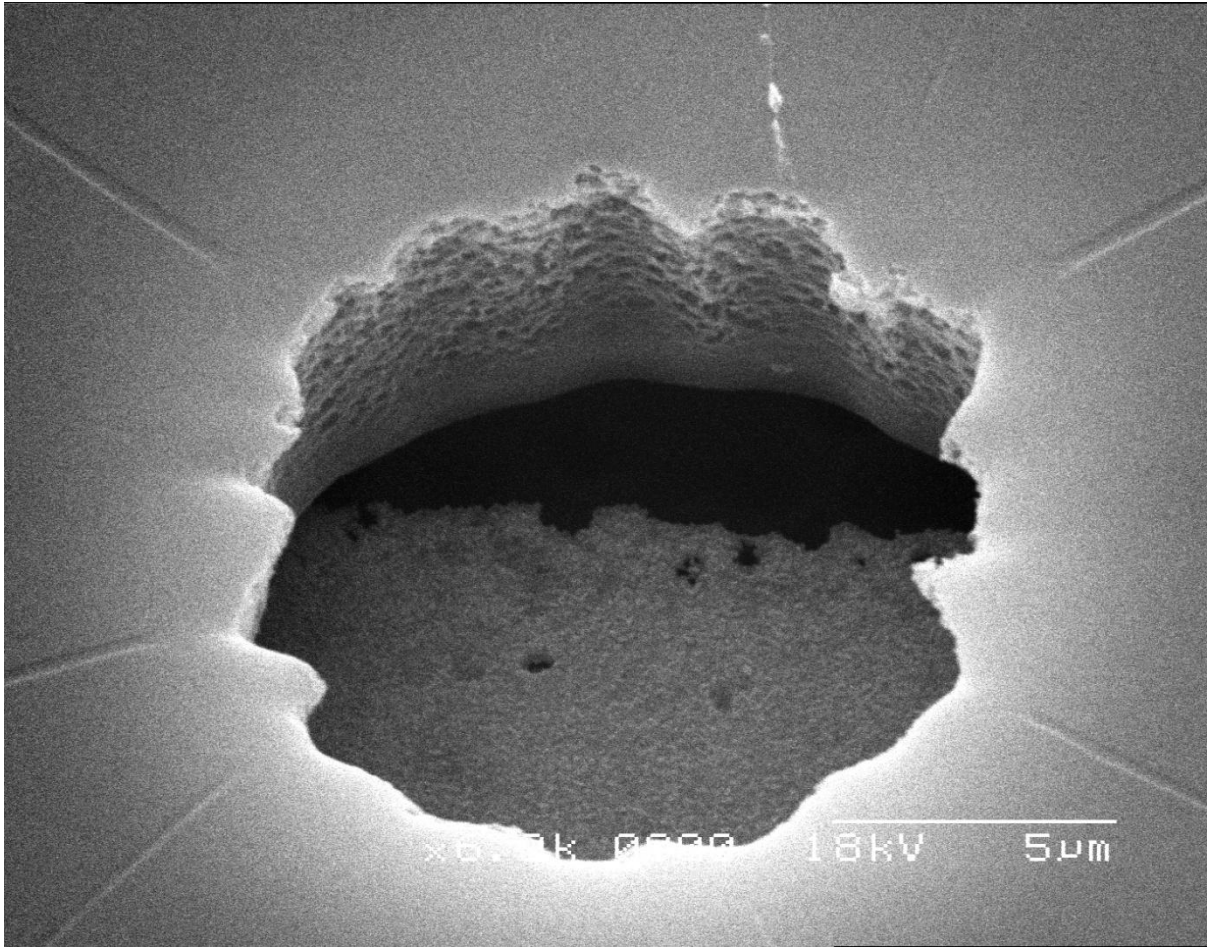


**Figure 2.15 – SEM images showing the pitting and cracking observed in metal tracks suspended underneath the SU-8 membrane, viewed through a patterned hole in the SU-8 membrane**

#### 2.2.2.2.2. *Polyimide based devices*

While SU-8 membrane devices offer a substantial improvement in sensitivity over silicon and glass devices, their reliance on a delicate silicon substrate limits their use and precludes real-time leaf-mounted sensing applications. To address this, polyimide was used to create a ~10  $\mu\text{m}$  thick self supporting substrate upon which the metal layers could be patterned to form the devices. A polyimide substrate offers a number of advantages, including:

- Very chemically stable and inert
- Good electrical insulator with a resistivity greater than  $10^{16} \Omega \text{ cm}$  and a dielectric breakdown field of at least  $2 \times 10^6 \text{ V cm}^{-1}$  [37]
- Low coefficient of thermal expansion of  $3 \text{ ppm } ^\circ\text{C}^{-1}$  [37], which prevents cracking of the metal layers during operation
- Heat resistance up to  $360 \text{ } ^\circ\text{C}$  [37]
- Biocompatibility [38]

As polyimide could be spin coated, the metallised areas were easily encapsulated by a thin (~2.5  $\mu\text{m}$ ) layer. This allowed the device to be used on a wide range of samples, as polyimide is very chemically inert, non-conducting and biocompatible. Thus, the device could be used to probe liquids, conducting surfaces and biological materials without the sample adversely affecting the performance. In addition, the very thin layers which were created ensured the devices were still thermally sensitive. These devices were also much more robust than previous iterations of the devices and the flexible nature and ability to encapsulate the sensing areas allowed calibration as described in Section 4.2.2.

SU-8 and polyimide have similar thermal conductivities ( $0.3 \text{ W m}^{-1} \text{ K}^{-1}$  [39] and  $0.1 \text{ W m}^{-1} \text{ K}^{-1}$  [37] respectively). As such, the device response for substrates of similar thickness should be broadly similar, although polyimide would be expected to show a slight improvement in sensitivity over SU-8. By contrast, silicon has a thermal conductivity of  $150 \text{ W m}^{-1} \text{ K}^{-1}$  [26] and so devices formed on bare silicon wafers had very poor thermal sensitivity. A comparison of all

three substrates is shown in Figure 2.16 and demonstrates the superior performance of polyimide ( $35.0 \text{ mV W}^{-1}$ ) over the SU-8 membrane and silicon based devices.

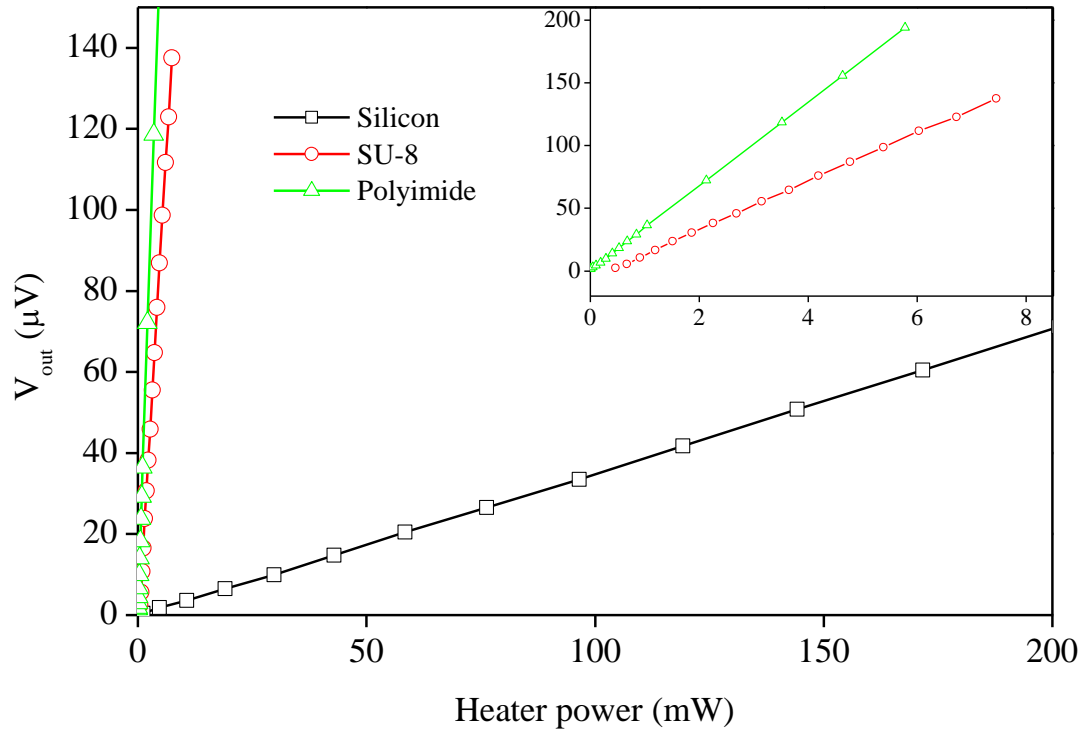


**Figure 2.16 – A comparison of the sensitivity of devices formed on silicon, SU-8 and polyimide. The TFTC was located  $50 \mu\text{m}$  from the heater on a Design A device. Inset shows the detail of the SU-8 and polyimide devices**

Both Design A and Design B patterns were used to form devices on polyimide substrates. However, Design B had specific design features incorporated to take advantage of the properties of polyimide. These devices were created with the aim of allowing leaf-mounted sensing and the design is discussed further in the following section. Photographs of Design A type polyimide devices are shown in Figure 2.17 and Figure 2.18 and details of the experimental operation of the devices are given in Chapters 4 and 6.

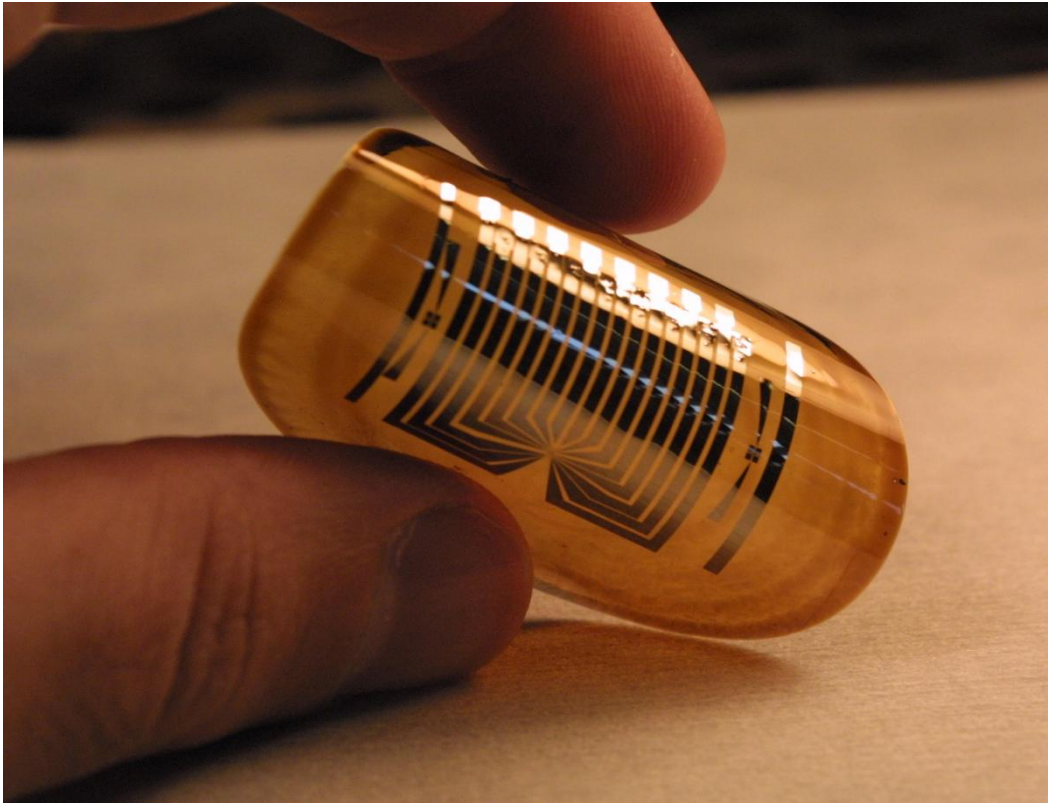


**Figure 2.17 – Photograph showing a Design A polyimide device**

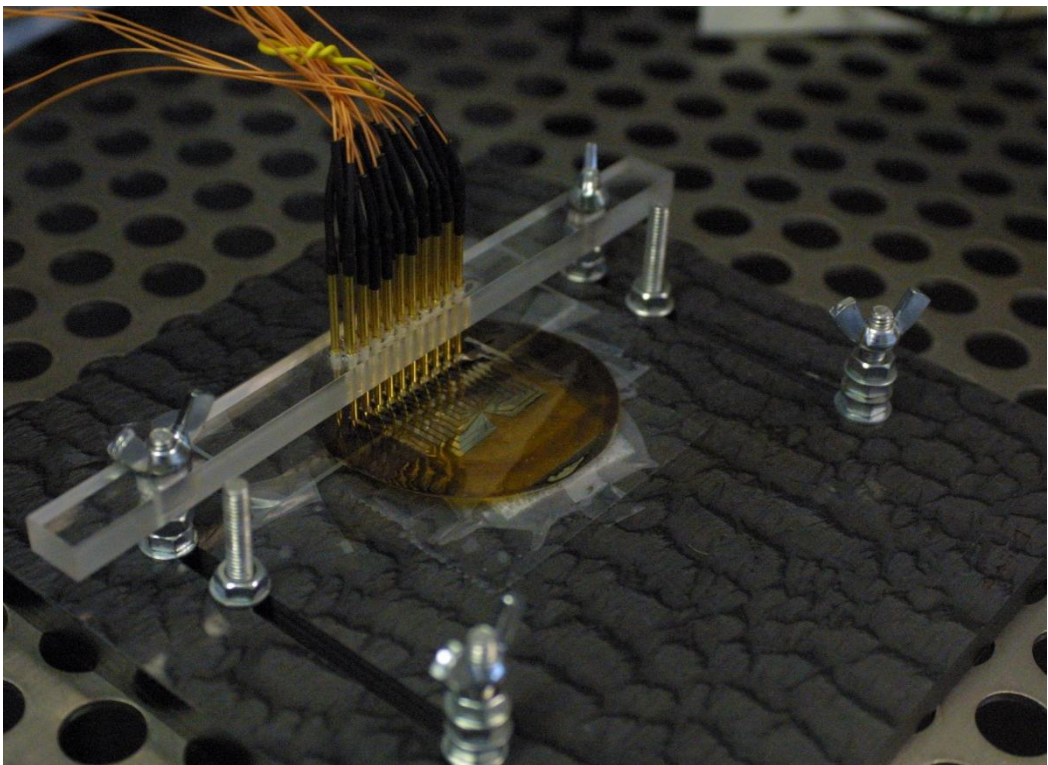


**Figure 2.18 – Photograph showing a Design A polyimide device with electrical connections made using the gold sprung-probe jig**

### 2.2.2.3. *Design B*

Design A was useful for demonstrating the principle of operation, however the reliance on a probing jig to make electrical connections limited its use. In addition, the shape of the resistive heater would not produce an even temperature distribution, potentially introducing geometrical inaccuracies. Design B was produced to overcome both of these limitations and allow a device to be created which could fully utilise the properties of the polyimide.

Design B incorporated a number of important design features (see Figure 2.20). Firstly, the layout of the pads used to make electrical connections was altered to allow a Molex connector to be used in place of the probing jig. This gave the device much more freedom, for example, allowing it to probe leaves attached to live plants. This would not be possible using the probing jig. Using an off the shelf connector also has implications for future work, as it is much cheaper and will allow several devices to be used simultaneously. A photograph of a Design B device is shown in Figure 2.19, highlighting the connection mechanism.

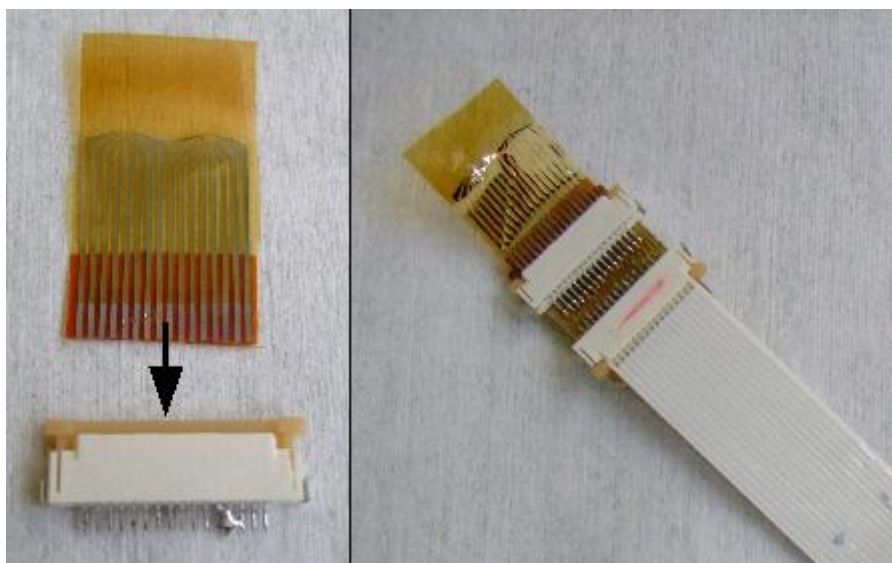


**Figure 2.19 – Photographs showing a Design B device and the Molex connector used to make electrical connections.**

Secondly, a circular heater geometry was adopted to ensure that a more consistent heat flow was achieved across the substrate and through the sample. Also, the arrangement of TFTCs around the heater was altered. Only two TFTCs were required to monitor the induced thermal gradient, although a third was located within the centre of the circular heater to monitor its temperature.

As the Molex connectors used were capable of making 16 connections, each substrate contained two sensors, each consisting of 3 TFTCs and a resistive heater. Each sensor was patterned with a circular heater and two TFTCs located at distances of 56  $\mu\text{m}$  and 166  $\mu\text{m}$  (from the nearest edge of the heater to the midpoint of the junction). The masks used to pattern the devices were produced with line widths of 12  $\mu\text{m}$ , offering improved spatial resolution from Design A, where line widths were 20  $\mu\text{m}$ . Reference junctions were at least 10 mm from the heater and experienced no heating as a result. All devices were fabricated from Cr / Ni with nominal thicknesses of Cr = 100 nm and Ni = 200 nm. The resistive heaters were patterned out of 200 nm thick Ni. Details of the design of the device are shown in Figure 2.20.

The flexibility of the polyimide substrate, in combinations with the flexible connection mechanism afforded by the Molex connector allowed Design B devices to be utilised for experimentation on plant leaves. Only Design B devices were used for these experiments. Details of the experiments conducted are given in subsequent chapters, with the design and substrate type given to indicate which combination was used. The following chapter outlines the fabrication methods used to create all the devices in this work.

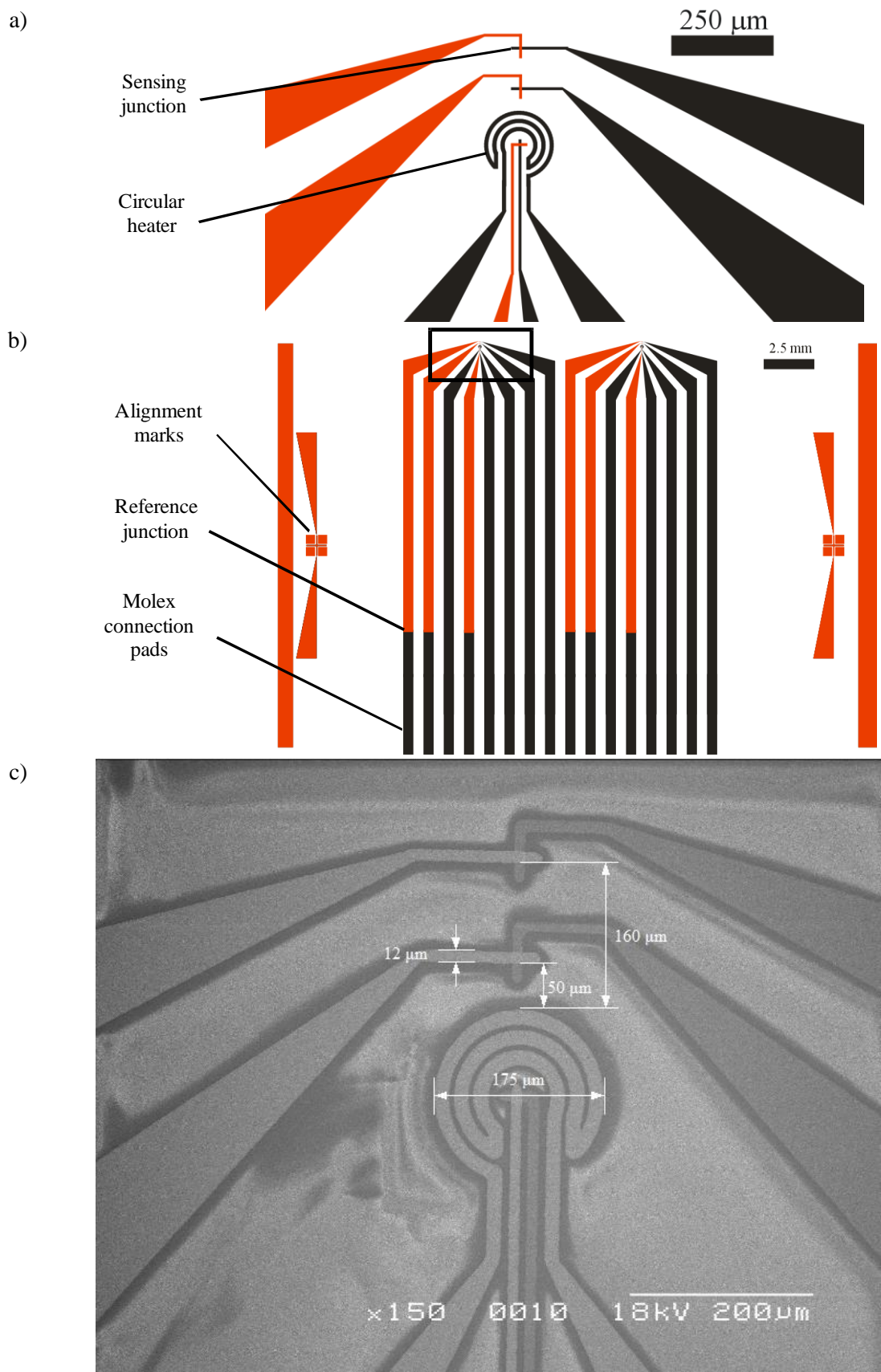


Figure 2.20 – Details of Design B: a) Detail of the sensing area (red tracks are Cr, black are Ni); b) View of the entire device, with the highlight area shown in detail in a) & c); c) Dimensioned SEM image of the sensing area

### 2.3. Conclusions

The aim of this work is to create a device which is capable of monitoring the thermal conductivity of a sample. As this is an intrinsic property of a material, thermal conductivity can be used to measure the composition of a mixture. Probing a material based on its thermal conductivity has the advantages that no direct electrical connections are required and it can be achieved without bulky or expensive equipment. By microfabricating the devices, they can operate on very small samples which will open up new applications. In particular, this work aims to show that thermal conductivity can be used to probe plant leaves in order to determine their water content.

The devices consist of a resistive heater with two TFTCs located at distances of less than 200  $\mu\text{m}$  from the heater. The difference in temperature recorded by the two TFTCs can be related to the thermal conductivity of the sample in contact with the device. TFTCs were chosen as temperature sensors as they are relatively easy to fabricate and do not suffer from size effects, if the lateral dimensions are larger than 1  $\mu\text{m}$ .

To improve the thermal sensitivity of the devices, they were formed on thin polymer substrates, two are described here: SU-8 membranes released from a silicon substrate and self-supporting polyimide substrates. Both the polymer substrates perform significantly better than the devices formed on a silicon substrate, due to the reduction in thermal mass surrounding the sensing area. The thermal sensitivities are compared in Table 2.2.

**Table 2.2 – A comparison of the sensitivity for 3 substrates used in this work**

<b>Substrate</b>	<b>Sensitivity (<math>\text{mV W}^{-1}</math>)</b>
Silicon	0.35
SU-8	19.3
Polyimide	35.0

Two metal patterns have been described which were used to form the active areas of the devices. Design A was used to pattern both SU-8 and polyimide substrates and consisted of a rectangular heaters with three TFTCs patterned at varying distances. Electrical connections made to this device relied on the gold sprung-probe jig outlined in Section 3.2.2. Design B was specifically

designed to take advantage of the properties of polyimide and consisted of a circular heater with two TFTCs patterned at two distances. These devices were designed to operate on more challenging and non-flat samples and electrical connections were made using Molex ribbon connectors. The following chapter outlines the fabrication processes used to create all the devices in this work.

## 2.4. References

1. **Gustavsson, M. and Gustafsson, S.E.** Thermal conductivity as an indicator of fat content in milk. *Thermochimica Acta*. 2006, 442, pp. 1-5.
2. **Dow Chemical Company.** True Coefficient of Thermal Conductivity of Glycerine-Water Solutions. [Online] [Cited: 7 May 2010.] <http://www.dow.com/glycerine/resources/table13.htm>.
3. **Tarara, J.M. and Ham, J.M.** Measuring Soil Water Content in the Laboratory and Field with Dual-Probe Heat-Capacity Sensors. *Agronomy Journal*. 1997 , Vol. 89, 4.
4. **Greswell, R.B., Riley, M. S., Alves, P.F. and Tellam, J.H.** A heat perturbation flow meter for application in soft sediments. *Journal of Hydrology*. 2009, Vol. 370, pp. 73-82.
5. **Phillipson, M.C. Baker, P.H. Davies, M. Ye, Z. McNaughtan, A. Galbraith, G.H. and McLean, R.C.** Moisture measurement in building materials: an overview of current methods and new approaches. *Building Services Engineering Research and Technology*. 2007, Vol. 28, 4, pp. 303-316.
6. **Government, HM.** *The Building Regulations 2000, Part L1A: Conservation of fuel and power*. 2010. 978 1 85946 324 6.
7. **Davidson, S.R.H. and James, D.F.** Measurement of thermal conductivity of bovine cortical bone. *Medical Engineering and Physics*. 2000, Vol. 22, pp. 741-747.
8. **Incropera, F.P. and DeWitt, D.P.** *Introduction to Heat Transfer*. 3. New York : Wiley, 1996.

9. **Wang, X., Xu, X. and Choi, S.U.S.** Thermal conductivity of nanoparticle–fluid mixture. *Journal of Thermophysics and Heat Transfer*. 1999, Vol. 13, 4, pp. 474-480.
10. **Muramatsu, Y., Tagawa, A. and Kasai, T.** Thermal Conductivity of Several Liquid Foods. *Food Science and Technology Research*. 11, 2005, Vol. 3, pp. 288-298.
11. **Suleiman, B.M.** Effective thermal conduction in composite materials. *Applied Physics A*. 2010, pp. 223-228.
12. **Williams, C.C. and Wickramasinghe, H.K.** Scanning thermal profiler. *Applied Physics Letters*. 1986, Vol. 49, 23.
13. **Harding, L. Wood, J. Reading, M. and Craig, D.Q.M.** Two- and Three-Dimensional Imaging of Multicomponent Systems Using Scanning Thermal Microscopy and Localized Thermomechanical Analysis. *Analytical Chemistry*. 2007, Vol. 79, pp. 129-139.
14. **Haeberle, W. Pantea, M. and Hoerber, J.K.H.** Nanometer-scale heat-conductivity measurements on biological samples. *Ultramicroscopy*. 2006, Vol. 106, pp. 678–686 .
15. **Brown, E. Hao, L. Gallop, J.C. and Macfarlane, J.C.** Ballistic thermal and electrical conductance measurements on individual multiwall carbon nanotubes. *Applied Physics Letters*. 2005, Vol. 87.
16. **Mattsson, C.G. Thungström, G. Bertilsson, K. Nilsson, H. and Martin, H.** Design of a Micromachined Thermopile Infrared Sensor With a Self-Supported SiO/SU8 Membrane. *IEEE Sensors Journal*. 2008, Vol. 8, 12, pp. 2044-2052.
17. **Holdgate, G. A. and Ward, W. H. J.** Measurements of binding thermodynamics in drug discovery. *Drug Discovery Today*. 2005, Vol. 10, 22, pp. 1543-1550.
18. **Schumer, D. Breuer, U. Harms, H. and Maskow, T.** Thermokinetic Analysis Reveals the Complex Growth and Haloadaptation Pattern of the Non-Conventional Yeast *Debaryomyces hansenii*. *Engineering in Life Sciences*. Vol. 7, 4, pp. 322-330.

19. **Maskow, T. and Harms, H.** Real Time Insights into Bioprocesses Using Calorimetry: State of the Art and Potential. *Engineering in Life Sciences*. 2006, Vol. 6, 3, pp. 266-277.
20. **Ahrens, R. and Schlote-Holubek, K.** A micro flow sensor from a polymer for gases and liquids. *Journal of Micromechanics and Microengineering*. 2009, Vol. 19.
21. **General Electric.** Thermocouples & Thermocouple wire. [Online] [Cited: 25th April 2011.] <http://www.thermometrics.com/assets/images/thermcpl.pdf>.
22. **Zhang, X. Choi, H. Datta, A. and Li, X.** Design, fabrication and characterization of metal embedded thin film thermocouples with various film thicknesses and junction sizes. *Journal of Micromechanics and Microengineering*. 2006, Vol. 16, pp. 900-905.
23. **Childs, P.R.N. Greenwood, J.R. and Long, C.A.** Review of temperature measurement. *Review of Scientific Instruments*. 2000, Vol. 71, 8.
24. **White, D. R., Galleano, R., Actis, A., Brixy, H., de Groot, M., Dubbeldam, J., Reesink, A. L., Edler, F., Sakurai, H., Shepard, R. L. and Gallop, J. C.** The Status of Johnson Noise Thermometry. *Metrologia*. 1996, 33, pp. 325-335.
25. **Murphy, A. B. and Farmer, A. J. D.** Temperature Measurement in Thermal Plasmas by Rayleigh Scattering. *Journal of Physics D: Applied Physics*. 1992, 25, pp. 634–643.
26. **Mattsson, C.G., Thungstrom, G., Bertilsson, K., Nilsson, H.L. and Martin, H.** Fabrication and evaluation of a thermal sensor formed on a thin photosensitive epoxy membrane with low thermal Conductivity. *Journal of Physics: Conference Series*. 2008, 100.
27. **Kasap, S.O.** *Principles of Electronic Materials and Devices*. New York : McGraw-Hill, 2006.
28. **Foiles, C.L.** *Thermopower of pure metals and dilute alloys*. New York : Springer, 1985.

29. **Buchner, R. Sosna, C. Maiwald, M. Benecke, W. & Lang, W.** A high-temperature thermopile fabrication process for thermal flow sensors. *Sensors and Actuators A*. 2006, 130, pp. 262-266.
30. **Chancellor, E.B. Wiksw, J.P. Baudenbacher, Radparvar, F. M. and Osterman, D.** Heat conduction calorimeter for massively parallel high throughput measurements with picoliter sample volumes. *Applied Physics Letters*. 2004, Vol. 85, 12.
31. **Kreider, K. G., Ripple, D. C. and DeWitt, D. P.** Calibration of Thin-Film Thermocouples on Silicon Wafers. *TEMPMEKO '99, The 7th International Symposium on Temperature and Thermal Measurements in Industry and Science*. 1999.
32. **Salvadori, M.C. Vaz, A.R. Teixeira, F.S. Cattani, M. and Brown, I.G.** Thermoelectric effect in very thin film Pt/Au thermocouples. [Online] [Cited: 25th April 2011.] <http://www.osti.gov/bridge/servlets/purl/889625-J2aoMi/889625.pdf>.
33. **Zhang, S. Sun, D. Fu, Y. Du, H. and Zhang, Q.** Effect of sputtering target power density on topography and residual stress during growth of nanocomposite nc-TiN/a-SiNx thin films. *Diamond & Related Materials*. 2004, Vol. 13, pp. 1777-1784.
34. **Randjelovic, D. Petropoulos, A. and Kaltsas, G.** Multipurpose MEMS thermal sensor based on thermopiles. *Sensors and Actuators A*. 2008, Vol. 141, pp. 404-413.
35. **Jeon, S. Oh, M. Jeon, H. Hyun, S. and Lee, H.** Effects of post-annealing on thermoelectric properties of bismuth–tellurium thin films deposited by co-sputtering. *Microelectronic Engineering*. 2011, Vol. 88, 5, pp. 541-544.
36. **Atherton, J.J, Rosamond, M.C. Johnstone, S. and Zeze, D.A.** Thermal characterisation of micro-litre volumes using a thin film thermocouple based sensor. *Sensors and Actuators A*. 2011, Vol. 166, pp. 34-39.
37. **HD MicroSystems.** *Product Bulletin: PI-2600 Series - Low Stress Polyimides*. 2008.

38. **Rousche, P.J., Pellinen, D.S., Pivin, D.P., Williams, J.C., Vetter, R.J. and Kipke, D.R.** Flexible Polyimide-Based Intracortical Electrode Arrays with Bioactive Capability. *IEEE Transactions on Biomedical Engineering*. 2001, Vol. 48, 3, pp. 361-371.
39. **MicroChem.** SU-8 Table of Properties. [Online] [Cited: 3rd October 2011.] <http://www.microchem.com/pdf/SU-8-table-of-properties.pdf>.

This chapter focuses on the practicalities of fabricating the devices, the probing jigs used to make electrical connections and the interface electronics. It begins with a detailed description of the microfabrication processes required to form the devices. In particular, there are sections devoted to the metallisation and patterning processes which are used to form the functional areas of the device. The patterning process relied upon a lift-off technique which had to be developed and the details of this development are given in Section 3.1.2. Due to the thin film nature and deposition method of the metals which form the device, bulk material properties were not observed for the device during operation. These effects are discussed before micromachining processes required to create the SU-8 and polyimide devices are described.

Three distinct types of devices were developed during this project. Early devices were used to develop the processes required to form basic devices and these were fabricated on oxidised silicon wafers or glass microscope slides. As such, they suffered from having a large thermal mass and poor sensitivity, however they were useful for developing the metallisation and patterning processes. In order to reduce the thermal mass of the substrate, the sensing areas of the device were formed on a suspended SU-8 membrane which improved the sensitivity. However,

these devices proved too delicate during operation. Fabrication details are given in Section 3.1.4 for the SU-8 devices. The final type of device was formed on a polyimide substrate, giving the thermal isolation required, whilst also being flexible and robust enough to operate on the leaves of a plant. Fabrication details for the polyimide devices are given in Section 3.1.5.

The final sections of this chapter focus on the jigs required to make electrical connections to the devices. Initially a probe station was used to test early devices, however this proved to be unsuitable for making electrical connections as the devices developed and a gold sprung pin jig was created to allow prototype devices to be tested. The final iteration of the connection method was a commercially available Molex ribbon connector, which allowed the device to be used whilst clamped to the leaf of a plant. The last sections discuss the control electronics used to condition the electrical signals and the chapter ends with a conclusion section.

### **3.1. Device fabrication**

Thermocouples are widely used as cheap and easy to use thermometers, particularly in applications which require the ability to monitor high temperatures. The basic principle for fabricating commercially available thermocouples has changed little since their introduction: two dissimilar wires are welded together (the welding simply forms a good electrical connection) at two points to form the sensing and reference junction. The reference junction is held at a known temperature while the sensing junction measures an unknown temperature. The potential difference generated across a gap in this circuit can be related to the unknown temperature. In all applications other than for very high accuracy calibration thermocouples [1], cold junction compensation is used where electronic compensation replaces the need to hold the reference junction at a known temperature.

Various ‘types’ of thermocouples are available commercially, with the wires of each ‘type’ being formed from a different pair of alloys. This gives each ‘type’ a known response, which is covered by international standards and reference tables (e.g. type-K thermocouples are covered by BS EN

60584-1). Commercial thermocouples are available in a variety of wire diameters, lengths and protective casings.

Thermocouples can also be formed from thin films of metal, so called thin-film thermocouples (TFTCs). TFTCs allow microfabrication processes to be used to pattern the thermocouples with very high spatial resolution [2], [3] and very fast response times e.g.  $\sim 1 \mu\text{s}$  [4]. It has even been suggested that carbon nanotubes [5] and DNA [6] exhibit thermoelectric effects, which would allow thermocouples to be formed with a spatial resolution of only a few nms. However such devices would suffer a number of practical constraints, limiting their application.

Lithographic patterning allows thin film metal layers to be patterned with very small features, with optical methods capable of reaching  $< 100 \text{ nm}$  resolution [7], while electron beam lithography can write lines with widths of  $2 - 5 \text{ nm}$  [8]. The limits on the resolution available for this project arise from the production of a mask, but line widths of around  $12 \mu\text{m}$  have been achieved. While this is a long way from the state of the art, it does allow heaters and TFTCs to be created at a scale beyond that seen using traditional discrete components. In particular, the photolithographic method allows both the heater and thermocouples to be precisely patterned in relation to each other. Figure 3.1 shows a comparison between a standard thermocouple and the microfabricated TFTCs used in this work.

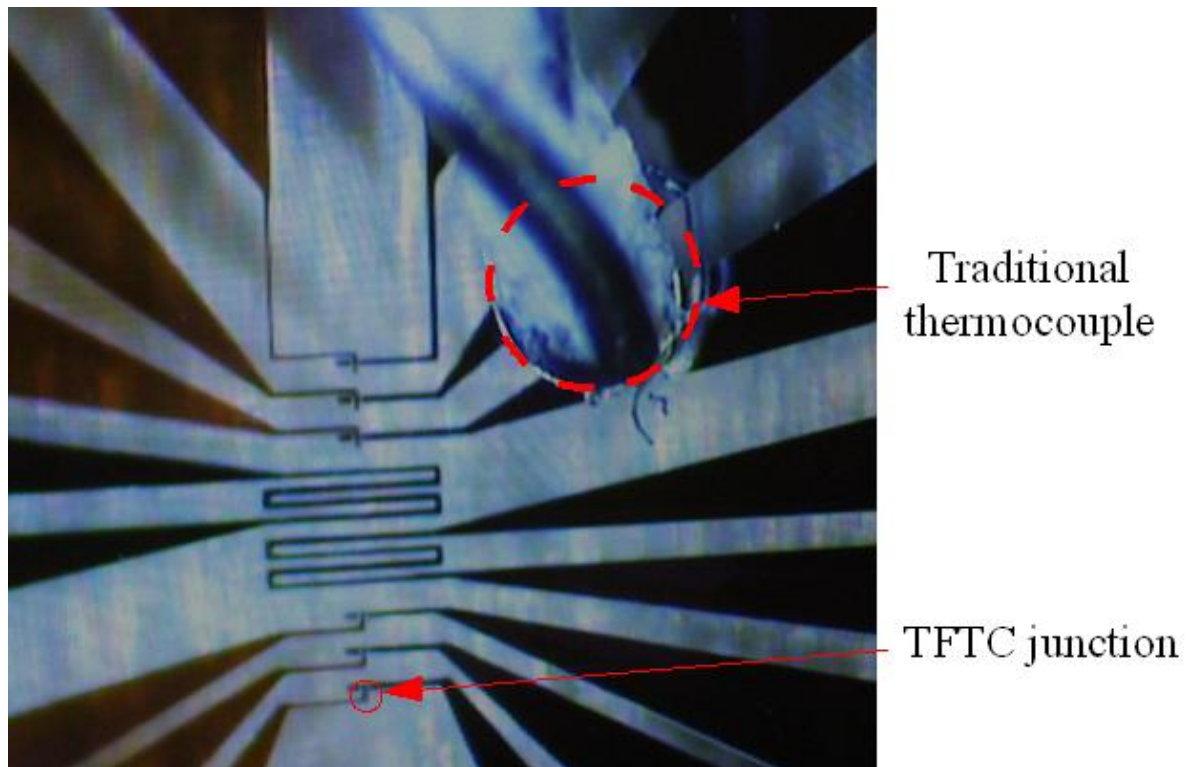


**Figure 3.1 – A photograph showing a traditional thermocouple alongside a Design A TFTC device**

While traditional wire thermocouples are self supporting, TFTCs require a substrate which provides structural support. This substrate is likely to dominate the thermal response of the TFTC. To improve the sensitivity of such devices, the substrate can be micro-machined to reduce the thermal mass. Common designs include stress compensated membranes or cantilevers formed out of silicon nitride / silicon oxide [9] [10] while polymer substrates such as SU-8 [11] and polyimide [12] are also popular.

Four substrates have been used in this work: glass microscope slides, 2” oxidised silicon wafers, SU-8 membranes and polyimide. The silicon and glass substrates were used in early devices due to the simplicity of fabricating devices on these. However they demonstrated poor sensitivity of  $0.35 \text{ mV W}^{-1}$ . Early devices were not calibrated, so a  $\text{mV } ^\circ\text{C}^{-1}$  value was not obtained, however a comparison was made between devices by applying a known input to the heater and monitoring the response of a thermocouple situated at a known distance from the heater. By way of a comparison, devices suspended on an SU-8 membrane increased the sensitivity of the device to  $19.3 \text{ mV W}^{-1}$ . The SU-8 devices showed promise in terms of improved sensitivity, however they were found to be too delicate for use on most samples.

Polyimide devices were used in the final iteration, as the flexible substrate can be formed with a thickness of around 10  $\mu\text{m}$ . This provided good thermal isolation of the device to improve sensitivity, whilst providing a suitably robust device which was capable of operating on samples such as plant leaves. Polyimide devices resulted in a sensitivity of 35.0  $\text{mV W}^{-1}$  due to the better insulating properties of polyimide over SU-8. Polyimide also allowed encapsulation of the sensing area of the device by spinning a 2.5  $\mu\text{m}$  thick layer of polyimide. This ensured the device was electrically isolated from the sample. Polyimide also offers number of other advantages, including biocompatibility, robustness and chemical resistance.

Details of the device designs can be found in Section 2.2.2. The following section describes the metallisation and patterning processes used to form basic devices on simple silicon or glass substrates. The subsequent sections give specific details about the additional fabrication processes required to create the SU-8 and polyimide substrates upon which the basic patterning processes could be used on.

### **3.1.1. Metallisation and patterning**

This section details the metallisation and patterning stages required to form the active area of a device on a 2" silicon substrate. This is the simplest of the devices produced during this work, with the SU-8 and polyimide devices requiring extra processing stages to modify the substrate. The oxidation and priming stages described below are not required for polyimide, however the other steps were identical when metalizing the SU-8 and polyimide devices, once the substrate had been appropriately prepared.

Figure 3.2 gives an overview of the processing steps required to metallise and pattern two layers of metal. Each stage is described in detail following.

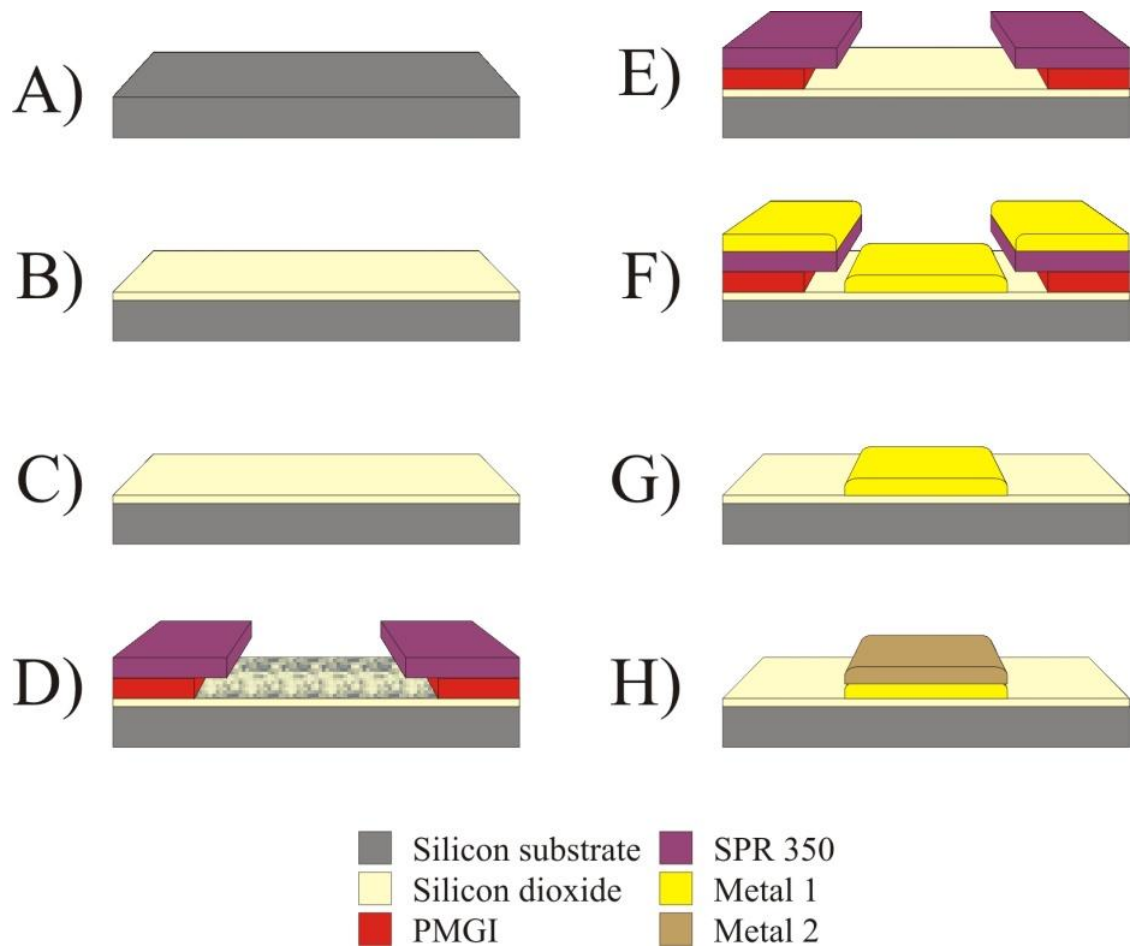


**Figure 3.2 – Fabrication stages required to form a device on a silicon substrate: A) Wafer cleaning; B) Oxidation of the wafer; C) Hexamethyldisiloxane Priming; D) Photolithography; E) RIE de-scum; F) Deposition of metal 1; G) Lift-off & H) Repeat C-G for metal 2**

### *A) Wafer cleaning*

Before any processing was done on the silicon wafer, it was cleaned. This began with ultrasonic cleaning in a mixture of one part Decon 90 to 10 parts de-ionised water (DI water) to remove any particulate contamination, followed by ultrasonic cleaning in acetone and then 2-propanol (IPA). To remove any organic compounds, the wafer was subjected to a piranha etch (1:1 sulphuric acid: hydrogen peroxide). For silicon and SU-8 devices, the wafer required the growth of an insulating oxide layer. Silicon forms a  $\sim 20 \text{ \AA}$  native oxide layer in air [13], which was stripped with a hydrofluoric acid etch (10:1 DI water : hydrofluoric acid) before the thicker oxidation processes were completed.

The cleaning steps outlined above are critical, as they ensure that the oxide layer that is subsequently formed is complete and uniform. In addition, poorly cleaned wafers result in poor adhesion of the photoresist, polymer and metal layers, which would lead to cracking, delamination and poor yields or failure of the device.

### ***B) Oxidation of the wafer***

For both silicon and SU-8 membrane devices, the underlying silicon wafer required oxidation to form an insulating layer. This was achieved using thermal oxidation. The wafer was loaded into an oxidation furnace which was pre-heated to 1050 °C and the wafer was allowed to match the temperature of the furnace in an inert nitrogen atmosphere for 10 min. Dry oxygen was introduced at a rate of 3 l min<sup>-1</sup> for 10 min to grow a high quality seed layer. The bulk of the oxide thickness was achieved by wet oxidation as this can achieve growth rates around 100 times faster than by dry oxidation [14]. Oxygen was passed through a water bath heated to near its boiling point before being introduced to the furnace, in order to introduce water to the reaction. The wet oxidation lasted for 90 min, producing an oxide thickness of around 750 nm. To finish the process the wafer was dry oxidised for 10 min before removal from the furnace. This stage was not required for polyimide devices, as the polyimide substrate was removed from the silicon carrier wafer.

### ***C) Hexamethyldisiloxane priming***

Photoresists often do not adhere well to a silicon wafer, particularly if the wafer has been subjected to humid or wet conditions [13]. As well as dehydration of the surface by baking at 120 °C – 200 °C, a hexamethyldisiloxane (HMDS) priming step helps to dehydrate the surface prior to application of a photoresist. This step causes the surface of the silicon to become hydrophobic and improves the photoresist adhesion.

The HMDS priming step causes a process called silylation to occur, in which reactive Si-NH-Si functional groups in the HMDS react with the oxide surface (Figure 3.3), leaving the methyls to bond to the photoresist [13]. To prime the surface, the wafer was baked on a hot plate at 200 °C

for 2 min before being suspended over a few drops of HMDS in an enclosed volume formed by an upturned beaker. The wafer was then returned to the hot plate for a further 1 min. It was found that the surface could be over primed if too much HMDS was applied. This prevented the photoresist from adhering to the surface, leading to areas of the substrate not being coated.

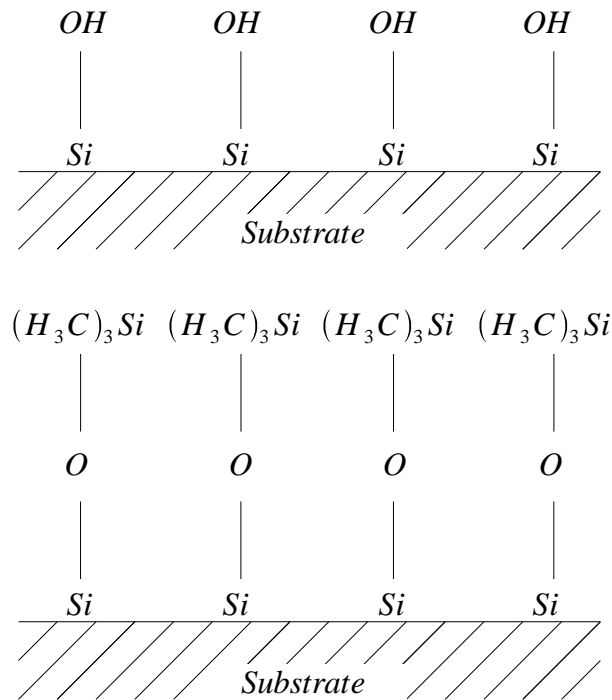


**Figure 3.3 – A schematic representation of the silylation process. Adapted from [15]**

#### ***D) Photolithography***

It was decided that using a lift-off process would provide superior results over an etching process, as two dissimilar metal layers were required. Etching the second metal layer could damage or alter the chemistry of the first. A bi-layer lift-off process was used: firstly a polymethylglutarimide (PMGI) layer was spun followed by a photo-definable layer of Megaposit SPR 350 1.2 (Rohm and Haas). This was exposed using a mask aligner (EVG 620, EV Group GmbH) and developed using Microposit MF-319 Developer (Shipley). Further details of the photolithographic steps and the development of a suitable lift-off profile are detailed in Section 3.1.2.

### ***E) Reactive Ion Etch (de-scum)***

The photolithographic steps defined area of the substrate where the subsequent metallisation processes would deposit metal. However, these areas required a de-scum step in order to remove any remaining traces of photoresist and provide a clean surface for the metal to adhere to. This is achieved using a plasma etch (Plasma Lab 80+, Oxford). The remaining patterned regions of photoresist would be thinned during the de-scumming process, however this has minimal effect if a low power and short time are used. The parameters used are set out in Table 3.1.

**Table 3.1 – Process parameters used for de-scum plasma etch**

<b>Parameter</b>	<b>Value</b>
Oxygen pressure	150 mT
Oxygen flow rate	50 sccm
Power	70 W
Platen	Quartz
Platen temperature	20 °C
Time	60 s

### ***F) Metal 1 Deposition***

A majority of the devices were metallised using sputter deposition (Minilab, Moorfield). Some of the early devices were produced by electron beam (e-beam) deposition, but these devices suffered from severe cracking issues. Further details of the two methods and the benefits of sputter deposition are given in Section 3.1.3.1.

The metals chosen for the devices were Cr and Ni as this combination gave the highest combined bulk Seebeck coefficient ( $\alpha$ ) out of the metals available ( $\alpha_{Cr} = 21.7 \mu\text{V K}^{-1}$ ,  $\alpha_{Ni} = -19.24 \mu\text{V K}^{-1}$  [16]). The Cr layer was deposited first, as it readily forms an oxide layer and thus adheres well to an oxidised silicon substrate. This ensured that the first metal layer was robust enough to survive subsequent processing. Both the Cr and Ni layers were found to adhere well to polyimide substrates.

The thickness of the metal layers was kept at 100 nm or above to achieve near-bulk Seebeck coefficients (see Section 3.1.3.2). Cr was deposited to a thickness of ~100 nm, while Ni was subsequently deposited to a thickness of ~200 nm to ensure that the Ni overlapped the Cr layer to give electrical continuity. The process conditions used for sputtering are given in Table 3.2.

**Table 3.2 – Process parameters used for sputter deposition**

<b>Parameter</b>	<b>Value</b>
Argon pressure	2 mT
Argon flow rate	5 sccm
Maximum deposition rate	5 Å s <sup>-1</sup>
Substrate bias	0 V

***G) Lift-Off***

Once the metal had been deposited, the photoresist was removed in Microposit Remover 1165 (Shipley). 1165 dissolves both the SPR 350 and the PMGI layers, causing the metal to “lift-off” from the substrate, leaving metal only in the areas not covered by photoresist during deposition. Once the 1165 had stripped all the photoresist, the wafer was placed in acetone and sonicated for 2 min, before rinsing in IPA and DI water.

***H) Repeat C-F for metal 2***

Stages C-F were repeated to deposit the second metal, with careful alignment during the photolithographic stage to ensure that the second metal layer was correctly positioned.

The active areas of all devices were patterned using the process outlined above, although different designs were used. In order to improve the performance of the device, the silicon substrate was replaced by an SU-8 membrane or polyimide. These polymer substrates offered a much lower thermal mass around the sensing area of the device and so improved the thermal sensitivity of the device. The extra processing stages required to form these substrates are described in Sections 3.1.4 & 3.1.5.

### **3.1.2.Lift-off trials**

#### **3.1.2.1. Introduction**

Photolithographic methods offer two discrete methods for patterning metal layers. The first method involves etching a previously deposited metal through holes defined in a layer of photoresist. The second option is to deposit the metal over an already patterned layer of photoresist and then remove the photoresist layer, leaving only the metal deposited through the holes. This process is known as lift-off, as the metal deposited over the photoresist ‘lifts off’ from the substrate and is removed. While lift-off processing requires greater process control and extra processing stages to create a suitable photoresist profile to aid lift-off, it offers the advantage that etchants are not required. Etching the second layer could damage the first metal layer which was previously patterned. Etching also precludes the use of certain combinations of metals and substrates.

It was necessary to develop a lift-off technique which was suitable for use with the metals required during this project which utilised the materials and equipment available. This chapter discusses the requirements of a lift-off profile and the development of a suitable technique to produce a reliable process for patterning the devices. Initially, a single layer of photoresist was used, with additional processing steps introduced to produce an inhibition layer in the top of the photoresist, which developed more slowly than the bottom, uninhibited region, leading to a T-shaped profile. However, this process was found to be unreliable, so a bi-layer process was adopted which was more reliable and produced a profile with a much larger overhang.

#### **3.1.2.2. Lift-off profile**

The lift-off technique relies on a solvent dissolving a layer of photoresist which has been patterned before a metal layer is deposited over the top. To ensure that the solvent can access the photoresist, a distinct ‘overhang’ profile is required at the edges of the photoresist to prevent the metal coating the side walls of the photoresist and forming a continuous layer. To achieve this profile, the process conditions must be altered and optimised to create a suitably large overhang

without compromising the integrity of the photoresist or reducing the resolution of the pattern which can be obtained.

To discuss the profile which is required, it will be assumed that a line structure is required. For this, the ideal photoresist profile will be T-shaped, with the base of the structure being smaller than the top, creating an overhang (Figure 3.4 A). If a metal layer is deposited anisotropically over such a structure, a discontinuity is formed between the metal on the substrate and the metal covering the photoresist as it cannot coat the side wall of the photoresist. This discontinuity allows a solvent to penetrate the metal layer and dissolve the photoresist during the lift-off stage. The process developed here can even be used for sputtering of metals, which is a more isotropic deposition method than other processes available, such as e-beam deposition or thermal evaporation.

Without optimisation, such a T-shaped profile will not be achieved. Figure 3.4 B-F shows a number of sub-optimal profiles which can be generated:

B) Over exposure leads to the line width of the being reduced and the size of the resulting structure will be smaller than the mask, potentially leading to small features being lost.

C) Generating an overhang which is too large compromises the structure and can lead to photoresist features collapsing.

D) Generating an overhang which is too small, or even vertical may allow metal to be deposited on the side walls of the photoresist. This can lead to 'ears' forming when the metal side wall shears during lift off or, in the worst case, this can entirely prevent the solvent from dissolving the photoresist.

E) Generating an inhibition layer (the top of the 'T') which is too large, limits the thickness of metal which can be deposited.

F) 'Kickback' (the base extending beyond the overhang) at the bottom of the profile can lead to metal being deposited partially up the side walls of the photoresist, again allowing 'ears' to form when the metal shears during lift-off.

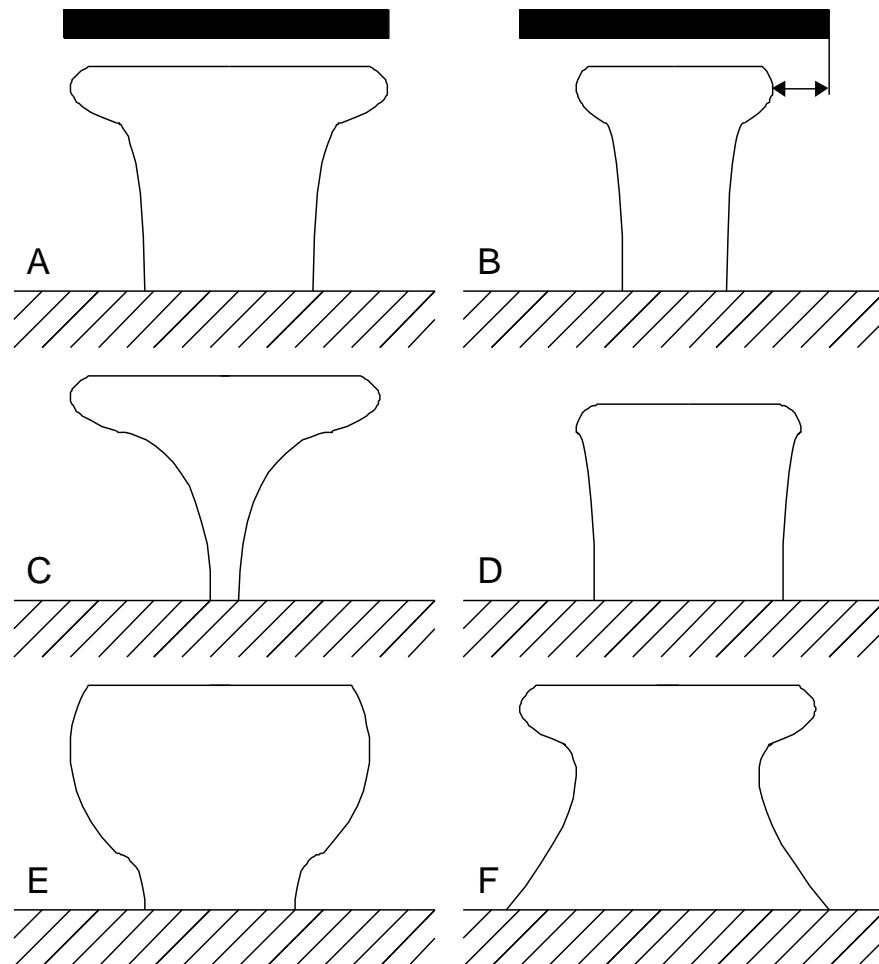


Figure 3.4 – Photoresist profiles for lift-off. A) shows the ideal profile while B) to F) show defective profiles

### 3.1.2.3. Single layer process

A process based on a single layer of positive photoresist was initially developed. The photoresist used was Megaposit SPR 350 1.2 (Rohm and Haas). SPR 350 is a positive photoresist which is responsive to i-line and g-line exposure wavelengths and is developed using Microposit MF-319 Developer (Shipley). In order to use a single layer of positive photoresist to create a lift-off profile, the standard photoresist processing parameters were altered. Without alteration, the

positive photoresist that was used would give vertical or sloping side walls with no overhang. This would lead to metal ‘ears’ forming and a ragged line edge would be achieved.

To create a lift-off profile, the photoresist required over-exposure and over-development. An extra stage to the process was also required which created an inhibition layer in the top proportion of the photoresist. This layer was chemically altered to render it less soluble than the unaltered resist beneath. The less soluble top is dissolved by the developer more slowly, creating the desired T-shaped profile.

To create the inhibition layer, the photoresist was soaked in the developer before soft baking and the subsequent exposure. This creates an inhibition layer as the developer is mostly tetramethylammonium hydroxide (TMAH), which catalyses the creation of azodyes on the surface of the photoresist [17]. This makes the photoresist less soluble, however the TMAH only penetrates about 100 nm into the far into the photoresist [18]. During development the less soluble top layer develops at a slower rate, leading to an overhanging, T-shaped structure as can be seen in Figure 3.5.

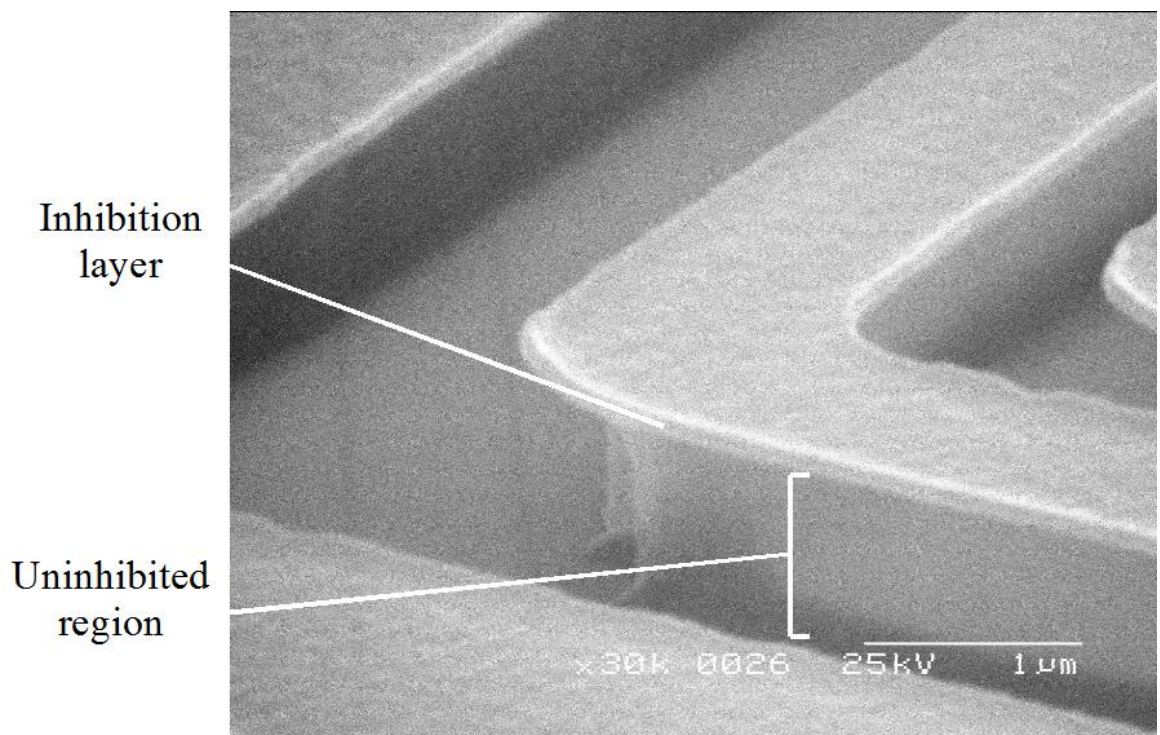


Figure 3.5 – SEM image of a line (with 90° bend) after processing using a single layer lift-off profile process

When optimised, the single layer process was capable of creating an overhang of around 300 nm, however the size of the overhang and resultant line width was found to be unreliable, as it was strongly influenced by the quality of the contact between the photoresist and the mask during UV exposure, the development time and the pre-bake soak time. Also, the inhibition layer tended to curl when metal was deposited as it was such a thin layer which led to variations in the line width of the deposited metal (shown in Figure 3.6). The curling was due to tensile stresses forming in the metal during deposition [13].



**Figure 3.6 – An SEM showing a 500 nm layer of Ni (e-beam deposited over a line feature formed using the single-layer lift-off process) which caused curling of the photoresist**

The optimised single-layer process is detailed in Table 3.3. All trials were run on clean 2” silicon wafers. To improve photoresist adhesion, each wafer was subjected to a HDMS prime, as described in Section 3.1.1. The photoresist was spun at 500 rpm to evenly distribute it across the wafer before the spin speed was increased to 3700 rpm for 30 s to achieve a thickness of around 1.2 µm. Before a soft bake on a hot plate, an inhibition layer was created by soaking the photoresist in developer (MF 319, Shipley). The photoresist was then exposed under UV using a mask aligner (EVG 620, EV Group GmbH). The photoresist was then developed in MF 319 after a post exposure bake.

**Table 3.3 – Process parameters used for creating a Single-Layer lift-off profile**

<b>Process</b>	<b>Condition</b>	<b>Time</b>
Dehydration bake (+HDMS prime for silicon substrates)	200 °C	>10 mins
Spin SPR 350 1.2	500 rpm	15 s
Spin SPR 350 1.2	3700 rpm	30 s
Soak in developer	MF 319	2 mins
Soft bake	95 °C	5 mins
Expose		4.5 s
Post exposure bake	95 °C	3 mins
Develop	MF 319	45 s

A more robust bi-layer process was developed and this process was used to fabricate the devices for all but the initial prototype devices.

#### **3.1.2.4. Bi-layer process**

A bi-layer lift-off process utilises two resist layers with different rates of dissolution. The top layer is photo-definable, while the bottom layer has a faster rate of dissolution, thus creating an overhanging structure. The benefit of this method is that the rate of dissolution is a function of the material and so is much more reliable than in the single layer process, where the rate of dissolution is a function of several processing steps.

SPR 350 1.2 was used as a photo-definable top layer, while polymethylglutarimide SF 9 (PMGI, Chestech) was used as a base layer. PMGI is not photo-definable, however it dissolves readily in MF-319 – the developer used with SPR 350 1.2. Thus the photo-definable layer was used to create a pattern and once the developer penetrated the SPR 350 1.2, it dissolved the PMGI layer more quickly, creating an undercut and producing a T-shaped profile.

The bi-layer process has the advantages that the thickness of each layer is easily controlled by the speed they are spun at and the overhang is controlled by the development time and exposure dose. For example, the spin speed curves are available for SPR 350 1.2 from its datasheet [19]. The follow sections detail trials that were run to gauge the optimum process conditions. Two factors are particularly important in controlling the size of the overhang created: the development time and the exposure time.

#### **3.1.2.5. Development time**

The development time will define the size of the overhang generated using the bi-layer process. Increasing the development time will increase the size of the undercut created. Trials were required to ascertain the optimal development time, which gave a suitable overhang without causing the top layer to collapse, or become overdeveloped, decreasing the feature sizes.

A light field mask with 7  $\mu\text{m}$  dots and the exposure dose was fixed at 3 s. Development times ranged from 1 to 4 minutes. The result of the trial is shown in Figure 3.7. 1 minute was around the minimum development time, below this time, the SPR 350 1.2 did not develop fully, so no overhang was created and the photoresist remained in some areas. A peak in the size of the overhang is seen with a development time of around 2 minutes. Increasing the development time further reduced the overhang as the SPR 350 1.2 layer began to become over developed, while the PMGI layer could not develop further due to diffusion limiting the etch rate in the overhang region.

At 2 minutes, there is a steep roll-off in the size of the overhang if the bi-layer is underdeveloped, whereas over development has a more gentle roll-off. Thus, a development time of 2.5 minutes was chosen for device processing to ensure that the overhang was generated.

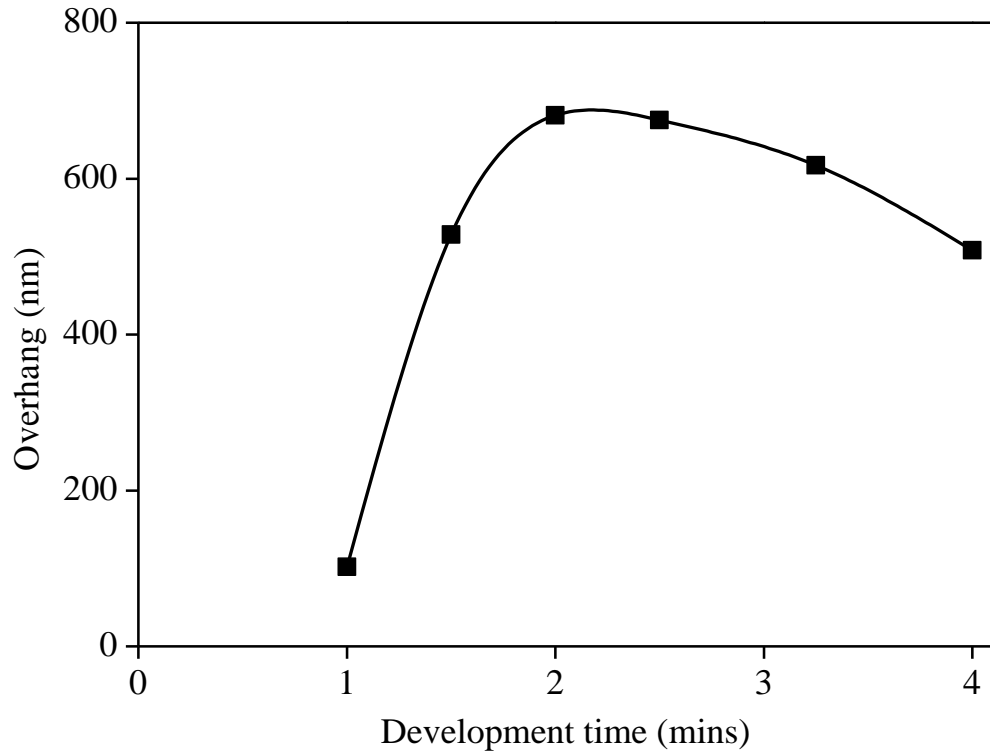


**Figure 3.7 – The effect of development time on the overhang produced using the bi-layer lift-off technique. The trial was run using a mask with 7  $\mu\text{m}$  dots and a 3 s exposure time**

### **3.1.2.6. Exposure time**

The exposure dose plays an important role in determining the overhang created. Overexposing the photoresist allows it to dissolve faster, so for the same development time, the PGMI will have more time to create a larger undercut. However, care is required as over-exposing the photoresist may lead to a reduction in the size of the features and even the loss of smaller features. A second trial was run, using a constant development time of 2.5 minutes with the exposure time varied before 1.5 to 5 s.

As the exposure dose received by the photoresist will be a function of the mask geometry, two masks were used: one a light-field mask with a series of 5  $\mu\text{m}$  dots and a second, dark-field (i.e. inverted) mask with 5  $\mu\text{m}$  holes. The results for both masks with varying exposure times are shown in Figure 3.8.

Both dark- and light-field masks show a similar trend, with a peak generated by an optimal exposure time of 2.1 and 4.0 s for light- and dark-field masks respectively. Below this exposure time, the photoresist was under exposed and the developer took longer to penetrate the SPR 350 1.2 and so created a smaller overhang. Beyond the optimal exposure time, the SPR 350 1.2 become over exposed and the feature size was reduced, as the edges of the SPR 350 1.2 were exposed and so become soluble. It should be noted that longer exposure times are required for the dark-field mask. This is to be expected, as a dark-field mask will prevent most of the UV energy reaching the photoresist.

The light-field mask shows a smaller overhang than the dark-field mask, this is likely to be due to over-exposure. As a majority of the mask is exposed, more UV light will be reflected from the substrate into the SPR 350 1.2, exposing the edges of the 'non-exposed' regions. This allows these areas of the SPR 350 1.2 to become more soluble, so during development it will recede, reducing the overhang. However, it should be noted that with both sets of masks the overhang is large and will create a good lift-off profile.

The mask used to create the devices was generally a dark-field mask, however an exposure of 3 s was chosen for device production, which lies approximately mid way between the peaks seen for light- and dark-field masks.

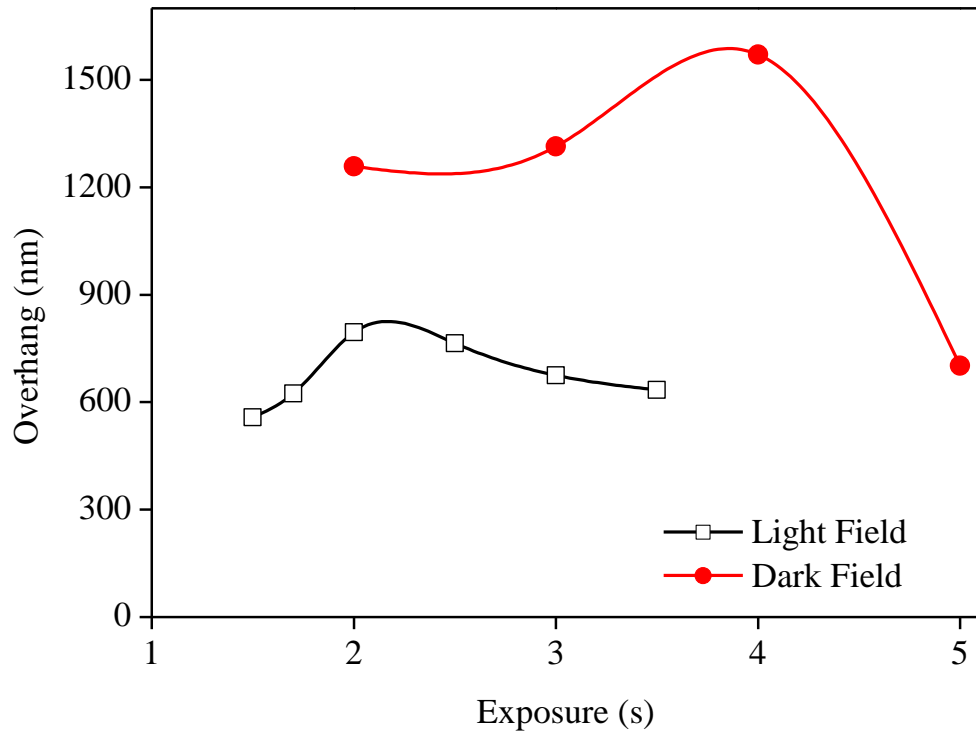


**Figure 3.8 – The effect of exposure dose (time) on the overhang produced using a bi-layer. Each exposure was developed for 2.5 minutes**

The final recipe that was chosen for processing devices is given in Table 3.4 and an SEM image is given in Figure 3.9 showing the profile given by this recipe.

Table 3.4 – Process parameters used for bi-layer lift-off

Process	Condition	Time
Dehydration bake	200 °C	>10 mins
Spin PMGI	6000 rpm	40 s
Bake	160 °C	5 mins
Spin SPR 350 1.2	3700 rpm	30 s
Bake	110 °C	4 mins
Expose		3 s
Bake	110 °C	30 s
Develop	MF 319	2.5 mins

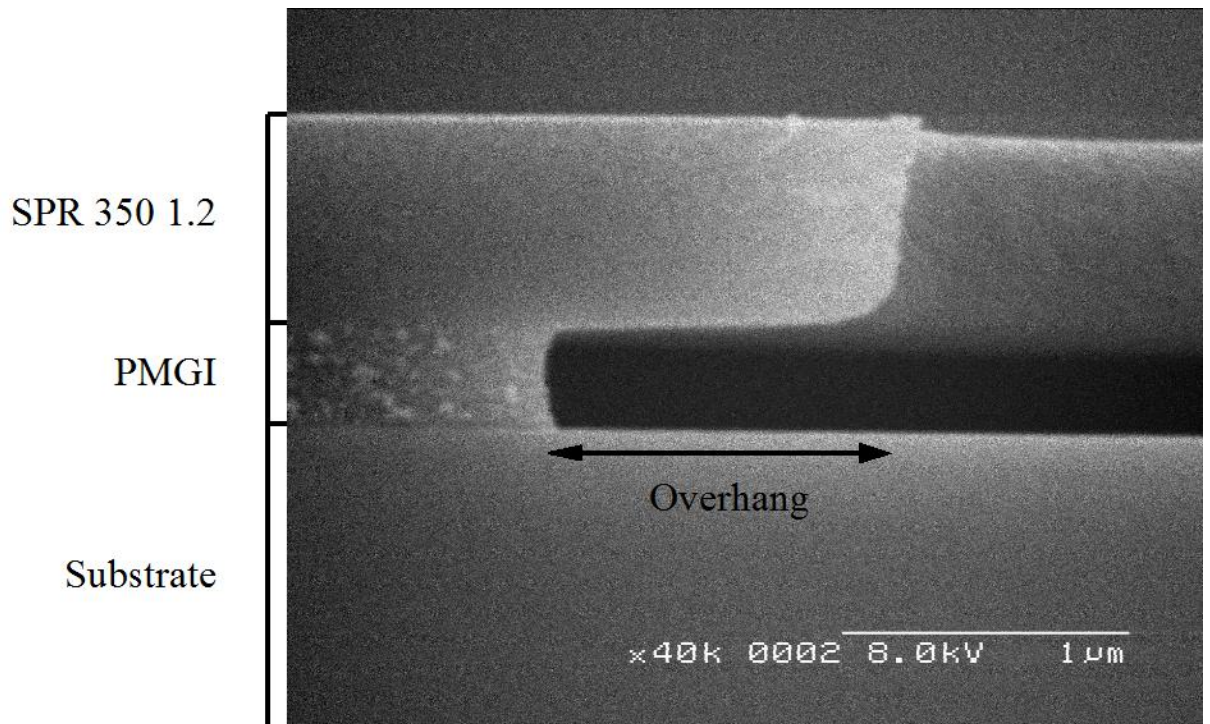


Figure 3.9 – An SEM image showing the lift-off profile obtained using the process outlined in Table 3.4

### **3.1.3. Metallisation effects**

While the bulk Seebeck coefficient values for common metals are well documented (e.g. [16]) thin metal films (below 100 nm) have been shown to exhibit different Seebeck coefficient to bulk values [20]. In addition to thickness effects, the processing methods used can play a role by altering the crystal structure of the metal, for example annealing bismuth-tellurium thin films was found to dramatically improve their thermal response [21]. In addition to affecting the Seebeck coefficient, the deposition method was found to be influencing the integrity of the metal films, with e-beam deposited films more liable to cracking during processing and operation than sputtered films. As such, the deposition methods and thickness of the metal films were investigated.

#### ***3.1.3.1. Deposition method***

The choice of deposition method used to create the thin metal films was seen to play an important role in the integrity of the films. Electron beam (E-beam) deposition was initially used to create the thin films, however the metal suffered from severe cracking and poor adhesion to the substrate. Sputtering was found to solve both these issues and was subsequently used to produce devices.

E-beam deposition is a thermal evaporation process, in which a beam of electrons is magnetically deflected within a vacuum to collide with and heat a small volume of metal contained within a crucible. The metal subsequently evaporates (or sublimates) and recondenses on a substrate mounted above the crucible. Such a method can achieve very high purity depositions, as only a small volume of the pure metal within the water-cooled crucible is heated to melting. E-beam deposition occurs in a vacuum, so the mean free path of the metal particles is relatively large (around 5 m at  $10^{-5}$  Torr [13]). Thus, the metal is unlikely to collide with any gas particles before reaching the substrate, leading to few gas inclusions and a very pure metal deposited on the substrate. Sputtering relies on the bombardment of a metal target with inert gas ions (argon was used in this work). Metal atoms are physically ejected from the target and re-deposit on the substrate.

During E-beam deposition, the metal particles arrive at the substrate with a relatively low energy (~0.1 eV [13]) and so they are unlikely to damage or implant into the substrate, whereas sputtering can lead to ion energies of 10 - 100 eV [13]. This increase in ion energy allows sputtered films to penetrate the substrate, leading to much better adhesion. The higher ion energy also causes recrystallisation in the metal layer, which reduces the internal stress built up during deposition [22]. The lower energy levels seen with e-beam deposition means that the intrinsic stresses generated will be higher than for sputtered films [23].

The higher intrinsic stress levels in e-beam deposited films lead to cracking during subsequent processing steps, particularly during the second metallisation. An example of a Cr layer cracking is shown in Figure 3.10. While sputtering offers better adhesion and lower intrinsic stresses, it also produces a more conformal coating than e-beam deposition as the mean free path of the metal during the deposition is much lower due to the inclusion of argon gas at a pressure of a few mT. This requires a very good lift-off profile to prevent the sputtered film coating the photoresist walls. The single photoresist layer technique outlined in Section 3.1.2.2 was unsuitable for sputtering, as the metal film would coat the walls, leading to poor edge definition and 'ear' formation. The bi-layer process introduced a significant overhang and thus was essential for masking during sputtering.

The reduction in cracking and lower intrinsic stresses produced during sputtering meant that this was the most practical solution for depositing the metal layers.

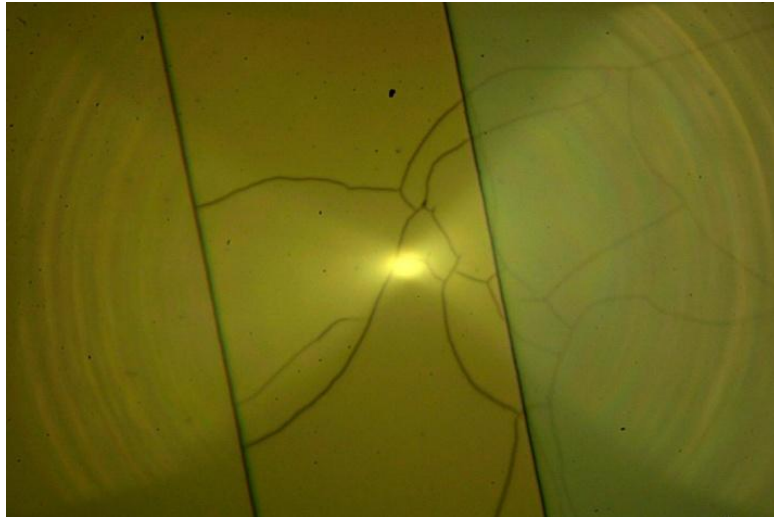


**Figure 3.10 – Microscope image showing overlapping layers of Ni (left) and Cr (right) with severe cracking in the Cr and overlapping region**

### **3.1.3.2. Thickness effect**

Thin films can present Seebeck coefficients which differ from bulk values. Zhang et al [20] suggest that thin films below 100 nm in thickness do not exhibit bulk Seebeck coefficients while Marshall et al. [24] suggest that film thicknesses should be at least 250 nm to achieve maximal thermal sensitivity. Despite operating with lower Seebeck coefficients, thin films must approach the mean free path length of the charge carriers to exhibit size effects and show a dramatic reduction in performance, with TFTCs demonstrated at thicknesses of 2.2 nm [4]. Thin metal films can even be used to create a thermocouple with one metal type (e.g. thin film platinum with a platinum wire [1]). As the junction widths in this work are at least an order of magnitude larger than the thickness, this dimension is unlikely to affect the Seebeck coefficient of the metals [20].

Achieving metal thicknesses greater than 250 nm to prevent thickness effects would have required the metals to be electroplated, as sputtering thick layers results in cracking due to the build up of internal stresses within thick metal layers. As two metal layers were required, electroplating would have introduced a number of challenges. Since the pure metal combinations would require calibration anyway (as standard pairings do not cover pure metal combinations), it was decided that the relatively small drop in performance of the thermocouple due to the metal thickness was acceptable.

In order to convert the emf generated by the device into a temperature difference between the sensing and reference junctions, each device required calibration. To achieve this calibration, and measure the Seebeck coefficient of the devices, a known temperature was applied to the sensing junctions, while the reference junctions were held at the ambient temperature. The sensing junctions were heated by a  $70\ \Omega$ ,  $5\ \text{W}$  wire wound power resistor, which was brought into intimate contact with the device. To reduce the thermal contact resistance between the resistor and the device, heat sink compound was applied. A standard K-type thermocouple was fastened to one face of the resistor to monitor its temperature. Various heating powers were applied to the resistor to control its temperature. The output from the K-type thermocouple was then compared with the voltage produced by the TFTCs to extract the temperature dependence.

The emf generated by the device was conditioned by the control electronics detailed in Section 3.3, using an instrumentation amplifier which had a voltage gain of around 10,000. An example calibration graph is shown in Figure 3.11 for a device with metal thicknesses of  $\text{Cr} = 40\ \text{nm}$  and  $\text{Ni} = 120\ \text{nm}$ . After amplification, the device showed a sensitivity of  $335\ \text{mV}\ ^\circ\text{C}^{-1}$ . Thus, before amplification the device demonstrated a sensitivity of  $33.2\ \mu\text{V}\ \text{K}^{-1}$ , which is close to the bulk value of  $36.3\ \mu\text{V}\ \text{K}^{-1}$  for Cr/Ni junctions [16]. Thus, while the device has a Seebeck coefficient which is lower than that expected for bulk materials, it is still sufficiently large for the thermocouples to be useful, so long as each is calibrated before use.

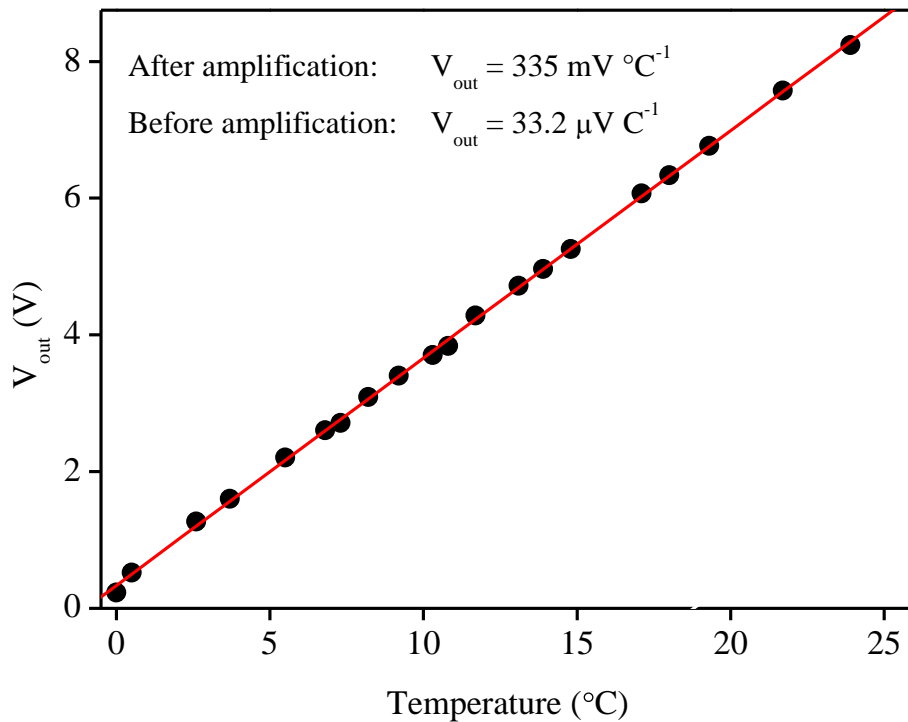


Figure 3.11 – A typical calibration graph obtained for a Design A device formed on a polyimide substrate

### 3.1.3.3. Metal choice

The output voltage response is determined by the choice of metals which form the thermocouple. Bulk values give a good indication of which metal combinations offer the largest combined Seebeck coefficients. However, the choice of metal is also influenced by practical fabrication considerations. For example, metals which readily form an oxide (e.g. Cr) adhere well to substrates [13], so gold (Au) and platinum (Pt) may be unsuitable due to their poor adhesion properties.

Several metal combinations were used during the prototyping stage of the project, on the early devices. Cr/Ni devices demonstrated the highest Seebeck coefficient of  $33.2 \mu\text{V } ^\circ\text{C}^{-1}$ . A range of metal combinations are shown in Figure 3.12.

It is interesting to note that annealing the devices after both metal layers had been deposited had a beneficial effect on the response of the thermocouple. This is likely to be due to beneficial

changes in the microstructure induced during the annealing process which improve the electrical transport and thermoelectric properties [21].

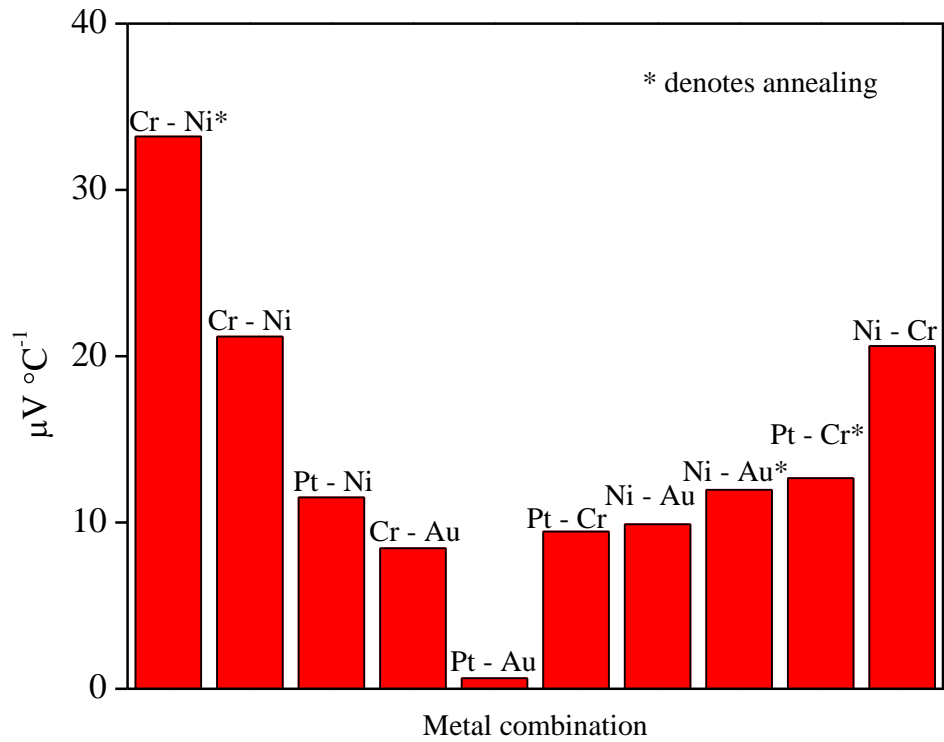


Figure 3.12 – Measured Seebeck coefficients for various metal combinations. Label denotes deposition order, \* denotes annealing after deposition

### 3.1.4.SU-8 membrane devices

#### 3.1.4.1. SU-8 as a substrate

The previous sections have introduced the basic metallisation and patterning processes required to form the devices. The following sections discuss the practicalities of modifying the substrate, in order to improve the performance of the device by increasing the thermal isolation of the sensing area.

Various authors have reported fabricating the sensing junctions of thermocouple devices on membrane or bridge structures (for example [25][26][27][28]). Such structures increase the thermal isolation of the sensing junctions, improving the sensitivity and response time. Devices have been reported on silicon nitride and oxide membranes [25][27] as well as SU-8 membranes [28]. Silicon based membranes have the advantage of good process integration and a rigid structure. However, SU-8 can be patterned using standard photolithographic process and as it is a polymer it has a low thermal conductivity of  $0.3 \text{ W m}^{-1} \text{ K}^{-1}$  compared to  $3.2 \text{ W m}^{-1} \text{ K}^{-1}$  for silicon nitride providing greater thermal isolation for the sensing junctions.

SU8 was developed by IBM in 1989 [29]. It is a photo-definable resist, which can be used as a structural material. Many applications have used SU8 since it was reported as a suitable resist for MEMS use [30]. The mechanical and chemical properties combined with its photolithographic patterning mean that SU-8 is well suited for use as both a structural layer, as well as an etch mask. Both of these properties were utilised during the fabrication of the membrane.

The SU-8 membrane devices followed a similar fabrication process to that for a silicon wafer-based device (Section 3.1.1). After metallisation, a  $10 \mu\text{m}$  layer of SU8-10 was spun. The area of SU-8 around the sensing junctions was then patterned with holes to act as an etch mask for the silicon substrate. The silicon substrate was etched by xenon difluoride ( $\text{Xe F}_2$ ) through the holes in the SU-8 layer.  $\text{XeF}_2$  isotropically etches silicon which created a void underneath the SU8, suspending the SU-8 and sensing elements on a  $10 \mu\text{m}$  thick SU8 membrane. SEM images of the

SU-8 membrane are shown in Figure 3.13. The fabrication stages required to create these devices are shown in Figure 3.14 and further details are given below.

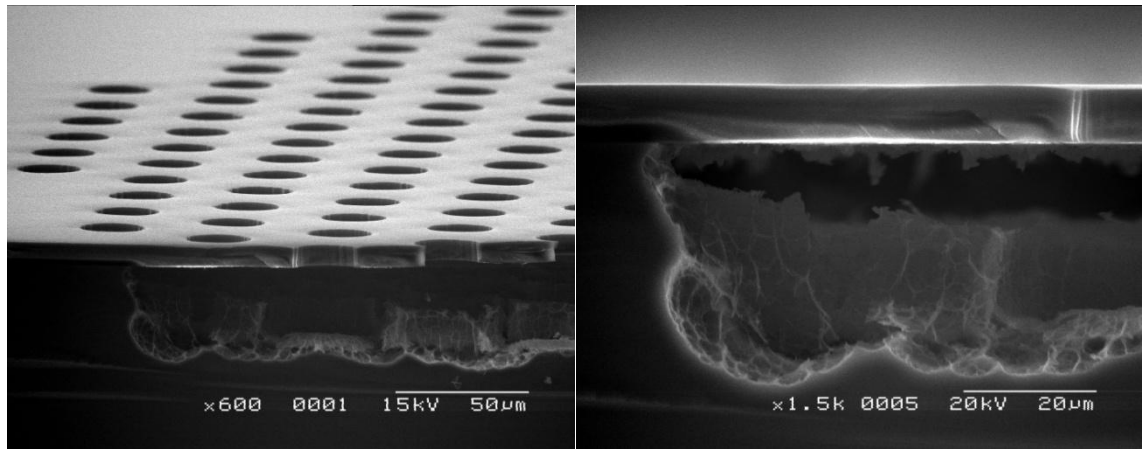


Figure 3.13 – SEM images showing the 10  $\mu\text{m}$  thick SU8 layer with holes acting as an etch mask for the  $\text{Xe F}_2$  silicon etch. The void created in the silicon is clearly visible beneath the holed region of SU8

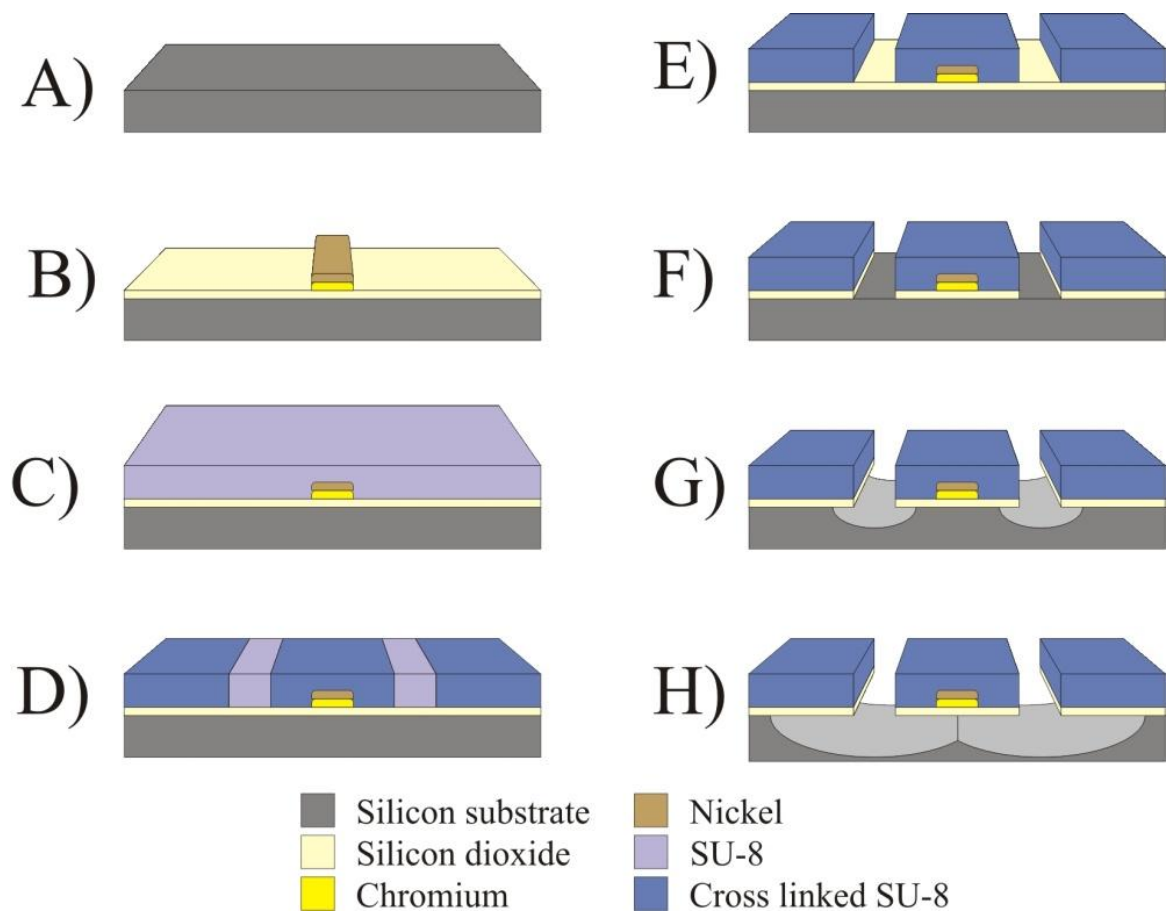


Figure 3.14 – Fabrication stages required to form an SU-8 membrane device: A) Cleaning; B) Oxidation and metallisation; C) Spin SU-8; D) Expose; E) Develop; F) Etch  $\text{SiO}_2$ ; G) & H)  $\text{XeF}_2$  etch

### **3.1.4.2. Fabrication of SU-8 devices**

#### **A) Cleaning**

Before the oxidation and metallisation stages, the wafer was cleaned. This process was the same as that outline in Section 3.1.1 Stage A) and consisted of ultrasonication in Decon 90, acetone and then IPA followed by a piranha etch.

#### **B) Oxidation and metallisation**

The wafer was oxidised with a ~500 nm layer of SiO<sub>2</sub> before being metallised and patterned with ~100 nm Cr and ~200 nm Ni, as detailed in Section 3.1.1 Stages B – H.

#### **C) Spin SU-8**

To create the SU-8 membrane, a 10 µm thick layer of SU-8 10 was spun at 500 rpm for 10 s and 3000 rpm for 30 s. Before the resist was exposed, it required a soft bake to evaporate the solvent and densify the film [31] for 2 min at 65 °C followed by 5 min at 95 °C. A two step baking process is suggested to improve adhesion and coating fidelity [31].

#### **D) Expose**

The SU-8 was patterned using mask Design A. It was aligned and exposed for 3 s (EVG 620, EV Group GmbH). SU-8 contains a photoacid generator [32] which catalyses the cross linking of the epoxy within SU-8. The photoacid is produced upon irradiation with UV, meaning that SU-8 is a negative resist and areas exposed to UV will remain during development. However, SU-8 requires a post exposure bake to accelerate the cross linking reaction [33]. The SU-8 was baked for 1 min at 65 °C and 2 min at 95 °C.

#### **E) Develop**

Development of the SU-8 was achieved using Microposit EC solvent (Shipley). A development time of 3 min with gentle agitation was experimentally found to be suitable. After development, the device was immediately washed in IPA and dried using a nitrogen gun.

### ***F) Etch SiO<sub>2</sub>***

To prevent the SU-8 membrane collapsing, only a small area was suspended around the sensing junctions and resistive heater. However, the entire silicon wafer required the growth of an oxide layer to act as an insulator for the metal tracks. XeF<sub>2</sub> is highly selective to silicon [34] meaning that an oxide layer would prevent XeF<sub>2</sub> from etching the underlying silicon. Thus the oxide layer required removal prior to the XeF<sub>2</sub> etch. This was achieved using a buffered hydrofluoric acid etch (4 : 1 ammonium fluoride to hydrofluoric acid), until the oxide layer had visibly undercut the SU-8 holes.

### ***G) & H) XeF<sub>2</sub> etch***

To release the SU-8 from the silicon substrate, an XeF<sub>2</sub> etch (Xetch E1, Xactix Inc.) was used. XeF<sub>2</sub> etches silicon based on the formula given in Equation (3.1) (taken from [34]):



Devices were etched until the membrane was released from the substrate. Observation using an optical microscope was sufficient for this purpose. SEM images of the released membrane are shown in Figure 3.13.

## **3.1.5. Polyimide devices**

### ***3.1.5.1. Advantages of polyimide as a substrate***

While devices fabricated on an SU-8 membrane demonstrate improved thermal sensitivity to those formed on a silicon substrate, several significant issues remain. Firstly, the SU-8 membrane and silicon substrate are both delicate. This caused issues during the fabrication process and would ultimately prevent the devices operating on certain samples, including the leaves of a plant. For reliable operation, the device must be robust and capable of making intimate contact with the surface of a leaf without damage. Devices formed on a polyimide substrate solve both these issues, whilst also improving the thermal sensitivity of the device.

The polyimide used to form the substrate was PI-2611 (HD Microsystems). This is a high molecular weight, fully aromatic polyimide which is formed from polyamic acid precursors

dissolved in an N-methyl-2-pyrrolidone based solvent carrier [35]. This means that the polyimide can be spin coated and cured by baking, creating a thin polymer substrate upon which the device can be patterned. The thickness is controlled by the spin speed and several layers can be applied to produce a thicker substrate, ensuring the device is robust. A final layer can also be spun over the device to encapsulate the sensing junctions.

Polyimide offers a number of useful properties from a fabrication view point in addition to the improvements in operating characteristics (detailed in Section 2.2.2.2.2). Firstly, it can be spun to form relatively thin, thermally insulating ( $k_{\text{polyimide}} = 0.10 \text{ Wm}^{-1} \text{ K}^{-1}$ ) layers which ensures that good thermal isolation can be achieved. However, even thin layers of polyimide are strong enough to act as a self-supporting substrate which is capable of being peeled from a silicon substrate. In addition, the self-supporting substrate is flexible and robust, which is vital when the device is used on soft surfaces (such as a leaf) as it allows the sensor to be brought into good contact with the sample.

### 3.1.5.2. Fabrication of polyimide devices

Once the polyimide substrate had been created on a silicon carrier wafer, the fabrication stages were similar to those for a silicon-based device. In addition, a layer of polyimide was spun over the completed device to provide encapsulation. An overview of the fabrication process is given in Figure 3.15 and a description of the steps is given below.

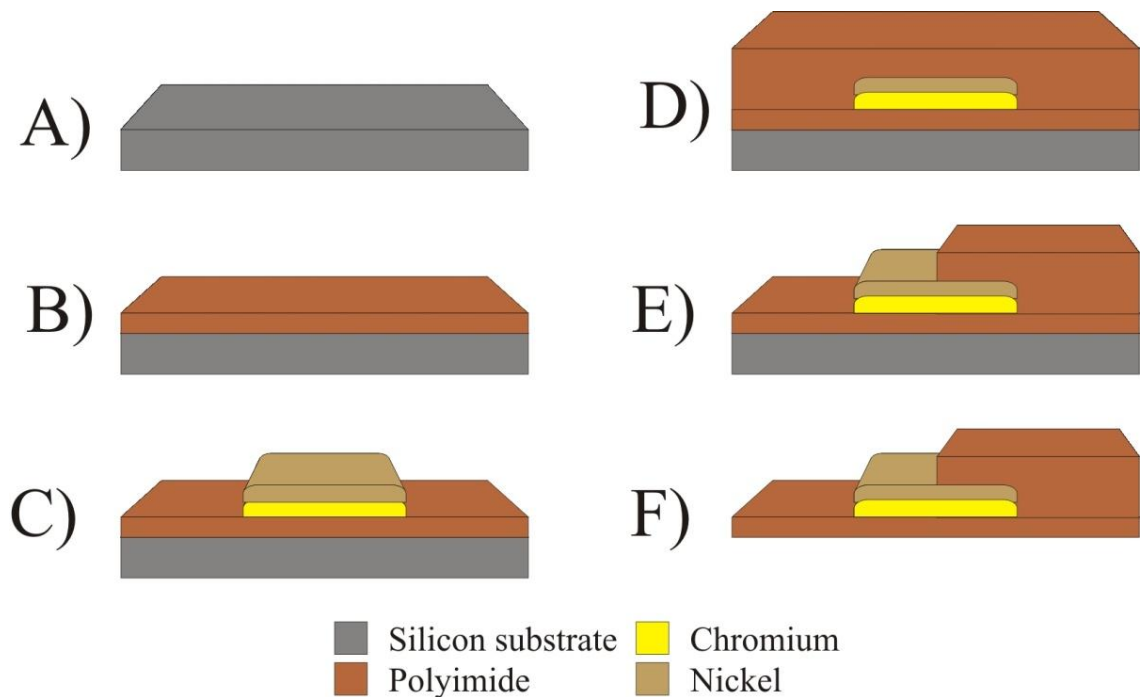


**Figure 3.15 – Fabrication stages required to form a device on a polyimide substrate: A) Clean wafer; B) Spin polyimide; C) Metallise and pattern; D) Encapsulate with polyimide; E) RIE etch to expose connections & F) Peel from substrate**

#### *A) Clean wafer*

A 2” silicon wafer was used as a carrier for the polyimide substrate. Before spinning polyimide, the wafer was cleaned by ultrasonication in Decon 90 (10 parts DI water to one part Decon 90), followed by acetone and finally IPA. The wafer was dried using a nitrogen gun and then baked for at least 5 min on a hotplate at 200 °C to dehydrate the surface.

#### *B) Spin polyimide*

The polyimide was applied to the silicon wafer by spin coating. A thickness of around 2.5 µm was achieved by spinning at 500 rpm for 10 s to spread the polyimide before ramping to 2000 rpm for 30 s. A single layer 2.5 µm thick was found to be too thin and the polyimide layer

ripped when it was removed from the silicon, so a 7.5  $\mu\text{m}$  substrate was formed by repeating the spin coating process 2 further times, with a 5 min bake on a hotplate at 85  $^{\circ}\text{C}$  between each coat. After the final coat, the polyimide was part-cured by increasing the hotplate temperature to 150  $^{\circ}\text{C}$  for 15 mins. To fully cure the polyimide, it was placed in a convection oven and heated to 350  $^{\circ}\text{C}$  at a ramp rate of 2  $^{\circ}\text{C min}^{-1}$ . Higher ramp rates were found to cause bubbles to form within the polyimide. By altering the number of layers or the spin speed, different thicknesses of polyimide could be produced.

An annotated SEM image is shown in Figure 3.16, allowing the thickness of the polyimide to be measured at 7.4  $\mu\text{m}$ .

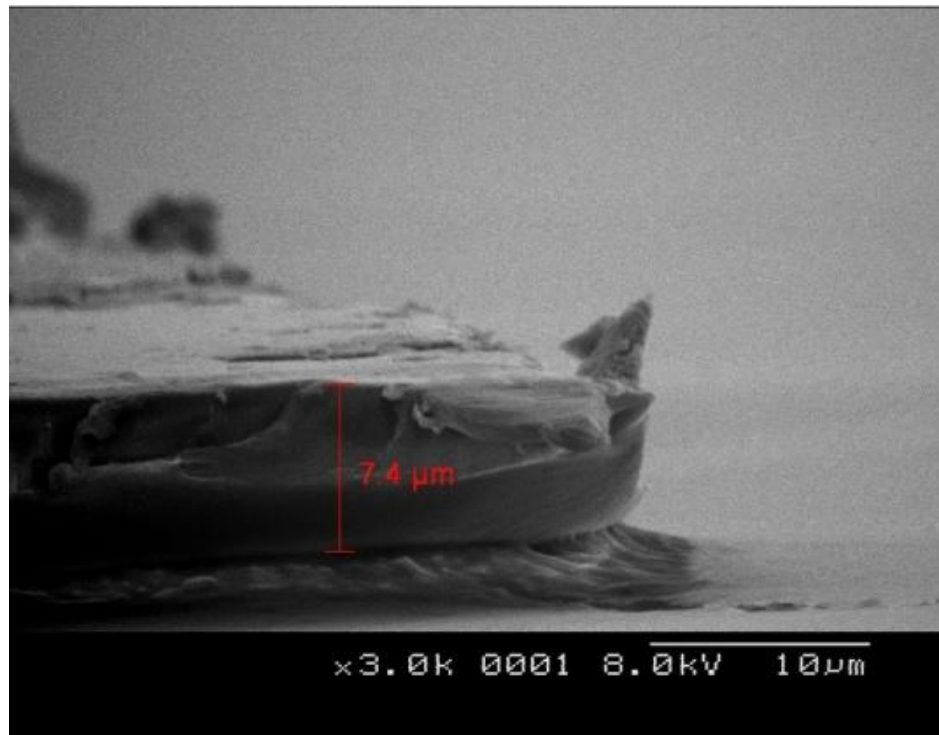


**Figure 3.16 – An SEM image showing the thickness of the polyimide after it has been spin coated with 3 layers and removed from the silicon carrier**

### ***C) Metallise and pattern***

Following the production of the polyimide substrate, the devices were metallised and patterned using the same recipe outlined in Section 3.1.1 Stages D – H. To improve adhesion of the metal to the substrate, it was subjected to a reactive ion etch (RIE) with the parameters given in Table 3.5.

**Table 3.5 - Process parameters used to improve the adhesion of metal to the polyimide substrate.**

<b>Parameter</b>	<b>Value</b>
Oxygen pressure	150 mT
Oxygen flow rate	50 sccm
Power	80 W
Platen	Quartz
Platen temperature	20 °C
Time	1 min

***D) Encapsulate with polyimide***

Once the devices had been patterned on the substrate, a final layer of polyimide was spun onto the device (10 s @ 500 rpm followed by 30 s @ 2000 rpm). This encapsulation protected the metal layers and ensured that they were electrically isolated from the sample. The polyimide was part-cured by baking for 5 min at 85 °C followed by 15 min at 150 °C and then fully cured in a convection oven at 350 °C for 30 min with a ramp rate of 2 °C min<sup>-1</sup>. This curing stage also acted as an annealing stage for the metal layers, improving their thermoelectric properties (see Section 3.1.3.3).

***E) RIE etch to expose connections***

After encapsulating the device, an RIE etch was required to remove the encapsulation in certain areas to allow electrical connections to be made to the device. Pieces of scrap silicon wafer were used to mask the areas which did not require etching, while any exposed areas were etched until the metal beneath the encapsulation had been uncovered. The parameters used to etch the polyimide are detailed in Table 3.6.

**Table 3.6 – Process parameters used for the polyimide etch (~2.5 μm)**

<b>Parameter</b>	<b>Value</b>
Oxygen pressure	150 mT
Oxygen flow rate	50 sccm
Power	300 W
Platen	Quartz
Platen temperature	20 °C
Time	10 min

#### ***F) Peel from substrate***

The final stage of processing was to remove the device from the carrier wafer. For delicate devices, it is possible to use a hydrofluoric acid etch to remove a 500 nm sacrificial oxide layer and release the polyimide substrate [36]. A polydimethylsiloxane (PDMS) can also be used as a sacrificial layer as the polyimide delaminates from the PDMS at around 100 °C [37]. However, it was found that with a suitably thick polyimide substrate, the device could simply be carefully peeled from the carrier wafer.

To allow probing using a Molex ribbon connector with a 1 mm pitch, a layer of Kapton was attached to the back side of the device using an epoxy resin. This increased the thickness and ensured good electrical connections could be made. See Figure 3.17 for a photograph of the finished polyimide device.

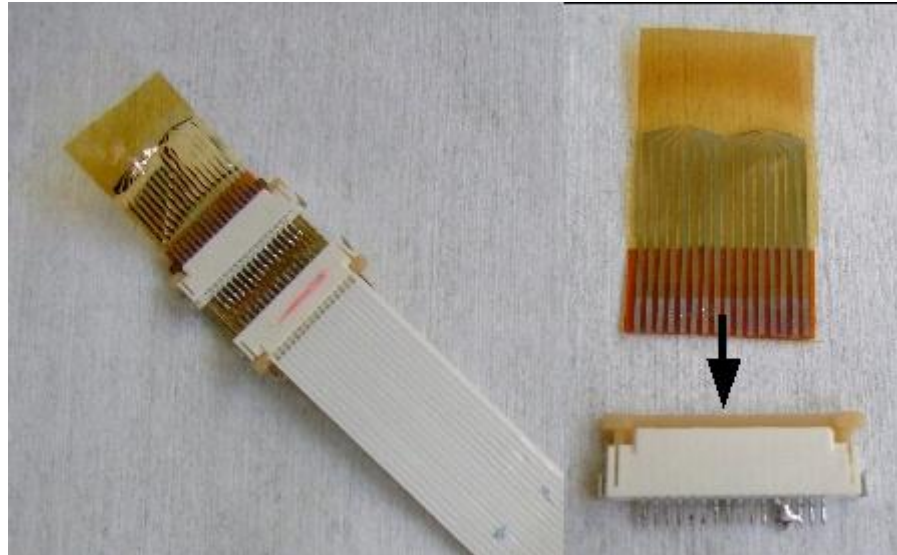


**Figure 3.17 – A Molex ribbon cable connector can be used to make electrical connections to Design B type devices. Note the Kapton which has been bonded to aid insertion into the Molex connector**

Polyimide devices patterned using Design B were used during all experiments on leaves. A mixture of Design A and Design B type devices were used during other experiments.

The following section details the various jigs which were developed to allow electrical connections to be made to the devices during prototyping and experimentation.

### **3.2. Jigs for probing the device**

Once fabricated, the devices required electrical connections to be made. The probing technique plays an important role in determining the complexity of the device's design. Early prototype devices required a simple connection mechanism as fabrication of the devices was the focus of the work. As the design progressed, the connection mechanism began to limit the utility of the devices and so it was necessary to incorporate the connection mechanism into the design of the device. This section introduces the three iterations of probing techniques which were used.

Initially, a probing station was used to directly make connections with the device. While it offered a simple solution, it offered only 4 probes, required manual alignment of the probes and was only suitable during early development work. A custom built jig was used to develop the designs. This allowed up to 20 individual connections to be made at one time, opening up testing of multiple thermocouple junctions and heaters. The final iteration of the connection mechanism was to use a

commercially available Molex ribbon connector. This represented a robust and easy to use solution for making connections with the final device design used during testing on plant leaves, however it required the device design to incorporate the Molex connector footprint and was only suitable for devices formed on a flexible substrate.

### **3.2.1. Probe station**

A 4 probe test station was used to probe early devices. Manipulators allow 4 needle probes to be positioned accurately onto the substrate to make electrical connections. Signals were recorded using a high precision 34420A nano-voltmeter (Agilent). The manual manipulation of the probes and ease of operation of the nano-voltmeter allowed early device to be probed easily in order to prove their operation. However, the high voltage resolution available by using the nano-voltmeter comes at the expense of sampling frequency which was 250 Hz at the lowest accuracy measurements, dropping to 0.15 Hz for high accuracy measurements. In addition, the probe station had only 4 manipulators available which required manual alignment, this prevented simultaneous testing of multiple junctions and resistive heaters and was very time consuming to probe devices with several thermocouple pairs. So, while the probe station was suitable for early prototype devices, it quickly became apparent that a custom probing method would be required.

### **3.2.2. Gold sprung-probe jig**

To allow simultaneous testing of many junctions and to simplify the probing procedure, a custom built test jig was designed and built. It consisted of a Perspex boom with an array of 20 gold sprung-probes which was mounted on a slotted base, giving movement of the probes with 2 degrees of freedom. Details of the jig are shown in Figure 3.18.

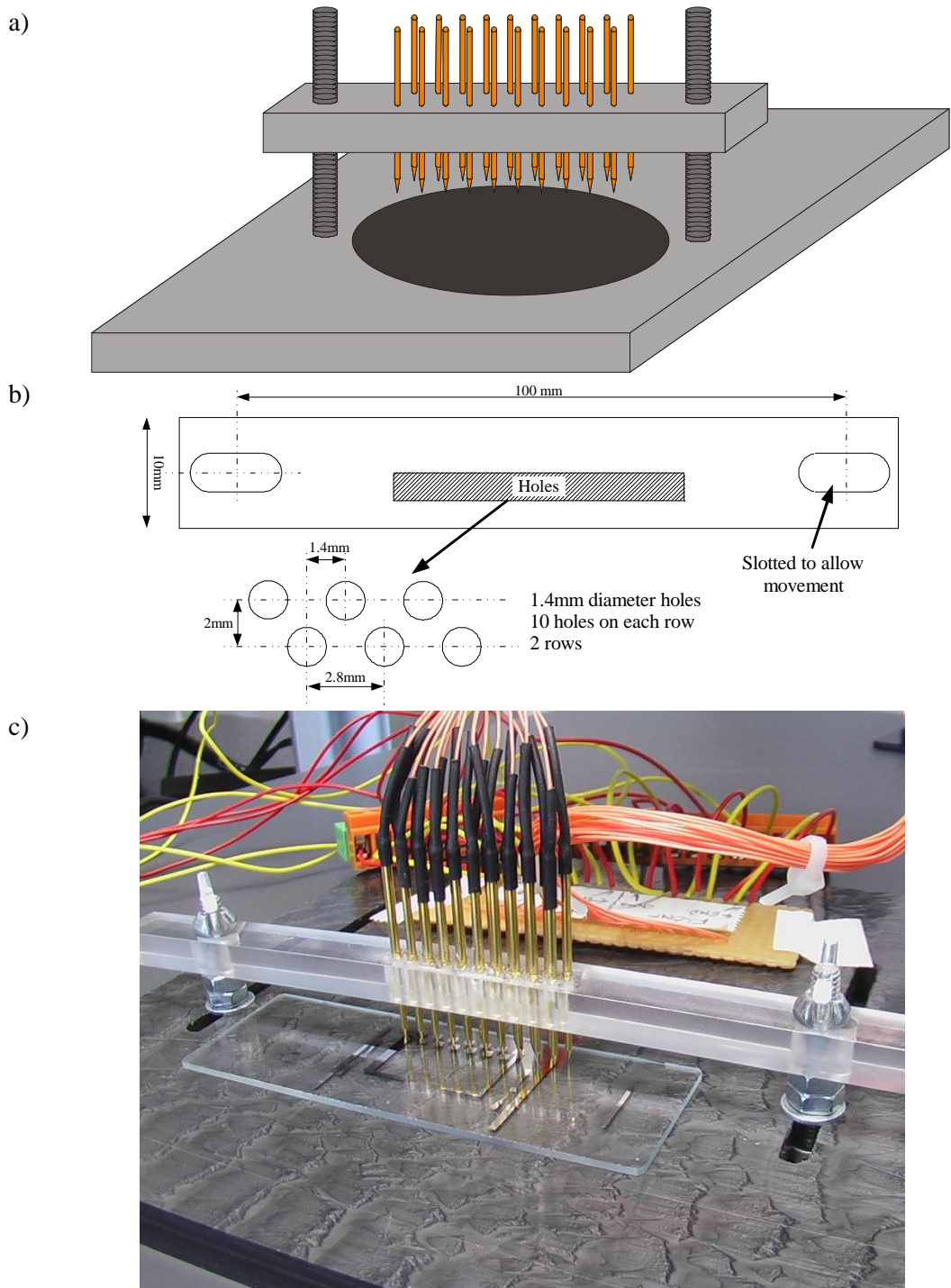


**Figure 3.18 – a) 3-D drawing of the sprung-probe testing jig; b) Schematic showing the details of the boom and the location of the sprung-probes & c) A photograph showing the sprung-probe test jig probing a device fabricated on a glass microscope slide**

The Perspex boom and base were CNC machined and the gold sprung-probes were bonded in place using an epoxy resin. Wires were soldered to the probes and a heat shrink wrap was used to provide mechanical strength. To allow devices to be probed by the device, the footprint of the electrical connections was designed to match the pattern of the probes.

The jig provided a mechanism for making up to 20 electrical connections at once and so allowed the probing of multiple thermocouples simultaneously. Each of the 20 gold probes was sprung to ensure that good contact was achieved between the device and the probe, across all probes. It was primarily used for device characterisation, as it allowed devices to be quickly and easily tested. However, it was unsuitable for testing on plant leaves, as it was relatively bulky. The final iteration of the connection mechanism was to utilise a commercially available Molex ribbon connector.

### **3.2.3.Molex connector**

To allow the device to take measurements on plant leaves, the connection mechanism was required to be much smaller and more flexible than the gold sprung-probe jig allowed. To this end, a Molex ribbon connector was used. This required a number of design changes to the device. Firstly, the footprint of the connection pads needed to be aligned with the Molex connector design which had 1 mm pitch spacing. Secondly and more importantly was the change in substrate, as the ribbon connector required a thin and flexible substrate. As such, the Molex connector was only suitable for use on polyimide devices.

A small PCB was created with two Molex connectors mounted upon it. The first connector made connections to the device, while the second connector accepted a flat, 16-way, 152 mm Molex ribbon cable. A photograph of a polyimide device mounted into the connector is shown in Figure 3.17.

The Molex connector offered a number of benefits. As it is commercially available, it was much cheaper than the custom built probe jig and several devices could be mounted simultaneously. It is also a much smaller and more flexible solution and it is ideal for making connections to devices

mounted on plant leaves. The flexibility of the connector and ribbon cable allows the polyimide device to operate to its full potential. However, it was unsuitable for use on silicon-based devices (including SU-8 membrane devices), so both the gold sprung-probe jig and the Molex connectors were used for device testing.

### 3.3. Control electronics

During the early prototyping stages, the focus of the project was on the design and fabrication of the devices. However, the emf generated by thermocouples is relatively low. For example, a bulk Ni/Cr junction is expected to have a Seebeck coefficient of  $36.3 \mu\text{V K}^{-1}$  [16], so if the temperature difference between the sensing and reference junctions was  $50 \text{ }^\circ\text{C}$ , then the expected voltage produced by the junction would be only 1.82 mV. To allow accurate, small voltage measurements to be taken, a 34420A nano-voltmeter (Agilent) was used as it has nV resolution and  $\sim 10 \text{ G}\Omega$  input impedance. However, this precision is achieved at the expense of sampling time: the fastest sampling frequency was 250 Hz, dropping to 0.15 HZ for the highest accuracy measurements. This meant that the nano-voltmeter was only suitable for testing early devices with very slow response times. The cost and size of the nano-voltmeter also meant that it was only suitable during prototyping and laboratory testing.

To move away from the expensive and slow nano-voltmeter, an instrumentation amplifier was used to condition the signal, prior to data capture using either an oscilloscope (DSO3102A, Keithley) or a datalogger (Picoscope 2104, Pico Technology). An LT1167 (Linear Technology) single resistor gain programmable, precision instrumentation amplifier was chosen, with an LT1112 (Linear Technology) op-amp used to provide output offset trimming. This could be used to null the output and remove any unwanted dc offsets present within the electronic of physical system. A schematic diagram of the circuit used is shown in Figure 3.19.

The gain of the instrumentation amplifier was set by a single resistor ( $R_g$ ). The value of this resistor could be used to give any gain in the range 1 to  $10^4$ . This was set to give a gain of around 10000.

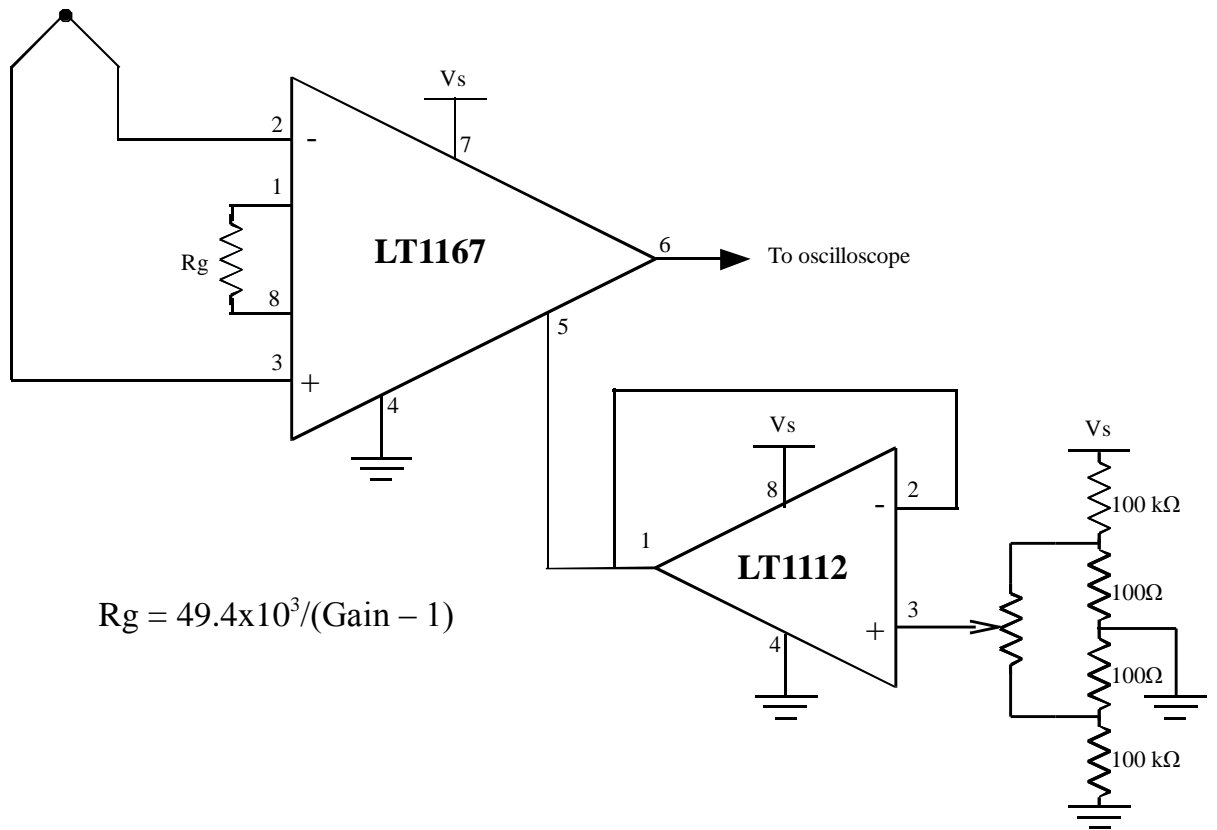


Figure 3.19 – Schematic diagram of the instrumentation amplifier

### 3.4. Conclusions

This chapter has detailed the fabrication methods required to form all the devices reported in this work. All devices were metallised and patterned using a common set of processes, which involve sputtering two layers of metal and patterning using a lift-off technique. To improve the thermal sensitivity of the device, the substrate required modification. Two methods for creating a polymeric substrate have been outlined here, the first created a suspended SU-8 membrane released from a silicon substrate by xenon difluoride etching while the second method created a self supporting polyimide substrate upon which devices could be patterned.

Photolithographic patterning of TFTCs required the use of a lift-off technique. Two methods for achieving this have been reported. The first was a single layer process which showed variable results as it was dependent on several processing parameters. The resulting structure was prone to curling under the tensile stresses induced during metal deposition, meaning that the edges of the deposited metal were compromised. The second, bi-layer technique was much more successful as the overhang created was robust and easily controlled by the exposure and development time

The sputtering method was found to play an important role in determining the integrity of the metal films which formed the TFTCs. E-beam deposited metal layers were prone to cracking when the second metal was overlaid on the first. This issue was overcome by sputtering, which produced thin metal films with lower intrinsic stresses due to the higher ion energies created. All devices were formed from Cr and Ni, as this metal combination was found to produce devices with the highest Seebeck coefficient of the metal combinations available.

When formed on an SU-8 membrane, the devices offered an improvement in thermal sensitivity (as reported in Chapter 2). However, these devices were very brittle and the metal and SU-8 layers were seen to crack frequently. In response, the substrate was modified and polyimide was used instead. Polyimide substrates offer a slight improvement in thermal sensitivity over SU-8 whilst also having a number of other benefits including: flexibility, chemical inertness, electrical and thermal insulation as well as biocompatibility. In particular, the flexibility and thermal

properties of the polyimide ensured that the devices were much more robust and capable of operating on the leaves of a plant.

The substrate also played a key role in determining the method of making electrical connections to the devices. In particular, the polyimide devices allowed flexible connections to be made using a commercially available Molex ribbon connector. This was a substantial improvement on the custom made gold sprung-probe jig used to make connections to the SU-8 and silicon devices. The robust and flexible nature of the Molex connector allowed the device to be mounted onto leaves, in-situ on a plant.

To enable the small emf generated by the devices to be monitored by a datalogger for later experiments, an instrumentation amplifier was designed and built. The amplifier operated with a gain of 10083. A second amplifier was used to provide dc offsetting, to null any unwanted dc offset in the physical or electronic system. The following chapter outlines the characterisation of the devices once they had been fabricated using the methods outlined in this chapter.

### 3.5. References

1. **Kreider, K. G. Ripple, D. C. and DeWitt, D. P.** Calibration of Thin-Film Thermocouples on Silicon Wafers. *NIST*. [Online] [Cited: 25th August 2011.] [http://www.nist.gov/manuscript-publication-search.cfm?pub\\_id=830629](http://www.nist.gov/manuscript-publication-search.cfm?pub_id=830629).
2. **Okamura, Y.** *Fabrication of nanoscale thermoelectric devices. US Patent 6,969,679* 2005.
3. **Lee, J and Kotov, N A.** Thermometer design at the nanoscale. *Nano Today*. 2007, Vol. 2, 1, pp. 48-51.
4. **Salvadori, M.C. Vaz, A.R. Teixeira, F.S. Cattani, M. and Brown, I.G.** Thermoelectric effect in very thin film Pt/Au thermocouples. [Online] [Cited: 25th April 2011.] <http://www.osti.gov/bridge/servlets/purl/889625-J2aoMi/889625.pdf>.
5. **Esfarjani, K., Zebarjadi, M. and Kawazoe, Y.** Thermoelectric properties of a nanocontact made of two-capped single-wall carbon nanotubes calculated within the tight-binding approximation. *Physical Review B*. 2006, 73.
6. **Mácia, E.** DNA-based thermoelectric devices: A theoretical prospective. *Physical Review B*. 2007, 75.
7. **Ito, T. and Okazaki, S.** Pushing the limits of lithography. *Nature*. 2000, Vol. 406, pp. 1027-1031.
8. **Cumming, D. R. S., Thoms, S., Weaver, J. M. R. and Beaumont, S. P.** 3 nm NiCr wires made using electron beam lithography and PMMA resist. *3 nm NiCr wires made using electron beam lithography and PMMA resist*. 1996, 30.
9. **Houlet, L.F., Shin, W., Tajima, K., Nishibori, M., Izu, N., Itoh, T. and Matsubara, I.** Thermopile sensor-devices for the catalytic detection of hydrogen gas. *Sensors and Actuators B*. 2008, 130, pp. 200-206.

10. **Zhang, Y. and Tadigadapa, S.** Calorimetric biosensors with integrated microfluidic channels. *Biosensors and Bioelectronics*. 2004, 19, pp. 1733–1743.
11. **Wang, L. Wang, B. and Lin, Q.** Demonstration of MEMS-based differential scanning calorimetry for determining thermodynamic properties of biomolecules. *Sensors and Actuators B*. 2008, Vol. 134, pp. 953-958.
12. **Lin, P., Wu, C., Cheng, Y., Lin, Y., Huang, F. and Huang, R.** Fabrication and Characterization of a Three-Dimensional Flexible Thermopile. *The Japan Society of Applied Physics*. 2008, Vol. 47, 3, pp. 1787–1793.
13. **Madou, M.J.** *Fundamentals of microfabrication*. London : CRC press, 2002.
14. **Deal, B.E. and Grove, A.S.** General Relationship for the Thermal Oxidation of Silicon. *Journal of Applied Physics*. 1965, Vol. 36, 12, pp. 3770-3778.
15. **Dammel, R.** *Diazonaphthoquinone-based Resists*. Washington : SPIE Press, 1993. p. 100.
16. **Foiles, C.L.** *Thermopower of pure metals and dilute alloys*. New York : Springer, 1985.
17. **Redd, R., Spak, M., Sagan, J., Lehar, O. and Dammel, R.** Lithographic Process For High-Resolution Metal Lift-Off. *Proceedings of SPIE, the International Society for Optical Engineering*. 1999, Vol. 3678.
18. **Redd, R., Maurer, D. and Klingbeil, L.S.** Revitalization of Single Layer Lift-off For Finer Resolution and Challenging Topography. [Online] [Cited: 2011 August 12th.] [http://www.csmantech.org/Digests/2001/PDF/7\\_3\\_Redd.pdf](http://www.csmantech.org/Digests/2001/PDF/7_3_Redd.pdf).
19. **Rohm and Haas Electronic Materials.** Datasheet: Megaposit SPR 350 Series Photoresist. 2007.
20. **Zhang, X., Choi, H., Datta, A. and Li, X.** Design, fabrication and characterization of metal embedded thin film thermocouples with various film thicknesses and junction sizes. *Journal of Micromechanics and Microengineering*. 2006, Vol. 16, pp. 900-905.

21. **Jeon, S. Oh, M. Jeon, H. Hyun, S. and Lee, H.** Effects of post-annealing on thermoelectric properties of bismuth–tellurium thin films deposited by co-sputtering. *Microelectronic Engineering*. 2011, Vol. 88, 5, pp. 541-544.
22. **Guilbaud-Massereau, V. Celerier, A. and Machet, J.** Study and improvement of the adhesion of chromium thin films deposited by magnetron sputtering. *Thin Solid Films*. 1995, 258, pp. 185-193.
23. **Suominen, L.S. Zhou, C. Korhonen, M.A. and Li, C.** X-Ray study of residual stresses in thin chromium metallizations on glass substrates. *The International Centre for Diffraction Data*. [Online] [Cited: 22nd August 2011.] [http://www.icdd.com/resources/axa/vol40/V40\\_544.pdf](http://www.icdd.com/resources/axa/vol40/V40_544.pdf).
24. **Marshall, R. Atlas, L. and Putner, T.** The preparation and performance of thin film thermocouples. *Journal of Scientific Instrumentation*. 1966, Vol. 43, pp. 144-149.
25. **Park, S.I., Lee, J.H., Lee, K.W. and Kim, K.J.** Characteristics of Micro-Thermoelectric Mass Flow Sensors with Si<sub>3</sub>N<sub>4</sub>/SiO<sub>2</sub>/Si<sub>3</sub>N<sub>4</sub> Thermal Isolation Membrane. *Japanese Journal of Applied Physics*. 2007, Vol. 46, 12, pp. 7916-7919.
26. **Petropoulos, A. Kaltsas, G. Speliotis, T. and Nassiolpoulou, A.G.** Evaluation of a gas flow sensor implemented on an organic substrate. *Physica status solidi*. 2008, Vol. 5, 12, pp. 3839-3842.
27. **Billat, S. Kliche, K. Gronmaier, R. Nommensen, P. Auber, J. Hedrich, F. and Zengerle, R.** Monolithic integration of micro-channel on disposable flow sensors for medical applications. *Sensors and Actuators A*. 2008, Vol. 145, pp. 66-74.
28. **Mattsson, C.G. Thungstrom, G. Bertilsson, K. Nilsson, H.L. and Martin, H.** Fabrication and evaluation of a thermal sensor formed on a thin photosensitive epoxy membrane with low thermal Conductivity. *Journal of Physics: Conference Series*. 2008, 100.

29. **Gelorme, J.D. Cox, R.D. and Gutierrez, S.** *Photoresist composition and printed circuit boards and packages made therewith.* 4882245 USA, 1989.
30. **Lorenz, H. Despont, M. Fahrni, N. LaBianca, N. Renaud, P. and Vettiger, P.** SU-8: a low-cost negative resist for MEMS. *Journal of Micromechanics and Microengineering.* 1997, 7, pp. 121-124.
31. **MicroChem.** Nano SU-8 Negative Tone Photoresist Formulations 2-25. [Online] [Cited: 23rd August 2011.] [http://www.microchem.com/pdf/SU8\\_2-25.pdf](http://www.microchem.com/pdf/SU8_2-25.pdf).
32. **Chatzichristidi, M. Rajta, I. Speliotis, T. Valamontes, E. Goustouridis, D. Argitis, P. and Raptis, I.** Aqueous base developable: easy stripping, high aspect ratio negative photoresist for optical and proton beam lithography. *Microsystems Technologies.* 2007, Vol. 14, 9-11, pp. 1423-1428.
33. **Solano, B.** *A Microgripper for Single Cell Manipulation.* PhD Thesis : Durham University, 2008.
34. **Chu, P.B. Chen, J.T. Yeht, R. Lin, G. Huang, J.C.P. Warneket, E.A. and Pister, K.S.J.** Controlled Pulse-Etching with Xenon Difluoride. *Solid State Sensors and Actuators.* 1997, Vol. 1, Transducers, Chicago, pp. 665-668.
35. **HD MicroSystems.** *Product Bulletin: PI-2600 Series—Low Stress Polyimides.* 2008.
36. **Rousche, P.J., Pellinen, D.S., Pivin, D.P., Williams, J.C., Vetter, R.J. and Kipke, D.R.** Flexible Polyimide-Based Intracortical Electrode Arrays with Bioactive Capability. *IEEE Transactions on BioMedical Engineering.* 2001, Vol. 48, 3, pp. 361-371.
37. **Xiao, S.Y. Che, L.F. Li, X.X. and Wang, Y.L.** A novel fabrication process of MEMS devices on polyimide flexible substrates. *Microelectronic Engineering.* 2008, 85, pp. 452-457.

## Chapter Four

### *Device Characterisation & Modelling*

---

Once fabricated, the device operation required verifying. This was achieved in two ways, firstly numerical models were created to demonstrate that the principle of operation was sound and secondly the devices were experimentally tested. The content of this chapter is split along these lines. The first section begins by discussing some relevant heat transfer theory before applying this to describe 1-D and 2-D models. These models are then used to demonstrate the device's operation by comparison with experimental data and used to justify the choice of substrates used in this work. The second section introduces the experimental operation of the devices. It begins with the characterisation requirements and discusses the method of calibration used to convert the emf generated by the thermocouples into a temperature. It concludes by demonstrating the proof of principle of the device as a tool for characterising the thermal conductivity of small volumes of liquid and porous materials. Before small volumes were probed, validation of the device's operation was conducted by measuring the thermal conductivity of large volume liquid samples. The size of the sample was then reduced to 100  $\mu\text{l}$  droplets to demonstrate that the sensor is capable of operating on smaller volumes. Finally, the ability of the device to monitor the water content of a thin porous sheet was established to demonstrate that the device could operate on a leaf-like material. For this, wetted paper served as a control specimen and the device was used to measure the drying time under various ambient temperatures.

## **4.1. Modelling**

Modelling served demonstrated that the principle of operation of the devices is sound. The models were compared with experimental data to validate their accuracy. They were then used to investigate the effect the substrate and sample had on the heat flow and hence results obtained. Some pertinent theory is introduced before the models.

### **4.1.1. Heat flow mechanisms**

#### **4.1.1.1. Conduction**

Macroscopic conductive heat transfer theory is based on the assumption that the mean free path of the carriers (phonons and electrons) is much smaller than the dimensions of the material in question. However, as the dimensions of a thermal conductor shrink to the microscopic scale, this may no longer be true. When the dimensions of the conductor begin to inhibit heat flow, the material is said to be in the size-affected domain. As the mean free path length varies with temperature and material composition, so too does the size at which size-affected domain features occur. However, Sobhan and Peterson [1] suggest that at around 293 K, size-affected domain features begin to occur when the thickness of a film is approximately 7 times the mean free path for conduction across a layer and 4.5 times the mean free path for conduction along the length of a layer.

In a metal (the thinnest layers used in this work) at 293 K, the mean free path length of an electron (the majority heat carrier) is of the order of 40 nm, meaning size-domain effects are important for thicknesses of 180 – 280 nm. The thinnest layers used in the work presented in this report were thin-film metal layers approximately 100 to 200 nm thick meaning size-domain effects would play a minimal role. The polymer layers had a thickness of  $\geq 10 \mu\text{m}$  and so would not be operating in the size-effected domain. Despite the polyimide layer being around 50 times thicker than the metal, the metal could still influence the flow of heat within the thermal system as it has a thermal conductivity approximately 1000 times higher. This would be mitigated as the

metal tracks were not continuous across the entire surface of the polyimide, however the effect could influence the modelling results and should be taken into account.

#### 4.1.1.2. Convection

Small dimensions can have an effect on the convective heat losses experienced by a microstructure. Conduction is dominant over radiative and convective heat losses in small thermal systems at the temperature the devices operate at [2]. A key parameter in convective heat transfer is the Rayleigh number. This is a dimensionless number which gives a measure of the importance of convection (i.e. buoyancy effects) to conduction. The Rayleigh number ( $Ra$ ) is given by Equation 4.1 and is the product of the Prandtl ( $Pr$ ) and Grashof ( $Gr$ ) numbers [3]:

$$Ra = Gr.Pr = \frac{g\beta(T_s - T_\infty)L_c^3}{\nu^2} \times \frac{C_p\rho}{k} \quad 4.1$$

Where  $g$  is the acceleration due to gravity,  $\beta$  the volumetric thermal expansion coefficient,  $T_s$  is the heated surface temperature,  $T_\infty$  the ambient temperature,  $L_c$  the characteristic length,  $\nu$  kinematic viscosity and  $C_p$  is the specific heat capacity,  $\rho$  is the density of the fluid and  $k$  the thermal conductivity.

Geometry plays an important role in determining this critical number. For example, the critical number for a free fluid heated by its lower boundary will be different to one heated by its upper boundary. However, for a free fluid heated by its lower boundary, the critical number is of the order of  $10^3$  [4], at which point convection begins to dominate over conduction. To give an indication of the importance of convection for the devices, Equation 4.1 was used to calculate  $Ra$  as 0.41 for water and 1.1 for IPA (using parameters from reference Table 4.1, which assume a heater at 60 °C on the lower surface of the liquid with characteristic dimensions of 100  $\mu\text{m}$  in a free volume at 20 °C, constrained only by its lower boundary). Thus, conduction will be dominant over convection for these micro-scale devices operating up to 60 °C.

**Table 4.1 – Parameters used to calculate the Rayleigh number for a heater on the lower surface of a volume of water and IPA**

Parameter	Unit	Water [3]	IPA [5] and [6]
$g$	$\text{m}^2 \text{s}^{-1}$	9.81	9.81
$\beta$	$\text{m K}$	$1.74 \times 10^{-4}$	$11 \times 10^{-4}$
$T_S$	K	353	353
$T_\infty$	K	313	313
$L_c$	m	$100 \times 10^{-6}$	$100 \times 10^{-6}$
$\nu$	$\text{m}^2 \text{s}^{-1}$	$1.08 \times 10^{-3}$	$2.4 \times 10^{-3}$
$C_p$	$\text{J kg}^{-1} \text{K}^{-1}$	4184	2370
$\rho$	$\text{kg m}^{-3}$	$1.0 \times 10^{-3}$	785
$k$	$\text{W m}^{-1} \text{K}^{-1}$	0.598	0.13

#### 4.1.1.3. Radiation

Radiative heat loss from a system is based on two factors: the surface area emitting the heat and the temperature difference between the surface and its surroundings. As the devices have a small area and achieve a temperature of less than 100 °C, heat loss through radiative processes will be minimal. As a guide, the emissive power due to radiation is given by Equation 4.2:

$$\frac{q_{RAD}}{A_S} = \varepsilon\sigma(T_S^4 - T_\infty^4) \quad 4.2$$

Where  $q_{RAD}$  is the radiative heat flow,  $A_S$  is the surface area from which heat is lost,  $\varepsilon$  is the emissivity,  $\sigma$  is Boltzman's constant,  $T_S$  is the temperature of the surface and  $T_\infty$  is the ambient temperature. Thus, for a circular area (e.g. heater in Design B devices) with a radius of 87.5  $\mu\text{m}$ , acting as a perfect black body radiator at a temperature of 60 °C and an ambient temperature of 20 °C, the heat lost through radiation will be  $1.7 \times 10^{-5}$  W. As the heater input is around 10 mW, such losses account for only 0.17 % of the total heat lost from the device and are effectively negligible.

#### 4.1.2.1-D model

By making some assumptions, it is possible to describe the device's operation using a 1-D steady state analytical model. The main assumption required is that the heat flow is isotropic, meaning

that the disturbance of the heat flow due to the substrate is negligible (i.e. it is a perfect insulator). If this is the case, the sample can be represented as a sphere with constant thermal conductivity. Using these assumptions and applying Fourier's law to a sphere leads to Equation 4.3:

$$q_{in} = -kA \frac{dT}{dr} = -k(4\pi r^2) \frac{dT}{dr} \quad 4.3$$

Where  $q_{in}$  is the heat transfer rate applied to the area represented by the locus of  $r_1$ , which is assumed to be the same as the power applied to the heater.  $k$  is the isotropic thermal conductivity,  $A$  is the area through which the heat flows,  $T$  is the temperature and  $r$  the radius. This is shown diagrammatically in Figure 4.1.

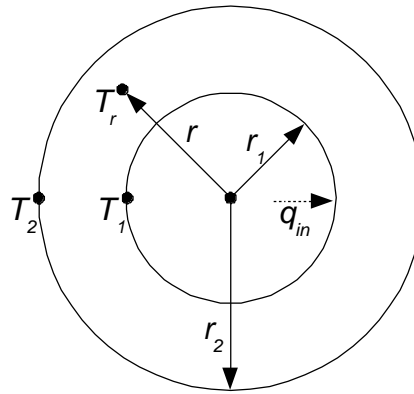


**Figure 4.1 – Simplified one-dimensional, steady state analytical model of conduction, based upon Fourier's law applied to a sphere with constant thermal conductivity**

Integrating Equation 4.3 and rearranging leads to Equation 4.4:

$$T_1 - T_2 = \Delta T_{1-2} = \frac{q_{in}(1/r_1 - 1/r_2)}{4\pi k} \quad 4.4$$

Where  $\Delta T_{1-2}$  is the temperature difference between points located at  $r_1$  and  $r_2$ .

For a device with a power input of 13.5 mW located in a large volume of liquid (i.e. with no edge effects), the temperature difference between points at radii of  $r_1 = 143.5 \mu\text{m}$  and  $r_2 = 253.5 \mu\text{m}$  is  $5.0 \text{ }^\circ\text{C}$  and if the water is replaced by IPA, the temperature difference increases to  $21.5 \text{ }^\circ\text{C}$ .

To validate this model, experimental results were obtained using a Design B type device on a polyimide substrate. The experimental method was similar to that in Section 4.2.3.1.1. The experimental results for water and IPA (taken from) are given in Table 4.2:

**Table 4.2 – A comparison of the 1-D model results with experimental values taken from Figure 4.13**

	Experimental results	1-D model
Water	2.3 °C	5.0 °C
IPA	11.4 °C	21.5 °C

The experimental results are significantly lower than the 1-D model suggests. This is likely to be due to the fact that the 1-D model assumes no losses through the substrate, leading to an isotropic heat flow. In reality, the heat flow will be disturbed by the substrate, suggesting that the assumption that the device acts like a sphere with constant thermal conductivity required to apply the 1-D model is flawed. Also, the heat source is planar, whereas the 1-D assumption requires a spherical heat source, this will also introduce geometric errors into the model.

A 2-D model is discussed further below, but a graphical representation of the results (Figure 4.2) clearly shows an asymmetry in the heat. Further details of the 2-D model are given in Section 4.1.3 and this model is shown to provide a much closer match to the experimental values obtained.

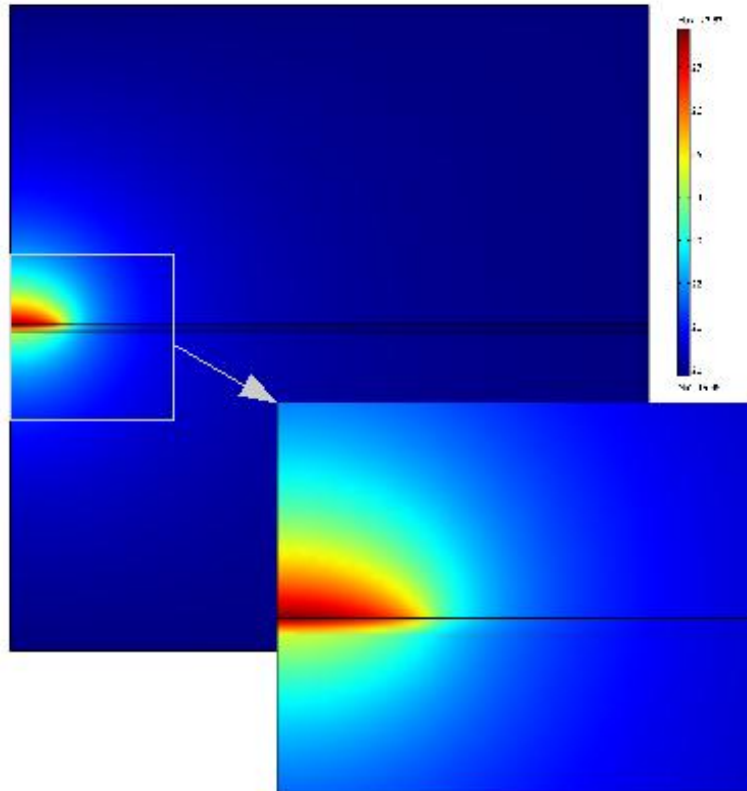


**Figure 4.2 – Visualisation from 2-D numerical model (COMSOL) based on a PI device surrounded by water**

#### **4.1.3.2-D model with axial symmetry**

The assumptions required to create a 1-D analytical model clearly exclude important elements of the physical phenomena affecting the device. These assumptions oversimplify the problem and introduce significant errors. However, moving to a 2-D or 3-D analytical model for all but the simplest geometries quickly complicates the mathematics required to describe the situation (e.g. [7]) and can even preclude any exact analytical solutions [3]. The best alternative in such cases is to move to a numerical method.

A full 3-D model quickly becomes computationally intensive due to the very refined meshes required to include the thin substrate and metal layers and relatively large sample volumes. However, Design B introduces a circular heater to the device. This offers a simplification to the model, as the problem can be described in two dimensions with the application of an axial symmetry.

All numerical models were run within COMSOL Multiphysics V3.5a (COMSOL), which is a modelling package designed to solve partial differential equations (PDE). COMSOL is designed to solve coupled physics phenomena. However, it is still a suitable package for modelling heat transfer describing the operation of the devices. The module used for the 2-D models described in this section was “Heat Transfer by Conduction” and both steady state and transient analysis were used.

The process for generating a model within COMSOL involves describing the geometry and creating a ‘mesh’ of nodes for which the PDE will be solved which fit within the geometry. COMSOL models heat transfer problems using the following PDEs (Equation 4.5 for transient problems and Equation 4.6 for steady state analysis):

$$\delta_{ts}\rho C_p \frac{\partial T}{\partial t} - \nabla(k\nabla T) = q \quad 4.5$$

$$-\nabla(k\nabla T) = q \quad 4.6$$

Boundary conditions are used to describe the geometry of the model. The boundary conditions for a ‘standard’ model are shown in Figure 4.3. Subsequent models use this ‘standard’ model and alter different aspects of the model (e.g. the mesh quality or the overall dimensions) to investigate the effect of each parameter on the device. The left hand edge of the model is set as an insulating boundary (Equation 4.7), and represents a symmetric boundary which forms the axis about which the model is swept to give axial symmetry. All other external boundaries were set to a constant ambient temperature of 293 K (Equation 4.8). A volume representing the sample under test was placed above and below a 10  $\mu\text{m}$  thick polyimide substrate, with dimensions as shown in Figure 4.3. The choice of these dimensions is justified in Section 4.1.4. The heater was modelled as a strip of Ni 87.5  $\mu\text{m}$  in radius and 200 nm in thickness with a heat flux discontinuity representing the heater input (Equation 4.9). A 200 nm thick layer of Ni at a depth of 2.5  $\mu\text{m}$  below the polyimide top surface was added to represent the TFTCs and tracks. While in reality the metal layer would not be continuous, a significant proportion of the surface was metallised and would influence the results (see Section 4.1.1.1).

Insulation:	$(k\nabla T) = 0$	4.7
Constant temperature:	$T = T_x$	4.8
Heat flux discontinuity:	$(k\nabla T) = q_{in}$	4.9

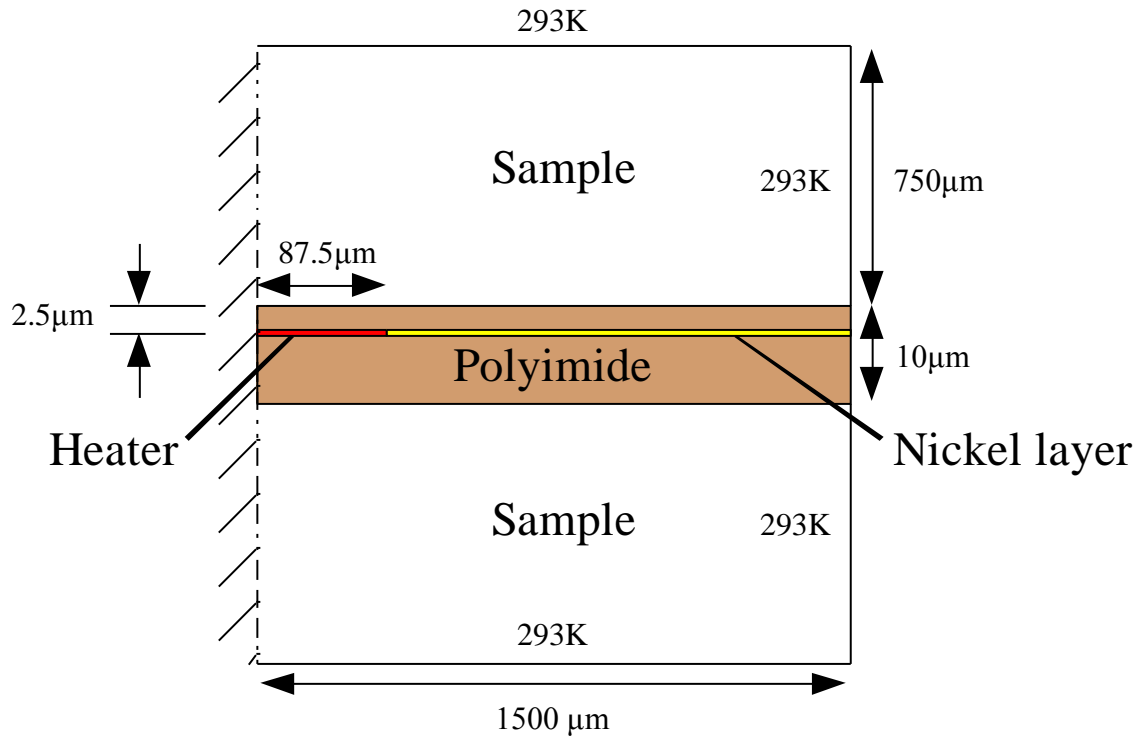


**Figure 4.3 – The ‘standard’ model. These geometries and boundary conditions were used to create a 2-D model with axial symmetry**

The following sections vary aspects of the ‘standard’ model to justify design choices and show the principle of operation of the device. Sections 4.1.4 and 4.1.5 discuss the effects of the model’s geometry and the quality of the mesh on the model’s output. Section 4.1.6 demonstrates the operation of the device by modelling two liquid samples with different thermal properties and Section 4.1.7 outlines how the substrate affects the device’s response.

#### **4.1.4. Dimensional effects of the model**

To allow a comparison between the numerical model results and those obtained experimentally, it was necessary to design a suitable setup that would allow such a comparison to be made. In order to describe the system to create the numerical model, the system boundaries and subdomains needed to be set up. As such, modelling small droplets would prove challenging as the exact

boundary conditions would depend on the size of the droplet and the losses that the droplet would experience. This would introduce too many variables, as gauging the correct losses would require an iterative process to compare the model and experimental results. This would be counterproductive, as the intention was to create a model which could independently verify the experimental results. Thus, to validate the model, the model's output was compared with experimental values obtained by submerging the device in a large volume of water, which is effectively infinite (i.e. edge effects have minimal effect). This simplifies the model by minimising edge effects. However, it also leads to a potentially very large volume to mesh. This results in a trade off between small, finely meshed models with edge effects or larger, coarsely meshed models with smaller edge effects.

To determine the optimal volume required to reduce the error induced by edge effects whilst producing a workable model, several models were created by systematically increasing the dimensions and comparing the outcomes. The nominal radius of 1500  $\mu\text{m}$  in the 'standard' model (Figure 4.3) was varied from a radius of 200  $\mu\text{m}$  to 20000  $\mu\text{m}$ , with the aspect ratio kept constant (height = half the width). The boundary conditions were otherwise unaltered. The model's boundary conditions are shown in Figure 4.4.

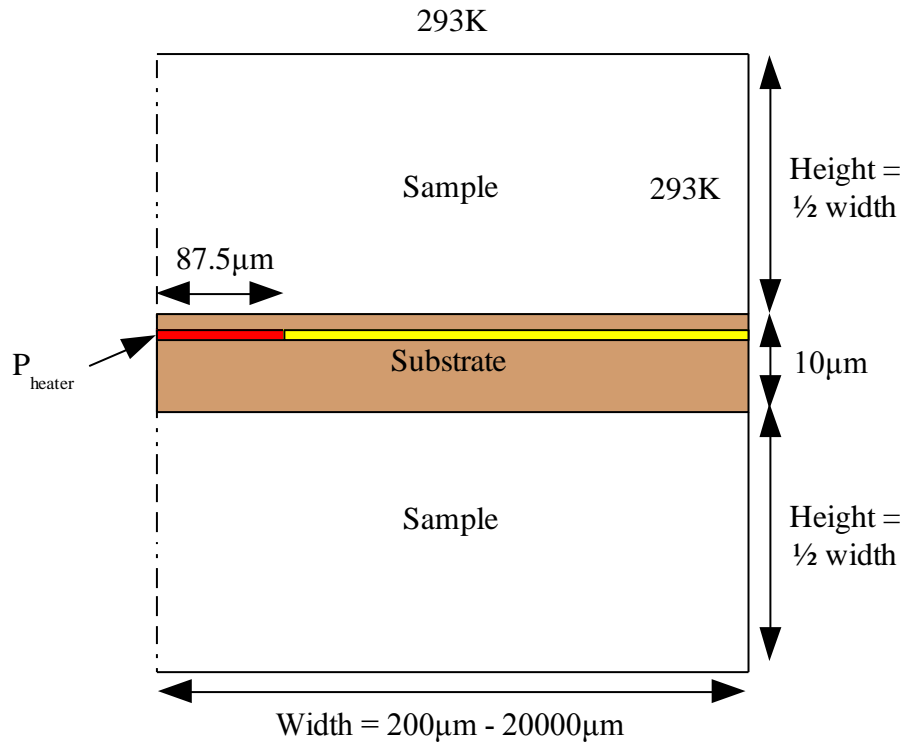


**Figure 4.4 – Boundary conditions used to investigate the effect of the model’s dimensions**

The results were obtained by extracting the maximum steady state temperature observed along a line drawn 2.5 µm below the top edge of the substrate (to represent the location of the TFTCs) and normalising these to the asymptotic maximum observed. For small radii, the influence of the constant temperature boundary was seen to cool the sample, creating artificially low readings. This could be corrected by modelling the boundary as a convective loss, however obtaining an accurate value for the loss rate would have to be verified experimentally.

As the radius of the sample increases, the effect is seen to diminish – see Figure 4.5. The difference in maximum temperature between a model with a radius of 1500 µm (the radius chosen for the ‘standard’ model) and a model with a very large radius of 20000 µm was only 2.9 %. Thus, 1500 µm was seen to be a suitable choice of radius, which introduces only a small error, while reducing the volume being modelled. This also indicates that real sample volumes with dimensions of only 3 mm (~50 µl for a hemispherical droplet) across would show little degradation in performance due to edge effects.

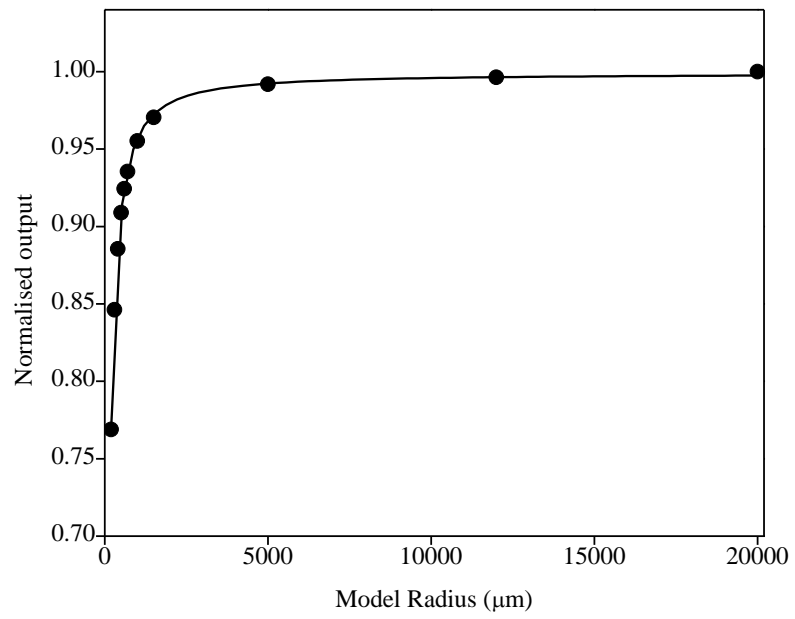


**Figure 4.5 – The radius of the model is seen to play a diminishing role as the volume of the model increases**

#### 4.1.5. Effect of the mesh quality

The accuracy of a numerical solution depends on the mesh quality [8]. A poorly produced model will offer different results for various mesh qualities. However, there is normally a trade off between computational time and mesh quality. To ensure that the mesh generated for the model was suitable, the mesh size was doubled to create a coarser mesh and the results compared by normalising the temperature observed along a line drawn 2.5  $\mu\text{m}$  below the top edge of the substrate. The results are shown in Figure 4.6. At either extreme of the line, the models agree and the maximum deviation was seen as the line cross the edge of the heater resulting in a discrepancy of only 1.1 %. Thus the coarser mesh was capable of producing very similar results to that of a finer mesh, indicating that the mesh quality was sufficient, while also being computationally efficient.

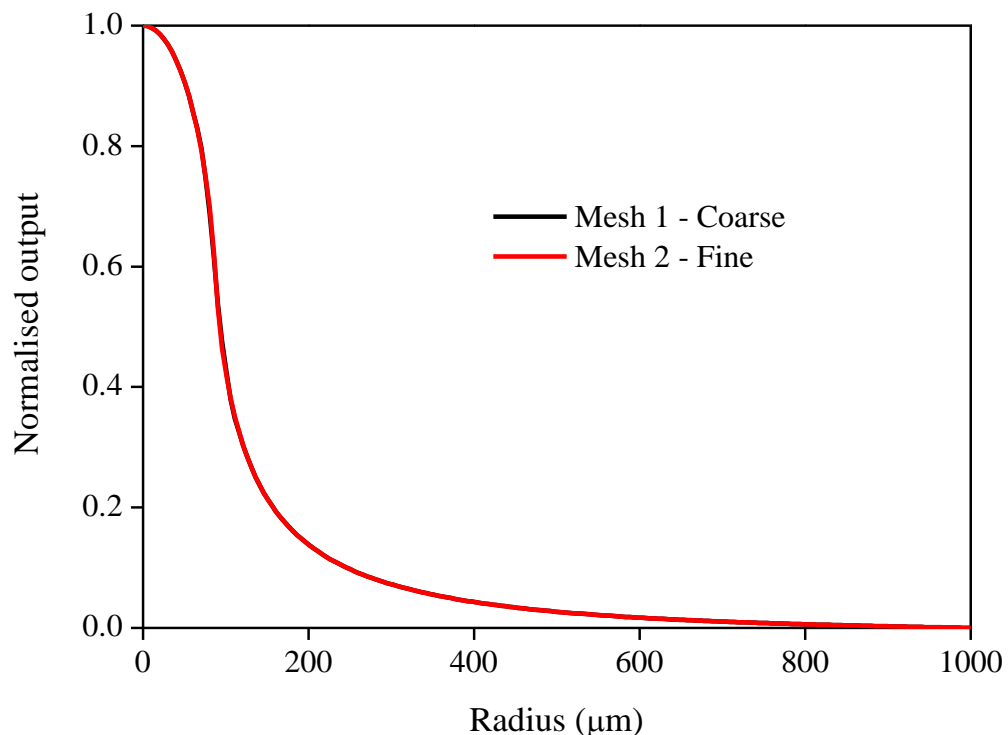


Figure 4.6 – A comparison of two meshes shows that the coarse mesh is adequate as decreasing the mesh size has no effect on the output

#### 4.1.6. Sample thermal conductivity

This section compares the model with experimental results. The aim is twofold: to validate the model and to demonstrate that the experimental results are consistent with heat transfer theory. The ‘standard’ model (Figure 4.3) was used with the thermal properties of two samples: water and IPA. It was run in transient mode to represent a time period of 2.2 s, which was seen to be long enough to give a good indication of the steady state response and was comparable to the period of time for which experimental values were recorded using a storage oscilloscope (for further details on the experimental results see Section 4.2.3.1.1). In brief, the sensing area of a Design A device formed on a polyimide substrate was submerged in the liquid under test and a power of 13.5 mW was applied to the heater. This power level was found experimentally to give a suitable range of readings for both the water and IPA samples, without excessively heating the sample and boiling the IPA (the nearest junction recorded a maximum temperature of ~42 °C). The liquids were contained in a 50 ml beaker, creating a relatively large volume of water to prevent any edge effects altering the results. The reference junctions were also submerged, to give a differential reading relative to the ambient temperature of the liquid.

The thermal properties used within the model are given in Table 4.3. The liquid samples were chosen as their thermal properties are widely available in literature and they do not suffer from the complication of thermal contact resistance and therefore allow a straightforward comparison between the model and the experimental data. The model assumes that the main mechanism of heat flow is through conduction, rather than convection or radiation, as justified in Section 4.1.1 and 4.1.1.2. The temperature was recorded 2.5  $\mu\text{m}$  below the top surface of the polyimide layer at radii of  $r_1 = 143.5 \mu\text{m}$  and  $r_2 = 253.5 \mu\text{m}$ . This is representative of the locations of the TFTC sensing junctions formed on Design B type devices at distances from the edge of the heater of 50  $\mu\text{m}$  and 160  $\mu\text{m}$  respectively.

**Table 4.3 - Thermal properties used to generate the model results shown in Figure 4.7**

	Water [3]	IPA [5]	Polyimide [9]
Thermal conductivity ( $\text{W m}^{-1} \text{K}^{-1}$ )	0.60	0.13	0.1
Heat capacity ( $\text{J kg}^{-1} \text{K}^{-1}$ )	4190	2370	1087
Density ( $\text{kg m}^{-3}$ )	1000	785	1400

The model and experimental results are compared in Figure 4.7. Each liquid sample produces a different thermal gradient which is based on its thermal properties (water give a  $\Delta T$  measurement of  $2.7\text{ }^{\circ}\text{C}$  while IPA gives  $\Delta T$  as  $12.2\text{ }^{\circ}\text{C}$ ). This is important as it indicates that the principle of the device is sound and the temperature difference ( $\Delta T$ ) between the two junctions can be used to distinguish between samples with different thermal conductivities.

The experimental results for water show a good agreement with only small differences observed between the experimental and model results. The IPA results show a large discrepancy. The maximum difference is observed at the furthest junction during the transient phase, where the discrepancy between the model and experimental results is within  $\sim 5\%$  however in steady state the difference is only around half this. The discrepancy for IPA is likely to be due to convective effects due to the increased Rayleigh number for IPA compared with water. However, it should be noted that the errors are still small and conduction is dominating the thermal system ( $Ra_{IPA}$  was much smaller than the critical value).

Such a result demonstrates that the model can be used to investigate certain parameters about the device's operation, without having to fabricate a number of devices. The following section utilises this to show the effect the substrate has on the device's operation.

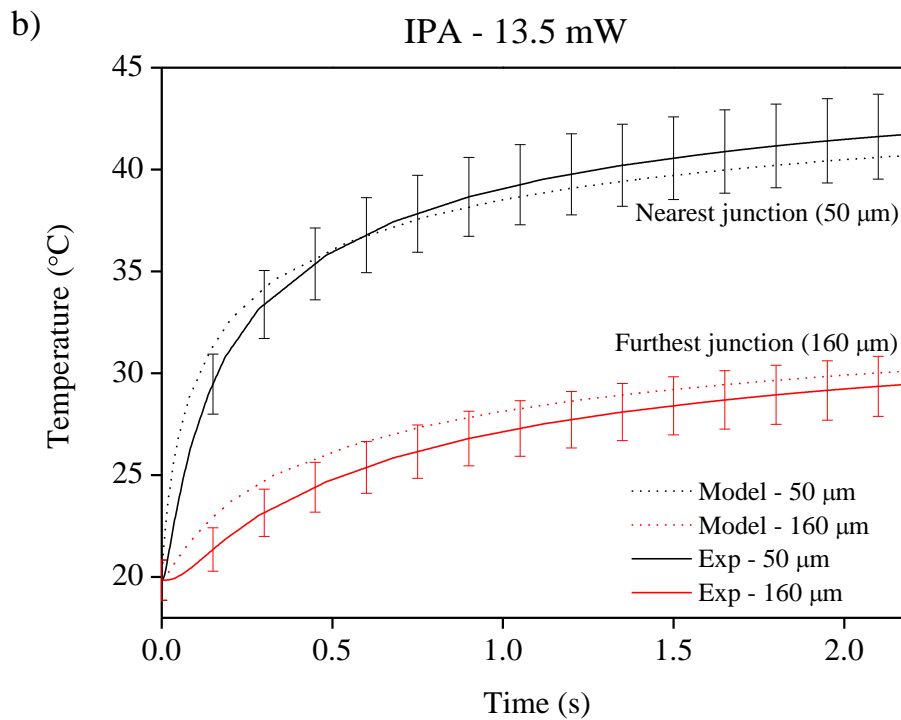
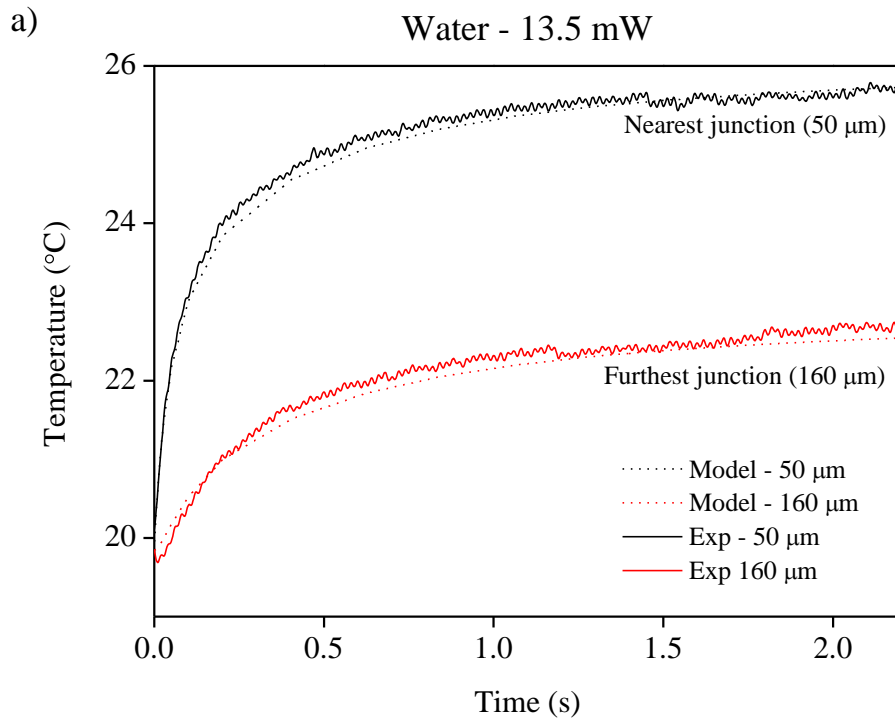


Figure 4.7 – Validation of model by comparison with experimental results for a) water and b) IPA, based on a heater input power of 13.5 mW ( $\pm 5\%$  error bars added to the IPA graph)

#### 4.1.7. Effect of the substrate

Microfabricated thermal sensors can offer much greater sensitivity than traditional devices, due to their small thermal mass (e.g. [10]). As the TFTCs are 200 nm thick or less, the substrate will tend to dominate the thermal response as they were at least 10  $\mu\text{m}$  thick. Within this work, 4 substrates were used: polyimide, SU-8 (membrane suspended from silicon substrate), glass microscope slides and oxidised silicon wafers. Early devices were fabricated on glass microscope slides and oxidised silicon wafers for ease of fabrication, as these substrates require little processing beyond metallisation and patterning. However, these substrates have a thickness of  $>100 \mu\text{m}$  and so offer a much larger thermal mass than the thin polymer based substrates used in later work which lead to early devices having a poor thermal sensitivity. The polyimide and SU-8 membrane devices have a thickness around 10  $\mu\text{m}$  as well as having much lower thermal conductivities – see Table 4.4.

**Table 4.4 – Thermal conductivity and thickness values used for the substrate within the model**

	Polyimide [9]	SU-8[11]	Glass [3]	Silicon [12]
Thermal conductivity ( $\text{W m}^{-1} \text{K}^{-1}$ )	0.1	0.3	1.4	150
Thickness of substrate available ( $\mu\text{m}$ )	1 - 20	1 - 50	275	275

The thermal properties and reduction in thickness means the polyimide and SU-8 devices are expected to outperform the glass and silicon devices. To demonstrate this, the ‘standard’ model from Figure 4.3 was used to investigate the 4 substrates. To compare the devices, the model was run with a sample with the thermal properties of water. The temperature was recorded along a line drawn across the top of the substrate, which is representative of the location of the TFTCs. The model was run in steady state mode and the outputs were normalised to the maximum steady state value (which was observed with the polyimide substrate) to allow a comparison to be made. Results are shown in Figure 4.8.

A higher normalised output indicates that more of the heat flows through the sample, which makes the device more sensitive to the changes in the thermal property of the sample. It is clear that the two polymer substrates outperform the glass and silicon substrates. This is due to the

combination of smaller substrate volume and better thermal properties. The polyimide is capable of producing the largest thermal gradient, however there is only a 10 % difference between the polyimide and the SU-8. As such, the decision over which substrate to use should rest with the ease of fabrication and suitability for application.

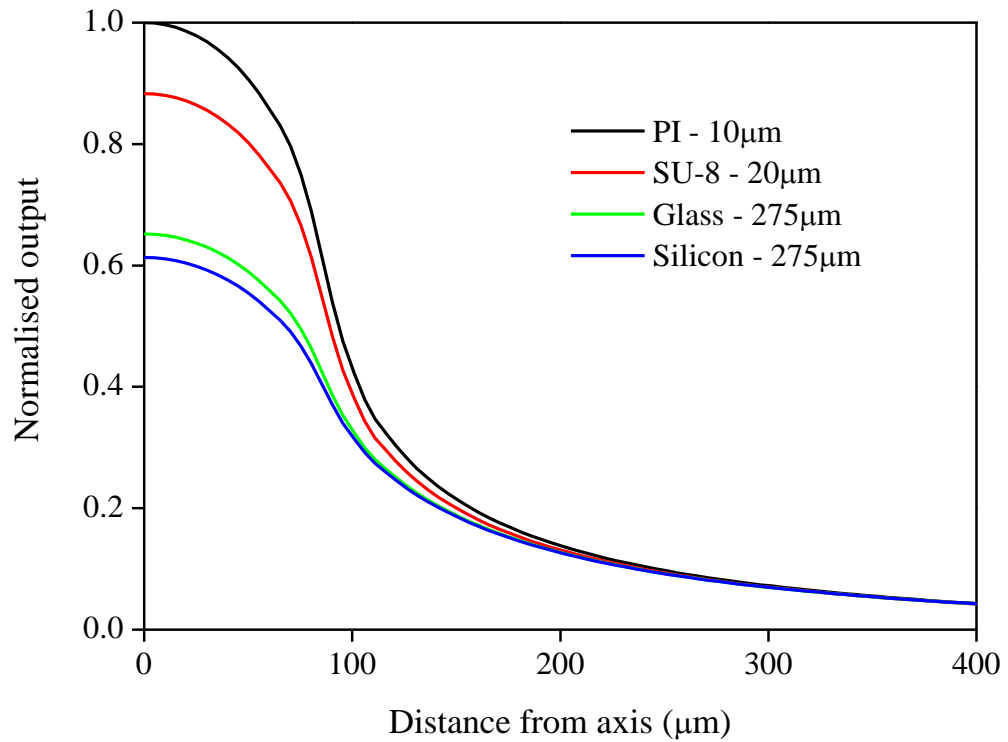


**Figure 4.8 – Normalised results from models run using the spatial and thermal properties of the 4 different substrate types used during this work. The key shows the substrate type and its thickness**

## 4.2. Characterisation

### 4.2.1. Characterisation requirements

There are two elements to the characterisation of the devices. The first requirement is calibration of the device (i.e. convert the thermally generated emf to a temperature). The second requirement is to relate the measured temperature difference between the two TFTCs ( $\Delta T$ ) to the thermal conductivity of the sample. This was achieved by comparing the device's output when samples of known thermal conductivity were brought into contact.

In actual fact, the comparative nature of the device's characterisation (comparing the output for known samples against unknown samples) negated the need for temperature calibration. Comparing the output voltage for different samples would be sufficient to allow the thermal conductivity to be ascertained. However, converting the voltage into a temperature allowed the operation of the thermocouples to be investigated (e.g. Section 3.1.3.2 – thin-film effects) and also gave a useful indication of the temperatures generated by the device. For example, excessively high temperatures may cause boiling of liquid samples or damage to leaves, so a knowledge of the absolute temperature was useful. Section 4.2.2 gives details of the calibration method used to convert the output voltage into a temperature.

To prove the principle of operation of the device, large volumes of liquid were used initially (Section 4.2.3.1.1). Three liquids with different thermal conductivities (water, IPA and glycerine) were tested and the outputs compared with the known thermal conductivity values of the samples. Once the operation proved to be successful, smaller volumes (100  $\mu\text{l}$ ) of liquid were tested in order to demonstrate that by microfabricating the devices, they were capable of operating on small samples.

Liquid samples were used initially as they remove the complex issue of thermal contact resistance. The final element of the characterisation of the devices was to measure changes in the thermal properties of a thin, porous material and relate these changes in its water content. This is demonstrated in Section 4.2.3.2 where the device is used to monitor the thermal properties of

wetted paper and relate these to its water content. As dry paper will have a low thermal conductivity (e.g. between  $0.05 \text{ W m}^{-1} \text{ K}^{-1}$  [13] to  $0.18 \text{ W m}^{-1} \text{ K}^{-1}$  [14]) and water has a higher thermal conductivity ( $0.60 \text{ W m}^{-1} \text{ K}^{-1}$  [14]), then it is clear that an increase in the water content of the paper will lead to an increase in the thermal conductivity. Section 4.2.3.2 demonstrates that the device is capable of detecting this change and relating the change to the water content of the paper. This work has been published in a peer reviewed journal [15].

#### **4.2.2. Temperature calibration**

Thermocouples generate an open circuit voltage which is proportional to the temperature difference between the sensing ('hot') junction and the reference ('cold') junction. For standard metal combinations (e.g. K-type: chromel / alumel) reference tables exist (e.g. [16]) which can be used to convert the generated emf into a temperature difference. However, as the thermocouples used during this project were sputtered, it was not possible to deposit thin films with precise alloy proportions. While this aided the fabrication of the devices it meant that each would have to be individually calibrated as the standard reference tables could not be used. In addition, the thin film nature of the thermocouples meant that bulk characteristics could not be guaranteed (Section 3.1.3.2).

To allow the generated emf to be converted into the temperature difference between the sensing and reference junctions, calibration was required. This was achieved by applying a known temperature to the sensing junction using an external, wire-wound  $68 \Omega$  power resistor. The temperature of the surface of the wire-wound resistor was monitored by a K-type thermocouple. The emf generated by the TFTCs on the device was compared with the temperature recorded by the K-type thermocouple. The reference junctions were maintained at the ambient temperature throughout. It should be noted that this calibration method could only be applied to polyimide based devices, as it would damage those devices patterned on silicon and glass substrates.

The wire-wound resistor was clamped over the surface of the device and a thermal paste was applied between the resistor and the device to ensure good thermal contact was achieved. The

same paste was also used to ensure good contact was achieved for the K-type thermocouple which was secured in place using an epoxy resin adhesive. Various electrical powers up to 500 mW were applied to the wire-wound resistor to generate a range of temperatures from the ambient 20 °C up to around 45 °C.

It should be noted that the calibration result can be shifted up and down by the control electronics as the instrumentation amplifier has an additional op-amp used to provide output offset trimming. Trimming is controlled by a variable resistor and provides a d.c. bias to the output of the instrumentation amplifier. This serves a useful purpose as the variable resistor can be used to null the output at the ambient temperature. To prevent any drift in the measurement due to thermally induced changes in the resistance of the variable resistor, the amplifier was powered up for around 15 minutes prior to operation.

The temperature measured by the K-type thermocouple was recorded and compared with the output of the device. A schematic diagram of the experimental set up is shown in Figure 4.9 and a photograph in Figure 4.10. A typical calibration result is shown in Figure 4.11. The devices were seen to operate with Seebeck coefficients slightly below that for bulk, generally achieving a value of 29 – 33  $\mu\text{V } ^\circ\text{C}^{-1}$  compared with the expected 36.3  $\mu\text{V } ^\circ\text{C}^{-1}$  [17]. The drop in performance versus bulk values was only 8 – 15 %, so the devices were still capable of operating once they had been calibrated and the signal amplified.

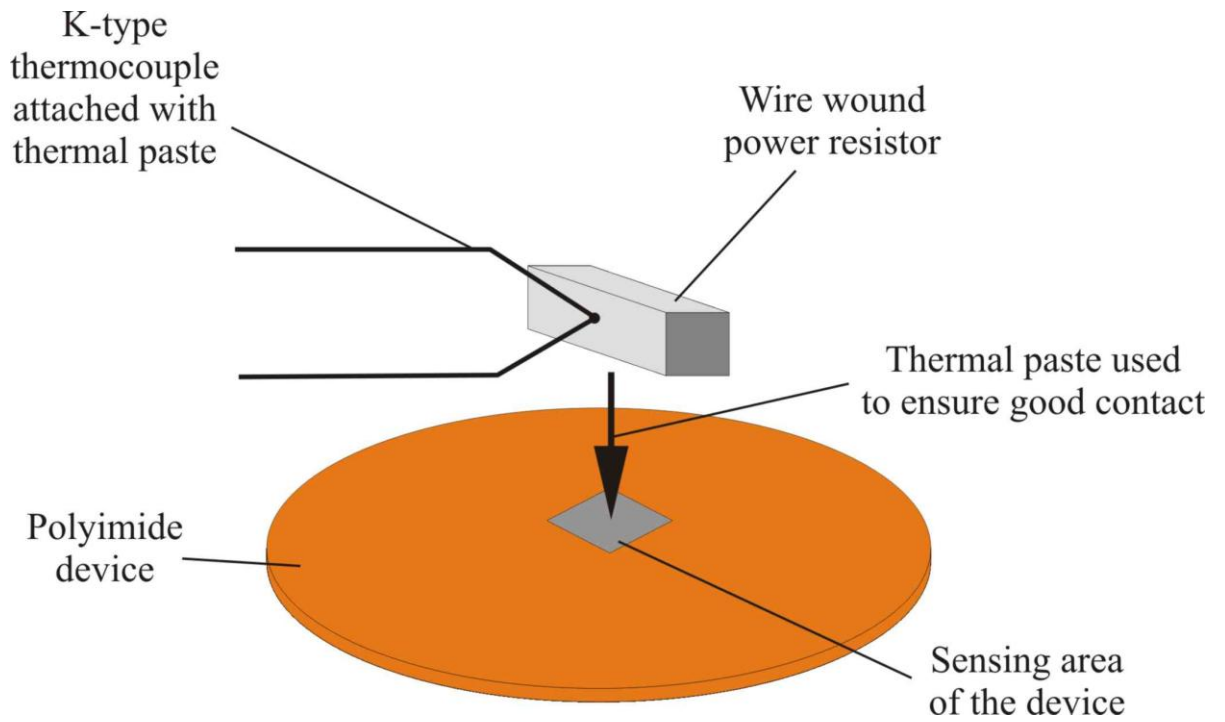


Figure 4.9 – Schematic diagram of the calibration set up

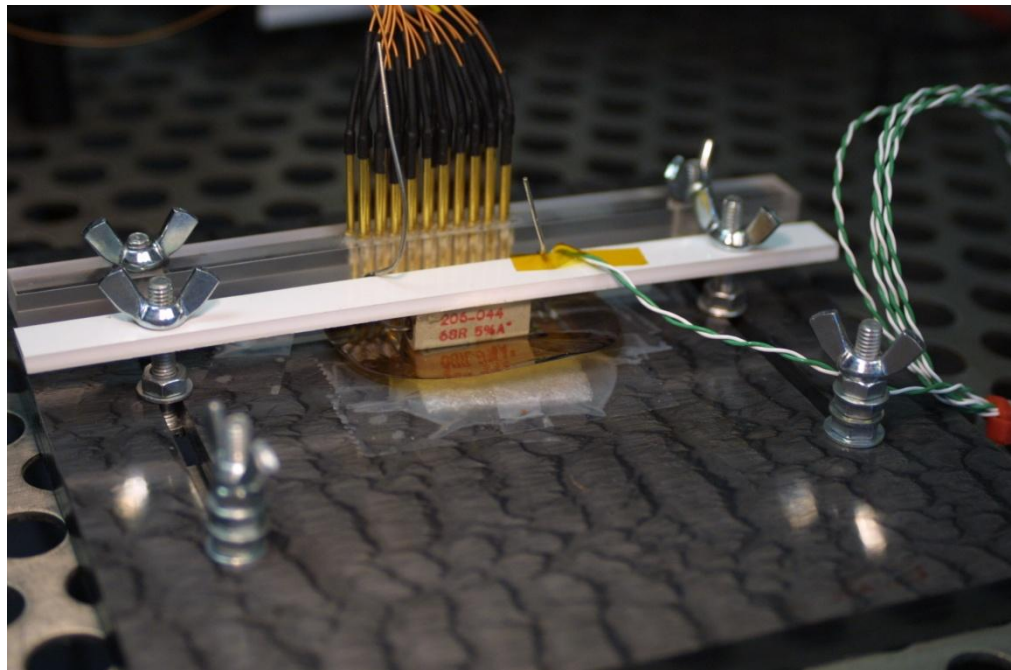
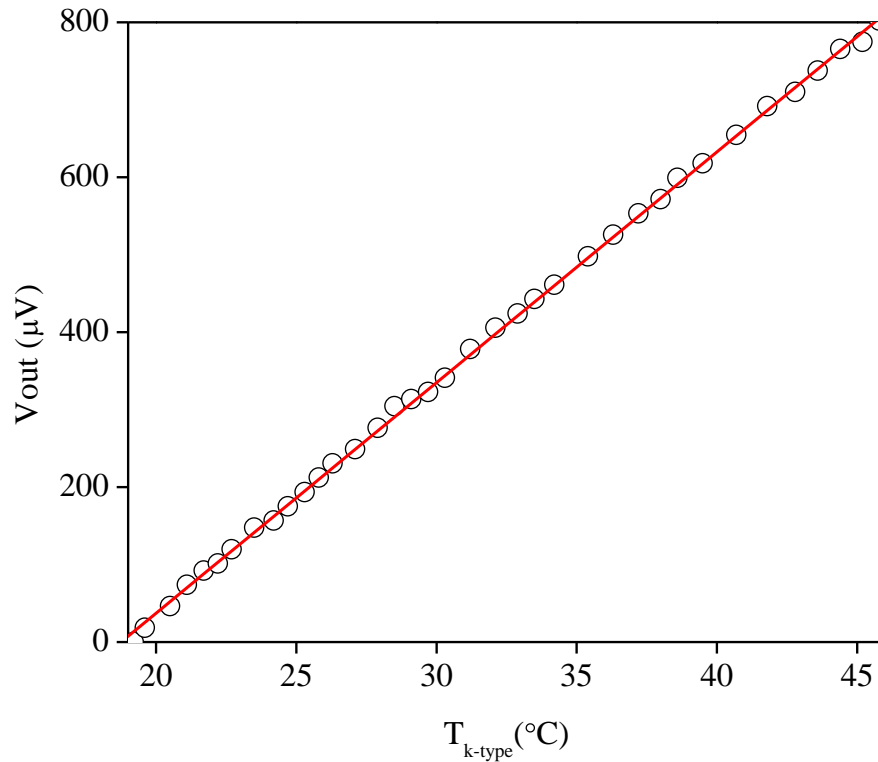


Figure 4.10 – Photograph of the wire-wound resistor clamped over the sensing area of the device for temperature calibration



**Figure 4.11 – A typical calibration result for a device fabricated with 100 nm Cr and 200 nm Ni ( $V_{\text{out}}$  calculated prior to amplification with a gain of 10083)**

#### **4.2.3. Monitoring thermal properties of small samples**

Once calibrated, the devices were used to measure the material properties of various samples. This section discusses experiments to measure the thermal conductivity of liquid samples and the drying rate of wetted paper (reported in [15]). To prove that the output of the device can be related to the thermal conductivity of a sample, experiments were initially conducted on large volumes of liquid (~50 ml) to remove the possibility of size dependent effects influencing the results. The size of the sample was then reduced to 100  $\mu\text{l}$  droplets, demonstrating that the small dimensions of the device and the thin polyimide substrate enable the device to operate on small volumes. For this, 100  $\mu\text{l}$  glycerine/water samples were used as the values for the thermal conductivity are available in literature [18]. Once this relationship was established, it was possible to use the device to monitor liquid samples of unknown thermal conductivity. For this, the

dependence of thermal conductivity of IPA/water mixtures on composition has been detailed (Section 4.2.3.1.2), as the nominal values are not available in literature.

In order to show that the device is capable of monitoring the thermal properties of smaller volumes with time dependent thermal properties, the final section outlines the relationship between water content and  $\Delta T$  by monitoring the drying rate of wetted paper. Paper was chosen due to its thickness ( $\sim 100 \mu\text{m}$ ) and ability to absorb water and dry over a reasonable time (10 - 60 minutes).

#### 4.2.3.1. *Liquid samples*

##### 4.2.3.1.1. *Large volumes – 50 ml*

Before small volumes were investigated, the operation of the device was validated on large volumes of liquid. Larger volumes reduce the complexity of the thermal system, as the body surrounding the device is very large in comparison to the device, preventing edge effects from interfering. To achieve this, the sensing area of the device was completely submerged within a beaker of liquid. This allowed the output of the device ( $\Delta T$ ) to be related to the nominal values of thermal conductivity ( $k$ ). For this experiment, three liquids were chosen based on their thermal conductivity, giving a range from  $0.13$  to  $0.60 \text{ W m}^{-1} \text{ K}^{-1}$ :

- Water  $k_{\text{water}} = 0.60 \text{ W m}^{-1} \text{ K}^{-1}$  [3]
- Glycerine  $k_{\text{glycerine}} = 0.29 \text{ W m}^{-1} \text{ K}^{-1}$  [18]
- IPA  $k_{\text{IPA}} = 0.13 \text{ W m}^{-1} \text{ K}^{-1}$  [19]

The sensing area of the device was submerged into a 50 ml beaker filled with the liquid being tested and a heater input of 13.5 mW was applied to the resistive heater of a Design A type device formed on a polyimide substrate. This heat input was found experimentally to be large enough to provide a measureable change for water, without causing boiling when operating on any of the liquids. While the transient response was recorded (after conditioning using the instrumentation amplifier described in Section 3.3) by a storage oscilloscope (DSO3102A, Keithley) from when the heater input was applied, for the validation of the device reported here, only the steady state

response was required. The steady state response of  $\Delta T$  was noted after a period of 2.2 s. An example of the transient response of the difference in temperature recorded by the two TFTCs when the device was submerged in IPA is shown in Figure 4.12 and the combined steady state results for all three liquids are shown in Figure 4.13.

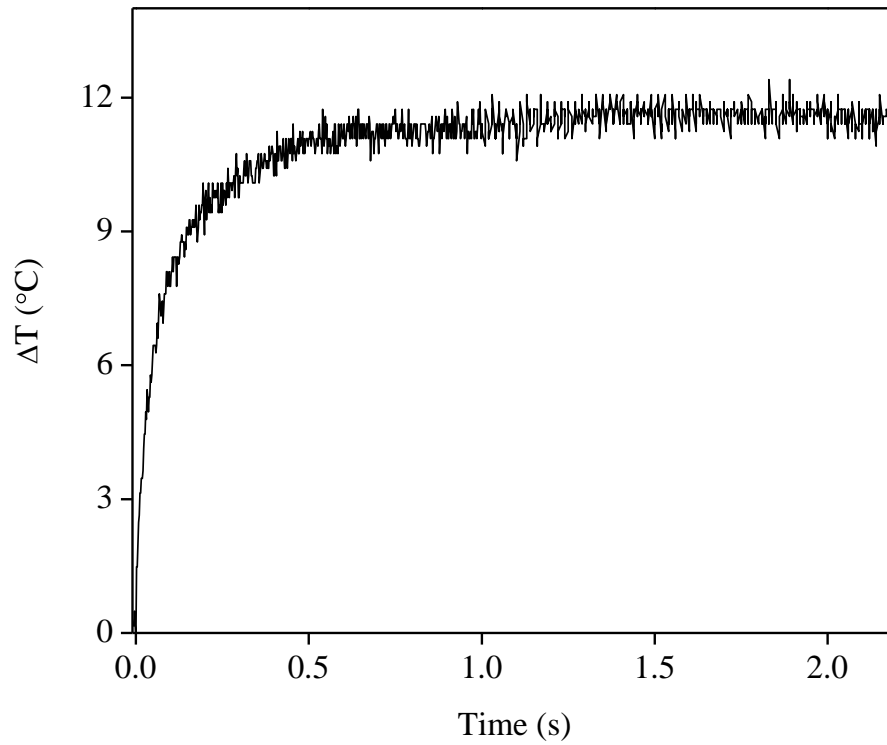


**Figure 4.12** – Transient response of  $\Delta T$  for a device submerged in IPA with a heater input of 13.5 mW

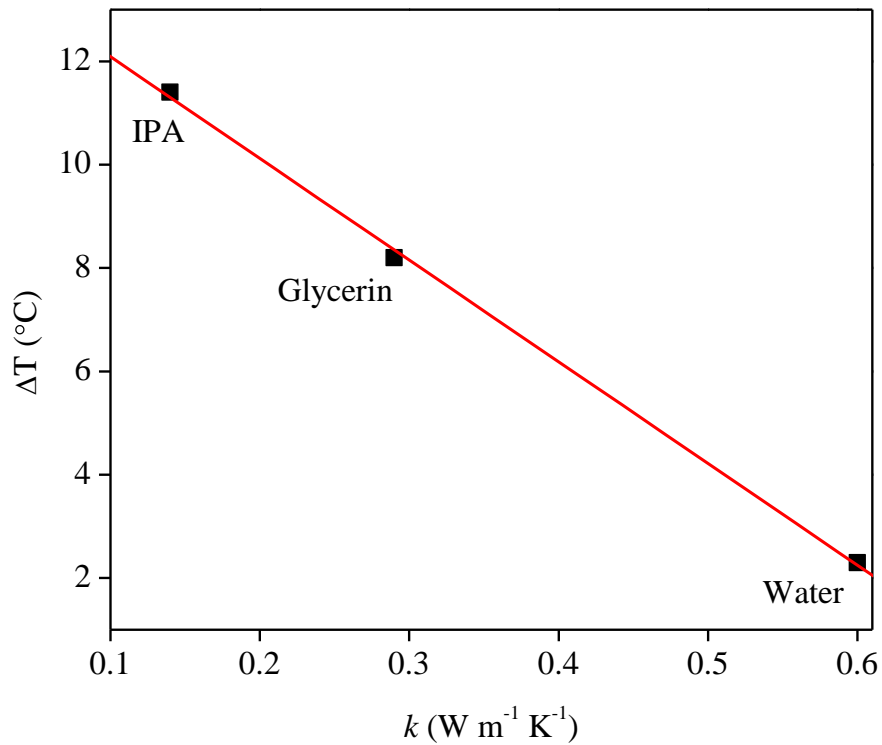


**Figure 4.13 – Steady state  $\Delta T$  values observed for large volumes of three liquid samples: IPA, glycerine and water**

While three data points are insufficient to draw a firm conclusion on the relationship between  $\Delta T$  and the thermal conductivity of the liquid, the three results appear to have a linear response which is inversely proportional to thermal conductivity. Theory and later experiments on smaller volumes back up this assertion. As the setup will broadly approximate the 1-D case for a point heat source located within an infinite volume, the  $\Delta T$  values should be inversely proportional to the thermal conductivity of the sample:

$$\Delta T \propto \frac{1}{k} \quad 4.10$$

Using a linear fit for the experimental results obtained during this experiment yields Equation 4.11:

$$\Delta T = -19.7k + 14.1 \quad 4.11$$

Equation 4.11 relates the device's output to the thermal conductivity of liquid samples in the range  $0.13 - 0.60 \text{ W m}^{-1} \text{ K}^{-1}$  and demonstrates that the device's output is intrinsically linked to the thermal conductivity of the sample it is in contact with. This shows that the device is capable of monitoring the thermal conductivity of a sample. The following section demonstrates that reducing the size of the sample to  $100 \mu\text{l}$  does not impede the ability of the device to make comparative assessments of the thermal conductivity of liquid samples.

#### **4.2.3.1.2. Small volumes – $100 \mu\text{l}$**

Having demonstrated that the device can distinguish between large volumes of liquid with differing thermal conductivities, the sample size was reduced to  $100 \mu\text{l}$ . Two important principles are demonstrated here: firstly that the device can perform a similar comparison of thermal conductivity on  $100 \mu\text{l}$  samples with known thermal conductivities. Secondly, that the device can be used to measure the thermal conductivity of samples of unknown thermal conductivity, by comparison with samples of known thermal conductivity.

To demonstrate that the device can operate on small samples, glycerine and water mixtures were made up at various mixture ratios at 20 % by weight intervals from pure water to pure glycerine. At  $20 \text{ }^\circ\text{C}$ , the thermal conductivities of the six samples so prepared ranged from  $0.60$  to  $0.29 \text{ W m}^{-1} \text{ K}^{-1}$  for pure water and pure glycerine respectively [18]. Intermediate values were interpolated from the values given in [18]. These mixtures were used to record reference  $\Delta T$  values for the device. Six mixtures of IPA and water were also made up at 20% intervals by weight. The thermal conductivity of IPA / water mixtures is not available in literature. However, pure IPA has a thermal conductivity of  $0.13 \text{ W m}^{-1} \text{ K}^{-1}$  at  $20 \text{ }^\circ\text{C}$  [19]. This offered an opportunity to use the device to measure the thermal conductivity of a sample with an unknown thermal conductivity.

A small piece of tubing was attached to the surface of the polyimide substrate of a Design A device, as shown in Figure 4.14. The purpose of the tubing was to contain the liquid and ensure that it covered the sensing area of the device. A  $100 \mu\text{l}$  droplet was placed within the tubing and

5 mW was applied to the resistive heater. 5 mW was chosen for the heater input as it was high enough to provide a measurable change when water was used, but low enough to prevent boiling when IPA was used. The power input was lower for the droplets due to the much smaller thermal mass present.

$\Delta T$  values detected by the TFTC junctions located at distances of 75  $\mu\text{m}$  and 150  $\mu\text{m}$  from the heater were recorded. Due to its small mass, the system reached 90% of its steady state value within 1 s and the final steady state value was recorded after 2.2 s. This period was therefore sufficiently long that steady state was reached, so differences in the heat capacity of the liquids did not influence the measurements. The results for both the glycerine and IPA mixtures are shown in Figure 4.15.

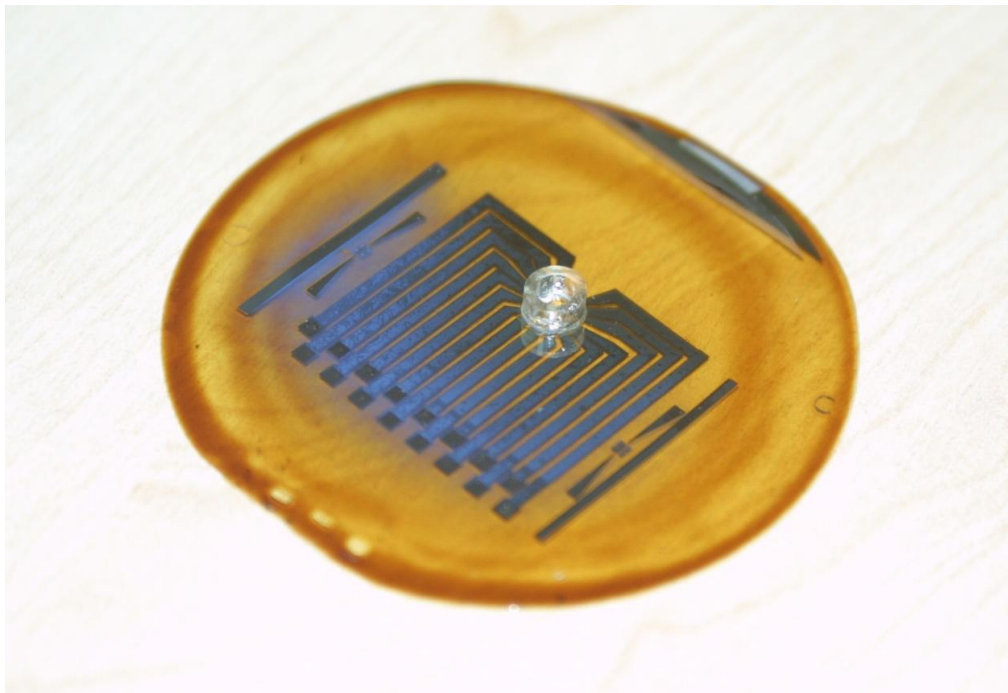


**Figure 4.14 – A photograph of the Design A device used for experimentation on 100  $\mu\text{l}$  droplets of liquid. The tubing was attached to the device to contain the liquid over the sensing area of the device**

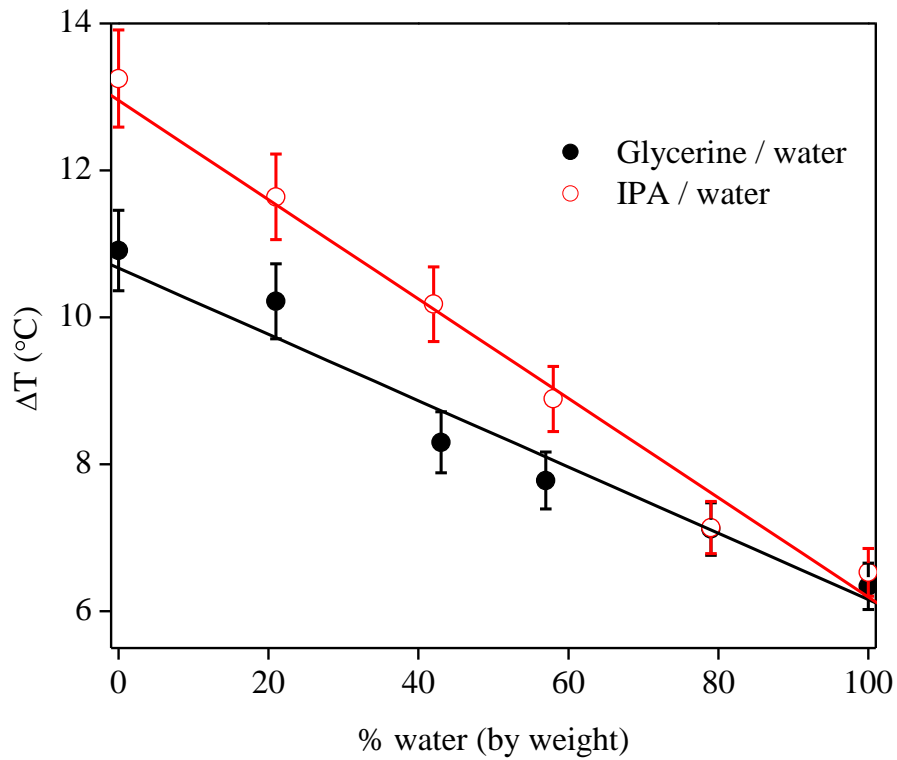


**Figure 4.15 – Experimental steady state  $\Delta T$  values as a function of water composition for 100  $\mu\text{l}$  droplets of glycerine / water and IPA / water mixtures**

Figure 4.15 shows that the  $\Delta T$  values decrease as the ratio of water increases for both glycerine and IPA mixtures. As the proportion of water within the glycerine mixture increases, the nominal thermal conductivity also increases [18]. A similar trend can be expected for the IPA mixtures based on the differences in thermal conductivity between pure IPA ( $0.13 \text{ W m}^{-1} \text{ K}^{-1}$  [19]) and pure water ( $0.60 \text{ W m}^{-1} \text{ K}^{-1}$  [3]). To understand how the  $\Delta T$  values relate to thermal conductivity, the experimental measurements are plotted in Figure 4.16 against the nominal thermal conductivities for pure water, glycerine and IPA as well as glycerine / water mixtures.

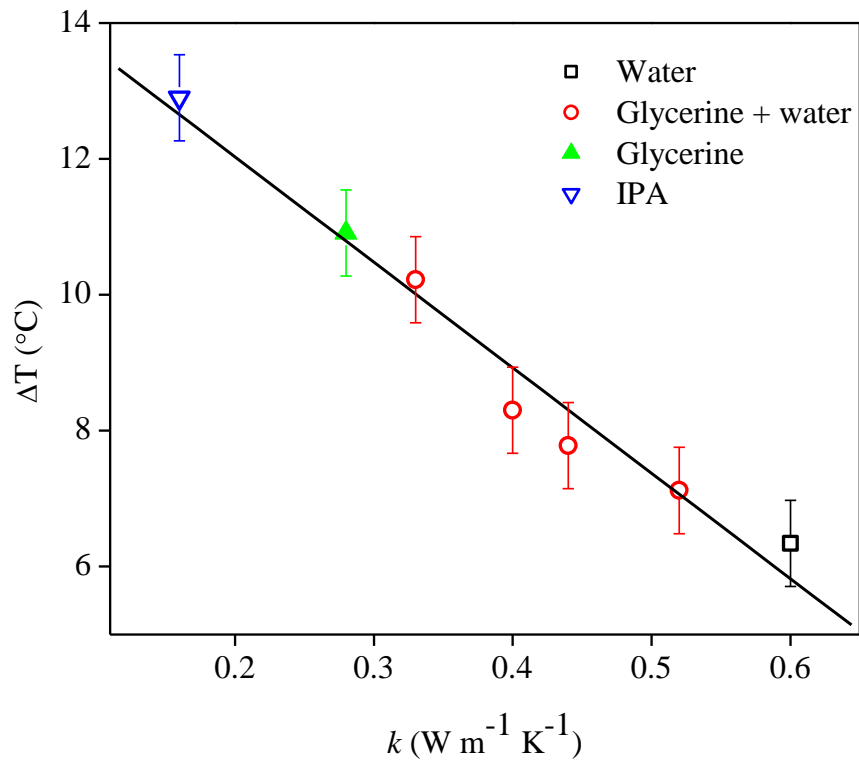


**Figure 4.16 – Experimental  $\Delta T$  values plotted against nominal thermal conductivity values for water [14], glycerine and water mixtures [18] and pure glycerine [18] and IPA [19] with a linear best fit line and  $\pm 10\%$  error bars (based on the  $\Delta T$  value for pure water)**

A linear dependence was observed for all of the samples which can be described by Equation 4.12:

$$\Delta T = 15.6 - 0.059 k(\Delta T) \quad 4.12$$

Re-arranging leads to Equation 4.13 which describes the thermal conductivity as a function of the measured  $\Delta T$  value:

$$k(\Delta T) = 0.92 - 0.059 \Delta T \quad 4.13$$

Thus,  $\Delta T$  can be used to estimate thermal conductivity for other liquid samples under the same experimental conditions. This result can be utilised to determine the thermal conductivity of IPA / water mixtures from the  $\Delta T$  values recorded in Figure 4.16. Thus the thermal conductivity of a mixture of IPA and water has a value given by Equation 4.14:

$$k_{IPA/water}(\omega_{water}) = 0.16 + 0.40\omega_{water} \quad 4.14$$

Where  $k_{IPA/water}(\omega)$  is the thermal conductivity of the IPA / water mixture with a composition of  $\omega_{water}$  which is the ratio of water to IPA by weight (1 being 100 % water and 0 being 0 % water).

These results clearly demonstrate that the device is capable of monitoring the thermal conductivity of 100  $\mu$ l samples as well as converting the measured  $\Delta T$  values into a thermal conductivity value for a sample of unknown thermal conductivity. The following section details the ability of the device to measure the time dependent thermal properties of a thin sheet and relate the changes in  $\Delta T$  measurements to the water content of the sheet.

#### 4.2.3.2. *Monitoring the drying rate of wetted paper*

The previous two sections demonstrate that the device responds to changes in the thermal conductivity of the sample it is in contact with and that small samples can be probed by the device. However, the aim of this work is to monitor the water content of a leaf, so this section aims to demonstrate that the device is also sensitive to changes in overall thermal resistance related to the water content of a porous sample. To provide a controlled sample, absorbent paper was wetted and allowed to dry under ambient conditions at various temperatures. Time dependent measurements were carried out to monitor the induced temperature gradient across wetted paper as it dried out. Since the thermal conductivity of the paper will vary with the amount of water present, measurements of the thermal conductivity as a function of time were used to monitor the water content. Paper was chosen because it has a thickness of only  $\sim 100 \mu$ m which is relatively small and comparable to that of a leaf. The paper was seen to dry out over a period of between 10 and 48 mins, as a function of the ambient temperature. As such, the sampling time of the device (2.2 s) was small in comparison to the overall drying time.

A 1 cm<sup>2</sup> piece of absorbent paper (Contec, C2-99) was taped over the sensing area of a Design A polyimide device. 5 mW was applied to the heater and the temperature difference between junctions located at 75  $\mu$ m and 150  $\mu$ m recorded to give a dry reference point. A 20  $\mu$ l droplet of water was applied to the paper and steady state  $\Delta T$  values were recorded at 30 second intervals

until the readings had returned to the dry reference value. Measurements were taken in a convection oven to allow the air temperature to be varied from the ambient 20 °C to 50 °C. All readings were taken in a cleanroom, where the ambient humidity was controlled at 50 %. A typical set of results for a sample allowed to dry at 27 °C is shown in Figure 4.17, while Figure 4.18 shows a summary of the drying time at various temperatures.

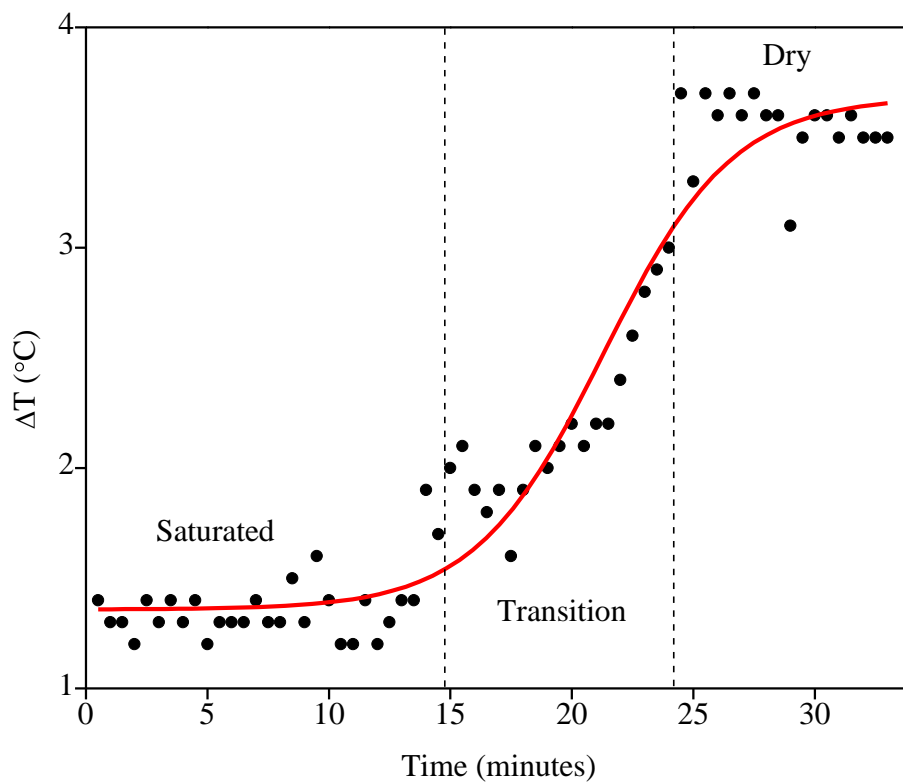
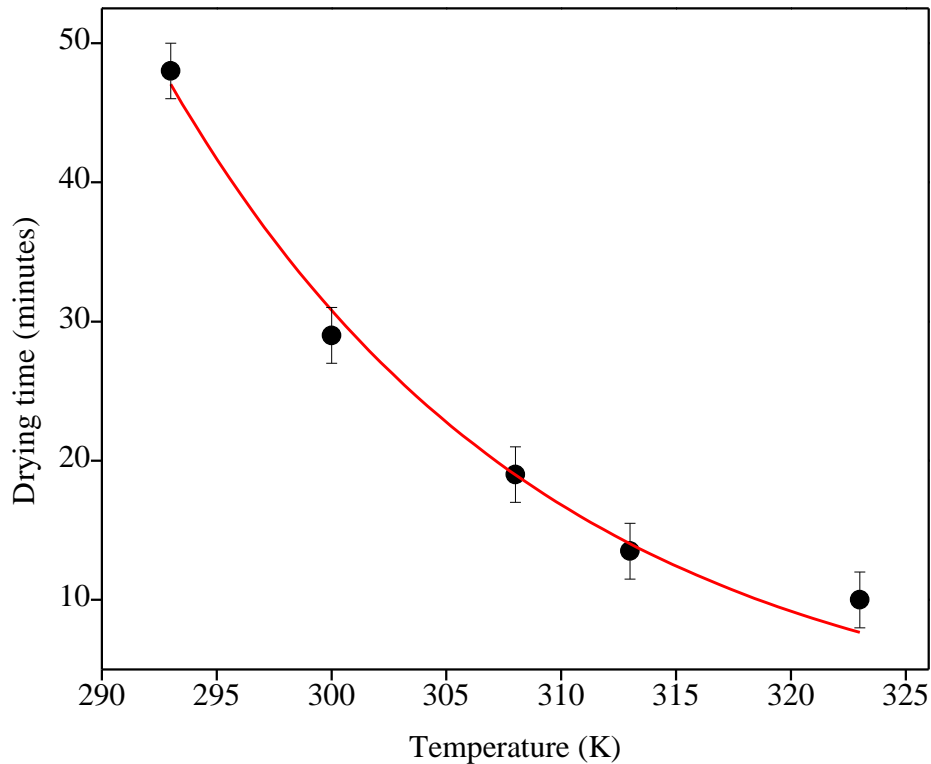


Figure 4.17 – Time dependent response of  $\Delta T$  measurements taken on wetted paper allowed to dry at 30 °C



**Figure 4.18 – Drying time for wetted paper at ambient temperatures from 20 °C to 50 °C (293 K to 323 K)**

While thermal conductivity values for the specific paper studied are not available, paper has a nominal thermal conductivity of around  $0.05 \text{ W m}^{-1} \text{ K}^{-1}$  [13] to  $0.18 \text{ W m}^{-1} \text{ K}^{-1}$  [14] versus  $0.60 \text{ W m}^{-1} \text{ K}^{-1}$  [18] for water. Thus the thermal conductivity of the paper increases and the thermal contact resistance will decrease as a result of the addition of water, which reduces the temperature difference recorded from the dry  $\Delta T$  value of  $3.7$  to  $1.4$  °C when the paper is saturated (for an air temperature of  $27$  °C). Once the paper is saturated, the temperature difference does not change notably for about 13.5 minutes. Between 13.5 and 24 minutes, the paper dries sufficiently to cause a significant change in the thermal properties. After 24 minutes, the paper is dry and no further changes occur. As the drying rate varies with the air temperature, the experiment was repeated at five different air temperatures. The paper was assumed dry when  $\Delta T$  reached 90% of the dry reading. The drying rate of a wet, porous solid can be obtained using Equation 4.15 (taken from [19]):

$$\frac{\Delta m_{water}}{\Delta t} = \kappa_g A [p_s(T) - p_{H_2O}] \quad 4.15$$

Where  $\Delta m_{water}/\Delta t$  is the rate of mass of water lost,  $\kappa_g$  the mass transfer coefficient,  $A$  the area available for evaporation,  $p_s(T)$  the vapour pressure of water at temperature  $T$  and  $p_{H_2O}$  the partial pressure of water in the ambient gas (a constant for the experiment).

The vapour pressure of water is given by the Goff-Gratch equation [20] shown in Equation 4.16:

$$\begin{aligned} \log p_s(T_{air}) = & -7.90298(T_s/T_{air} - 1) + 5.02808 \log(T_s/T_{air}) \quad 4.16 \\ & - 1.3816 \times 10^{-7} (10^{11.344(1-T_{air}/T_s)} - 1) \\ & + 8.1328 \times 10^{-3} (10^{-3.49149(T_s/T_{air}-1)} - 1) \\ & + \log(1.01325 \times 10^5) \end{aligned}$$

Where  $T_s$  is the boiling point of water at 1 atm and  $T_{air}$  is the air temperature. Plotting this over the range 20–50 °C (Figure 4.19) with an exponential best fit shows that this can be approximated by Equation 4.17:

$$p_s(T) = 3.3 \times 10^{-7} \exp [0.05T] \quad 4.17$$

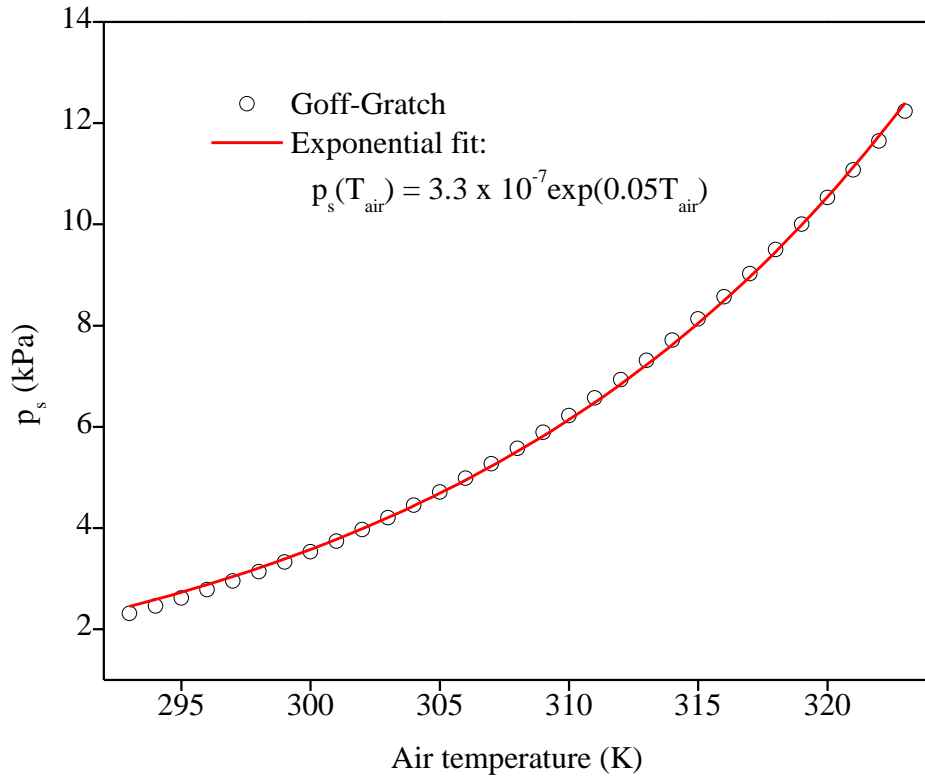


**Figure 4.19 – Vapour pressure calculated from the Goff-Gratch equation and the exponential approximation over the range 295 – 325 K (20 – 50 °C)**

Combining Equations 4.15 and 4.17 leads to:

$$t_{dry}(T) = \frac{\Delta m_{water}}{\kappa_g A (3.3 \times 10^7 \exp[0.05 T] - p_{H2O})} \quad 4.18$$

Where  $t_{dry}$  is the time in minutes required to dry and  $\Delta m_{water}$  the change in mass of water.

Because  $\kappa_g$  is a constant dependent on the liquid and the drying porous material, values are not readily available. However, to predict the drying time as a function of the ambient temperature, the correlation between drying time  $t_{dry}$  and air temperature  $T_{air}$  is of interest and may be derived from Equation 4.19:

$$t_{dry}(T_{air}) \propto \exp[-0.05 T_{air}] \quad 4.19$$

An exponential fit of the experimental drying time plotted against air temperature in Figure 4.18 gives the relationship shown in Equation 4.20:

$$t_{dry}(T_{air}) = 2.3 \times 10^9 \exp[-0.06 T_{air}] \quad 4.20$$

This indicates that the experimental data and theory have a similar dependence on the air temperature, showing that the device is capable of monitoring the time varying thermal properties of a material and relating these to other physical parameters. It also demonstrates the device's ability to probe materials with critical dimensions of  $\sim 100 \mu\text{m}$ , roughly the thickness of a sheet of paper or the thickness of a leaf. This demonstration has a clear application to monitoring the water content of a leaf. While the underlying properties and microstructure of a leaf will be different from that of paper, the principle is clearly sound.

### 4.3. Conclusions

This section has demonstrated that the principle of operation of the devices is sound by creating numerical models which have been verified against experimental results. Due to the dimensions of the device and the temperature ranges under investigation, it was demonstrated that convection and radiation would have a minimal effect on the overall heat transfer and that conductive heat transfer mechanisms would dominate. A 2-D numerical model was found to show good agreement with the experimental data and was subsequently used to investigate the substrates utilised in this work as well as the effect of the sample on the operation of the device, demonstrating that the principle of operation was sound.

The second half of the chapter focused on the experimental calibration and operation of the devices. Polyimide devices were suitably robust to allow calibration which was achieved by applying a known temperature to the sensing area of the device using a wire-wound power resistor with a K-type thermocouple attached. A comparison of the emf generated by the device against the temperature recorded by the K-type thermocouple demonstrated that the devices had a linear response and, despite being formed from thin metal films, only suffered an 8 – 15 % drop in Seebeck coefficient compared with the expected bulk values at  $29 - 33 \mu\text{V } ^\circ\text{C}^{-1}$  compared with the expected  $36.3 \mu\text{V } ^\circ\text{C}$  [17].

Once calibrated, the devices were used to probe the thermal conductivity of relatively large (50 ml) volumes of liquids (water, IPA and glycerine). The output of the devices showed a linear response to the thermal conductivity of the liquids, although this conclusion is difficult to verify as only 3 liquids were chosen. However, subsequent testing on smaller volumes appears to back up this result.

In order to demonstrate that the devices were equally capable of operating on small volumes, they were used to probe the thermal conductivity of 100  $\mu$ l droplets of liquid. Glycerine / water mixtures were used to calibrate the device, as the thermal conductivity values were available in literature. This confirmed the linear response of the device. Subsequently, IPA / water mixtures were tested and the dependence of the mixture's composition on thermal conductivity was determined.

The chapter concluded by demonstrating that the device can also relate thermal properties to the water content of a porous material as a guide for further work on plant leaves. Wetted absorbent paper was used, as it easily absorbs and loses water while also being a similar thickness to plant leaves. The output of the device ( $\Delta T$ ) was seen to be dependent on the water content of the paper. The drying times for the paper, detected by the device, showed a trend consistent with the Goff-Gratch equation, which can be used to relate the drying rate with the ambient air temperature.

The following section discusses thermal contact resistance. This has a strong influence on the flow of heat between two solids and so can play an important role in understanding and interpreting the results on plant leaves.

#### 4.4. References

1. **Sobhan, C.B. and Peterson, G.P.** *Microscale and Nanoscale Heat Transfer*. Florida : CRC Press, 2008.
2. **Solano, B. Rolt, S. and Wood, D.** Thermal and mechanical analysis of an SU8 polymeric actuator using infrared thermography. *Proceedings of the IMechE*. 2007, Vol. 222, Special Issue Paper, pp. 73-86.
3. **Incropera, F.P. and DeWitt, D.P.** *Introduction to Heat Transfer*. 3. New York : Wiley, 1996.
4. **Palmer H.J. and Berg, J.C.** Convective instability in liquid pools heated from below. *Journal of Fluid Mechanics*. 1971, Vol. 47, pp. 779-787.
5. **Perry, R.H Green, D.W. and Maloney, J.O.** *Perry's Chemical Engineers' Handbook*. New York : McGraw-Hill, 1997.
6. **Shell Chemicals**. Datasheet: Isopropyl alcohol. [Online] [Cited: 11th July 2011.] [http://www.scdynamiccontent.shell.com/Files%5alcoholsglycols\\_isopropylalcolipa\\_americas.pdf](http://www.scdynamiccontent.shell.com/Files%5alcoholsglycols_isopropylalcolipa_americas.pdf).
7. **Ramadan, K.** Semi-analytical solutions for the dual phase lag heat conduction in multilayered media. *International Journal of Thermal Sciences*. 2009, Vol. 48, pp. 14-25.
8. *Accuracy Tests for COMSOL - and Delaunay Meshes*. **Holzbecher, H. and Si, E.** Hannover : European COMSOL Conference, 2008.
9. **HD MicroSystems**. *Product Bulletin: PI-2600 Series - Low Stress Polyimides*. 2008.
10. **Xu, J, Reiserer, R, Tellinghuisen, J, Wikswo, J.P and Baudenbacher, F.J.** A Microfabricated Nanocalorimeter: Design, Characterization, and Chemical Calibration. *Analytical Chemistry*. 2008, 80, pp. 2728-2733.
11. **MicroChem**. SU-8 Table of Properties. [Online] [Cited: 3rd October 2011.] <http://www.microchem.com/pdf/SU-8-table-of-properties.pdf>.

12. **Mattsson, C.G., Thungstrom, G., Bertilsson, K., Nilsson, H.L. and Martin, H.** Fabrication and evaluation of a thermal sensor formed on a thin photosensitive epoxy membrane with low thermal Conductivity. *Journal of Physics: Conference Series*. 2008, 100.
13. Thermal Conductivity of some common Materials and Gases. *The Engineering Tool Box*. [Online] [Cited: 15th July 2011.] [http://www.engineeringtoolbox.com/thermal-conductivity-d\\_429.html](http://www.engineeringtoolbox.com/thermal-conductivity-d_429.html).
14. **Incropera, F.P. and DeWitt, D.P.** *Intorduction to Heat Transfer*. 3. New York : Wiley, 1996.
15. **Atherton, J.J, Rosamond, M.C. Johnstone, S. and Zeze, D.A.** Thermal characterisation of micro-litre volumes using a thin film thermocouple based sensor. *Sensors and Actuators A*. 2011, Vol. 166, pp. 34-39.
16. **Omega.** Revised Thermocouple Reference Tables. *Omega.com*. [Online] [Cited: 18th July 2011.] <http://www.omega.com/temperature/z/pdf/z204-206.pdf>.
17. **Foiles, C.L.** *Thermopower of pure metals and dilute alloys*. New York : Springer, 1985.
18. **Company, Dow Chemical.** True Coefficient of Glycerine-Water Solutions. [Online] [Cited: 07 05 2010.] <http://www.dow.com/glycerine/resources/table13.htm>.
19. **Perry, R.H. and Green, D.** *Perry's Chemical Engineer's Handbook*. New York : McGraw-Hill, 1984.
20. **Goff, J.A. and Gratch, S.** Low-pressure properties of water from -160 to 212 F. *Transactions of the American Society of Heating and Ventilating Engineers*. 1946, Vol. 52, pp. 95-122.

Liquid samples offer an easier thermal system to probe using the device, as they do not suffer from thermal contact resistance. This was advantageous when demonstrating the functionality of the device, as it simplified the analysis. However, the effect thermal contact resistance has on the output of the device needs to be understood if solid samples are to be probed. This chapter introduces the theory behind thermal contact resistance and the process of experimental determination of the effect of thermal contact resistance on the device.

#### **5.1. Thermal contact resistance theory**

For 1-D, steady state conduction through a solid with constant thermal conductivity, the temperature varies linearly with distance, and thus can be described using Fourier's law (Equation 5.1):

$$q = -kA \frac{dT}{dx} = -kA \frac{(T_1 - T_2)}{(x_1 - x_2)} = -kA \frac{(T_1 - T_2)}{L} \quad 5.1$$

Where  $q$  is the heat flow rate,  $k$  is the thermal conductivity,  $A$  is the cross sectional area of the volume,  $L$  is the length of the volume,  $T_1$  is the temperature at position  $x_1$  and  $T_2$  is the temperature at location  $x_2$  ( $T_1 > T_2$ ).

This can be re-written to introduce an electrical analogy:

$$R_{thermal} = \frac{(T_1 - T_2)}{q} = \frac{L}{kA} \quad 5.2$$

Where  $R_{thermal}$  is the thermal equivalent of electrical resistance. To demonstrate this principle, an isotropic solid cylinder can be used, with its circumferential faces insulated and the two end faces held at temperatures  $T_1$  and  $T_2$  (with  $T_1 > T_2$ ). This geometry is shown in Figure 5.1 a).

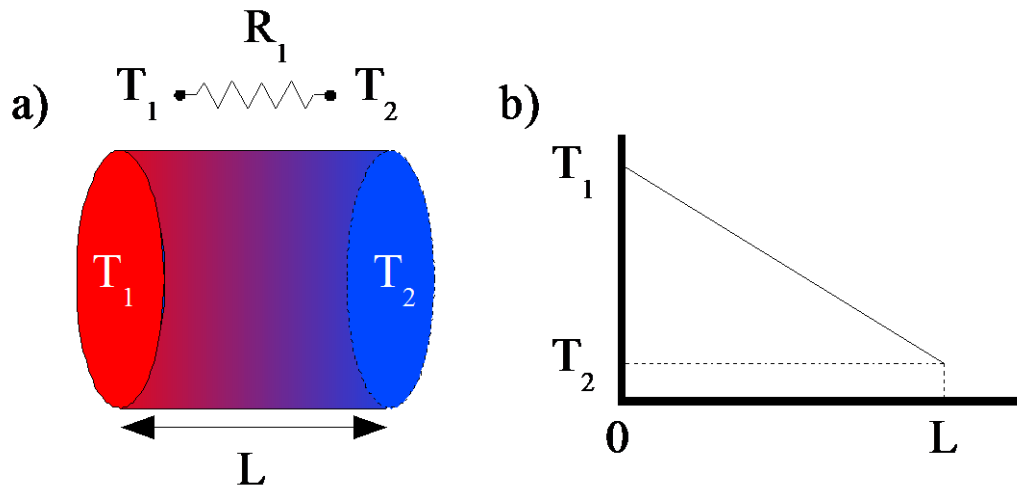


**Figure 5.1 – a) A diagram showing 1-D heat flow through an isotropic cylinder with insulated edges and one end heated; b) the resulting temperature profile**

The heat flow through the cylinder will be a function of the temperature difference ( $T_1 - T_2$ ) and the thermal resistance, which is a function of the geometry and thermal properties of the cylinder and is shown in Figure 5.1 b) and Equation 5.3:

$$q = (T_1 - T_2) \frac{kA}{L} = \frac{T_1 - T_2}{R_{thermal}} \quad 5.3$$

If two identical cylinders were brought into contact, it would be expected that this rule may still apply, as if the two solids were one whole. However, a dislocation in the temperature gradient is observed. This dislocation arises as an additional thermal resistance ( $R_j$ ) is seen at the interface between the materials. This additional thermal resistance is known as the thermal contact resistance (TCR). The equivalent diagram and temperature profile generated by two cylinders is shown in Figure 5.2.

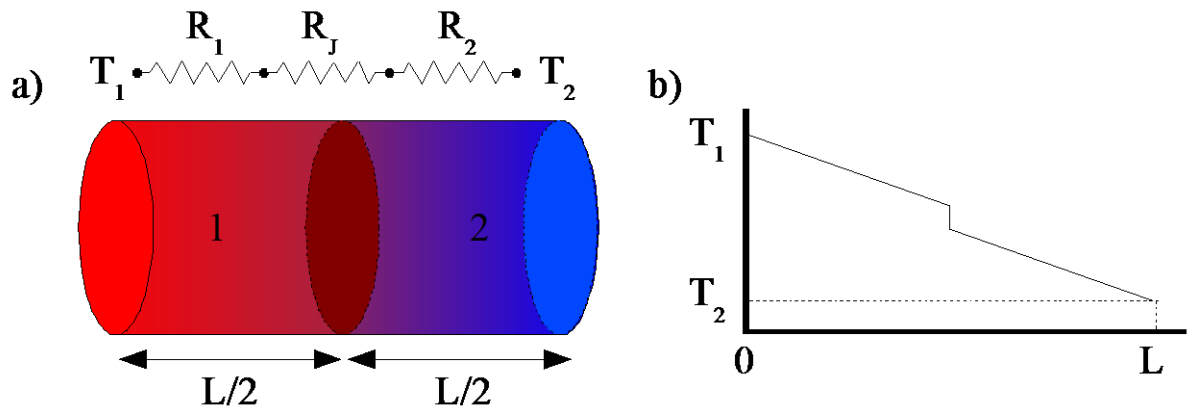
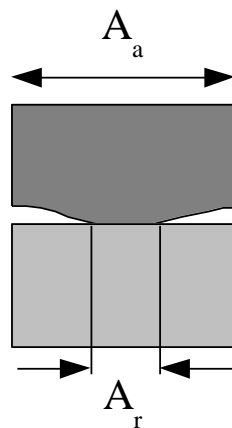


Figure 5.2 – a) A diagram showing 1-D heat flow through two identical cylinders with TCR; b) the resulting stepped temperature profile

TCR is caused by two factors, which are shown in Figure 5.3.

- Macroscopic: Non-conforming (non-flat) interfaces [1]
- Microscopic: Surface roughness decreasing the effective area of contact [2]

Non-conforming faces



Surface roughness

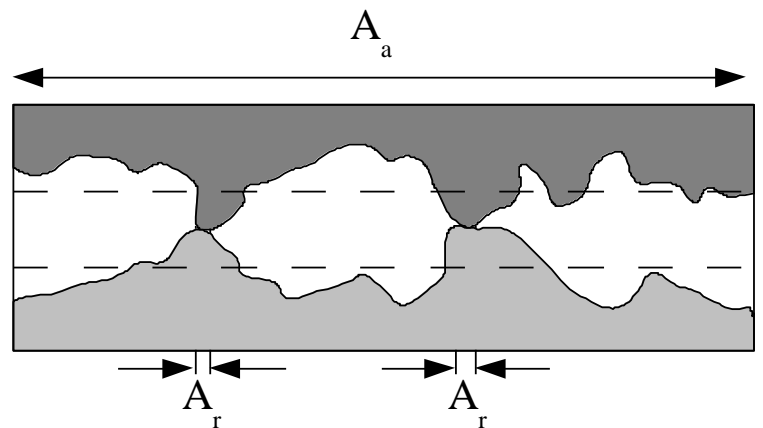


Figure 5.3 – The two mechanisms which act to reduce the effective contact area ( $A_r$ ) and cause thermal contact resistance: non-conforming faces and surface roughness

Non-conforming interfaces occur when the two surfaces are not flat. This has the effect of decreasing the effective contact area between the two materials, leading to an increase in the thermal resistance. Microscopic surface roughness effects also decrease the effective contact area, as real contact occurs only at the top of touching surface asperities. Micro-contact spots at the tips of asperities will bridge the two materials, so the actual area in contact will be dominated by these

asperities and as such, the real contact area ( $A_r$ ) will be much smaller than the nominal area ( $A_a$  – i.e. the area of the cylinder faces in Figure 5.2) [2].

If a contact force is applied to compress the two surfaces into each other, the asperities will begin to deform and flatten out. This process will depend on the materials involved as well as the force applied. Harder, flatter materials will deform less under compression, whereas soft materials with asperities with large heights and smaller radii will deform more easily under a compressive force, meaning there will be a strong relationship between contact force, surface properties and the TCR [1].

There are three mechanisms by which heat can flow across the gap created by the asperities and the overall heat flow across the joint ( $q_j$ ) is given by Equation 5.4:

$$q_j = q_c + q_g + q_r \quad 5.4$$

Where  $q_c$  is conduction via the micro-contacts,  $q_g$  is conduction/convection through the interstitial fluid and  $q_r$  is radiative heat flow. This is shown diagrammatically in Figure 5.4.

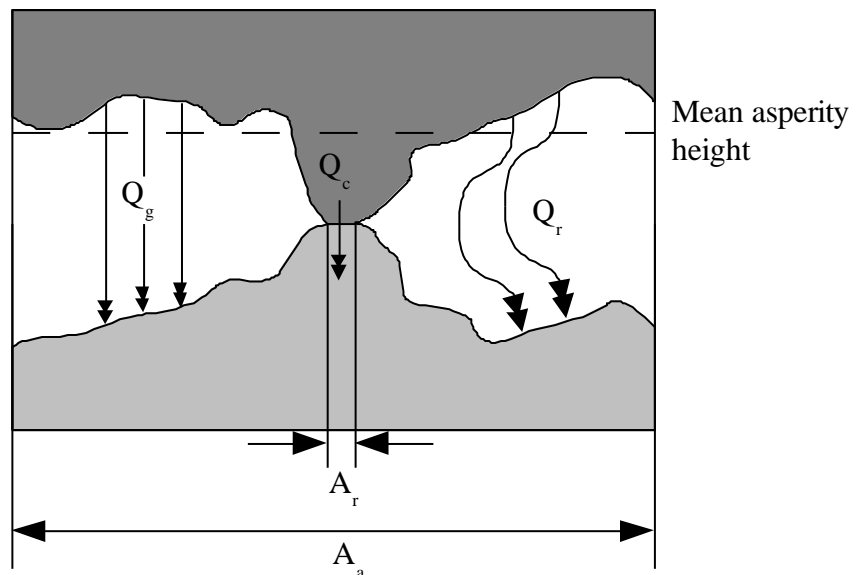


Figure 5.4 – Heat flow mechanisms across the TCR gap created by surface roughness

For interface temperatures below 600 °C and for cases where the interstitial fluid is opaque, radiation can be neglected [3]. As the temperatures used throughout this project are much lower

than 600 °C (generally 70 °C or lower), radiation is unlikely to have a large effect and can be neglected.

For relatively flat surfaces with small asperity heights, the gap between the two surfaces will be small, so the Grashof number will be below 2000 which means natural convection of the interstitial fluid (air) can also be neglected [4]. This leads to the simplified case given by Equation 5.5 and the temperature drop across the junction is given by Equation 5.6:

$$q_j = q_c \quad 5.5$$

$$\Delta T_j = q_j R_j \quad 5.6$$

Where  $\Delta T_j$  is the temperature drop across the junction and  $R_j$  is the effective thermal resistance of the gap. Thus, with a knowledge of the power applied and the temperature drop across the joint, a value for the TCR (i.e.  $R_j$ ) can be calculated. This joint resistance can be related to a joint conductance by Equation 5.7:

$$h_j = \frac{1}{A_a R_j} \quad 5.7$$

Where  $h_j$  is the heat transfer coefficient across the gap, based on a purely conductive mechanism. Much work over the past seven decades has focused on understanding the pertinent factors affecting this coefficient [1]. One such representation is the Song and Yovanovich model, shown in Equation 5.8, taken from [5]:

$$h_j = 1.25 k_j \frac{m}{\sigma} \left( \frac{P}{H_m} \right)^{0.95} \quad 5.8$$

Where:  $k_j = \frac{2k_1 k_2}{k_1 + k_2}$ ,  $k_1$  is the thermal conductivity of material 1,  $k_2$  is the thermal conductivity of material 2,  $m$  is the effective surface slope,  $\sigma$  is the rms surface roughness in microns,  $P$  is the contact pressure and  $H_m$  is the hardness of the softer material. This model for the joint conductance indicates that heat flow will increase for softer, flatter joints with lower surface roughness and higher contact pressures. However, in order to use this model in practice, a number of values must be experimentally acquired. The Song and Yovanovich model is relatively simple

in comparison to others, which take various factors into account. For example, changes in the thermal properties due to localised deformation of the asperities and limitations in thermal conductivity related to the asperities being smaller than the phonon free mean path length can influence the TCR [2]. Despite not discussing these smaller scale effects, the Song and Yovanovich model provides a robust description of the important factors affecting TCR for a joint without an interstitial fluid; the solid surface characteristics and the contact pressure.

The Song and Yovanovich model indicates how the TCR can be reduced by altering the surfaces which are in contact, for example by reducing the surface roughness or the hardness. However, it may not always be possible to perform these alterations to the surface without damaging or changing other parameters to be measured. A much simpler way to achieve a reduction in the TCR is given by replacing the interstitial fluid (air) with a thermal interface material (TIM). A TIM alters the TCR by inserting a material which reduces the contact resistance, for example by adding a softer material between the surfaces, which moulds to the asperities and increases the effective contact area ( $A_r$ ).

If a solid is used as a TIM, it introduces two contacting surfaces each of which must have a lower TCR than the original joint. Thin sheets of a soft metal can be used, however care must be exercised as the issue of TCR still exists and a solid TIM complicates the electrical equivalent model as there are now two junctions as well as conduction through the TIM. However, if the interstitial fluid is changed from a gas (i.e. air) to a liquid with a relatively high thermal conductivity, then the situation is simplified. The electrical equivalent circuits are shown in Figure 5.5, which clearly indicates that the simplest case is for a liquid TIM. In this case, it can be assumed that the liquid perfectly wets the gap [6], meaning that conduction through the liquid dominates, thus:

$$h_j = h_g = \frac{k_{liquid\ TIM}}{Y} \quad 5.9$$

Where  $h_g$  is the heat transfer coefficient of the gap,  $k_{liquid\ TIM}$  is the thermal conductivity of the liquid TIM and  $Y$  is the mean separation between the two materials. Thus, the TCR is entirely dependent on the thermal conductivity of the liquid and its thickness.

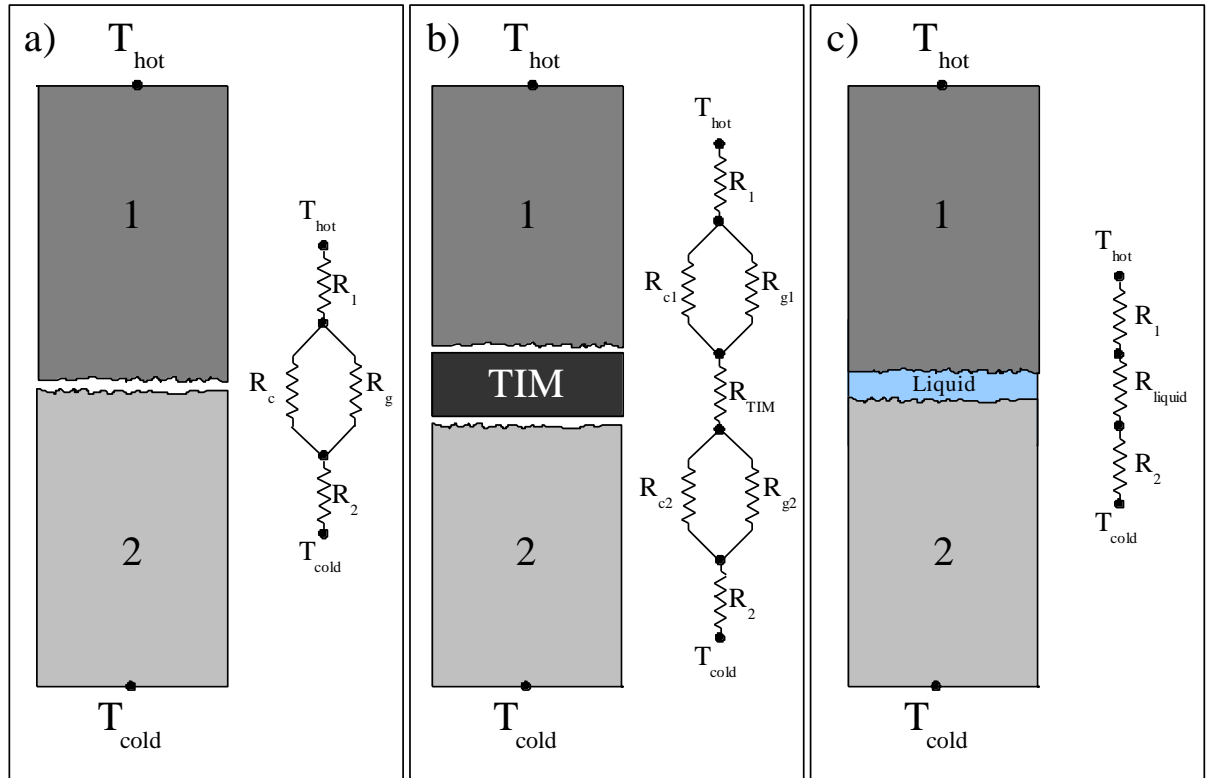


**Figure 5.5 – Electrical equivalent models for: a) bare solid-solid interface; b) a solid TIM & c) a liquid TIM**

The case of two identical cylinders allows simple electrical equivalent models to be created. However, the geometry of the polyimide devices presented here does not lend itself to a simple electrical equivalent model which could be used to convert experimental results into absolute values for TCR between the device and a solid sample. However, experimental measurements can give an indication of the effect TCR has on the measurements. The following section outlines the experimental method and results which were used to understand the effect of TCR on the operation of the device.

## 5.2. Experimental determination of thermal contact resistance

The Song and Yovanovich model [5] requires a number of physical parameters of the mating surfaces to be known if the TCR is to be accurately modelled. However, these values will vary between surfaces and materials. However, the model gives a good indication of the factors which influence the TCR. In particular, TCR is strongly related to the contact force applied [2]. Thus to investigate the effects of TCR on the device, it was systematically varied by applying different contact forces to the device. By compressing the device into samples of a known thermal conductivity, the effect of TCR on the device's operation could be understood. To act as a control, a TIM was utilised to provide a nearly constant TCR between the two surfaces.

To allow the contact pressure to be varied, a Design B type device formed on a polyimide substrate was mounted to an arm attached to a linear translation stage capable of vertical movements with a precision of  $\pm 2 \mu\text{m}$ . The translation stage was then used to compress the device against a sample placed on top of a micro balance. The micro balance was used to measure the force being applied which was a function of the elastic properties of the bodies involved and the degree of displacement of the translation stage. The area of the arm used to compress the device was  $2 \text{ cm}^2$ , which allowed pressures of up to  $\sim 12 \text{ kPa}$  to be applied (based on the maximum load measured by the micro balance). For all samples detailed in this section, a power of  $23.7 \text{ mW}$  was applied to the heater with  $\Delta T$  and contact force/pressure measurements recorded as the stepper was lowered (loading phase) and raised (unloading phase). A schematic diagram and photograph of the setup is shown in Figure 5.6. To demonstrate that the device was detecting changes in the TCR, loading and unloading curves were recorded for a quartz sample which was much thicker than the device ( $\sim 10 \text{ mm}$ ). The curves are shown in Figure 5.7.

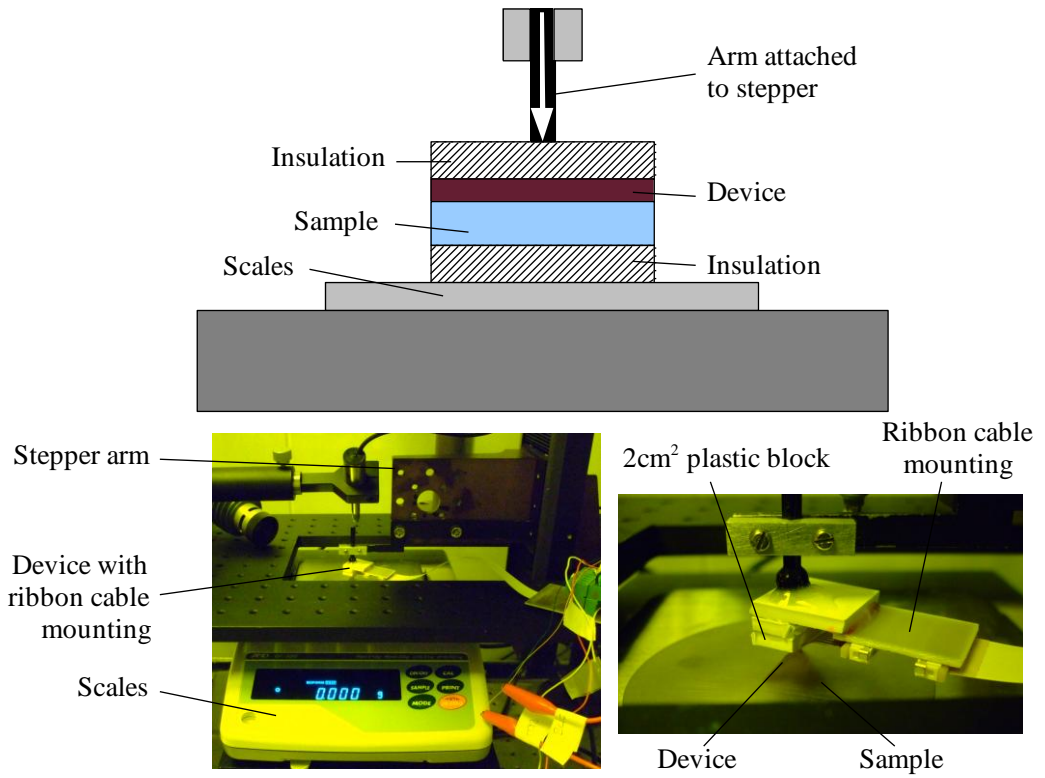


Figure 5.6 – Schematic diagram and photograph of the experimental setup used to investigate the effect of a compressive force on the TCR

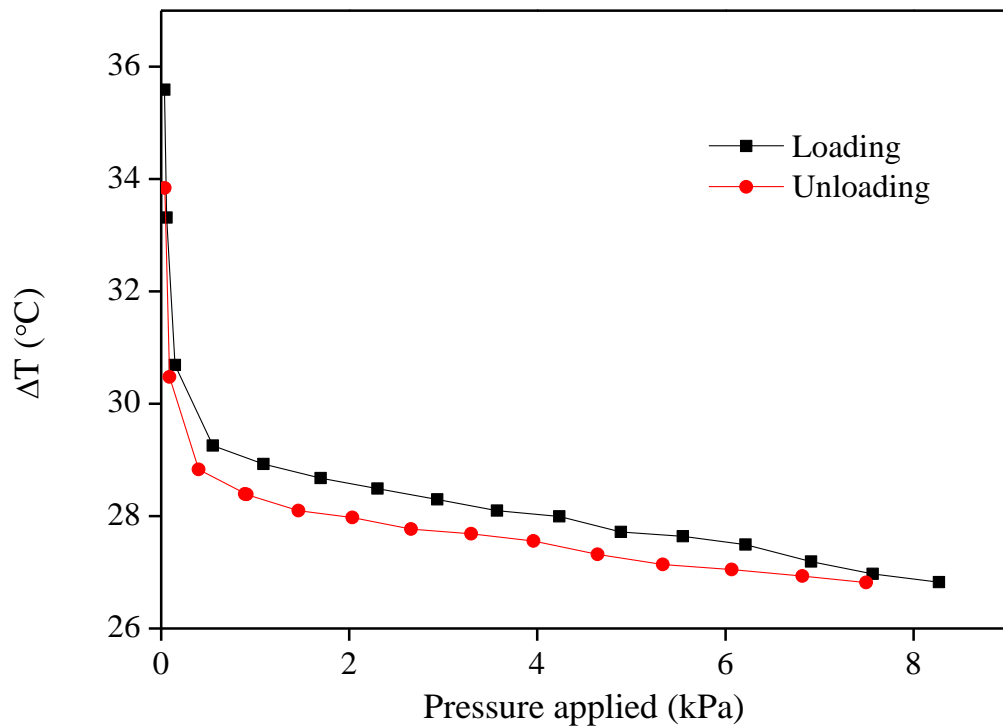


Figure 5.7 – Loading and unloading curves for a quartz sample

The experimental trend is similar to that predicted by theory: as the pressure is increased,  $\Delta T$  measurements are seen to decrease due to a reduction in the TCR caused by the asperities on the device and sample deforming. During the loading cycle, the  $\Delta T$  measurement decreased rapidly from around 36 °C when initially in contact to around 29 °C when under a pressure of 0.5 kPa. As the pressure was increased further,  $\Delta T$  measurements decreased by  $\sim 0.29 \text{ }^\circ\text{C kPa}^{-1}$ . This decrease in the  $\Delta T$  measurement indicates that there is a decrease in the overall thermal resistance between the heater and the sensing junctions. As the sample's thermal conductivity and the device's operation will not change significantly with the relatively low pressures used here, the change must be due to a decrease in TCR as the pressure increases.

During unloading the reverse trend is seen, with the  $\Delta T$  measurement increasing as the pressure decreases, however there is a slight hysteresis. The hysteresis is due to irreversible (plastic) deformations that occur during the loading cycle [7] i.e. once the load has deformed the two surfaces, they remain with this larger contact area until the pressure is reduced further. The experimental setup was subsequently used to investigate the effect of TCR on the measurements taken by the device, which is outlined in the following sections.

### 5.3. Material effects

To investigate the effect of TCR on the device's operation, three samples were chosen with different surface properties and thermal conductivity: quartz, nickel and acrylic. Each sample had a thickness of  $> 10$  mm, many times the thickness of the device, so sample thickness was not expected to influence the results. The experimental details outlined in the previous section (Section 5.2) were repeated and  $\Delta T$  was recorded during the loading phase for each sample, up to a maximum pressure of  $\sim 9$  kPa. Two sets of loading curves are shown in Figure 5.8 for each material.

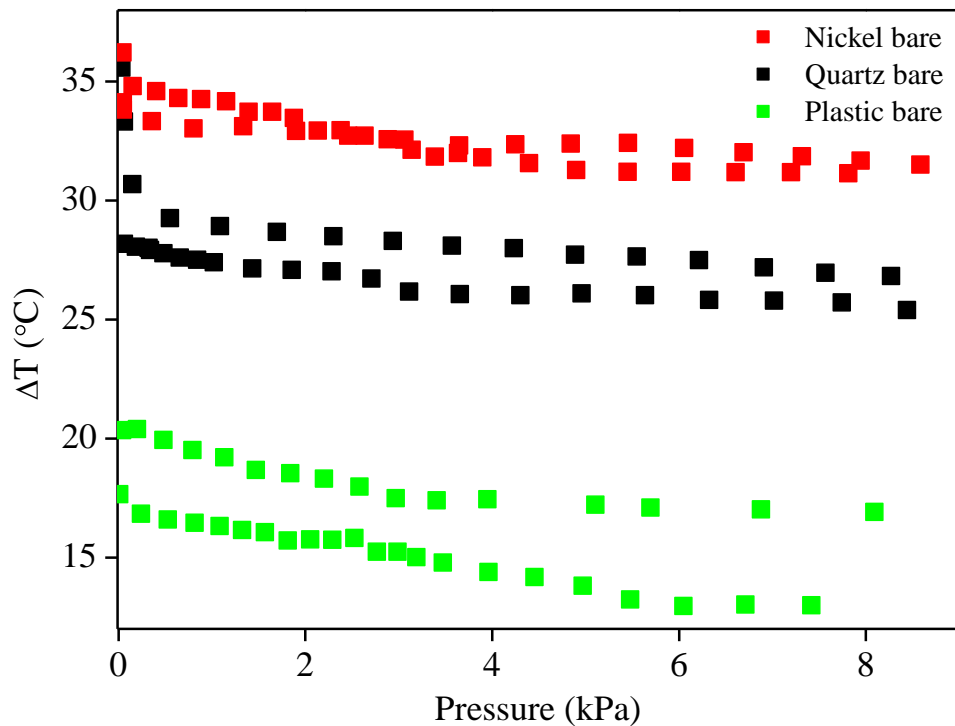


Figure 5.8 –  $\Delta T$  loading curves for quartz, nickel and acrylic (2 curves are presented for each material)

Each material followed a similar trend, with the  $\Delta T$  measurement decreasing as the pressure increased. However, acrylic shows the smallest  $\Delta T$  measurement, implying that it has the highest overall thermal conductivity, while nickel shows the largest  $\Delta T$  measurement, implying it has the lowest overall thermal conductivity. The material properties shown in Table 5.1 indicate that the

TCR must be having a strong influence on the measurements as the relationship is inverted, based on the bulk thermal conductivity values of the three materials.

**Table 5.1 – Thermal and surface properties of the materials used in the experiment**

<b>Material</b>	<b>Thermal conductivity (W m<sup>-1</sup> K<sup>-1</sup>)</b>	<b>Surface roughness (nm)<sup>1</sup></b>	<b>Hardness</b>
Nickel	90 [8]	124	3.5-5 Mohs [9]
Quartz	1.4 [10]	1.16	7 Mohs [8]
Acrylic	0.2 [11]	50.2	35-78 Rockwell M

To understand this result, it is necessary to look at other material properties of the samples. While nickel has the lowest bulk thermal conductivity, the sample used had the highest surface roughness and it is a relatively hard material, with values generally in the range 3.5-5 Mohs. Both these factors will increase the TCR to a point that it dominates the measurements. The reverse is true for the acrylic sample: the surface is softer and flatter and has a lower thermal conductivity, so the bulk thermal properties of the sample dominate rather than the TCR. This hypothesis is investigated further in Section 5.4 which investigates how a TIM can be used to decrease the effect of the TCR on thermal conductivity measurements.

For all samples, TCR decreases with contact pressure. This relationship is less pronounced with higher pressures, as the readily deformed asperities will make good contact at lower pressures. Thus, for reliable measurements on solid and relatively hard samples, it is necessary to apply a contact pressure of at least 1 kPa. Ideally, the contact pressure should be the same for comparable measurements. However, as the results presented here show, increasing the pressure alone does not guarantee accurate measurements that can be converted into a thermal conductivity value, as the TCR can dominate. As the Song and Yovanovich model [5] suggests, the pressure applied is only one factor that must be controlled along with the surface properties.

<sup>1</sup> An atomic force microscope (Veeco) was used to measure the surface roughness of the samples. RMS (nm) values are shown.

## 5.4. Effect of a TIM

The results in the previous section show that TCR cannot be ignored when making measurements on solid samples. While increasing the contact pressure will reduce the TCR, it does not remove the effect. However, the application of a TIM between the two contacting surfaces should introduce a constant value for the TCR between the two surfaces and mitigate against the effect, allowing the thermal conductivity of the samples to be probed despite TCR being present. As suggested earlier, a TIM can take the form of a thin solid layer, or a thermally conductive liquid. This section outlines an investigation into the effect a liquid TIM has on the  $\Delta T$  measurements recorded for samples with varying thermal conductivity.

The choice of material to be used for the TIM is important: if the TIM layer is too thick or of a very high thermal conductivity, then the TIM will dominate the measurements, effectively ‘shorting out’ the thermal equivalent circuit. The thermal resistance of the TIM layer will be strongly dependent on its thickness, so variations in thickness will introduce inaccuracies. Thermal pastes are generally used to improve TCR and find many uses, for example for ensuring good thermal contact for heat sinks. Such thermal pastes are generally formed by suspending ceramic particles in a liquid or gel, leading to the paste having a high thermal conductivity. However the nature of the paste means they are viscous, meaning that they are impractical for this application as they will not generate a uniform and consistent thickness. While this does not affect the operation of a thermal paste when connecting a heat sink, it will lead to significant variation between samples when used with the devices reported here. In addition, many thermal pastes would be incompatible with leaves and so unsuitable for the experiments detailed in Chapter 6.

Water was found to be a suitable replacement for thermal pastes for two reasons. Firstly, it is a relatively good thermal conductor with a thermal conductivity of  $0.6 \text{ W m}^{-1} \text{ K}^{-1}$  [11] compared with a thermal paste:  $0.9 \text{ W m}^{-1} \text{ K}^{-1}$  [12]. While this is lower than the thermal conductivity of nickel ( $90 \text{ W m}^{-1} \text{ K}^{-1}$  [8]), the water should still reduce the TCR bridging the air gap, allowing the thermal properties of the sample to dominate. Secondly, water forms a thin, conformal and void

free layer between the device. As such, water was expected to both decrease the TCR and also provide a constant contact resistance. Images of the device and the water as it is compressed are shown in Figure 5.9.

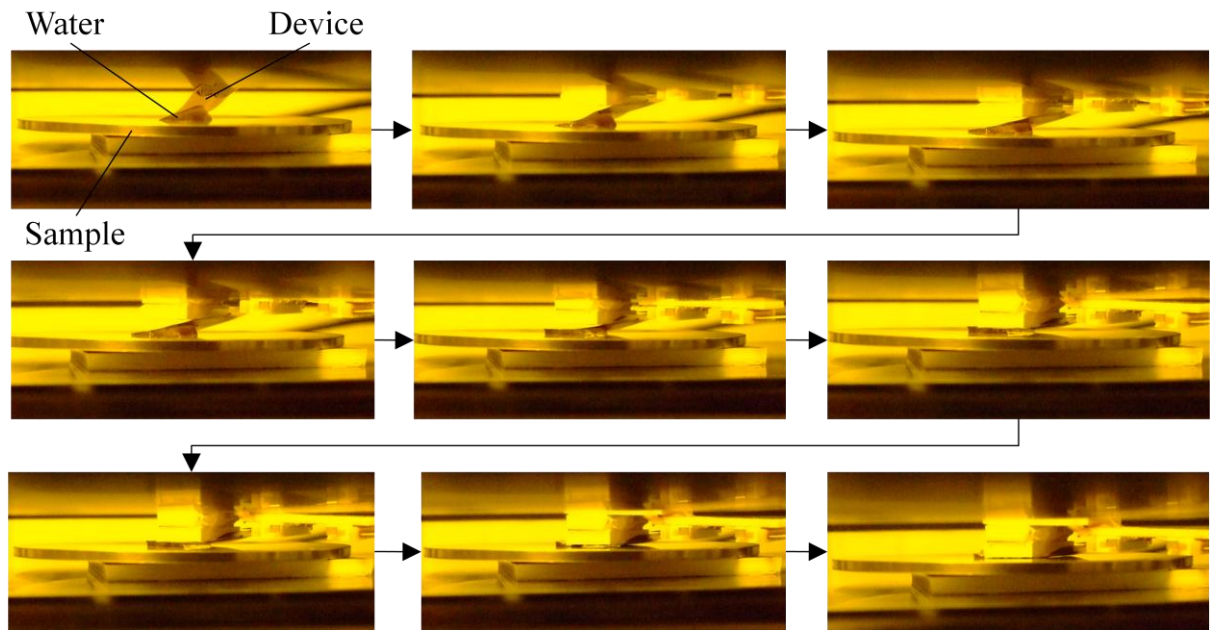


**Figure 5.9 – Photographs showing the water droplet deforming as the device is lowered into the sample by the stepper**

Using water as a TIM,  $\Delta T$  measurements were taken on the same 3 samples as in the previous section. A droplet of water was placed on the sample and the device was lowered onto the sample, compressing the droplet so it deformed to create a conformal and void free layer. Two sets of loading curves were recorded for each material and (for clarity) averaged curves of the two sets of data are shown in Figure 5.10. The largest discrepancy between two data sets before averaging was observed for bare acrylic with ~20 % difference between results.

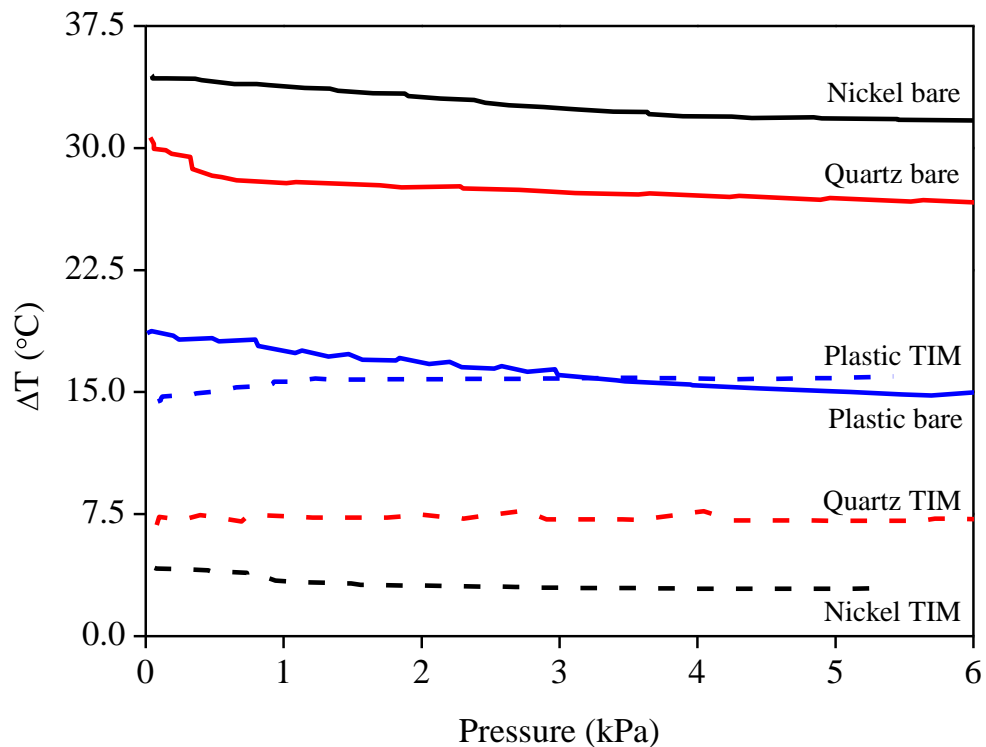
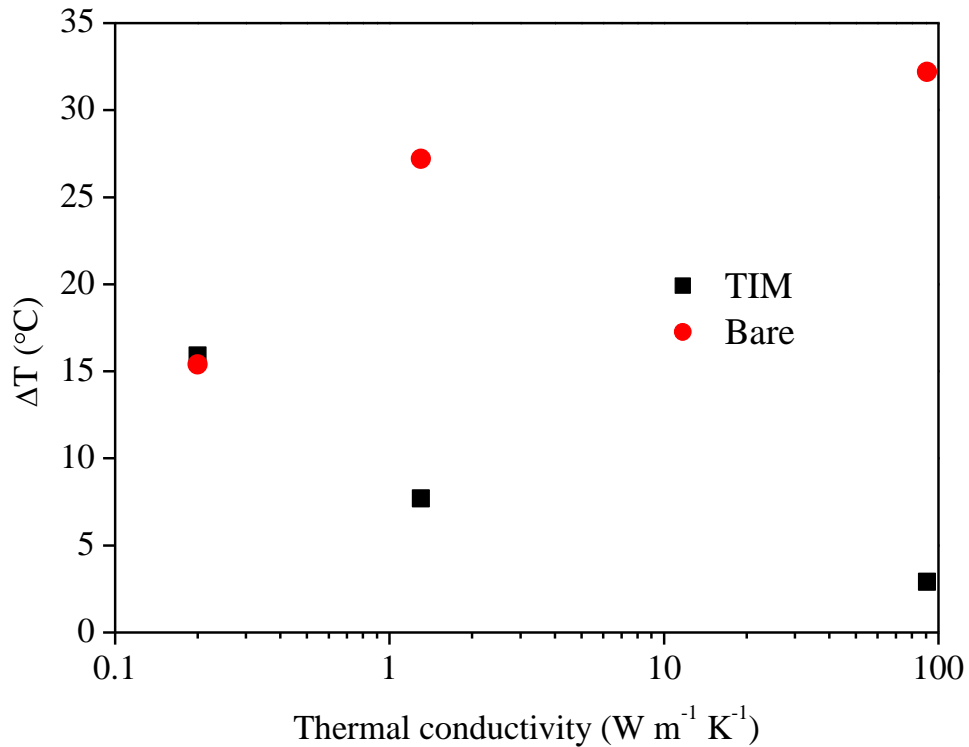


Figure 5.10 –  $\Delta T$  loading curves for quartz, nickel and acrylic with and without a TIM (each curve is an adjacent average fit of 2 data sets based on 10 points)

For all three materials, the  $\Delta T$  measurements showed little change when pressures above 2 kPa were applied, indicating that the water had formed a uniformly thick layer and the differences in measurements between samples was due to the bulk thermal properties of the samples rather than the TCR and surface properties of the samples. Both the water and acrylic samples show rapid changes in  $\Delta T$  at low pressures. This is likely to be due to surface tension effects and changes in the thickness of the water layer, as only small forces were applied.

All samples recorded lower  $\Delta T$  values when a TIM was applied. This is to be expected, as the water layer bridges the air gap between the two surfaces, reducing the thermal resistance. However, the results for nickel and quartz show a dramatic decrease in  $\Delta T$  compared with the bare measurements. The results also appear to be in line with the expected results based on the nominal thermal conductivity of the samples: higher thermal conductivities should result in lower  $\Delta T$  measurements. To show this, nominal values of thermal conductivity are plotted in

Figure 5.11 against  $\Delta T$  for a contact pressure of 4 kPa for samples with and without a TIM applied.



**Figure 5.11 –  $\Delta T$  measurements taken with a contact pressure of 4 kPa with and without a TIM, plotted against nominal values of thermal conductivity taken from Table 5.1**

When no TIM was used, the TCR dominated and the  $\Delta T$  measurements do not fit the trend expected to be seen with the nominal values for thermal conductivity (i.e.  $\Delta T$  decreasing with increasing bulk thermal conductivity). However, when a TIM is applied, the trend matches expectations and demonstrates the difference in bulk thermal conductivity between the samples is detected by the device.

Interestingly, the acrylic results show very similar values of  $\Delta T$  with and without a TIM. This is likely to be due to the relatively smooth and soft nature of the plastic surface, meaning that even without a TIM the sample and the device are in good contact and the value of the TCR is comparable with the thermal conductivity of the poorly conducting polymer.

## 5.5. Conclusions

Thermal contact resistance disrupts the flow of heat between two solids and is caused by a decrease in the actual area of contact from the nominal surface area. The main cause is due to surface roughness which reduces the effective contact area between the two surfaces. This inhibits the dominant form of heat transfer (conduction) as heat can only flow across the joint through areas where asperities are in contact. However, non-flat surfaces can also influence TCR by decreasing the effective area in contact. To enable the operation of the device on leaves to be understood, it was therefore necessary to investigate the effect TCR has on the device.

Theory shows [5] that the value of TCR is dependent on surface properties (surface roughness, hardness, thermal conductivity and slope) and the force applied bringing the two surfaces together. To investigate the effects of TCR on the device, it was systematically varied by applying different contact forces between the device and samples of known thermal conductivity. Loading curves were recorded for the device when it was brought into contact with the bare surfaces of acrylic, quartz and nickel. The results did not match the expected trend, as the acrylic sample gave the lowest  $\Delta T$  values, indicating the sample had a lower overall thermal resistance, despite acrylic have the lowest nominal thermal conductivity.

To investigate this anomaly, water was used as a TIM with the intention of providing a constant and low TCR between the device and all three samples. Loading curves for all three materials showed a decrease in  $\Delta T$  for all loading pressures, indicating that the TIM decreased the TCR. The loading curves followed the expected trend when a TIM was applied, with nickel giving the lowest  $\Delta T$  values and acrylic the highest. This indicates that the TCR was dominating measurements when no TIM was applied but application of water as a TIM can prevent the TCR from dominating and allow the device to operate on solid samples. As such, care must be taken interpreting measurements on solid samples, as the TCR could influence the results. The following section uses this effect to monitor the water content of leaves.

## 5.6. References

1. **Yovanovich, M.M.** Four Decades of Research on Thermal Contact, Gap and Joint Resistance in Microelectronics. *IEEE Transaction on components and packaging technologies*. 2005, Vol. 28, 2, pp. 182-206.
2. **Jackson, R. L., Bhavnani, S. H. and Ferguson, T. P.** A multiscale model of thermal contact resistance between rough surfaces. *Journal of Heat Transfer*. 2008, Vol. 130.
3. **Savija, I., Culham, J.R. and Yovanovich, M.M.** Review of Thermal Conductance Models for Joints Incorporating Enhancement Materials. *Journal of Thermophysics and Heat Transfer*. 2003, Vol. 17, 1.
4. **McAdams, W.H.** *Heat Transmission*. New York : McGraw-Hill, 1954.
5. **Song, S. and Yovanovich, M.M.** Relative Contact Pressure: Dependence on Surface Roughness and Vickers Microhardness. *International Journal of Thermophysics*. 1988, Vol. 21, pp. 43-47.
6. **Rauch, R.A.** Test Methods for Characterizing the Thermal Transmission Properties of Phase-Change Thermal Interface Materials. *Electronics Cooling*. 1995, Vol. 5, 2.
7. **Sadeghia, E., Djilali, N. and Bahramib, M.** Effective thermal conductivity and thermal contact resistance of gas diffusion layers in proton exchange membrane fuel cells. Part 2: Hysteresis effect under cyclic compressive load. *Journal of Power Sources*. 2010, Vol. 195.
8. **Lide, D.R., [ed.]**. *Handbook of Chemistry and Physics*. 83rd edition. Florida : CRC press, 2002.
9. **Tabor, D.** *The Hardness of Metals*. Oxford : Oxford Press, 1951.
10. **Abdulagatov, I.M, Emirov, S.N, Tsomaeva, T.A, Gairbekov, K.A, Askerov, S.Y.A and Magomedova, N.A.** Thermal conductivity of fused quartz and quartz ceramic at high

temperatures and high pressures. *Journal of Physics and Chemistry of Solids*. 2000, Vol. 61, pp. 779-787.

11. **Incropera, F. P. and DeWitt, D. P.** *Introduction to Heat Transfer*. 3. New York : Wiley, 1996.

12. Servisol technical datasheet: Heat Sink Compound - Non-silicone. [Online] [Cited: 18th March 2011.] [http://common.leocom.jp/datasheets/107022\\_319602.pdf](http://common.leocom.jp/datasheets/107022_319602.pdf).

This chapter demonstrates the prototype device in operation, monitoring the water content of the leaves of a plant. The underlying assumption is that the thermal properties of a leaf will vary with its water content. To allow these changes to be detected, a small scale thermal sensor is required. Previous chapters have demonstrated that the devices reported here are capable of operating on small samples, and this section builds on this work with a demonstration that the device can also be used on leaves.

The first experimental details in this chapter was designed to prove that the  $\Delta T$  measurements recorded by the device can be related to the water content of a leaf to which the device is attached. The experiment was conducted on abscised leaves (i.e. removed from the plant) which were allowed to dry under ambient conditions. This allowed the leaves to be weighed in order to determine the water content. The weight was converted into a relative water content value, which was compared with the device's response to demonstrate the dependence of  $\Delta T$  on water content. The relationship between water content and  $\Delta T$  is likely to be determined by the thermal contact resistance between the leaf and the sensor. This is discussed in Section 6.2.3.

Once the device was shown to be sensitive to the water content of an abscised leaf, the device was mounted on a plant in order to demonstrate that it is capable of measuring water content of a leaf in real-time while it is alive and still attached to a plant. To provide a control, the plant was subject, separately, to water stress conditions. The chapter begins with an introduction to some of the theory behind water loss from plants.

### **6.1. Plant water status theory**

It is generally known that plants require water to survive and that water is drawn from the soil, through the stem, into the leaves. Around 98 % of the water required by a plant is lost through transpiration and plays no role in the metabolic processes that sustain the plant [1]. While only a small proportion of a plant's supply of water is actively converted into sugars in metabolic processes, the bulk of the water volume still plays important roles within the plant. For example, water is used as a transport mechanism, bringing dissolved nutrients from the roots and the soil to the leaves, where metabolic activity occurs [2] while the 'hydraulic architecture' of a plant is essential to give it structural rigidity [3]. With an insufficient supply of water the plant will become water stressed as the cells within the leaves lose turgor. In response, the plant will act to halt the transpiration stream, reducing the water loss, but also preventing the flow of nutrients required for metabolic activity. Sensors are available which monitor the transpiration stream by detecting sap flow rates [4], however such sensors can only provide an estimate of the current water content of the leaves as losses to the environment will be dictated by the external conditions.

Water stressed plants stop growing and can even be damaged or die if water is unavailable or limited for long periods of time [5]. However, many plants have adapted to survive prolonged periods of water stress (e.g. Populus [6]) and some plants, such as Olives, even require periods of water stress to produce high quality crops [7]. Evolutionary pressures have shaped the way that different species manage their water supply; homeohydric plants are those which have developed the ability to restrict cellular water loss regardless of the environmental conditions [8]. A good example is that of cacti in a dry desert environment. Such homeohydric plants would make a poor

subject for this work, as the plants actively prevent water loss from their leaves and have evolved so that they do not show signs of water stress. Thus, only non-homeohydric plants were tested for this work (specifically Lettuce (*Lactuca sativa*) and Pak Choi (*Brassica rapa chinensis*)).

For non-homeohydric plants the water inside the cells of the leaf escapes into the intercellular spaces between cells, during transpiration. In order to draw more water from the roots, a water potential is required and so water must be lost from the leaves. Holes within the cuticle (called Stomata) undertake this role. Stomata regulate water loss from the plant and dominate the transpiration rate (80 – 90% of transpiration is stomatal transpiration [1]). Only a small amount of water is lost through the waxy cuticle layers and other mechanisms. Plants have developed homeostatic mechanisms to control the rate of water loss by opening and closing their stomata. As stomatal transpiration dominates water loss, understanding the mechanisms underlying the way the stomata open and close is key to understanding the factors effecting the water content of a leaf.

Stomata are simply holes within the epidermal layer of a leaf, formed and controlled by a pair of guard cells. Figure 6.1 shows a colourised SEM illustrating a stoma on the underside of a Pak Choi leaf. The turgor of these guard cells (and to some degree the epidermal cells in the vicinity of the stomata) dictates whether the stomata are open or closed [2]. The exact mechanism varies between different stomata within a plant and between species. However, they generally operate by means of having cell walls of differing thickness. As the turgor of the plant changes, the guard cells become more or less concave, thus controlling the opening and closing of the hole, as discussed below.

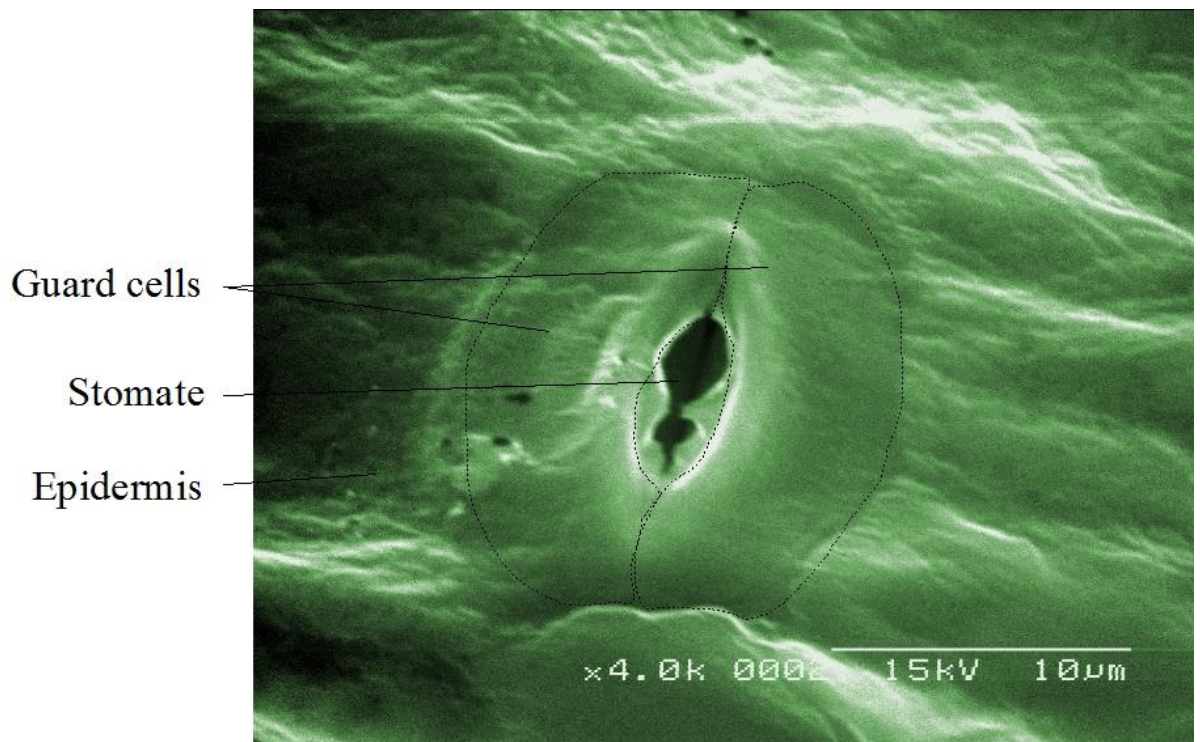


**Figure 6.1 – A coloured SEM image showing a stoma on the underside of a leaf. A dotted line has been drawn to highlight the guard cells, which form the stoma**

There are three principle factors which influence the opening and closing of stomata: light levels, internal water relations and temperature. Unless other conditions are limiting, the guard cells respond to light levels [1]. Under light conditions, they open to allow the gaseous exchanges required for photosynthesis. In turn, when in darkness, they close to prevent unnecessary water loss. During conditions of internal water deficit (e.g. on warm, dry days) there is a decrease in the turgor of the guard cells due to osmotic movement of water. This leads to the guard cells closing the stoma, regardless of the light levels, in order to preserve the turgidity of the plant. Extremes of temperature ( $>40\text{ }^{\circ}\text{C}$  or around  $0\text{ }^{\circ}\text{C}$ ) can also inhibit or promote stomatal opening. These homeostatic mechanisms control the level of water within the leaves, preventing unnecessary water loss and preserving the turgidity of the cells within the leaves. The purpose of the homeostatic mechanisms is to regulate the water content of the leaf and maintain constant and optimal conditions. However, the overall transpiration rate is also affected by external conditions, such as ambient temperature, air movement and humidity [1].

In general, water stress is detrimental to plants, primarily because it causes the closing of stomata, inhibiting the diffusion of carbon dioxide into the leaf. Prolonged water stress will lead to smaller plants, as carbon dioxide is required by plants to photosynthesise and produce carbohydrates which are essential for growth. Thus, plants grown with an unrestricted water supply will be larger than those grown under permanently water stressed conditions [2]. This is advantageous for agricultural crops. However, short periods of water stress or abundance can also affect a plant, particularly during specific development phases. Different species will react at different parts of their development cycle. For example, peas will produce more peas per pod if they have an abundance of water as they flower [2]. However, an abundance of water is not always beneficial. For instance the flavour of turnips, carrots and tomatoes are improved if the plant suffers mild water stress when the fruit is developing [2]. However, severe and prolonged water stress is universally detrimental to plants and will likely cause permanent wilting, growth inhibition and eventually death [1].

It is clear that for most crops, an abundant supply of water will produce the greatest yield. However, water is becoming increasingly scarce and expensive [9]. Thus, a balance must be found whereby the highest yield can be obtained using the resources available. A knowledge of the level of water within the leaves of a plant could be used to inform producers when to apply water in order to maximise production while minimising water use.

The following sections demonstrate that the device is capable of being mounted upon the leaves of a plant and that it is sensitive to the water content of the leaf. Initial work reports the proof of principle of the device, by monitoring an abscised leaf as it dries. The subsequent sections then build on this work and demonstrate that the device is capable of providing real-time information about the water status of a live plant.

## **6.2. Relating induced thermal gradient to water content**

The previous chapters have demonstrated that the device has the ability to monitor the thermal properties of small volumes. This and subsequent sections aim to demonstrate that such

measurements can be used to monitor the water content of leaves in real-time. This verification is important since the device could offer a non-destructive method for real-time, direct monitoring of the water status of plants. Such a sensor would be of interest as an irrigation scheduling tool. The sensor could fit into an intelligent irrigation system, allowing tailored watering of plants. By linking the irrigation to the real-time needs of the plants, such an irrigation system could prevent growth inhibition and increase crop yield, whilst reducing water consumption.

It was decided that abscising a leaf from a plant and monitoring its water content as it dried would offer a practical solution to allow validation of the operation of the device. Firstly, the abscised leaf would have no mechanisms to replenish any water lost, significantly reducing the number of variables affecting the water content. Secondly, the water content of the abscised leaf could be easily monitored by recording its weight over a period of time. This gave a sound method of comparing the device's output with the water content of the leaf as it dried.

Removing the leaf from the plant prevented replenishment of any water lost. A healthy leaf will lose water at a rate of up to 0.5 to 2.5 g dm<sup>-2</sup> hr<sup>-1</sup> [1], which for a leaf with a surface area of 3 cm x 3 cm represents a drying rate of 45 mg hr<sup>-1</sup> to 225 mg hr<sup>-1</sup>. As the abscised leaf cannot replenish its water, some homeostatic mechanisms are likely act so as to reduce the drying rate below these figures. The following sections detail an experiment in which a device is attached to an abscised leaf in order to monitor the response as the leaf dries out. The weight of the leaf is used to compare the water content to the device's output.

### **6.2.1. Experimental measurements on an abscised leaf**

Two similar sized leaves were abscised from a Pak Choi (*Brassica rapa chinensis*) plant. The device was attached to the first leaf and  $\Delta T$  measurements were recorded over a period of around 5 hours, while the leaf was allowed to dry under ambient conditions (~20 °C and ~45 % relative humidity). The second leaf acted as a control. Its weight was recorded periodically for the same 5 hour period using a set of scales (Ohaus Explorer Pro EP64C). The second leaf was allowed to dry under the same ambient conditions as the first leaf. Comparing the time dependence of the  $\Delta T$

measurements and the control leaf's weight allowed the device's output to be related to the water content of the leaf.

A calibrated PI device (Design B) was used for this experiment and a power of 8.8 mW was applied to the heater and  $\Delta T$  was recorded at 20 second intervals. 8.8 mW was found experimentally to give suitably large  $\Delta T$  values of 8 – 12 °C, well above the noise level. The maximum temperature recorded at the nearest junction was 39 °C, so the heat input was unlikely to damage the leaf and no visible damage was observed. The sensing area of the device was carefully positioned so it was not in contact with any vein structures or visibly damaged areas of the leaf. See Figure 6.2 for a photograph of the setup.

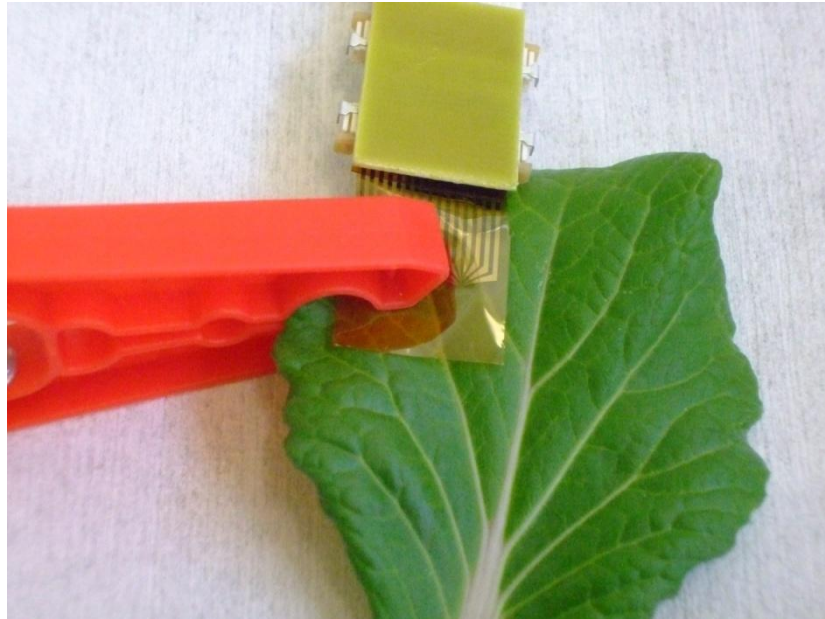


**Figure 6.2 – Photograph showing the device clipped onto an abscised Pak Choi leaf to monitor its water content as it dries**

The weights of the second leaf were converted into relative water content (RWC) values using a similar method to that originally proposed by Weatherley [10]. The method involves monitoring the weight of the leaf over time; this gives the *fresh weight* (FW) values. At the end of the experiment, the leaf was floated on the surface of a beaker of de-ionised (DI) water for a period of 2 hours to replace all the water lost and ensure that the leaf was fully turgid (i.e. contains the maximum amount of water it can hold). The leaf was then removed from the DI water and any excess droplets on the surface of the leaf were dried and the leaf weighed, giving the *turgid weight* (TW). The leaf was then dried in a vacuum oven at 80 °C for a period of 2 hours, before being weighed a final time to determine the *dried weight* (DW). The fresh weight measurements were then converted into RWC values using Equation 6.1:

$$RWC (\%) = \frac{(FW - DW)}{(TW - DW)} \times 100 \quad 6.1$$

The RWC value gave a measure of the water content of the leaf, with 100 % RWC representing a leaf that is fully turgid and 0 % representing a completely dehydrated leaf. Healthy leaves will generally have RWC values between 75 % and 95 % [11]. As both the  $\Delta T$  and weight measurements were taken on similar leaves from the same plant, a comparison could be made

between the two data sets to indicate how the  $\Delta T$  measurements responded to changes in the water content of the leaf.

### 6.2.2. $\Delta T$ dependence on water content

Plotting both the RWC and  $\Delta T$  measurements versus time allows a comparison to be made between the two sets of results. A typical example of one of the sets of results is shown in Figure 6.3. The RWC measurements show a monotonic trend which (in Figure 6.3) decreases from a starting value of 90.0 % to 75.4 % after the leaf had dried for 5.7 hours. The  $\Delta T$  measurements also show a decreasing trend with time, from a maximum value of 11.0 °C to 9.0 °C over the same period.

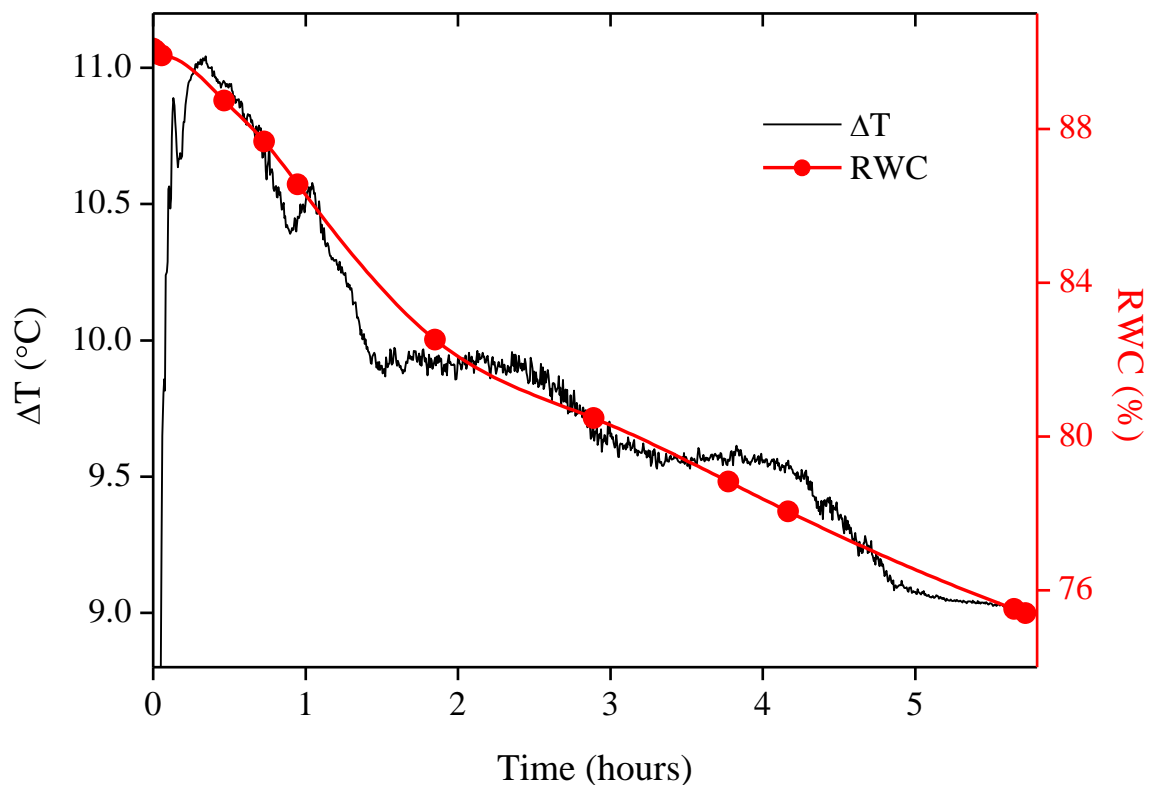


**Figure 6.3 – Time dependence of RWC and  $\Delta T$  for an abscised Pak Choi leaf, allowed to dry under ambient conditions for a period of 6 hours**

As the two sets of data were taken simultaneously on similar leaves taken from the same plant, the data can be used to relate RWC to  $\Delta T$ . Plotting RWC against  $\Delta T$  (Figure 6.4) shows that there is a clear positive, linear correlation between the two sets of data. This indicates that the  $\Delta T$

measurements are linearly proportional to the water content of the leaf. This relationship demonstrates that the device's output is sensitive to the water content of the leaf. However,  $\Delta T$  is seen to decrease as the leaf dries, indicating that the thermal conductivity is increasing. This trend is the reverse of that observed as wetted paper dries (Section 4.2.3.2). The opposing trends indicate that two separate mechanisms must be causing the change in the  $\Delta T$  measurements. This is discussed further in Section 6.2.3.

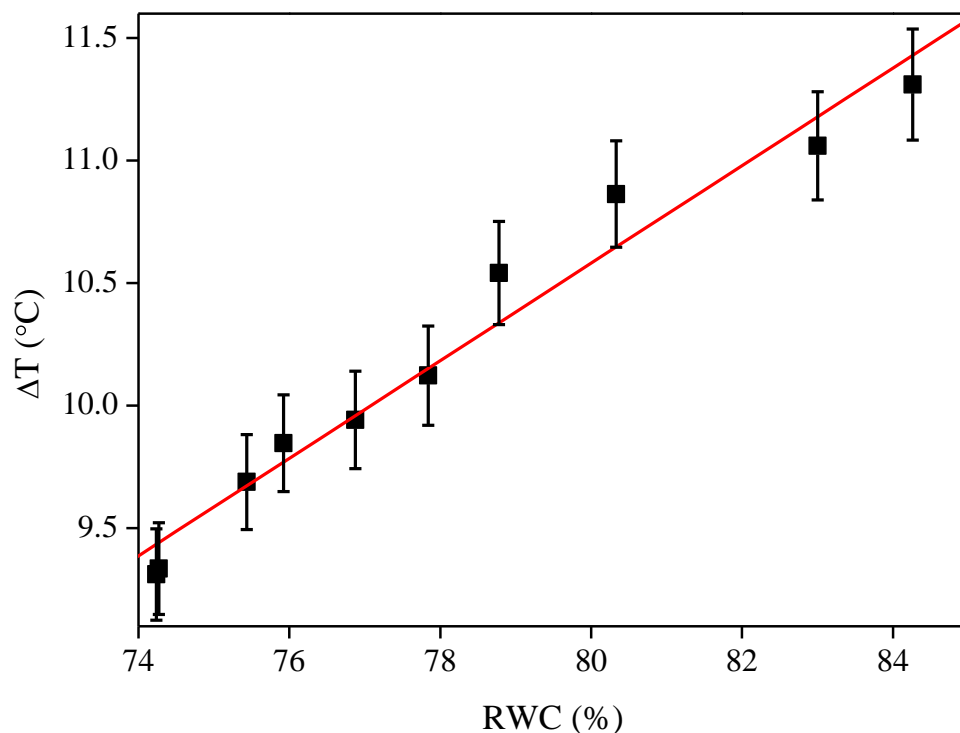


**Figure 6.4 –  $\Delta T$  measurements increase linearly with the relative water content (RWC) of the leaf. Error bars represent the maximum variation observed across three repeated experiments using different leaves**

It should be noted that the  $\Delta T$  measurements in Figure 6.3 show rapid and non-monotonic changes, despite the overall downward trend. These fluctuations are likely to have two causes. The first is the sampling time:  $\Delta T$  measurements were recorded by a data logger, with a sampling time of 20 s, whereas the weight of the leaf was recorded manually every 5 – 20 minutes. Thus, rapid fluctuations in the weight of the drying leaf would not be recorded. Increasing the frequency of weight sampling may pick up subtle changes, however, observation of the weight during the

experiment did not indicate that the weight was changing rapidly or non-monotonically. Thus, the chosen sampling time was sufficient for monitoring the weight of the leaf and more frequent sampling would not reconcile the differences between the two datasets. The second cause for the rapid fluctuations is the relatively small volume of the leaf which the device was monitoring ( $\Delta T$  was measured with 110  $\mu\text{m}$  between the TFTC sensing junctions). Structural changes due to a loss of turgidity could alter the local flow of heat within the leaf, so the small volume being probed is much more likely to demonstrate rapid changes in water content than the whole leaf.

Repeating the experiment and converting the  $\Delta T$  measurements into a RWC value on 3 sets of Pak Choi leaves gives the results shown in Figure 6.5. Each leaf follows a similar trend, indicating that the device is indeed responding to the water content of the leaf. However, each also shows rapid, non-monotonic changes at different periods. This is consistent with the device picking up localised variations related to structural changes within the leaf.

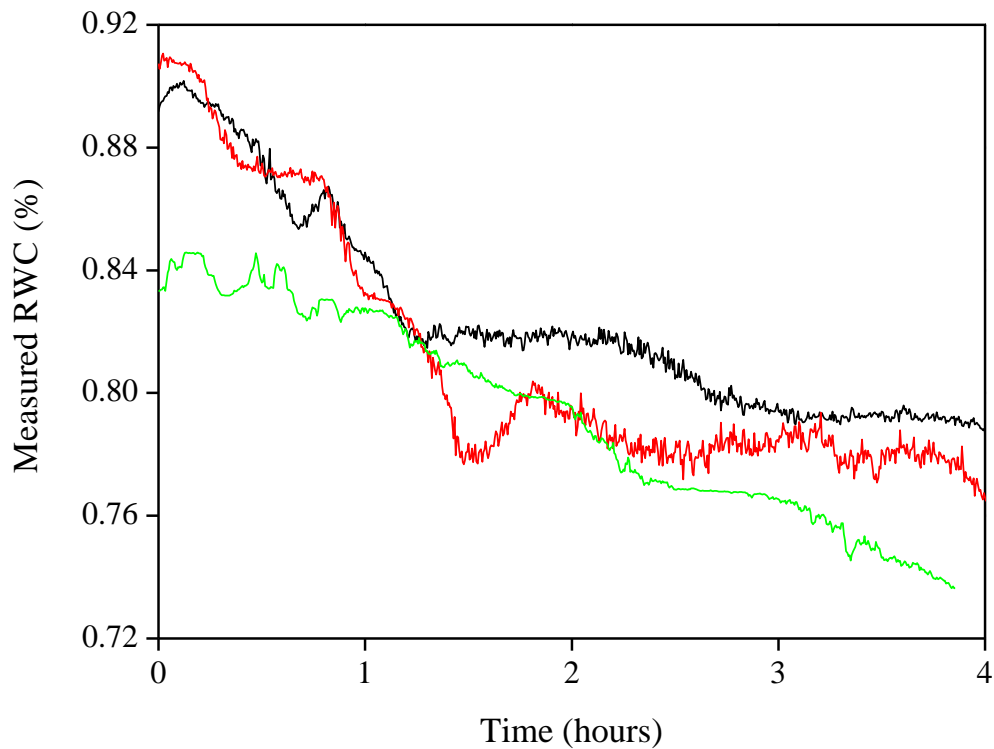


**Figure 6.5 – Time dependence of measured RWC taken on three abscised Pak Choi leaves over a period of 4 hours**

The device is designed to probe a small volume, so it is capable of giving real-time information about specific areas of a leaf. This allows the water content of leaves to be studied with much better spatial resolution than other methods permit (e.g. thermal imaging [7] or magnetic patch clamp sensors [12]). This could allow the overall water status of a plant to be better understood, by probing individual areas of leaves and repeating across the whole plant. However, care must also be taken as localised variations in water content could lead to spurious results in terms of the overall water status of the plant, as each device only monitors a small volume of one leaf. Thus, for accurate measurements of the whole plant, several sets of sensors should be used. As the devices are relatively small and simple to implement, producing multiple sensors on each device and attaching multiple devices to each plant would minimise the small volume sampling issue and improve the reliability in terms of the overall water status of the plant.

### **6.2.3. Dependence of $\Delta T$ on leaf water content**

There are two important aspects to the results outlined in Section 6.2.2. Firstly, the device is clearly capable of detecting a change in the water content of the abscised leaf, as the  $\Delta T$  measurements decrease. Secondly, the  $\Delta T$  measurements taken on wetted paper and a leaf show opposing trends. This indicates that the mechanisms controlling the change in  $\Delta T$  are different in the two materials. To discuss why the two materials show differing trends, it is necessary to understand the structure of the materials involved. In paper the water directly alters the thermal conductivity by altering the flow of heat within the material by replacing the low thermal conductivity air filled voids with high thermal conductivity water. In a leaf, the turgidity of the cells plays a more important role in the  $\Delta T$  measurements. The following section outlines the differences in the micro-structure of leaves and paper and relates these to the differing results observed.

#### **6.2.3.1. *Structural effects***

The micro-structure of a leaf and paper are markedly different. These differences lead to the opposing trends in  $\Delta T$  seen the materials lose water. Figure 6.6 shows diagrams, SEM images and the device's response as a function of time for both the leaf and paper samples. Figure 6.6 a) & b)

shows that the paper consists of interlinked cellulose fibres lying in random directions, with no organised structure. The fibres have widths of  $\sim 1 - 10 \mu\text{m}$  while the voids around the fibres are  $\sim 10 - 100 \mu\text{m}$  wide. The paper is able to hold water by filling these voids and when it is saturated the water will completely fill the voids. As the paper dried, water evaporated and the water-filled voids gradually became air-filled. As such, thermal conductivity decreased as water has a higher thermal conductivity ( $0.6 \text{ W m}^{-1} \text{ K}^{-1}$  [13]) when compare with air ( $0.026 \text{ W m}^{-1} \text{ K}^{-1}$  at  $20 \text{ }^\circ\text{C}$  [13]). Thus, as the paper dried out  $\Delta T$  increased, as shown in Figure 6.6 c).

The micro-structure of a leaf is significantly different from that of paper. Firstly, there are discrete structures, such as the waxy cuticle, epidermal layers and mesophyll layers [1], these are shown in Figure 6.6 d). Towards the upper-side of the leaf, the cells will be tightly packed together to form the palisade mesophyll which has little space between cells to maximise light capture for photosynthesis. The lower layers of the leaf form the spongy mesophyll, which has more rounded cells. These are less tightly packed and form voids which allow diffusion of the gasses required for photosynthesis and respiration. Larger vein structures also occur within the leaf to transport water. Secondly, the majority of the water within the leaf will be contained within the cells. This inhibits water loss, as the water must pass through the cell membrane before it can enter the void between cells and then leave the leaf in the form of water vapour. This inhibition to water loss can be seen in the difference in drying times for the two materials (Figure 6.6 e) & f)). Wetted paper completely dried in around 1 hour at  $20 \text{ }^\circ\text{C}$ , whereas a leaf lost only around 20 % of its water content over a period of 5.75 hours at  $20 \text{ }^\circ\text{C}$ .

As a plant cell loses water, it will also lose turgor [1]. This may influence the flow of heat through the leaf, due to the decreased water content and changes in intercellular pressure which will affect the TCR between cells. On a larger scale, the leaf became softer. This may allow the device to form a better contact with the leaf, reducing the overall TCR observed. The result is seen in Figure 6.6 f) as a decrease in the  $\Delta T$  measurements as the leaf dries. The following section outlines an experiment which investigates the effect of changes in the TCR have on the observed trend in  $\Delta T$  seen as the leaf dries.

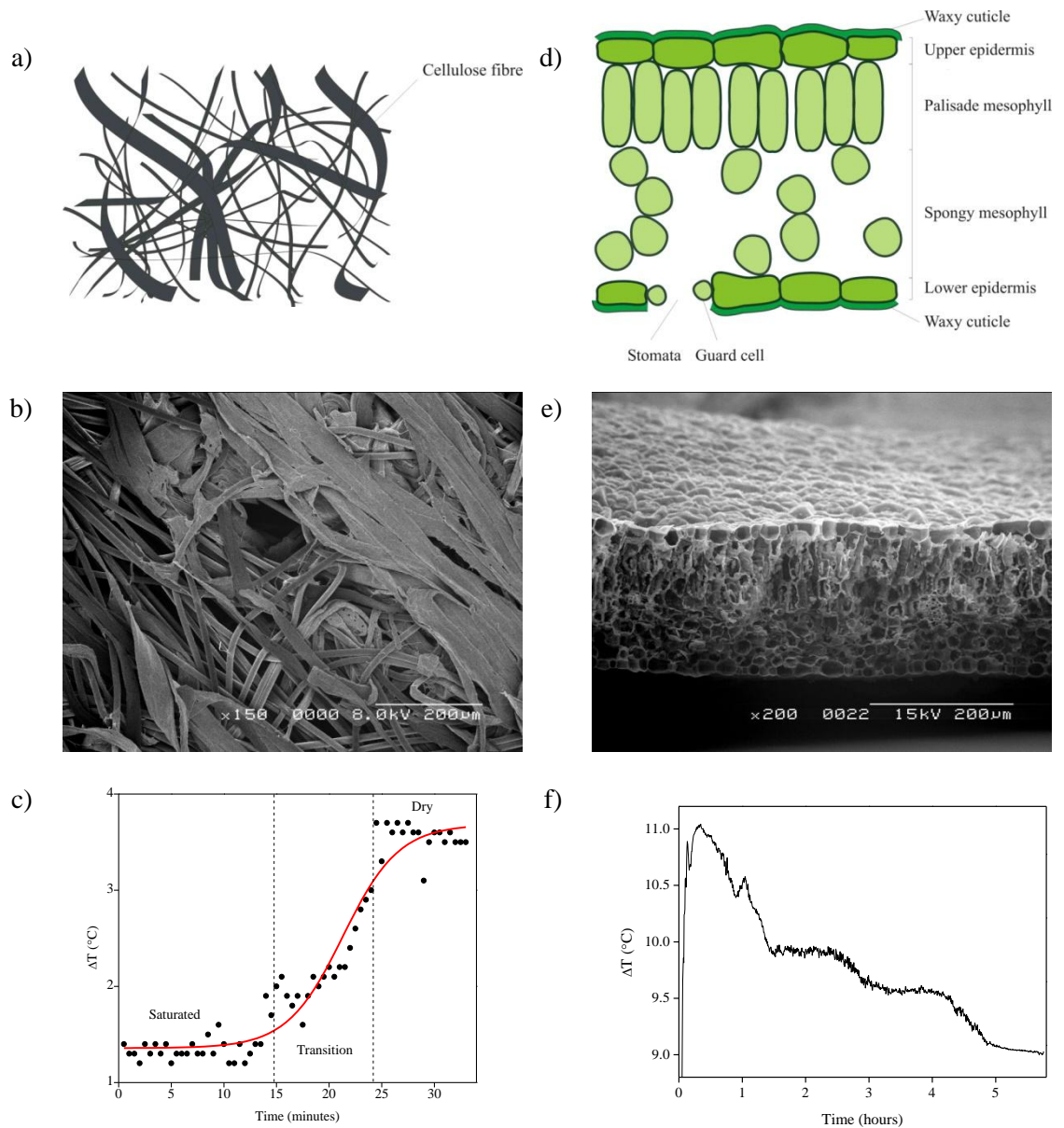


**Figure 6.6 – a) Diagram of the microstructure of paper; b) SEM of paper used in Section 4.2.3.2; c)  $\Delta T$  as a function of time for paper as it dries (taken from Figure 4.17); d) Diagram of the microstructure of a leaf; e) SEM of a Pak Choi leaf & f)  $\Delta T$  as a function of time for a leaf as it dries (taken from Figure 6.3)**

### 6.2.3.2. Effect of thermal contact resistance on leaf measurements

To investigate the hypothesis that the TCR is dominating the  $\Delta T$  measurements taken on a leaf, the contact resistance experiment described in Chapter 5 was repeated on a leaf when it was freshly abscised and again after it had been allowed to dry. Repeating the measurements using water as a TIM allowed the effect of TCR to be investigated.

To achieve this, a leaf was abscised from a well watered Pak Choi plant. A Design B polyimide based device was attached to the arm of a stepper motor and a power of 8.8 mW was applied to the resistive heater.  $\Delta T$  measurements were recorded during loading and unloading on the freshly abscised leaf and on the same leaf after it had been allowed to dry under ambient conditions ( $\sim 20^\circ\text{C}$  and 45 % relative humidity) for a period of 4 hours. Other experimental details were as described in Section 5.2. The loading and unloading curves are shown in Figure 6.7.

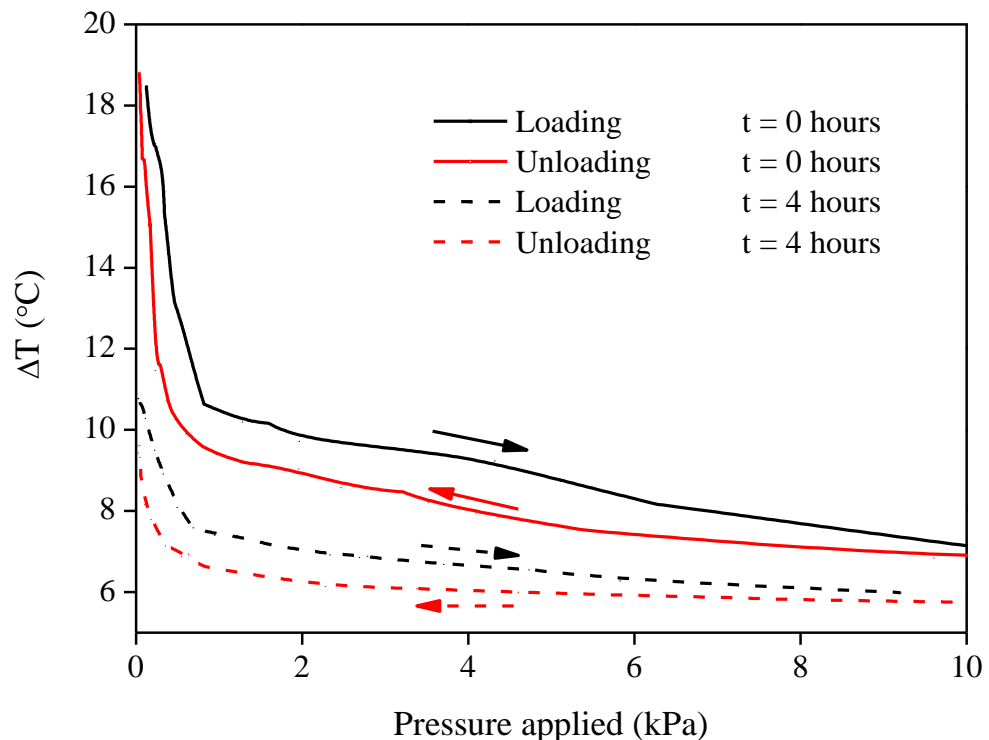


Figure 6.7 – Two loading and unloading curves for an abscised Pak Choi leaf. Solid lines indicate the curve was recorded immediately after abscission and the dotted lines indicate the curve was recorded 4 hours after abscission

The loading and unloading curves show a similar trend when freshly abscised and after drying for 4 hours. As the contact pressure increases, the  $\Delta T$  measurement decreases indicating that the contact resistance is reducing, as would be expected (see Section 5.1 for TCR theory). A rapid decrease in  $\Delta T$  is seen until the applied pressure reaches around 1 kPa, at which point the gradient reduces and the curve steadily decreases as further load is applied. Both curves show hysteresis as the load was removed. This is due to the flattening of asperities during the loading phase. However, the  $\Delta T$  measurements taken on freshly abscised leaves have higher values. With a contact pressure of 4 kPa, the freshly abscised leaf demonstrates a  $\Delta T$  measurement of 9.3 °C during loading and 8.1 °C during unloading, compared to 6.7 °C and 6.0 °C for the same leaf after 4 hours.

The reduction in  $\Delta T$  measurements between the fresh and 4 hour leaf indicates that the overall thermal resistance seen by the device decreases as the leaf dries. As the leaf is losing water which has a high thermal conductivity, the decrease in overall thermal resistance is likely to be due to a decrease in the TCR caused by the cells within the leaf becoming more flaccid and the surface of the leaf softer, improving the contact between the leaf and the device. However, the 4 hour leaf may also present a higher thermal conductivity, as the flaccid cells will more easily deform under the compressive force, improving the intercellular heat flow.

To demonstrate that there was little change in the bulk properties of the leaf, the experiment was repeated with a thermal interface material (TIM) used to reduce the contact resistance. Water was chosen as the TIM as it would not have an adverse effect on the leaf as well as for the reasons outlined in Section 5.4.

A small droplet of water was placed on the surface of the leaf immediately prior to the measurements being taken. Measurements were taken as quickly as was practical, to prevent the leaf from absorbing water, which would influence the result. The loading curves for both a fresh and 4 hour old leaf obtained with a TIM are shown in Figure 6.8. Only the loading curves are

shown for clarity. The hysteresis seen without a TIM was not seen when the water was applied, as the thin liquid layer prevents the asperities from being deformed.

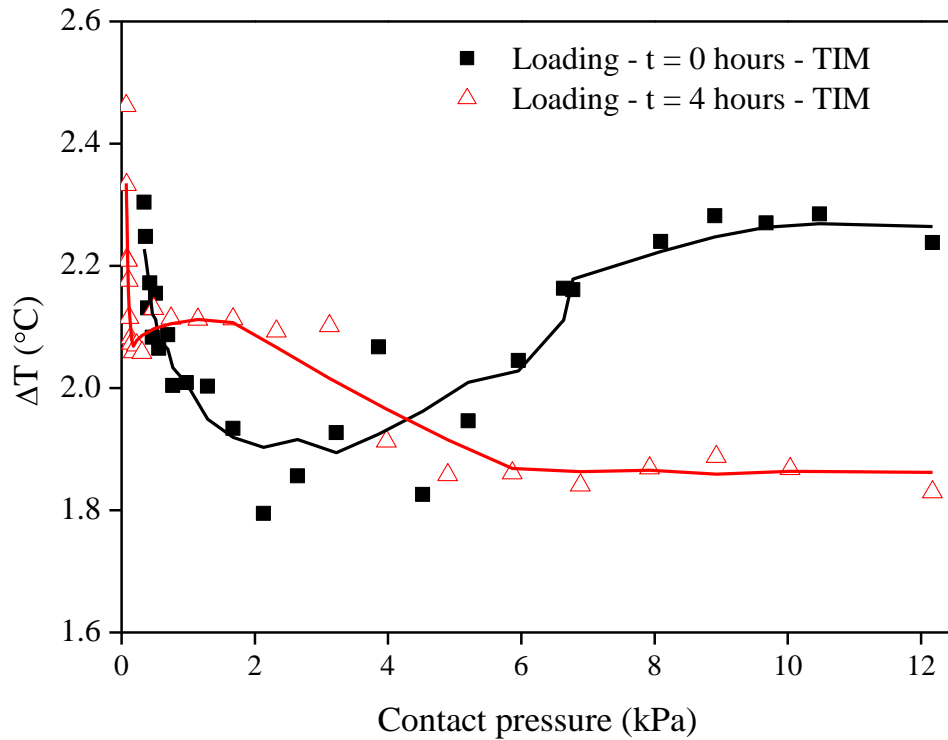


**Figure 6.8 – Loading curves for a freshly abscised leaf (black) and a 4 hour old leaf (red) using water as a TIM. Unloading curves are not shown for clarity and a 5 point averaged curve is fitted to the data**

The introduction of water as a TIM produced a broadly constant  $\Delta T$  measurement above  $\sim 0.7$  kPa with fluctuations due to noise in the relatively small  $\Delta T$  measurements. Both the fresh and 4 hour leaves, gave  $\Delta T$  of  $\sim 2^\circ\text{C} \pm 0.4^\circ\text{C}$ . This is a much smaller  $\Delta T$  value than that observed during both sets of measurements without a TIM and there is a much smaller difference between the  $\Delta T$  measurements on the fresh and 4 hour old leaf when the TIM was applied ( $0.4^\circ\text{C}$  maximum difference with a TIM compared to  $8^\circ\text{C}$  without). To allow a comparison to be made and to show the effect of the TIM on the results, loading curves for both results are plotted together in Figure 6.9.

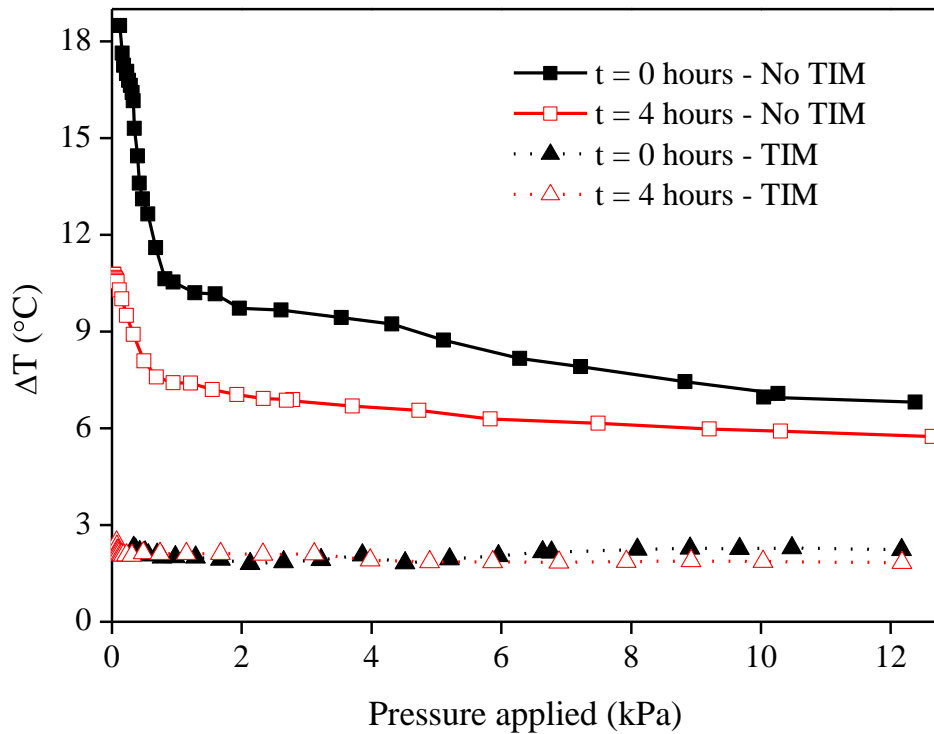


**Figure 6.9 – Loading curves for abscised leaves with and without a TIM. Black lines indicate the freshly abscised leaves and red lines indicate loading curves for leaves 4 hours after abscission. Dotted lines indicate that water was used as a TIM and solid lines were recorded without a TIM**

Without a TIM, the measurements follow a curve which decreases with contact pressure, as the asperities on the surface of the leaf deform with increasing pressure. This leads to a larger effective contact area between the two surfaces and hence the device recording a lower overall thermal resistance. When a TIM was applied, the TCR between the device and the leaf was effectively constant. While the thin water layer may influence the absolute measurement taken by the device, it shows that changes in the leaf's bulk thermal conductivity were negligible after it had dried for a period of 4 hours. Thus, the difference in the results observed between the fresh and dried leaf when no TIM was applied could be due to changes in the TCR.

While changes in TCR are one potential interpretation of the results shown above, it should be noted that the process of water loss from a leaf will be subject to a number of complex mechanisms. For example, changes in thermal conductivity through a leaf could be influenced by

morphological changes related to the intercellular pressure of the leaves. Turgid cells may offer a higher resistance to heat flow by offering a smaller contact area between cells while the compressive force of the clamp could increase the thermal conductivity of flaccid leaves by compressing the cells.

This work suggests one potential explanation for the observed results, however understanding the mechanisms underpinning the operation of the device would require a greater understanding of the biological responses and structural changes caused by water deficit within a leaf. For the purposes of this work, it is clear that the device detects a change in the water content of the leaf which is related to a change in the overall thermal resistance of the leaf.

As a final point, it is important to note that when the device is clamped to a freshly abscised leaf without a TIM (e.g. during the experiment detailed in Section 6.2.1) the  $\Delta T$  measurements are around 10 °C, indicating that the clip is providing a contact pressure of around 2 kPa. Contact pressures below 2 kPa risk being influenced strongly by the applied force (see Figure 6.7), as this area of the curve is seen to change quickly for a small change in pressure (for a fresh leaf the change is 17.2 °C kPa<sup>-1</sup>). At 2 kPa, the rate of change of  $\Delta T$  with applied pressure is only 0.18 °C kPa<sup>-1</sup>, meaning that variations in the contact pressure would have a minimal effect.

## 6.3. Plant water status monitoring

### 6.3.1. Aims

Section 6.2 demonstrates that the device is capable of monitoring the water content of a leaf. To provide a rapid, easily controlled decrease in the water content and allow its weight to be recorded, the leaf was removed from the plant. This section builds on the previous results and demonstrates that the device can be used in-situ to take real-time measurements when the leaf is still attached to the plant. This is achieved by subjecting a plant to dry conditions in order to monitor the device's response as the plant becomes water stressed.

In order to run a controlled experiment, it is necessary to understand how various factors affect the water content of a leaf. The water content of the leaves of a plant is the result of a balance between the water drawn up from the roots against the water lost from the leaf to the environment. This balance is governed by a complex mixture of factors, for example:

- **Soil water content** – Insufficient water within the soil prevents the plant from replenishing the water it loses through transpiration. This will lead to water stress within the plant [3].
- **Light level** – Exposure to light induces photosynthesis, causing the cells within the leaves to consume water and stomata to open, increasing transpiration. Assuming sufficient water is available to the plant and transpiration losses are not high, water will be drawn from the roots and increasing the water content of the leaves [1].
- **Carbon dioxide (CO<sub>2</sub>) levels** – CO<sub>2</sub> is required for photosynthesis to take place. If a plant is in an environment with little CO<sub>2</sub>, then it will not photosynthesise and transpiration will be reduced [2].
- **Ambient atmospheric conditions** – The temperature, humidity, wind speed etc... will all inhibit or promote water loss and affect the transpiration rate, as a result [1].
- **Health of the plant** – Damage or infection can prevent the plant from functioning correctly and maintaining a normal transpiration flow [1].

As it was not possible to get an independent measure of the water content of a leaf in-situ on a plant, it was necessary to limit the number of variables which could influence the water content of the leaf being probed. To achieve this, variables such as light level, temperature and humidity were monitored and controlled where possible. The plant received no water over a period of several days, causing the soil to dry out which in turn lead to the plant becoming water stressed. This lead to a decrease in the water content in the leaves, which was detected by a device attached to one of the leaves. The aim of the experiment was to demonstrate that the device has the ability to detect significant changes in the water content of the plant's leaves in real-time and non-destructively.

### **6.3.2. Real-time detection of water stress in a plant**

As water evaporates from a plant, the xylem draws water from the roots up to the leaves to ensure a constant water potential within the leaf [2]. When this flow is interrupted (e.g. by a lack of water within the soil), homeostatic mechanisms (generally changes in the osmotic potential of the guard cells) close the stomata and the evaporative losses are dramatically reduced [1]. Even with the stomata closed, water will still be lost from the plant by diffusion through the waxy cuticle and from the soil through evaporation. Thus, a plant will act to keep sufficient water within its leaves to promote photosynthesis. Eventually, the water content of the soil may become so low that the plant is unable to replenish the water that is lost to the atmosphere and the water content of the leaf will decrease. If this situation lasts for a sufficiently long period, the plant is said to be water stressed, which will cause it to wilt, become damaged and eventually die.

To demonstrate that the device is capable of detecting water stress in a plant, it was attached to Pak Choi (*Brassica rapa chinensis*) which was allowed to become water stressed. For this experiment, a polyimide based device (Design B) was used with a power input of 8.8 mW applied to the heater and  $\Delta T$  measurements were taken at 20 s intervals over a period of several days. The plant was placed within a Perspex 'dry-box' which was not fully sealed as it had a small hole to allow electrical connections to be made to the device and to allow gaseous exchange and prevent the build up of oxygen, carbon dioxide or water vapour. A humidity and temperature sensor (EL-

USB-2, Lascar Electronics) was located within the box to monitor the ambient conditions. Typically, the temperature and humidity observed were  $25\text{ }^{\circ}\text{C} \pm 2\text{ }^{\circ}\text{C}$ ,  $60\% \pm 20\%$ , respectively. As light plays an important role in controlling the transpiration rate and water content of the leaves, the sides of the box were covered to prevent ambient light affecting the results and a lamp was located above the box to provide a constant light source. The plant was only watered when it began to visibly wilt. A diagram of the setup is shown in Figure 6.10. By monitoring the output of the sensor throughout the experiment, the effect of water stress on the plant could be related to changes observed in  $\Delta T$  measurements.

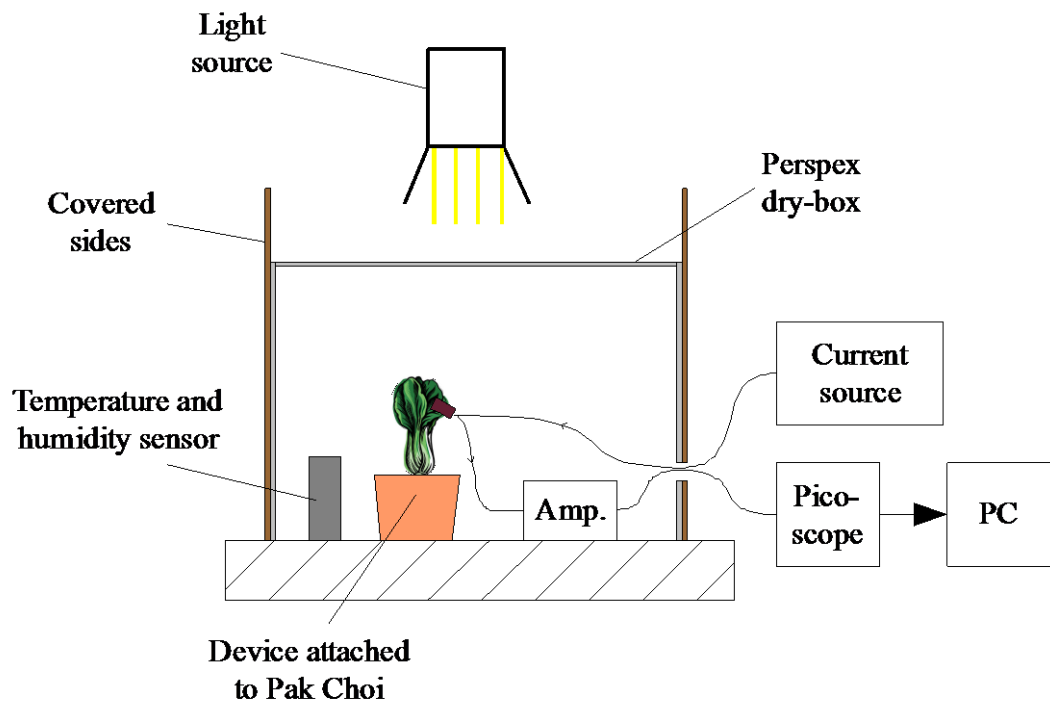
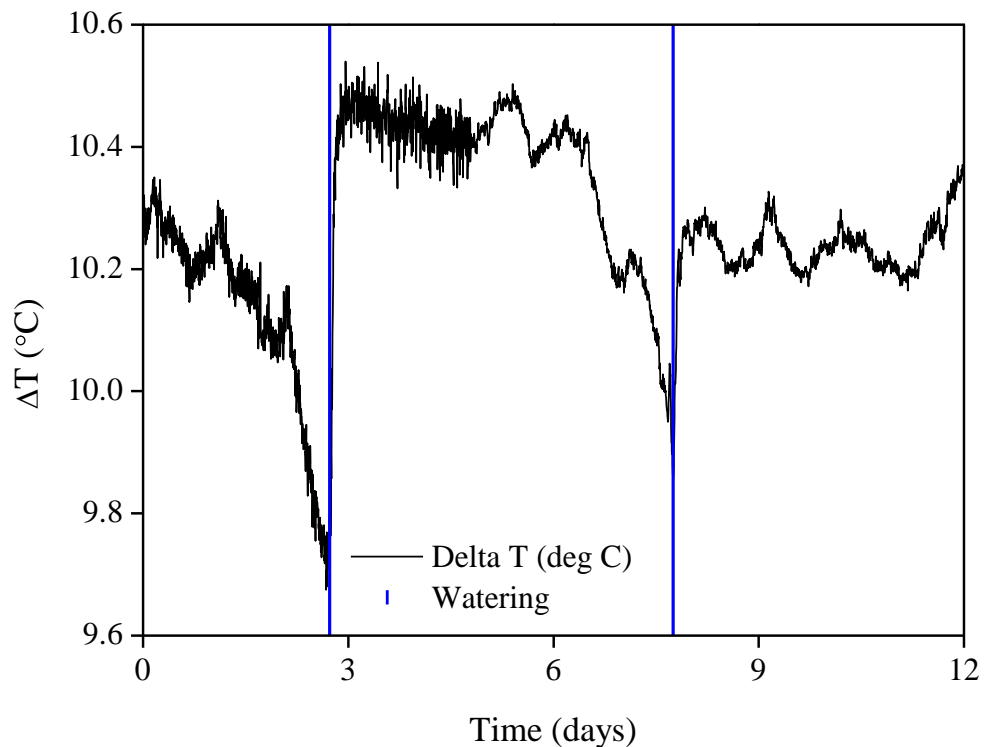


Figure 6.10 – A diagram showing the experimental setup for plant water status monitoring

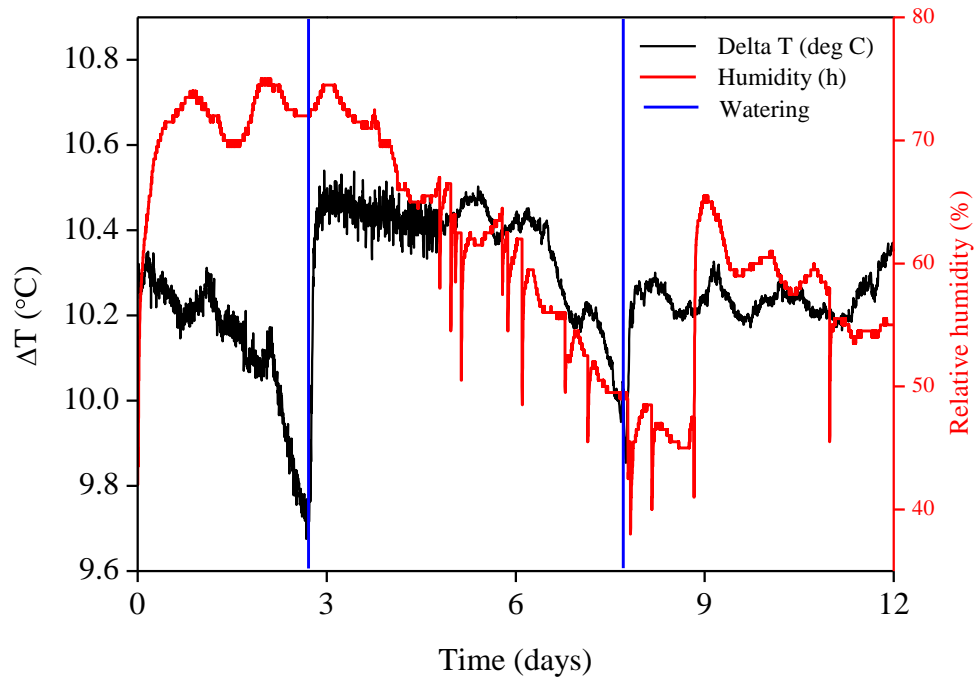
Section 6.2.3 showed that as a leaf dries out  $\Delta T$  measurements decrease due to the change in contact resistance between the device and the leaf. Thus, it is expected that a sensor attached to a plant under controlled conditions with sufficient water available should demonstrate a constant  $\Delta T$  measurement. If the water available to the plant becomes limited, over a period of time the water content of the leaf will drop accordingly. This will be recorded by the device as a decrease in  $\Delta T$  measurements as the cells within the leaf lose turgor.

Figure 6.11 shows the experimental results obtained on a Pak Choi plant over a period of 12 days. The plant was watered twice (marked as blue vertical lines on Figure 6.11). During stable periods when the plant was not water stressed, the  $\Delta T$  measurements showed a value of  $\sim 10.3\text{ }^{\circ}\text{C} \pm 0.2\text{ }^{\circ}\text{C}$ . As the plant became water stressed  $\Delta T$  decreased markedly, reaching  $9.7\text{ }^{\circ}\text{C}$  before the first watering. This is consistent with a change in the RWC of  $\sim 4\%$ , based on the work in Section 6.2. Before the second watering,  $\Delta T$  reached  $9.9\text{ }^{\circ}\text{C}$ . After watering in each case, the  $\Delta T$  value was seen to return to the original  $\sim 10.3\text{ }^{\circ}\text{C}$  value. This result clearly indicates that the changes in  $\Delta T$  observed were due to the plant under test becoming water stressed. The results are in line with those seen in Section 6.2.2, indicating that the device is detecting real-time changes in the water status of the plant by monitoring the changes in  $\Delta T$  induced by a decrease in the turgor of the leaf's cells.



**Figure 6.11 – Time dependence of  $\Delta T$  for a device attached to a Pak Choi plant suffering water stress conditions. Blue vertical lines show when the plant was watered**

In order to demonstrate that the changes were related to the water content and not external changes in the ambient conditions, the temperature and humidity within the dry-box were recorded. Superimposing these externally induced changes in the ambient conditions against the  $\Delta T$  values appears to show that they have no influence on the results. To demonstrate this, the ambient temperature and humidity values were plotted against the relevant  $\Delta T$  values in Figure 6.11 and Figure 6.14. These graphs indicate that the  $\Delta T$  measurements were independent of the ambient conditions over the range of conditions experienced during the experiment. This is an important result as it demonstrates that the change in water content is the dominant effect, rather than any externally induced effects.



**Figure 6.12 – Relative humidity measurements within the dry-box superimposed over the  $\Delta T$  measurements shown in Figure 6.11. Blue vertical lines show when the plant was watered**

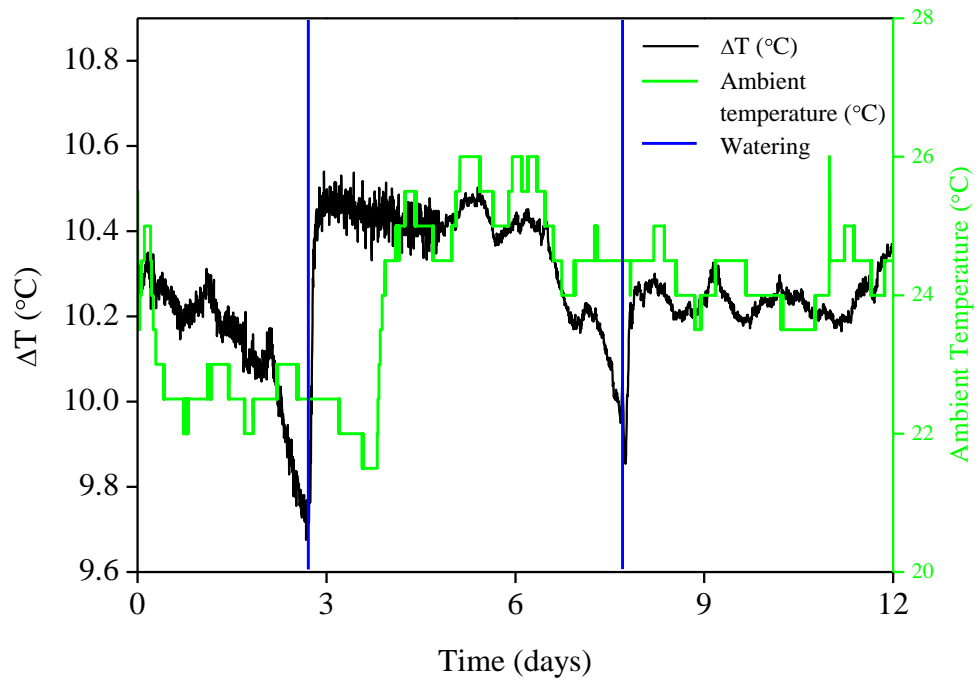


**Figure 6.13 – Ambient temperature measurements within the dry-box superimposed over the  $\Delta T$  measurements shown in Figure 6.11. Blue vertical lines show when the plant was watered**

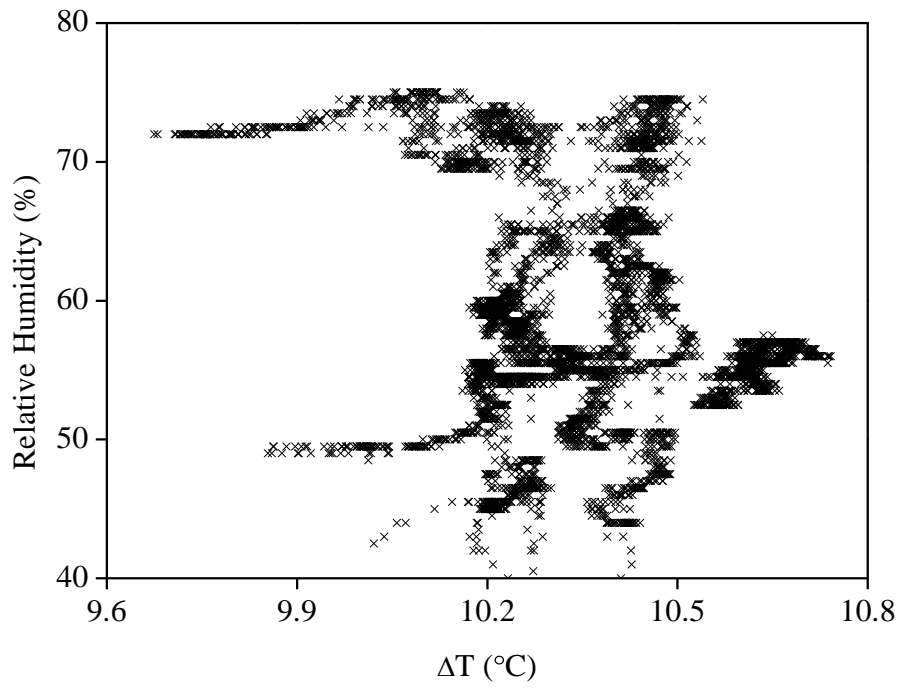


**Figure 6.14 – Ambient relative humidity values recorded within the dry-box plotted against the  $\Delta T$  values obtained on a Pak Choi plant (taken from Figure 6.12)**

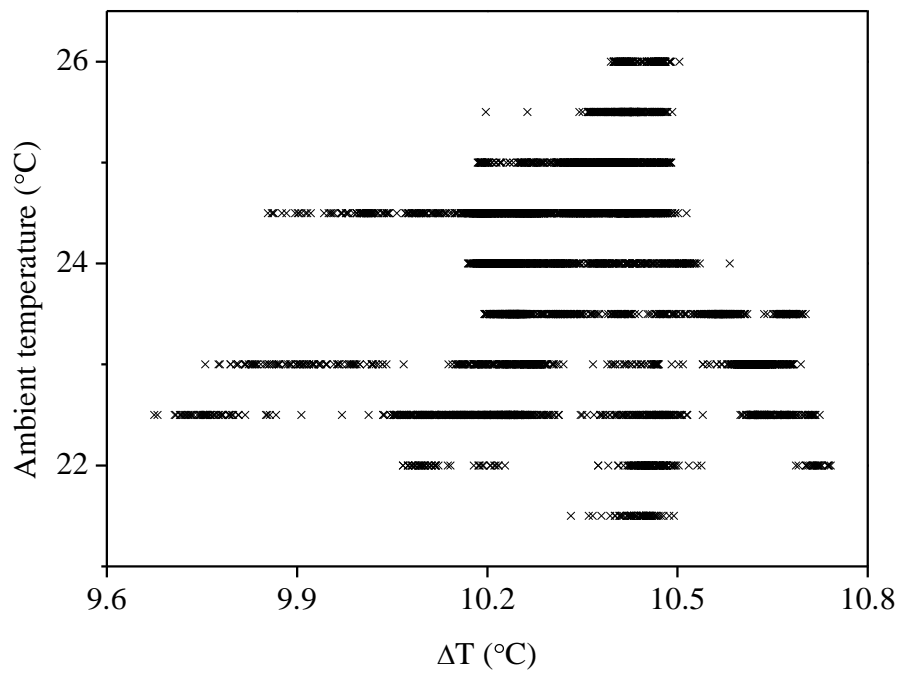


**Figure 6.15 – Ambient temperature values recorded within the dry-box plotted against the  $\Delta T$  values obtained on a Pak Choi plant (taken from Figure 6.13)**

**6.3.2.1. A comparison between Pak Choi and Lettuce plants suffering water stress**

To provide a comparison between different plant types, a second set of measurements were taken on a Lettuce (*Lactuca sativa*) plant over a period of six days. The results are shown in Figure 6.16. The second experiment was run over a shorter period as the Lettuce was seen to dry out more quickly. This was caused by the volume of soil in which the plants were grown: the Pak Choi was in a 9 cm diameter pot (~350 cm<sup>3</sup>) while the Lettuce was in a smaller volume of soil ~4 cm in diameter (~35 cm<sup>3</sup>). The smaller volume of soil contained less water, so the plant suffered water stressed conditions more quickly.

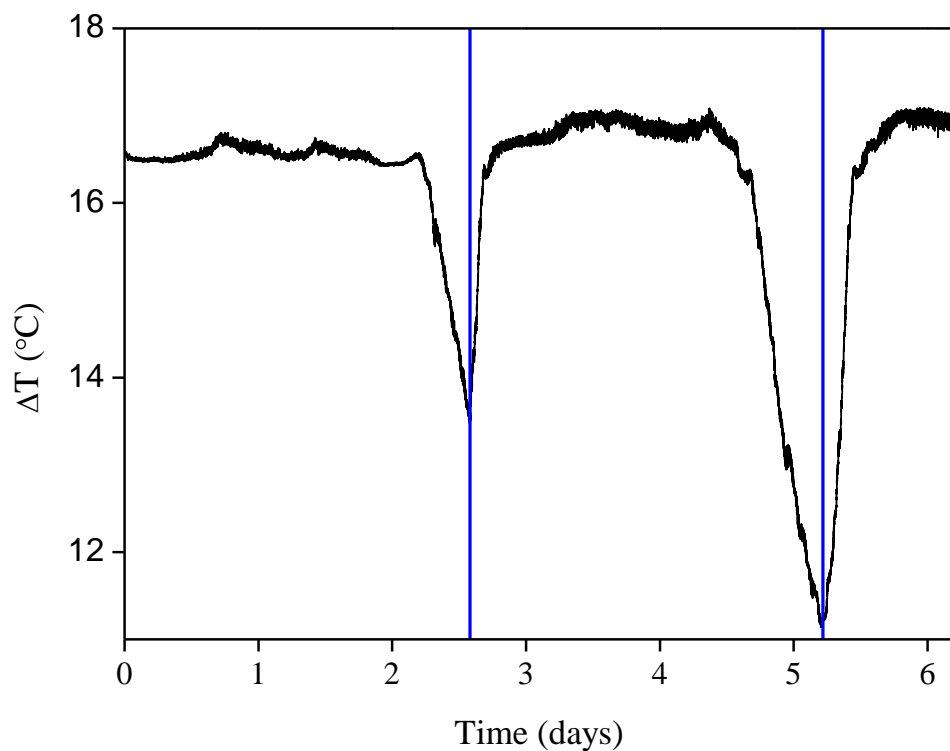


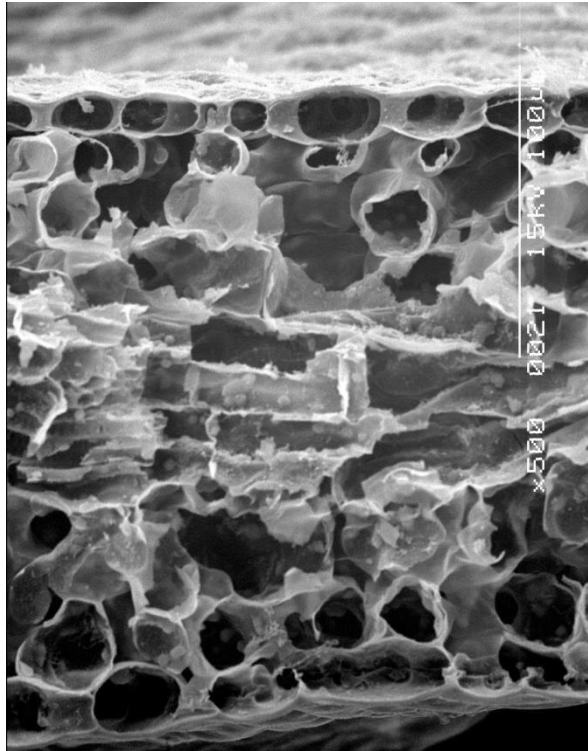
**Figure 6.16 – Time dependence of  $\Delta T$  for a device attached to a Lettuce plant suffering water stress conditions. Blue vertical lines show when the plant was watered**

The  $\Delta T$  measurements show a similar trend for the lettuce as for the Pak Choi. During stable periods when the plant had sufficient water, the  $\Delta T$  measurement was around 16.25 °C  $\pm$  0.2 °C. As the plant began to dry, the  $\Delta T$  measurements dropped to 13.6 °C and 11.2 °C respectively.

As well as drying faster, the lettuce demonstrated a different range of  $\Delta T$  measurements during the stable periods when the plant was not water stressed. This is likely to be due to structural differences between the Lettuce and Pak Choi. To investigate this, both leaves were imaged using a scanning electron microscope (SEM). Before the leaves could be imaged, they required dehydration, as the vacuum of the SEM would cause the cell to rupture, preventing an accurate image of the cellular structure being recorded.

A method similar to that suggested by Peacock et al [14] was used. The leaf was initially dehydrated by immersion in IPA for a period of 48 hours before critical point drying (Autosamdri 815B, Tousimis). The critical point drying removed the IPA while preventing damage to cells due to surface tension effects. This method is widely used for biological sample preparation and Pathan et al [15] report that it gives an acceptable level of preservation, although it can cause shrinking in some artefacts. Specimens were sectioned and coated with gold by sputtering before imaging in the SEM. The SEM images were used to compare the structure of the leaves and examples are shown in Figure 6.17.

a)



b)

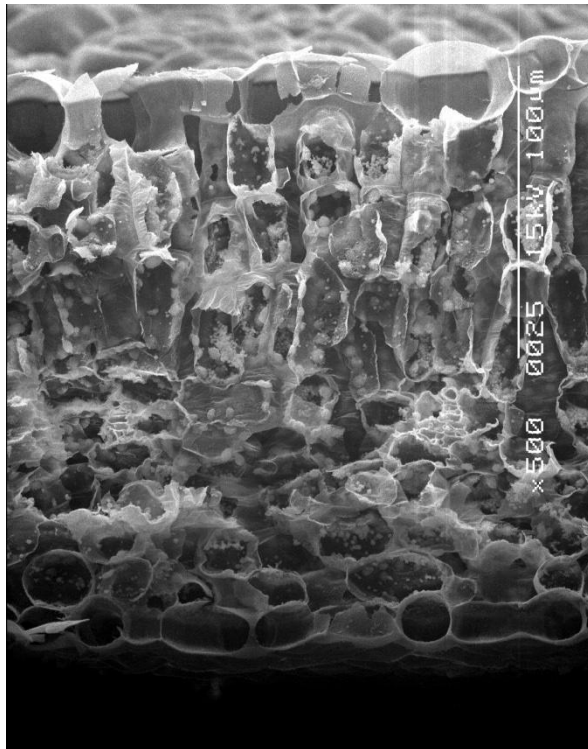


**Figure 6.17 – SEM images of a) Lettuce & b) Pak Choi**

The Pak Choi (Figure 6.17 b)) appears to show a structure similar to the classic leaf structure (e.g. [1]). At the top and bottom of the leaf, there is clearly an epidermal layer of cells aligned horizontally, while the cells in the upper half of the leaf appear more tightly packed together and

vertically aligned, forming the palisade mesophyll. The bottom half of the leaf forms the spongy mesophyll and the cells are more spherical and less densely packed. By contrast, the Lettuce (Figure 6.17 a)) does not demonstrate any difference between the top and bottom of the leaf.

The differences in structure can be attributed to the position of the leaves on each plant. Pak Choi arrange their leaves to face the available light, meaning a majority of the light falls only on one surface. Lettuce do not arrange their leaves in such an ordered manner, meaning that each leaf may receive light from any direction. This translates into the micro-structure of the leaf, as the Pak Choi form a palisade mesophyll layer on the light receiving side of the leaf, whereas the Lettuce leaves do not demonstrate this as light may be received on either surface of the leaf.

To give a quantitative description of the differences in the structure of the leaves, a dry weight ratio was calculated for each leaf type using Equation 6.2:

$$\text{dry weight ratio} = \frac{DW}{TW} \quad 6.2$$

Where TW is the fully turgid weight, measured after the leaf has been floated on DI water for a period of 2 hours and DW is the fully dry weight after baking in a vacuum oven at 80 °C for a period of 2 hours.

The dry weight ratio gives the percentage of the leaf that remains after all the water has been removed. Thus it is a measure of how much of the leaf's mass is solid material and how much is water. Lettuce has a dry weight ratio of 14 % meaning that water accounts for 86 % of the total mass of the leaf whereas Pak Choi has a dry weight ratio of 9 %.

Lettuce demonstrate a higher  $\Delta T$  value than Pak Choi when both plants are not water stressed. This indicates that the overall thermal resistance (i.e. the thermal conductivity of the leaf and its TCR) of the Lettuce is lower than that of the Pak Choi. While not conclusive, the higher dry weight ratio (i.e. lower water content) of the Lettuce may account for the differences observed in  $\Delta T$  between the two plants.

Despite these differences, it is clear that water stress can be detected in both types of plant. The decrease in  $\Delta T$  seen as the plant dries out is consistent in both. However, it is clear that much further work is required in order to quantify specific  $\Delta T$  values which are representative of healthy and water stressed conditions in specific plants. Fluctuations in water content related to other factors, such as ambient humidity and light intensity, must also be accounted for and separated from genuine drops in water content related to water stress. Defining specific thresholds is an important element for agricultural use of sensors, however extensive information and trialling is required [16]. This work was beyond the scope and time constraints of this project which acts as a proof of principle.

## **6.4. Potential applications**

This chapter has demonstrated that the device can be used to monitor the water content of a leaf. The design also allows the device to monitor the water content of a leaf in-situ and in real-time on a plant. This section discusses the potential applications for such a device.

### **6.4.1. Real-time irrigation feedback**

A variety of methods for monitoring plant water status in the field exist; for example thermal monitoring of sap flow rates within the stem of a plant [17]. Such sensors are widely used, but do not give a direct measure of the water content of leaves, unless accurate evaporative loss rates are known. Attempts have also been made to detect water stress using thermal imaging to relate increases in leaf temperature to stomatal closure and hence water content [18]. However, these remote methods require expensive equipment and the measurement technique can be influenced by factors such as sunlight levels or changes in humidity. As terahertz radiation is strongly absorbed by water, it has also been suggested as a method of measuring leaf water content [19], however the nature of the equipment renders it suitable only in laboratory settings. Cheaper sensors, which can be dispersed across a field offer more viable solutions. Examples include leaf thickness measurements [20] and patch clamp pressure sensors [12]. In addition to plant-mounted sensors, other indicators such as meteorological devices, soil water content sensors [21] and irrigation models [22] feed valuable information into irrigation decision systems.

The devices outlined in this work could be linked into a wireless system (e.g. [23]), to offer a relatively cheap, field-wide system that monitors the real-time water content of plant's leaves and relate this to their water content and general status. The advantages of a system capable of this are [8]:

- Instrumentation which is mobile and can be used in multiple locations
- Assurance that plant function is normal
- Irrigation systems which respond directly to the requirements of the crop
- Improved water use efficiency because water input is tightly coupled to crop requirement
- Reduced water wastage which is better for the environment

The devices presented in this work have a number of advantages which would aid their use in such an application. Firstly they are thin-film sensors, which allows them to be attached to a plant easily and require no specialist equipment or skilled operators. The attachment method is cheap, only requiring a suitable clamp. The thin nature of the device will also allow it to withstand movement more easily than bulkier devices which may also have adverse effects on the leaf such as shadowing or bending. The linear response and simple electronics required to probe the devices would also help to reduce the cost of a product based on these devices as signal processing of the device's output would be minimal.

These leaf-sensors offer a unique method for monitoring the water content of the most delicate and sensitive part of the plant. A number of devices spread across a field would give an indication of the requirements of specific areas, potentially leading to a reduction in water use and cost by tailoring the irrigation system to meet the needs of the plants. The water requirements across a field of a few hundred meters can vary significantly, depending on the soil composition and micro-climate [24], so such a system could lead to more efficient use of the water available. Detecting severe stress in the plants could also help to provide warnings of crop damage during extreme weather conditions.

To achieve real-time feedback to an irrigation system, the devices could be linked into a network of sensors, monitoring a number of different factors, such as the soil water content, sap flow rates, air temperature and humidity, wind speed, light level etc... This would allow an intelligent irrigation system to ascertain whether the plants need watering and how much water should be applied. Such a system could save water, whilst also improving yield by controlling water stress within plants. By linking together information from the various sensors, a much better picture of the health and condition of the crop could be achieved. A schematic diagram of a ZigBee based system is shown in Figure 6.18. Networks designed to operate over a wider area have also been suggested [25].

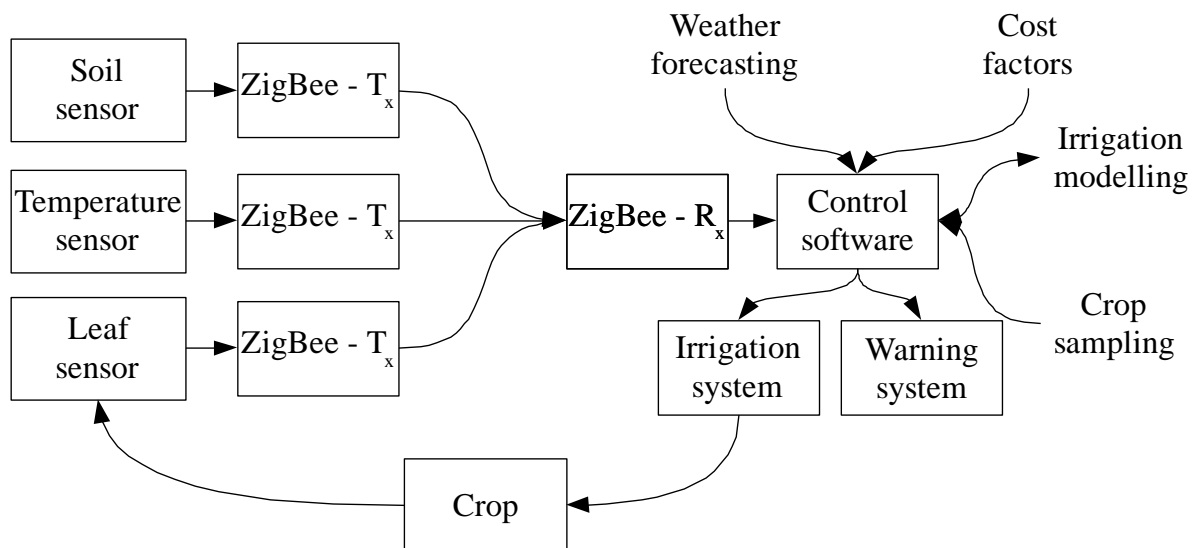


**Figure 6.18 – Schematic diagram showing how the leaf-sensors could fit into an intelligent irrigation system**

A number of communication systems could be used, from a basic wired system to a more complex wireless system. As an example, a ZigBee wireless network would offer a robust and low power mechanism for collecting information from a number of different sensors located over a range of up to several hundred meters [26]. The combination of data from the field along with other information, such as weather forecasting, cost factors, irrigation modelling or crop sampling could then be evaluated from a central control point (e.g. a PC) and fed back into the irrigation system to control watering and generate warnings. By combining a variety of sensors into the network, each could be used to improve the accuracy of the others. While many of the elements of an intelligent irrigation system are currently available, leaf sensors add an extra dimension to

the system. This removes the need to estimate how much water the plant requires and is essential if the system is to be able to respond directly to the needs of the plants.

#### **6.4.2. Fresh produce monitoring**

A second application for the device is monitoring fresh produce. From the moment that Lettuce or other fresh products are picked, they begin to deteriorate. Supermarkets have introduced efficient logistical networks to reduce the time between picking and consumption as well as using modified atmosphere packaging (MAP) (e.g. [27]). As the name implies, MAP involves packaging the produce within a protective atmosphere, normally high in CO<sub>2</sub>, which helps to prevent the produce from rotting. However, many supermarkets offer 'Living Lettuce' [28], where the plant is still alive and sold with a small amount of soil or hydroponic material to ensure that the plant's root system remains intact, prolonging its shelf life.

The devices presented here could be utilised to monitor the 'freshness' of leafy produce such as Lettuce, Spinach or Pak Choi. As demonstrated in Section 6.2.2,  $\Delta T$  is seen to decrease with time as the abscised leaf loses water. When packaged correctly this process is slowed, but not eliminated. By attaching sensors to leaves their shelf life could be monitored. This could give an insight into which batches are deteriorating faster, whether storage conditions are correct or whether the product has deteriorated and should be removed from the shelves. Wireless sensors could automatically warn of produce requiring attention, while a hand-held sensor could be used for periodic tests.

#### **6.4.3. Detection of water variations across a leaf**

The small scale of the features which form the device and photolithographic patterning technique used to create the features would allow the device to be developed to monitor the variations in water content across a leaf. This could allow the movement of water within a leaf to be studied in more detail than is currently available. Alternatively, several sensing areas could be patterned onto a single device. Multiple measurements could improve the accuracy of the measurements and prevent local structures from impacting on the accuracy of the device.

## 6.5. Conclusions

It has been demonstrated that the device is responsive to changes in the thermal conductivity of samples brought into intimate contact and that TCR will influence the measurement of solid samples. This chapter brings together this knowledge and acts as a proof of principle for using the devices to monitor the water content of a leaf. To demonstrate that the device can be used to monitor the water content of a leaf, it was initially attached to an abscised leaf which was allowed to dry for a period of 6 hours. By comparing the device's output over this period with the weight of the leaf, it has been shown that the device is sensitive to the water content of the leaf. The mechanisms which underpin the changes in  $\Delta T$  observed are likely to be complex. However, one potential explanation is that the device detects changes in TCR related to the turgidity of the cells.

This principle was subsequently exploited to show that the device can also monitor water content in-situ on living plants. Real-time measurements were taken over a period of several days on plants subjected to water stress conditions, which caused a reduction in the water content of the leaves. These measurements demonstrated that the variations in the water contents of the leaves were detectable using the sensor. Externally driven changes in the ambient temperature and humidity were not seen to influence the  $\Delta T$  measurements.

The devices could find applications as a sensor to provide real-time feedback about plant water status to irrigation decision systems, monitoring of fresh produce or as a tool for studying variations in water content across a leaf. To allow the device to act as an early warning for plants becoming water stressed, further work is required to provide information on specific thresholds for various plants species and demonstrate that the device is capable of operating in a range of environments. However, current data clearly demonstrate that the device is sensitive to the water status of a plant's leaves and is capable of operating in-situ on plants.

## 6.6. References

1. **Meyer, B.S. Anderson, D.B. and Bohning, R.H.** *Introduction to Plant Physiology*. New York : Van Nostrand, 1960.
2. **Winter, E.J.** *Water, Soil and the Plant*. London : MacMillan, 1974.
3. **Smith, J.A.C. and Griffiths, H., [ed.]**. *Water Deficits: Plant Responses from Cell to Community*. Oxford : BIOS Scientific, 1993.
4. **Skinner, A. J. and Lambert, M.F.** A Log-Antilog Analog Control Circuit for Constant-Power Warm-Thermistor Sensors - Application to Plant Water Status Measurement. *IEEE Sensors*. 2009, Vol. 9, 9, pp. 1049-1057.
5. **Cochard, H. Coll, L. Le Roux, X. and Ameglio, T.** Unraveling the Effects of Plant Hydraulics on Stomatal Closure during Water Stress in Walnut. *Plant Physiology*. 2002, Vol. 128, January, pp. 282-290.
6. **Eitel, J.U.H. Gessler, P.E. Smith, A.M. and Robberecht, R.** Suitability of existing and novel spectral indices to remotely detect water stress in Populus. *Forest Ecology and Management*. 2006, Vol. 229, pp. 170-182.
7. **Ben-Gal, A. Agam, N. Alchanatis, V. Cohen, Y. Yermiyahu, U. Zipori, I. Presnov, E. Sprintsin, M. Dag, A.** Evaluating water stress in irrigated olives: correlation of soil water status tree water status and thermal imagery. *Irrigation Science*. 2009, Vol. 27, pp. 367-376.
8. **Loveys, B.R. McCarthy, M. Jones, H.G. Theobald, J.C. Skinner, A.** When to water? Assessment of plant-based measurements to indicate irrigation requirements. *Final contract report (CSP02/02) from CSIRO to the Australian Grape and Wine Research and Development Corporation*. 2005.
9. **HM Government.** *Foresight: The Future of Food and Farming*. London : The Government Office for Science, 2011.

10. **Weatherley, P.E.** Studies in the Water Relations of the Cotton Plant. I. The Field Measurement of Water Deficits in Leaves. *New Phytologist*. 1950, Vol. 49, 1, pp. 81-97.
11. **Weatherley, P.E.** Studies in the Water Relations of the Cotton Plant. II. Diurnal and Seasonal Variations in Relative Turgidity and Environmental Factors. *New Phytologist*. 1951, Vol. 50, pp. 36-51.
12. **Zimmermann, D., Reuss, R., Westhoff, M., Geßner, P., Bauer, W., Bamberg, E., Bentrup, F.W. and Zimmermann, W.** A novel, non-invasive, online-monitoring, versatile and easy plant-based probe for measuring leaf water status. *Journal of Experimental Botany*. 2008, Vol. 59, 11, pp. 3157-3167.
13. **Incropera, F.P. and DeWitt, F.P.** *Introduction to Heat Transfer*. 3. New York : Wiley, 1996.
14. **Peacock, J. van Rensburg, L. Krüger, H. and van der Merwe, C.F.** Liquid substitution - an alternative procedure for leaf surface studies with scanning electron microscopy. *Scanning Microscopy*. 1998, Vol. 12, 2, pp. 401-412.
15. **Pathan, A.K. Bond, J. and Gaskin, R.E.** Sample preparation for scanning electron microscopy of plant surfaces - Horses for courses. *Micron*. 2008, Vol. 39, pp. 1049-1061.
16. **Jones, H.G.** Irrigation scheduling: advantages and pitfalls of plant-based methods. *Journal of Experimental Botany*. 2004, Vol. 55, 407, pp. 2427-2436.
17. **Gonzalez-Altozano, P., Pavel, E. W., Oncins, J. A., Doltra, J. and Cohen, M.** Comparative assessment of five methods of determining sap flow in peach trees. *Agriculture Water Management*. 2008, Vol. 95, pp. 503-515.
18. **Leinonen, H. G. and Jones, I.** Thermal imaging for the study of plant water relations. *Journal of Agricultural Meteorology*. 2003, 59, pp. 205-214.

19. **Hadjiloucas, S., Karatzas, L. S. and Bowen, J. W.** Measurements of Leaf Water Content Using Terahertz Radiation. *IEEE Transactions on Microwave Theory and Techniques*. 1999, Vol. 47, 2, pp. 142-149.
20. **Barvdo, B., Sharon, Y. and Selieman, R.** *Leaf thickness sensing device*. 6185833B1 U.S. Patent, Filed 13th February 2001.
21. **Lu, S., Ju, Z., Ren, T. and Horton, R.** A general approach to estimate soil water content from thermal inertia. *Agricultural and Forest Meteorology*. 2009, Vol. 149, pp. 1693-1698.
22. **Hedley, C. B. and Yule, I. J.** A method for spatial prediction of daily soil water status for precise irrigation scheduling. *Agricultural Water Management*. 2009, Vol. 96, pp. 1737-1745.
23. **Vellidis, G. Tucker, M. Perry, C. Kvien, C. and Bednarz, C.** A real-time wireless smart sensor array for scheduling irrigation. *Computers and Electronics in Agriculture*. 2008, Vol. 61, pp. 44-50.
24. **Hedley, C.B. and Yule, I.J.** A method for spatial prediction of daily soil water status for precise irrigation scheduling. *Agricultural Water Management*. 2009, Vol. 96, pp. 1737-1745.
25. **López Riquelme, J.A., Soto, F., Suardiáz, J., Sánchez, P, Iborra, A. and Vera, J.A.** Wireless Sensor Networks for precision horticulture in Southern Spain. *Computers and Electronics in Agriculture*. 2009, 68, pp. 25-35.
26. **Zhou, Y. Yang, X. Wang, L. Ying, Y.** A Wireless Design of Low-Cost Irrigation System Using ZigBee Technology. *International Conference on Networks Security, Wireless Communications and Trusted Computing*. 2009, Vol. 1, pp. 572-575.
27. **ILAPAK.** Produce industry. [Online] [Cited: 6th June 2011.] [http://www.ilapak.com/pages/solutions/ind\\_produce.php](http://www.ilapak.com/pages/solutions/ind_produce.php).
28. **Tesco.** Fresh And Naked Living Leaves 130g. [Online] [Cited: 6th June 2011.] <http://www.tesco.com/groceries/Product/Details/?id=267078061>.

## Chapter Seven

### *Conclusions and Further Work*

---

#### **7.1. Conclusions**

This thesis presents the design, fabrication and characterisation of a thermal micro-sensor. It has established a proof of principle that the device can be exploited as a leaf-mounted sensor for the determination of water content. The device consists of a micro-heater and two thin-film thermocouples formed on a flexible polyimide substrate with the output being the difference in temperature recorded by the two thermocouples ( $\Delta T$ ).

Microfabrication of the sensors and use of polyimide as a substrate and encapsulant gives the device a number of useful properties including: i) small precisely patterned dimensions with a sensing area of  $350\ \mu\text{m} \times 175\ \mu\text{m}$ ; ii) thermal sensitivity (polyimide devices obtained  $35.0\ \text{mV W}^{-1}$ ); iii) biocompatibility which allows operation on biological samples; iv) chemical inertness for probing on aggressive samples; v) electrical isolation between the device and the sample; vi) flexibility so the device conforms to non-flat surfaces such as plant leaves.

Experiments on liquids have demonstrated that the device is sensitive to changes in the bulk thermal conductivity. 100  $\mu\text{l}$  droplets of glycerine / water mixtures were used as thermal conductivity standards and the relationship between thermal conductivity and  $\Delta T$  was established. The measurement of mixtures of propanol / water further demonstrated that the device could be used to indirectly monitor the composition of small volume binary solutions by measurement of the thermal conductivity.

The device is actually sensitive to the total thermal resistance of a sample, which consists of bulk thermal conductivity and thermal contact resistance (TCR). The effect of TCR on the device was studied by systematically varying the contact force between the device and samples of known thermal conductivity. A comparison of the results showed that the measurements taken on bare surfaces could be strongly influenced by the contact resistance. Investigations have shown that a droplet of water can act as a thermal interface material and act to provide a constant and low contact resistance. The effect of TCR was found to influence measurements taken on plant leaves.

The drying rate of wetted paper was used to investigate the device's response to changes in a specimen's water content. Paper was used, as it is a similar thickness ( $\sim 100 \mu\text{m}$ ) to the plant leaves studied latterly. In addition, it is porous and so easily absorbs water, yet it dries over a reasonably fast period (around 48 mins at  $20^\circ\text{C}$ ) and dry paper has a much lower thermal conductivity than water. The output of the device ( $\Delta T$ ) was seen to be dependent on the water content of the paper. To verify that the changes were related to the water content, the drying times were compared with the theoretical drying time which are related to the vapour pressure of water and were estimated by the Goff-Gratch equation. Both showed a similar dependence on air temperature, indicating that the device was indeed sensitive to the water content of the paper.

To demonstrate that the device could be used to take measurements on plant leaves and relate these to the water content, it was clamped in place on an abscised Pak Choi leaf which was allowed to dry for a period of 6 hours. By comparing the device's output over this period with the weight of the leaf, it was shown that the device is sensitive to the water content of the leaf.

Repeating contact resistance experiments on a leaf indicated that TCR at the interface dominating the device's output rather than changes in the bulk thermal properties of the leaf as a potential explanation for the observed results. It is proposed that the change is due to a loss of turgidity in the leaf's cells which increase the effective contact area between the device and the leaf. This reduces the overall thermal resistance and results in lower  $\Delta T$  values.

Similar measurements were subsequently taken in-situ on a plant. As the water content of the leaves could not be determined, a controlled change in the water content was introduced by placing the plant in a controlled environment and subjecting it to water stress conditions. Changes in the water content were once again detected by the device when the plant became water stressed. Watering the plant was seen to reverse the trend, with  $\Delta T$  returning to and stabilising at the original measurement level. No relationship was seen between externally driven changes in the ambient temperature and humidity, and the  $\Delta T$  measurements. This work has demonstrated a proof of principle that the device can be utilised as a sensor to provide real-time feedback about plant water status.

In conclusion this work presents a microfabricated sensor which utilises thin-film thermocouples to measure the overall thermal resistance of small volume samples. 100  $\mu\text{l}$  droplets of liquids and sheets of wetter paper have been probed successfully. The device is also capable of operating on plant leaves with the output sensitive to water content. Such a device could find many uses in physical and biological applications, such as monitoring the water status of plants for real-time irrigation feedback or measuring the otherwise unknown thermal conductivity of small volume samples.

## 7.2. Further work

The ultimate aim of this work was to demonstrate a proof of principle application for the device. As such, the work opens up a number of potential avenues for further research which are beyond the scope and time constraints of the project, which focussed on the engineering development of a sensor. In particular, the plant testing element of the work has a number of questions which need to be answered before the device could be said to be fully capable and reliable enough to fit into a commercial irrigation system.

Firstly, the mechanism behind the change in TCR observed as the water content of a plant decreases is suggested to be related to the turgidity of the plant cells and the subsequent increase in effective contact area created by the loss of turgidity. Further work could utilise methods more familiar to biologists, such as pressure probes which can directly measure the water potential of individual plant cells. By relating the device's output to a measure of the turgidity, a better understanding of the mechanisms which affect the overall thermal conductivity could be found.

In this work, two types of plants have been studied (Lettuce and Pak Choi). It was shown that there is a variation in the results obtained which is likely to be related to their micro structure. Thus, for reliable operation across a range of plants, much more statistical work with a variety of species and a larger number of plants is required. However, such a scheme of work would also have to deal with other variables such as changes in the operating conditions and variability between individual plants. Such issues would complicate the actual water content of the leaves under investigation and therefore a suitable calibration would be required for each plant type.

To enable the device to operate as an indicator of plant water stress, it would be necessary to define specific thresholds, differentiating between mild water stress which may be acceptable (or desirable) over the short term, and more severe stress which could cause permanent damage or the death of the plant. In addition to investigating the sensitivity threshold, understanding how the device responds to more extreme changes in the ambient conditions could also provide important information for operation in a field setting.

The final element of further work required to enable field based monitoring is to gain an understanding of the device as a sensor and its stability and capability over a longer period of time. For example, drift in the TFTC response may be induced over extended operating periods, while the leaf-mounted nature of the device introduces a number of complexities. As the leaf grows, and potentially becomes compromised through damage or the influence of the device, calibration parameters may shift.

Beyond utilising the device as an input to an irrigation decision system, the device's design and operation could open up new opportunities for research. For example, the small scale nature of the device and its ability to sense localised changes in water content could allow variations in the water content of a leaf to be mapped with high spatial resolution. This concept could also feed into the plant-sensing elements of the work and increase the reliability of the device by allowing multiple sensing areas to be clamped to a single leaf. Further applications requiring small scale temperature and thermal conductivity measurements could also make use of the device. In particular the chemical inertness and biocompatibility of the device could open up further biological applications, while integration of the device into microfluidic systems would aid this goal. Finally, the device could easily be adapted to function as a flexible flow sensor for liquids and gases.

### **8.1. Journal articles**

**Atherton, J.J. Rosamond, M.C. Johnstone, S. and Zeze, D.A.** Thermal characterisation of micro-litre volumes using a thin film thermocouple based sensor. *Sensors and Actuators A*. 2011, Vol. 166, pp. 34-39.

**Atherton, J.J. Rosamond, M.C. Johnstone, S. and Zeze, D.A.** A leaf-mounted sensor for the detection of water content. 27<sup>th</sup> November 2011. *Manuscript submitted for publication in Sensors and Actuators A*.

**Alba Martin, M. Firmager, T. Atherton, J.J. Rosamond, M.C. Gallant, A.J. Petty, M.C. Al Ghaferi, A. Ayes, A. Ashall, D. Mabrook, M.F and Zeze, D.A.** Using carbon nanotubes to improve the characteristics of hybrid metal-semiconductor-insulator memory devices. 28<sup>th</sup> November 2011. *Manuscript submitted for publication*.

### **8.2. Conferences**

**Atherton, J.J. Rosamond, M.C. Johnstone, S. and Zeze, D.A.** Measuring thermal properties of small volumes of liquid using a robust and flexible sensor. *21<sup>st</sup> Micromechanics and Micro systems Europe Workshop*. 26<sup>th</sup> – 29<sup>th</sup> September 2010. Enschede, Netherlands.

**Atherton, J.J. Rosamond, M.C. Johnstone, S. and Zeze, D.A.** A device for the measurement of the thermal properties of small ( $\mu\text{L}$ ) volumes. *Thermal Investigations of ICs and Systems (THERMINIC), 2010 16th International Workshop on Thermal investigations of ICs and Systems*. 6<sup>th</sup> – 8<sup>th</sup> October 2010. Barcelona, Spain.

Poster: **Atherton, J.J. Rosamond, M.C. Johnstone, S. and Zeze, D.A.** Measurement of heat transfer using microscale thermoelectric probes. *UK Nanoforum & Emerging Technologies*. 3<sup>rd</sup> – 4<sup>th</sup> November 2009. London, England.

Poster: **Atherton, J.J. Rosamond, M.C. Johnstone, S. and Zeze, D.A.** Device to thermally interrogate biological cells. *RASOR Symposium 2010: Lab-on-a-Chip for Cell and Proteomics*. 5<sup>th</sup> March 2010. Glasgow, Scotland.

**Rosamond, M.C. Gallant, A. Atherton, J.J. Petty, M. Kolosov, O. Zeze, D.A.** Transparent Gold Nanowire Electrodes *IEEE NANO 2011 Conference*. 15<sup>th</sup> – 18<sup>th</sup> August, 2011. Portland, USA.

**Alba Martin, M. Firmager, T. Atherton, J.J. Rosamond, M.C. Gallant, A. Petty, M. Al Ghaferi, A. Ayesh, A. Ashall, D. Mabrook, M.F and Zeze, D.A.** Single-Walled Nanotube MIS Memory Devices. *IEEE NANO 2011 Conference*. 15<sup>th</sup> – 18<sup>th</sup> August, 2011. Portland, USA.